FROM FAULTING ON EARTH TO FAULTING ON OTHER WORLDS: MODELING THE STRESS EVOLUTION OF STRIKE-SLIP FAULTING ON THE SAN ANDREAS FAULT SYSTEM, ON TITAN, AND ON GANYMEDE

A DISSERTATION SUBMITTED TO THE GRADUATE DIVISION OF THE UNIVERSITY OF HAWAIʻI AT MĀNOA IN PARTIAL FULFILLMENT OF THE REQUIREMENTS FOR THE DEGREE OF

DOCTOR OF PHILOSOPHY

IN

GEOLOGY AND GEOPHYSICS

September 2022

by

Liliane M.L. Burkhard

Dissertation Committee:

Paul Lucey, Chairperson
Bridget Smith-Konter, Co-Chairperson
Sarah Fagents
Niels Grobbe
Emily Costello
Ian Robertson

Keywords: Strike-slip faults, Coulomb failure, tidal stress, earthquake gate, icy moons

ACKNOWLEDGMENTS

First and foremost, I wish to thank my advisor Bridget Smith-Konter, who invited me to join her research group and draw maps of icy moons in my first semester at UHM. She opened the door for me to geology and planetary sciences and without her continued support, confidence and trust, all that is would not have been possible. I dedicate this dissertation to her and her late husband, Jasper Konter, a wonderful professor and loving father. He may have left our lives, but he will never leave our hearts.

I am also very grateful for all the guidance, mentorship and advice I was fortunate to receive from Marissa Cameron, and for my dissertation committee and their contributions: Paul Lucey, who very graciously transitioned to chairperson after the tragedy, committee members Sarah Fagents, Emily Costello, Niels Grobbe and Ian Robertson; as well as Kate Scharer, Bob Pappalardo and Geoff Collins, who all have taken time out of their busy schedules for me. I wish to thank the department for all their support, my family and friends for all their love and encouragement.

ABSTRACT

Strike-slip interaction between rigid lithosphere plates causes many of the world's most dangerous earthquakes since plate displacement can be quite large in a single event. Strike-slip tectonism appears to be also widespread throughout the icy ocean worlds in our Solar System, acting as a driver of surface structural evolution and perhaps as a conduit for the exchange of surface and subsurface materials via shear heating processes. Understanding the stress variations of such fault networks can give us an insight into the geologic evolution of planetary bodies throughout the universe. The first study presented in this work models the stress changes of the San Andreas Fault System, analyzing the magnitude and build-up of Coulomb stress along the segments in the area of the Cajon Pass in southern California. As in the past, similar joint ruptures of these segments might occur in the future, and our work suggests that the junction between the San Andreas and San Jacinto faults at the Cajon Pass plays a larger role in seismic hazard in southern California than previously understood because it could function as an 'earthquake gate'. This research also demonstrates how we can evaluate paleoseismic data sets and comprehend prehistoric and historic fault activity using physics-based models. The second study presented focuses on modeling the possibility of strike-slip faulting on Titan, an icy moon of Saturn, where limited returned data at present hinders the remote exploration of the surface. Titan has stable liquids both on the surface and in the subsurface, and is consequently a prime candidate for astrobiological exploration. We investigate the potential of strike-slip tectonics governed by Coulomb failure laws and tidal stresses, and undertake a sensitivity analysis of Titan's shear failure inclinations, given optimal failure circumstances that may occur due to pore fluid interactions. Findings of this study indicate that shear failure is possible at shallow fault depths and for ideally orientated faults under diurnal tidal stress conditions due to such pore fluid pressures, especially in the polar areas. Strike-slip faulting is not only plausible, but it may also be an active deformation process on Titan's surface and subsurface based on interpretation of

geologic features observed in radar imagery. On Ganymede, an icy moon of Jupiter, strike-slip faulting has been identified through observational data and studied with tidal stress models, suggesting that a higher past eccentricity and/or nonsynchronous rotation must have existed to generate the stresses needed for fault displacement. In the last study presented in this work, we produce a crater count analysis on Ganymede to verify the published relative ages and shear deformation of tectonic units, investigate a period of higher eccentricity using the previously established methods and raise the hypothesis of impacts producing widespread tectonic features. The unique geodynamics of an ice shell may permit an extensive effect from an impact generated seismic event, causing rapid fault slip and spreading features. The analyzed tectonic features in the Nippur/Philus Sulci region appear to be clustered in age, suggesting three eras of distinct activity: One era was ancient, following the high impact rate that produced the heavily cratered dark terrain, the second intermediate era could be correlated with a period of higher orbital eccentricity, causing fault slip and deformation, and some features in the third and youngest era might be associated in time with the most recent basin-forming impact of Gilgamesh. Taken together, these three studies motivate future research and investigations into strike-slip tectonism and impact craters on icy moons and elsewhere, as they can help uncover the tectonic past and form estimates for the future.

TABLE OF CONTENTS

LIST OF TABLES

LIST OF FIGURES

CHAPTER 4. UNCOVERING GANYMEDE'S PAST: TECTONICS AT NIPPUR/PHILUS SULCI

CHAPTER 1. INTRODUCTION

Strike-slip faults are structural features of first-order importance on Earth, affecting vast areas of the crust, and include major plate boundaries thousands of kilometers long. Characteristically, long faults consist of networks of smaller faults, which in turn consist of a system of even smaller faults, and so on. The similar geometrical features at each scale help us identify different types of tectonism on other planetary bodies beyond Earth. Strike-slip faulting may be important not only to the structural development of the surfaces of planetary objects, but can also serve as a pathway for the exchange of surface and subsurface materials through shear heating mechanisms. Investigating this surface-subsurface transport indicator is an important part of searching for life-signatures beyond Earth.

Determining the displacement on a fault requires knowledge of the direction and magnitude of such through field work or satellite observations. Some features reveal total displacement, while others permit a partial or approximate indication, and some can only place a constraint on a possible displacement. The original orientation of features and the associated displacement is important for understanding faults as they can provide an interpretation for their tectonic significance.

In case of the San Andreas Fault System (SAFS), it is possible to determine absolute motion and deformation with respect to a reference using satellite-based Global Navigation Satellite System (GNSS) surveying. For other planetary bodies, we often do not have appropriate high-resolution observational datasets available. However, many icy satellites in our Solar System show distinctive morphological evidence for strike-slip faulting even at a coarse resolution. Sources of stress that can produce this faulting may be connected to the tidal deformation that moons experience as they orbit their parent planet. In order to understand the geologic history of strike-slip tectonics, we must understand the relationship between observed faulting features on icy moons and the potential sources of stress. In this research, we use a combination of computer modeling techniques and an analysis of data returned from spacecraft to relate observed features to possible stresses that created them.

1.1 Development of strike-slip faults

A strike-slip fault is a zone of fractures between two blocks of rock that allows them to move past one another sideways due to a state of shear and stress (Figure 1.1). This movement may be rapid in the form of an earthquake, or slow in what is referred to as fault creep. Over geologic

time, faults create recurrent displacements, which can range from a few millimeters to many kilometers. Strike-slip faults are per definition vertical or nearly vertical fractures where blocks move mostly horizontally. During an earthquake, the block on one side of the fault abruptly slips with respect to the other and the surface might be vertical, horizontal, or at an angle. The angle of the fault with respect to the surface is referred to as the dip. For the modeling in this dissertation, strike-slip faults are assumed to move absolutely vertically past one another to calculate the stress field necessary to induce movement and stress accumulation.

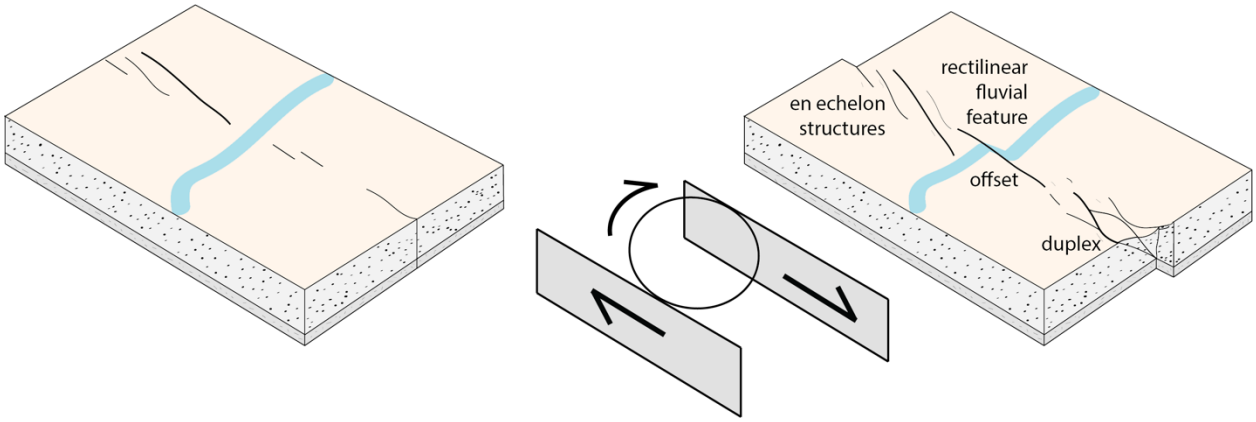

Figure 1.1. Strike-slip fault morphology cross section illustrating movement in a right-lateral sense. Features labeled are examples of large-scale characteristics of strike-slip faults that can be identified in the field and through spacecraft imagery that will be examined in this dissertation.

During an earthquake however, the abrupt movement combines horizontal with vertical displacement associated with thrust and/or normal faulting. The resulting landscape (Figure 1.2) gives us references for geomorphological analysis from which we can infer the stress field acting on the fault zone. Stress may be transmitted over large distances and have several sources. This includes the negative buoyancy of descending tectonic plates in a subducting zone, gravitational sliding, and temperature changes that can cause thermal stresses as rocks contract or expand. The removal or addition of surface loads such as glaciers or sediments through climate change and erosion can also cause stress to be released or built up. Because planetary bodies are not perfect spheres and have equatorial bulges and flatter areas at the poles, tectonic plates deform as they move latitudinally, which leads to membrane stresses (Turcotte and Schubert, 1982). High stress levels on faults will eventually lead to earthquakes and measurable displacement. Strike-slip fault movement in particular can be induced in high tensional regimes where the shear stress

then exceeds the frictional resistance acting on a fault plane. Several factors can also contribute to the reduction in friction, such as changes in material/crystal structures and lubrication.

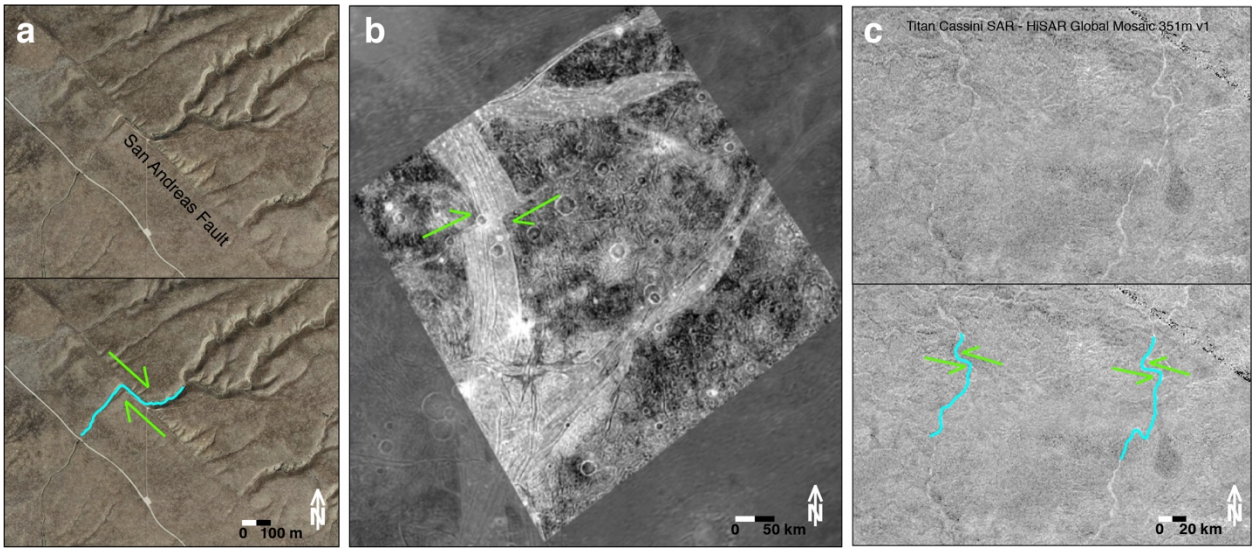

Figure 1.2. Examples of strike-slip faulting features with arrows indicating the slip direction of displacement of fluvial features and offsets: **a)** Rectilinear fluvial feature offset by the San Andreas Fault at Wallace Creek (Google Maps satellite image), **b)** offset at Dardanus Sulcus on Ganymede (Galileo SSI, orbit G29, 2 km/px resolution), **c)** Western Xanadu bright radar features on Titan of a rectilinear fluvial drainage pattern, bending close to 90° (Titan Cassini SAR-HiSAR Global Mosaic, 351m/px resolution). The offset reach is subparallel to the fault and the up- and downstream reaches are parallel.

1.2 Strike-slip movement in California

The San Andreas Fault System (SAFS) is a right-lateral strike slip fault that forms the boundary between the North American and the Pacific tectonic plates and presents a great earthquake hazard for California (Figure 1.3). Most of the movement between these two tectonic plates is accommodated by the displacement on the SAFS. Because of its proximity to a large portion of the population of the United States, it is the most studied and observed strike-slip fault on Earth, with geodetic observations of crustal deformation provided by Global Navigation Satellite Systems (GNSS) and Interferometric Synthetic Aperture Radar (InSAR). Heat flow data can be used as a proxy for elastic plate thickness (Ward et al., 2021) and in combination with earthquake chronologies can provide a good approximation of the conditions for modeling the motion and stress accumulation of the fault system. This tectonically very active area has experienced at least 37 moderate earthquakes (M_w >6.0) over the past 200 years as well as four

major events (M_w >7.0) from 1812 to 1906 (Scharer et al., 2020). Some of these ruptures overlap in the south-central portion of the SAFS around the Cajon Pass area, which this dissertation will have a special focus on. Recently however, major activity has only occurred along fault segments in the Eastern California Shear Zone (ECSZ), paralleling the main San Andreas Fault, like the M_w 7.3 1999 Hector Mine and M_w 7.1 2019 Ridgecrest earthquakes. Several sections of the main San Andreas Fault have not ruptured in up to 350 years, suggesting that future slip events could be quite large (Sieh, 1978). Chapter 2 of this dissertation focuses on a stress accumulation study of southern California, incorporating the most recent earthquake chronologies obtained through trenching reports and fault properties into the updated analytical model *maxwell* (Smith and Sandwell, 2004; Sandwell and Smith-Konter, 2018). Through studying the stress release and accumulation over time, we can improve estimations for earthquake hazard assessments and inform continuing future modeling endeavors.

Figure 1.3. A M_w 7.9 earthquake struck by San Francisco on April 18, 1906 and ignited fires that were even more disastrous (Photograph: AP).

1.3 Strike-slip faulting on the icy moons of Jupiter and Saturn

Faulting is a natural process of any planetary surface subjected to changes in stress, and manifestations of strike-slip faulting are well documented on multiple ocean worlds (e.g., Europa, Enceladus, and Ganymede) that are tidally locked in synchronous rotation with their parent planet. These icy moons are likely to have a differentiated structure composed of a water-ice crust, a subsurface liquid water ocean, and a rocky core possibly surrounded by dense layers of ice. In 1979, the *Voyager 1* and *2* spacecraft returned images from the Jupiter system (Smith et al., 1979 a, b), presenting the first close photographs of the surface of the icy Galilean moons. In particular, the largest moon Ganymede shows clear strike-slip faulting features on its surface that can be identified even from a global view, with offsets as large as ~50 km (Figure 1.2 b). The *Galileo* space probe entered the Jupiter system in 1995 and until 2003 returned patches of high-resolution images of the surface of Ganymede (Carr et al., 1995), which have been used in geologic studies to identify features and relative ages of regions according to the principle of superposition (Lucchita, 1980; Head et al., 2002; Kattenhorn, 2004; Collins, 2009; Cameron et al., 2018) and crater counts (Shoemaker et al., 1982; Melosh, 1989; Murchie et al., 1989; Neukum et al., 1997; Zahnle et al., 1998; Schenk, 2004). In addition to the images, *Galileo* provided magnetic field measurements that delivered evidence of the presence of a subsurface liquid ocean underneath the icy crust (Kivelson et al., 2002). The smaller Jupiter moon Europa also shows evidence of strike-slip displacement on its icy crust (Hoppa et al., 1999), however, Ganymede displays very large and clearly pronounced offsets, and its surface is estimated to be much older (Collins et al., 2010) whereas Europa has been more recently resurfaced (Schmidt et al., 2011).

The proposed sources of stress that can deform these surfaces are potentially tied to the deformation the moons experience as they orbit their parent planets, and it has been suggested that tectonic features and faults on icy satellites result from gravitational tidal stresses (Helfenstein and Parmentier, 1985; Hoppa et al., 1999; Kattenhorn, 2002; Schenk et al., 2008; Rhoden et al., 2010; Smith-Konter and Pappalardo, 2008, Cameron et al., 2018; 2019). Several other factors could have influenced the placements and displacement of faults on icy moons besides tidal stresses, such as the rotation of the outer part of the satellite relative to the interior (nonsynchronous rotation, NSR), a shift in the body relative to the rotation axis (polar wander), volume changes induced by the melting or freezing of subsurface layers, a change in obliquity or a change in the orbital characteristics like eccentricity, orbital recession or decay. As these mechanisms are mostly speculative and not well understood through time, this dissertation will focus on the tidal stresses in the current configuration and relate possible factors to each other

that could lead to the presently observed effects. Most researchers use a combination of data returned by spacecraft and computer modeling to correlate observed geological features to the possible stresses that created them. For calculating stresses, a variety of modeling programs exist that typically assume a thin elastic shell and/or a multi-layered viscoelastic body. The only open-source code, *SatStress,* was developed by Zane Selvans and described by Wahr et al. (2009), and has been used by numerous researchers for modeling diurnal tidal stresses, NSR, and to calculate Love numbers describing the satellite's susceptibility to change shape (Groenleer and Kattenhorn, 2008; Smith-Konter and Pappalardo, 2008; Beuthe, 2010; Jara-Orué and Vermeersen, 2011; Olgin et al., 2011; Cameron et al., 2019; 2020), which is used in this dissertation as well. Studying strike-slip tectonism on icy worlds is important as it could be significant not only to the structural evolution of the surfaces of these satellites but may also act as a conduit for the exchange of surface and subsurface materials through shear heating mechanisms. To understand the geological history of these tectonized icy moons, we must understand the relationship between the observed surface features and potential stress sources, which are explored in Chapters 3 and 4 of this dissertation through modeling diurnal tidal stresses with *SatStress* and using the Coulomb failure criteria for fault initiation.

Most icy satellites exhibit primarily features of extensional tectonism (e.g., normal faults, graben, fractures), with rare and little evidence of contractional tectonism (e.g., thrust faults and folds; Collins et al., 2010). To form contractional structures on Ganymede, it is estimated that a stress of 10-25 MPa is required, which is 4-8 times the value necessary to achieve extensional features on an icy crust (Pappalardo and Davis, 2007). Diurnal tidal stresses on Ganymede can only generate <0.1 MPa with its current value of eccentricity (Collins et al., 2010; Cameron et al., 2020), and other sources of stress sufficient to produce any type of faulting do not exist on Ganymede at present. However, a past configuration of higher eccentricity could have existed, which this dissertation will explore in Chapter 4 through the modeling of an example region in combination with crater counts in an effort to uncover the tectonic history of Ganymede.

Sources of contractional stress sufficient for thrust faulting probably do not exist on most icy satellites, including those in the Saturn system. The *Cassini* RADAR instrument began imaging Saturn's largest icy moon Titan in 2004, operating in Synthetic Aperture Radar (SAR) mode, obtaining images up to 351 m/px resolution of many landforms, but only for 46% of the Surface (Lopes et al., 2019). Titan is of similar size to Ganymede (Table 1.1) but with a thick atmosphere and is the only known planetary body in our Solar System besides Earth that has surface liquids (Lorenz et al., 2008). However, the hydrological system that can be seen as analogous to Earth

is a methane-based cycle with a water-ice crust (Lunine and Lorenz, 2009). Nevertheless, liquids can significantly reduce the shear strength of the icy crust and may play a key role in the tectonic evolution of Titan, as liquids have for Earth. There is strong evidence that contractional features exist on Titan (Lunine et al., 2008; Cook-Hallett et al., 2015; Liu et al., 2016). If there have been stresses high enough to produce these features, it can be suspected that strike-slip faults can exist as well. This hypothesis is explored in Chapter 3 of this dissertation, with novel mapping results of possible strike-slip features (Figure 1.2 c) and modeling diurnal tidal stresses. Titan's present eccentricity is 22 times as much as Ganymede's and may therefore generate enough stress to drive faulting in a state of active tectonism. On Ganymede however, a period of a past high eccentricity might have produced the large offset features observed today.

Table 1.1. Satellite characteristics.

Satellite	Diameter (km)	Mass (kg)	Mass parent planet (kg)	Semi-major axis (km)	Orbital period (days)	Eccentricity
Ganymede	5268.2	1.48×10^{23}	1.90×10^{27}	1.070×10^{6}	7d 4h	0.0013
Titan	5149.5	1.35×10^{23}	5.68×10^{26}	1.221×10^{6}	15d 22h	0.0288

The findings of this dissertation consider the evolution of Ganymede through time and attempt to describe its complex geologic history. For Titan, this dissertation explores the possibility of strike-slip faulting without confirmed evidence from previous mapping efforts. The global oceans underneath these icy crusts may have implications for life beyond Earth, and finding evidence for prospective pathways for surface and subsurface materials is directly relevant to the objectives of NASA's Outer Planets Research Program, the Europa Clipper mission, the Dragonfly mission to Titan, and ESA's Jupiter Icy Moons Explorer (JUICE) mission.

CHAPTER 2. THE SAN ANDREAS FAULT SYSTEM: EARTHQUAKE CYCLE STRESS ACCUMULATON DISPARITIES OF THE CAJON PASS REGION IN SOUTHERN CALIFORNIA

Note: This chapter will be submitted pending co-author notes to the *Journal of Geophysical Research: Solid Earth* with co-authors B.R. Smith-Konter, K.M. Scharer, Xiaohua Xu and D.T. Sandwell.

Abstract

4D simulations of stress evolution provide rare insights into earthquake cycle stress variations at seismogenic depths where earthquake ruptures nucleate. Paleoseismic estimates of earthquake offset and chronology, spanning multiple earthquake cycles, are available for many well-studied segments of the San Andreas Fault System (SAFS). The Cajon Pass at the junction of the San Andreas and San Jacinto faults represents a critical site for future through-going ruptures in Southern California. We constructed new 4D earthquake cycle deformation time-series simulations to further study the temporally and spatially varying stress threshold conditions using a 1000-year paleoseismic record documenting the slip chronology. A semi-analytic Fourier transform model calculated surface deformation and stress associated with 3D dislocations embedded in an elastic plate overlying a Maxwell viscoelastic half-space. Our modeling results show that stress accumulation rates are highest north of Cajon Pass (~1.8 MPa/100 yrs) due to larger slip rates. Stress rates south of Cajon Pass are lower (~1.0-1.5 MPa/100 yrs) because of smaller slip rates and distributed stress accumulation on paralleling segments. Current Coulomb stress accumulation near the Cajon Pass is estimated at 2.8 MPa on segment Mojave South (MOS), 1.8 MPa on segment North San Bernardino (NSB1) and 3.6 MPa on segment San Jacinto Bernardino (SJB). Results conclude an elevated range of mean stress accumulation characteristic to each segment, with threshold ranges of 1.2-2.7 MPa for the Mojave South segment, 0.4-1.6 MPa for North San Bernardino, and 1.2-2.9 MPa for segment San Jacinto Bernardino. Further analysis suggests that when the stress disparity between the San Jacinto fault (segment SJB) to the Mojave section of the San Andreas fault (segment MOS) is within a threshold range, the segments appear to rupture jointly, implying an ‘earthquake gate’ opening behavior of the Cajon Pass during marked episodes of paleoseismic events. Due to the extent of stress lobes and spatial proximity of segments to each other, earthquake events on participating host faults can cause

differences in stress values on non-participating segments, inducing stress changes without a rupture on the segment. The work presented here advances our understanding of strike-slip fault failure sensitivity to stress accumulation over time in order to support and improve seismic hazard and risk assessment of the SAFS.

2.1 Introduction

The San Andreas Fault System (SAFS) in California is a complex transform plate boundary that has experienced at least 37 moderate earthquakes ($M_w > 6.0$) over the past 200 years and at least 118 over the past 1000 years. Of these, four major earthquakes ($M_w > 7.0$) ruptured the SAFS from 1812 to 1906, including a pair of overlapping ruptures in 1812 and 1857 in the south-central portion of the SAFS around the Cajon Pass area (Toppozada et al., 2002; Scharer et al., 2010; Scharer et al., 2017; Scharer and Streig, 2019; Scharer and Yule, 2020). Recently, major earthquake activity has been limited to faults adjacent to the SAFS in the Eastern California Shear Zone (ECSZ; i.e., M_w 7.3 1992 Landers, M_w 7.1 1999 Hector Mine, M_w 7.1 2019 Ridgecrest), while several sections of the SAFS have not ruptured in over 150 to 350 years. With a magnitude of M_w 7.9, the rupture of 1857 was the last 'Big One' in Southern California and stopping at the Cajon Pass, spanning multiple segments to the north. Since then, some portions of the southern SAFS seem to have settled into a period of rest, although the established earthquake sequence suggests periodic large events at least every 100 years (Scharer et al., 2010). This unusual seismic quiescence of the southern SAFS has given rise to the suggestion that future slip events on the SAFS may be large (Sieh, 1978; Scharer et al., 2010; Scharer et al., 2017). It is therefore critical to investigate the present-day stress conditions of the southern SAFS in context with most likely stress scenarios of the past, especially given the major ramifications for nearby heavily populated communities like Los Angeles, San Bernardino, Riverside, and the Coachella Valley.

The southern San Andreas Fault (SAF) and the San Jacinto Fault (SJF) branches carry the majority of the plate motion in Southern California (Dawson and Weldon, 2013; Scharer and Yule, 2020) and distribute about 45 mm/year of strike-slip motion over a region of ~200 km (Sandwell et al., 2016). Located at the intersection between the southern SAF and the SJF, the Cajon Pass (Figure 2.1) is of particular importance and its earthquake history of special interest. The region comprises of two SAF segments (Mojave to the north and San Bernardino to the south) and the northernmost San Jacinto segment. The Cajon Pass is thought to be the southernmost terminus

of the M_w 7.9 1857 Fort Tejon earthquake, which ruptured multiple segments spanning ~330 km of the SAF (Scharer et al., 2014). Prior to 1857, the Cajon Pass also experienced slip during the 1812 event, which is estimated to be M_w 7.5 (Scharer and Streig, 2019; Padilla et al., 2021). Unlike the 1857 earthquake however, in which the Cajon Pass served as the terminating point, the 1812 event may have nucleated on the SJF and propagated northwards through the Cajon Pass (Lozos, 2016). When examining the paleoseismic record, the Cajon Pass must have experienced at least 12 events within the past 1000 years. Fault interactions and rheological conditions at the Cajon Pass may control whether a north-moving rupture could propagate from the SJF to the SAF at the Cajon Pass (Roten et al., 2014). Thus, improving our understanding of fault interactions at the Cajon Pass is the next step in an effort to improve seismic hazard assessments of Southern California.

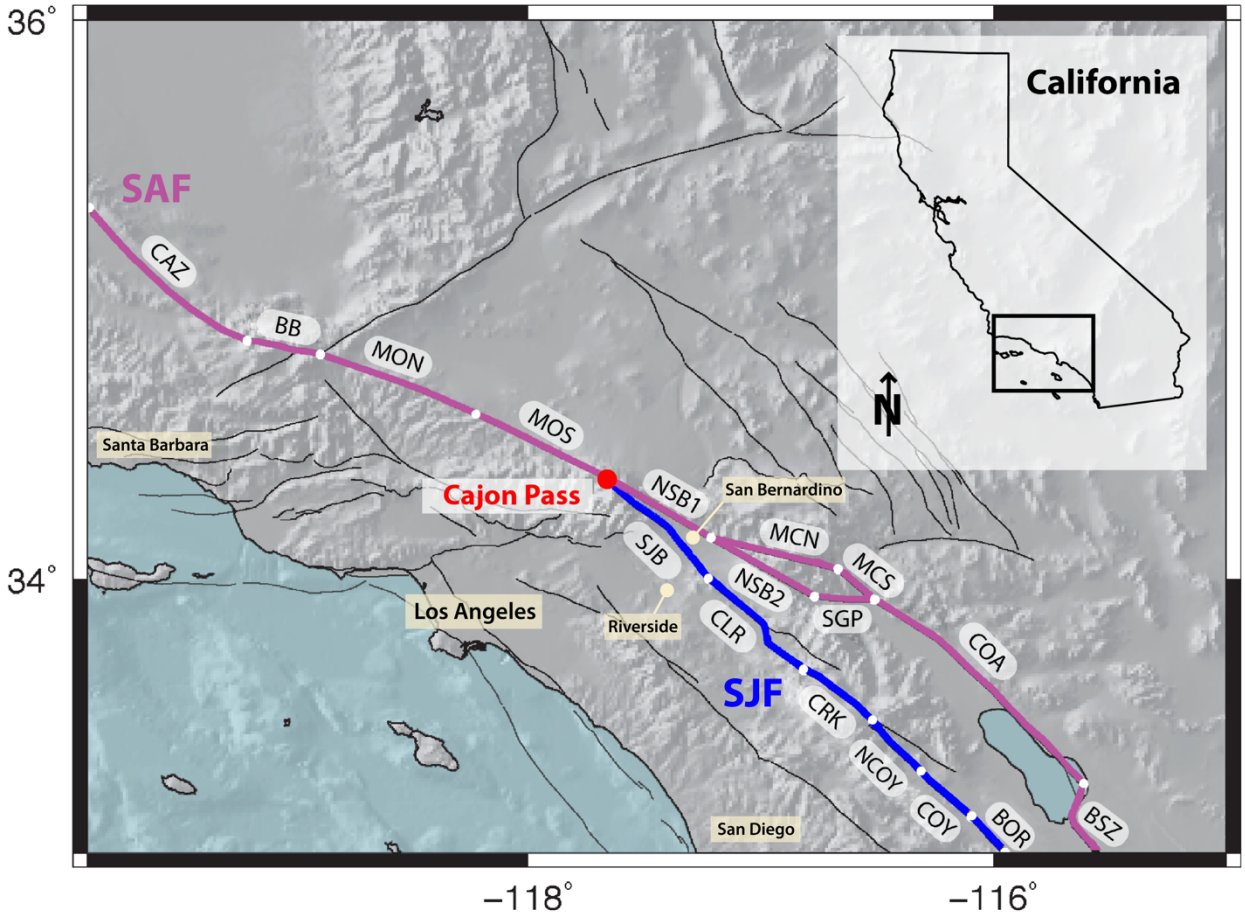

Figure 2.1. The San Andreas Fault System (SAFS) in Southern California, with main SAF fault trace in purple and San Jacinto Fault (SJF) trace in blue. Model segment boundaries used in this study are marked by dots and abbreviated names are specified per section (Table 2.1). The Cajon Pass is indicated in red.

Although there is an absence of morphological surface connection between the SAF and SJF, where they converge has been suggested to act as a critical junction for possible through-going ruptures, classified as a principal volumetric intersection with clear interaction or connection at depth due to the long-term partitioning of slip (Schwartz et al., 2012; Padilla et al., 2021). Such a fault junction can act as a conditional barrier or 'earthquake gate', where earthquakes terminate but when stress conditions are favorable, permitting passing events (Lozos, 2016; Padilla et al., 2021; Liu et al., 2022). Stresses have a lobe and shadow-effect on segments that causes values to drop or rise with an event on another segment depending on their proximity and geometry (King et al., 1994; Harris and Simpson, 1998). We refer to this kind of drop or increase as an induced stress change during an event on a non-participating segment. Furthermore, a participating-stopping ('Gate-Closed') event denotes an earthquake on a segment but terminating on this segment, while a participating-passing (Gate-Open') event is an earthquake where stress levels were favorable to pass through the earthquake gate region, possibly acting as a trigger for participation and segments acting as receiver faults of the event. A rupture of all three segments at the Cajon Pass would therefore represent a complete junction, or 'tripartite', rupture, while an event on the two segments of the SAF trace joining at the Cajon Pass is a 'joint' earthquake.

In order to study these interactions, we examine (1) how earthquake cycle stress accumulates at adjacent segments of the Cajon Pass before major slip events over the past 1000 years, (2) how current stress accumulation levels coincide and compare with past stress, and (3) how future stress drop scenarios might affect Cajon Pass earthquake gate-like behavior. For this analysis, we constructed a new earthquake stress evolution simulation to investigate the spatially and temporally varying stress threshold conditions using a 1000-year paleoseismic record detailing slip chronology (Scharer and Yule, 2020). We use the 4-D semi-analytic crustal deformation modeling code *maxwell* (Smith and Sandwell, 2004; Sandwell and Smith-Konter, 2018), which rapidly calculates time-dependent surface deformation and Coulomb stress associated with 3D dislocations embedded in an elastic plate overlying a Maxwell viscoelastic half-space. Fault loading rates are kinematically prescribed for each segment that extend from a variable locking depth to the base of the elastic plate. Locking depths are derived from geodetic surface deformation measurements (i.e., GPS and InSAR velocity analyses, Tong et al., 2014), and geologic slip rates are adopted from the Uniform California Earthquake Rupture Forecast (UCERF3; Field et al., 2017). Thus, this earthquake cycle model can lend insight into faulting mechanics and stress evolution of the Cajon Pass employing the most recent database of paleoseismic earthquake chronologies of the SAFS (Scharer and Yule, 2020) and latest updated

maxwell code accommodating heterogeneous rheology and refined fault segmentation (Sandwell and Smith-Konter, 2018; Burkhard et al., 2018; Ward et al., 2021).

4D (3D + time) simulations of plate boundary stress evolution provide us with a rare insight into earthquake cycle crustal stress variations. Stress accumulation from variable fault locking depth within the seismogenic crust, combined with paleoseismic evidence of earthquake events over multiple earthquake cycles can be used to explore stress accumulation thresholds of past major events of the Cajon Pass over the last 1000 years. Because of the distinctive arrangement of fault segmentation at the Cajon Pass, combined with the apparent inconsistent nature of connected ruptures at its intersection, the motivation of this analysis is to explore 4D stress accumulation over multiple earthquake cycles as well as triggering conditions of nearby segments. Moreover, 4D stress models may provide a lower bound on stress estimates throughout the historical era as well as an upper bound on the expected recurrence interval of a particular fault segment.

We can refer to the fundamental behaviors of the earthquake cycle (Reid, 1910; Thatcher, 1983, Cohen, 1999) for insight into the mechanics of stress accumulation (Figure 2.2). Deep plate tectonic motion, or slip, accommodated along fault networks like the SAFS, produces stress accumulation on the locked upper segments of a fault system, loading faults to failure thresholds throughout the interseismic interval (Figure 2.2 bottom). These stresses are released during an earthquake (coseismic period), which can last a few seconds to minutes. An earthquake event is then followed by viscoelastic relaxation (Freed and Lin, 1998; 2001; Guns and Bennett, 2020) and as the stresses relax during this postseismic period, stress accumulation recovers as a function of mantle viscosity and thickness of the elastic and viscoelastic crust and mantle layers (i.e., Hearn, 2003). Eventually, the relaxing layer rebounds and returns to its pre-earthquake configuration.

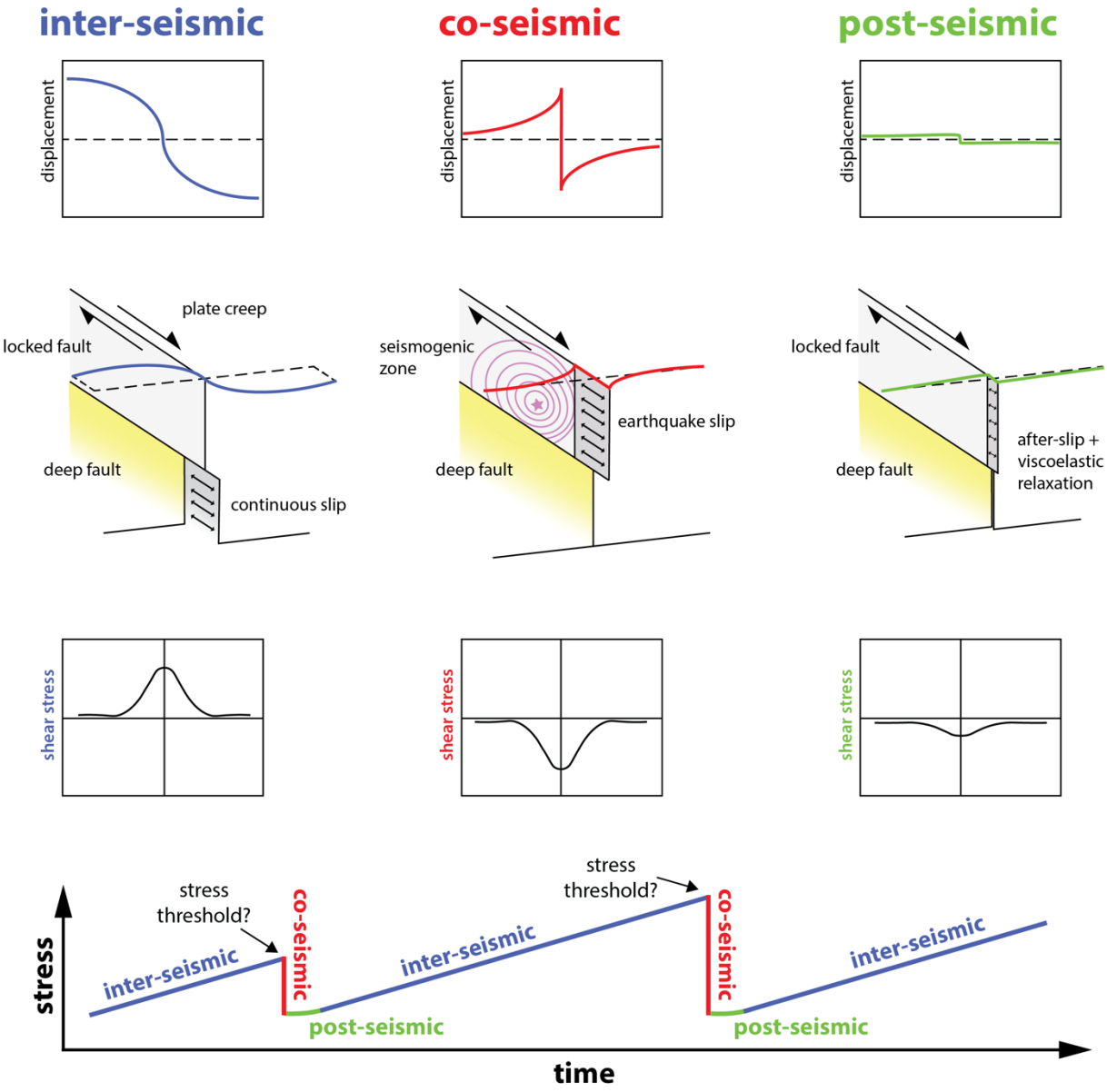

Figure 2.2. Earthquake cycle diagram for a simple strike-slip fault displaying the far- and near-field displacement and shear stress accumulation, drop and viscoelastic relaxation during the period between earthquakes (interseismic), during (coseismic) and after an earthquake (postseismic). Figure modified from Jiang and Lapusta (2017). Bottom: Earthquake cycle time-series depicting the stress accumulation, drop and relaxation over time during inter-seismic, co-seismic and post-seismic stages.

Following this model, the basic behavior of the earthquake cycle stress assumes a constant stress accumulation rate on a shallow locked fault due to deep creeping from below, which eventually fails at some threshold stress level, resulting in an earthquake and reducing the stress

on the fault and nearby regions. While this basic model provides a conceptual framework for investigating the conditions that lead a fault to failure, there is little evidence that faults rupture periodically (Scharer et al., 2010) or at a uniform threshold (Murray and Segall, 2002). Figure 2.2 (bottom) demonstrates this conundrum, where semi-uniform stress accumulation rates may give rise to aperiodic earthquakes (and stress drops) over time. Also, while stress rate is largely a function of the slip rate and locking depth of a fault segment (Smith and Sandwell, 2003; Loveless and Meade, 2011), stress accumulation is dependent on the time between earthquake events, which is constrained by the paleoseismic/historic earthquake record. Thus, our understanding of earthquake cycle stress behaviors, even at well-studied places like the Cajon Pass, is strongly limited by the accuracy of the paleoseismic record of slip at isolated locations along faults. Yet, while patterns of earthquake occurrence remain somewhat enigmatic, this study aims to illuminate stress behaviors that promote (or inhibit) spatially and temporally connected ruptures of the Cajon Pass. We also attempt to reconcile stress thresholds of multiple earthquake cycles to assess the present-day stress of the Cajon Pass and nearby fault segments of the SAFS.

2.2 Paleoseismic data

For this study, we use estimates of rupture history of the SAFS based on 118 published historical and paleoseismic events (e.g. Scharer et al., 2017; Scharer and Streig, 2019; Scharer and Yule, 2020) with moment magnitudes (M_w) exceeding 6.0 over the past 1000 years. Specifically, we adopt the Maximum Rupture Model (MRM) of Scharer and Yule (2020; Figure 2.3), which accommodates all paleoseismic eras with the fewest ruptures. The length of a rupture is measured by comparing sites along strike; if site earthquake ages at adjoining sites coincide, the rupture is expanded; if they do not, the rupture terminates midway between sites. The accuracy and completeness of site records are assumed for the model. Earthquake ages for the MRM were calculated using Bayesian modeling of radiocarbon dates from plant remains in layers that bound the paleoground surface of the earthquake (e.g., Lienkaemper and Bronk Ramsey, 2009), as well as historical records and other environmental data such as European pollen or tree rings (Scharer and Yule, 2020). Given the varying uncertainties in dating techniques and suggested magnitude of each identified earthquake, alternate rupture histories are feasible; at one extreme for example, the MRM model predicts over 120 M_w ~6.7 ruptures given the average spacing of 22 km per studied site; if each identified earthquake event is a single rupture, it would equal to a rate of about one per decade on average. This is a rather unlikely scenario given the

historic period and records after 1800 (Scharer and Yule, 2020). Other data, such as rupture extent determined from displacement (Biasi and Weldon, 2009) or dynamic modeling using complex geometries such as bends and splays have been used in other studies to infer rupture behavior (e.g., Lozos et al., 2011; Douilly et al., 2020; Liu et al., 2022), but they do not cover as large an area as the MRM. However, at least 30% of historical ruptures on strike-slip faults end at no evident geometric complexity (Biasi and Wesnousky, 2016), and Scharer and Yule (2020) estimate that adding a geometrically based criterion would lower the average magnitudes produced in the MRM and lead to larger magnitude dispersion.

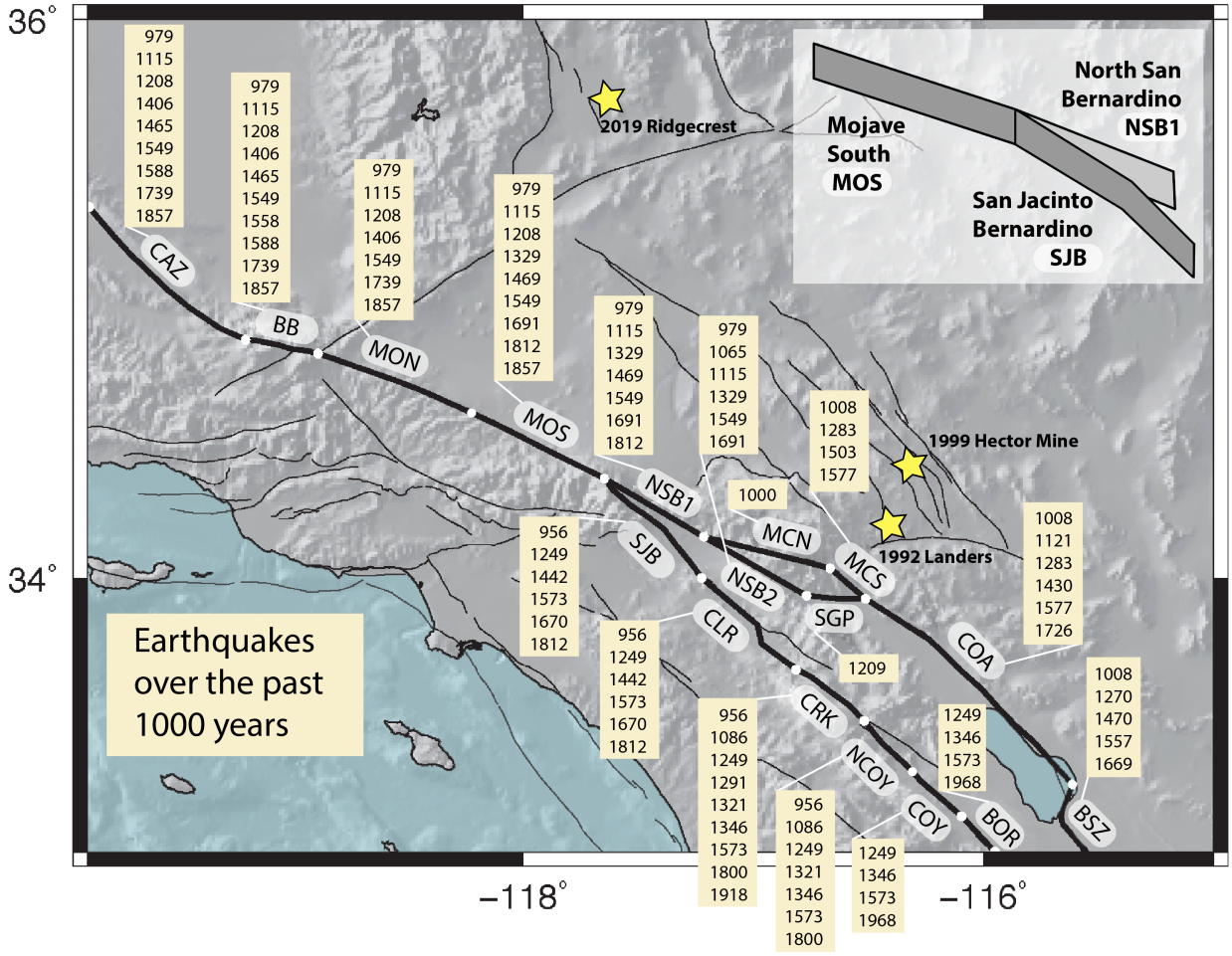

Figure 2.3. Paleo-seismic rupture data summary for Southern California with maximum rupture slip chronology (MRM) from Scharer and Yule (2020) per model segment (bound by white circles) over the past 1000 years. Segment name abbreviations are used here; full names can be found in Table 2.1. Yellow stars indicate large recent earthquakes in the Eastern California Shear Zone (ECSZ): M_w 7.3 1992 Landers, M_w 7.1 1999 Hector Mine, and M_w 7.1 2019 Ridgecrest. Inset: Configuration of the Cajon Pass segment junction (MOS, NSB1 and SJB) examined in this study.

In summary, the MRM incorporates the spatially longest plausible ruptures in order to find periods of earthquake activity akin to the 1800s, when scientific observations of ruptures using instruments were established. Therefore, this model provides the best possible published record to evaluate stress accumulation. However, it is important to note that the complete paleoseismic slip distribution of the SAFS is not known and earthquake epicenters are uncertain.

Several notable event characteristics can be gleaned from a paleoseimic database like the MRM for the Cajon Pass. For example, the earthquake events of Wrightwood 1812 (M_w ~7.5) and Fort Tejon 1857 (M_w 7.9), which both ruptured the southern Mojave segment (MOS), have measurable slip at the Cajon Pass (Scharer and Streig, 2019; Padilla et al., 2021), These particular events represent the two most recent events at the Cajon Pass (Figure 2.4) and share partially overlapping ruptures, but are estimated to have had different magnitudes, rupture lengths, and possibly rupture propagation directions. For example, historic observations of the 1812 earthquake are best explained by a rupture that propagated northwards from the SJF onto the SAF (Lozos, 2016; Onderdonk et al., 2019). Slip models suggest that this event released residual stress which was built up from prior earthquakes terminating at the SJF that did not step over to the SAF (Padilla et al. 2021). The earthquake of 1812 represents a participating-passing ('Gate-Open') event, which is when stress levels were favorable for the rupture to pass through the Cajon Pass. Alternatively, 44 years later, the epicenter and rupture extent of the 1857 earthquake is known to have originated at Fort Tejon along the Cholame segment and ruptured primarily southward for over 330 km (Toppozada et al., 2002). Here, the SJF did not participate in measurable slip. The earthquake of 1857 ruptured the southern Mojave segment (MOS) on the SAF and terminated at the Cajon Pass, representing a participating-stopping ('Gate-Closed') event.

Moreover, the Cajon Pass represents a critical intersection for past (and possible future) through-going ruptures. The MRM indicates 12 slip events (Figure 2.4) within the last 1000 years on the three segments that form a junction at the Cajon Pass: Mojave South (MOS), North San Bernardino (NSB1) and San Jacinto Bernardino (SJB). Of these events, 6 ruptures passed the junction, but only one earthquake event (1812) may have involved slip on all three segments (Padilla et al., 2022; Lozos 2016; Scharer and Yule, 2020). The other five passing events (1115, 1329, 1469, 1549, 1691) produced slip only on the main San Andreas fault trace (segments MOS and NSB1), not involving the SJB segment. Four of the six stopping events at the Cajon Pass are ruptures on the SJB segment, while only two are on the MOS segment to the north (1208 and 1857). Understanding stress accumulation and these fault segment interactions is the next step

in an effort to improve seismic hazard assessments, and this earthquake cycle study can provide quantitative estimates of stress thresholds at the Cajon Pass with one of the best paleoseismic records available today.

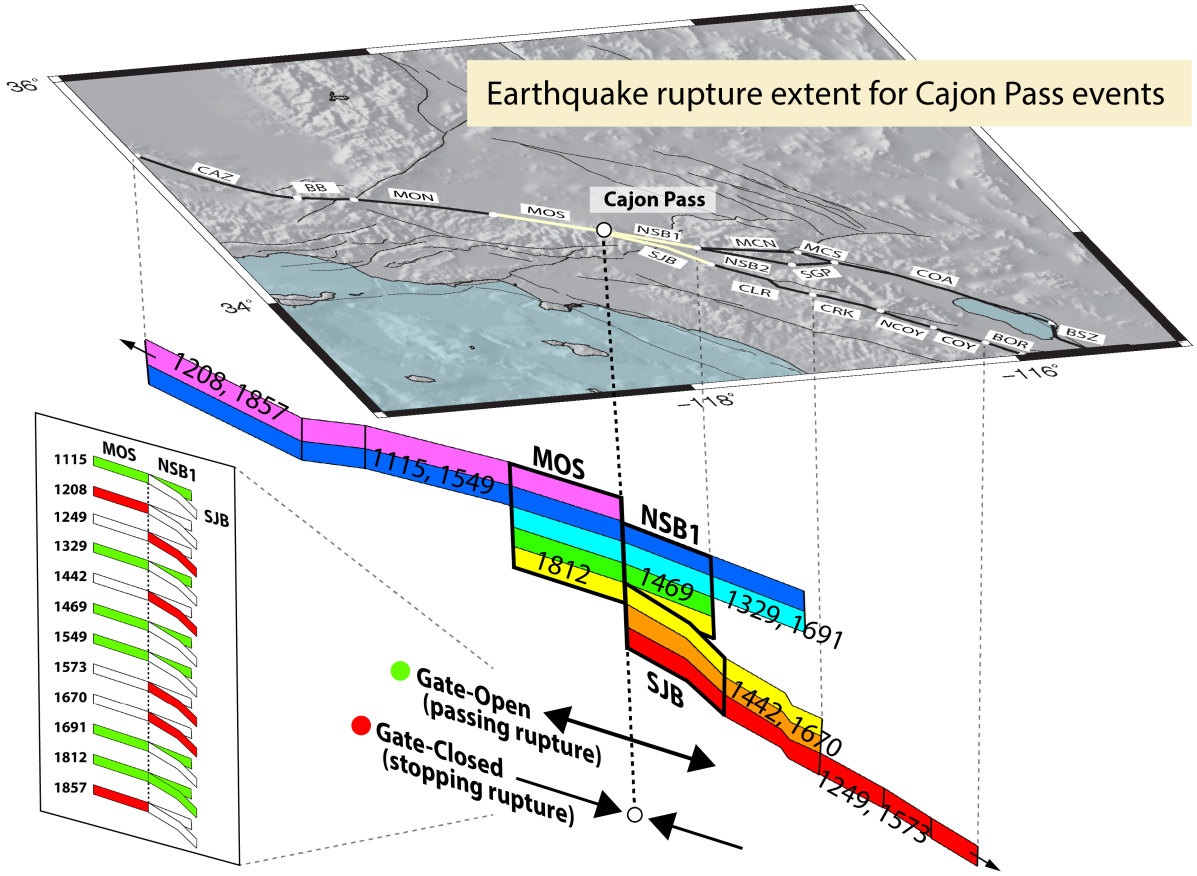

Figure 2.4. Earthquake rupture extent for events passing and stopping at the Cajon Pass from the Maximum Rupture Model (MRM) of Scharer and Yule (2020). Segments that participated in a shared event are indicated by continuous color (i.e., red indicates slip extent in 1249 and 1573, rupturing segment SJB and several segments to the south; magenta denotes slip in 1208 and 1857 which ruptured segment MOS and further segments to the north). Small arrows indicate extent of ruptures beyond map excerpt. Left inset: Sketch of 'Gate-Open' or 'Gate-Closed' events of the Cajon Pass, i.e., ruptures stopping/passing at segments Mojave South (MOS), North San Bernardino (NSB1) and San Jacinto Bernardino (SJB).

2.3 San Andreas Fault System earthquake cycle stress modeling

To evaluate earthquake cycle stress accumulation of the Cajon Pass over the past 1000 years, we used the semi-analytic Fourier transform model *maxwell* (Smith and Sandwell, 2004; Sandwell and Smith-Konter, 2018) to rapidly compute surface deformation and stress associated

with 3D dislocations embedded in an elastic plate overlying a Maxwell viscoelastic half-space (Figure 2.5). The *maxwell* model simulates earthquake cycle interseismic strain accumulation and coseismic displacements in the upper brittle crust, and viscoelastic relaxation in the lower crust and upper mantle, while also including the restoring force of gravity. The entire model spans the Carrizo segment in the north to the Borrego Mountain segment in the south (Figure 2.1, Table 2.1) and consists of 34 major fault segments that are projected into a Cartesian coordinate system of 450 × 900 km in the east-west (x-axis) and north-south (y-axis) directions, respectively. Geodetically-constrained slip rates and locking depths (UCERF3; Field et al., 2017; Tong et al., 2014; Ward et al., 2020) are kinematically prescribed along each segment down to the base of the elastic plate, which drives the secular interseismic crustal block motions. Episodic slip is assigned for each fault segment from the surface to locking depth through time, guided by the paleoseismic and historical earthquake record (e.g., Scharer and Yule, 2020). The full earthquake cycle model requires the accumulated slip deficit on each segment to equal to the amount of co-seismic slip for each event, which is estimated by the time and slip rate since the last major earthquake. We assume a Young's modulus of E = 70 GPa, shear modulus μ = 30 GPa, elastic plate thickness H = 60 km, and a viscosity of η = 1 x 10^{19} Pa following previous studies (Fay and Humphreys, 2005; Smith and Sandwell, 2006; Smith-Konter and Sandwell, 2009).

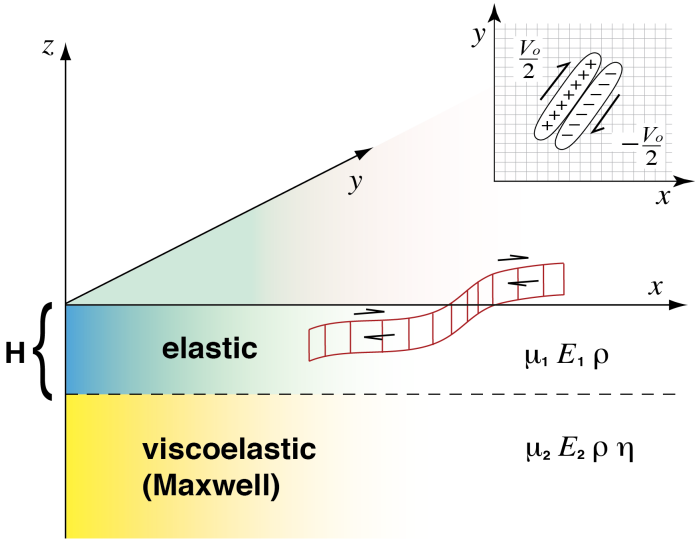

Figure 2.5. Schematic of the model simulating an elastic layer of thickness H overlying a linear Maxwell viscoelastic half-space of viscosity η. A displacement discontinuity across each fault element is simulated using a finite width force couple. Both layers indicate shear modulus (μ), Young's modulus (E), and density (ρ). Figure adapted from Smith and Sandwell (2004).

For this earthquake cycle stress analysis, stress tensor grids are generated at each time step for specified crustal depths. By making the simplifying assumption of modeling the SAFS as a vertical screw dislocation, only the horizontal stress components are needed (σ_{xx}, σ_{yy}, τ_{xy}).

Assuming standard Coulomb failure mechanics (Byerlee, 1978), both shear (τ_s) and normal (σ_n) stresses are resolved along each fault segment to compute the Coulomb stress (τ_c) for each fault plane (i.e., King et al., 1994; Eq. 1),

$$(1) \quad \tau_c = \tau_s - \mu_f \sigma_n$$

where μ_f is the coefficient of friction (0.6 for this study; Smith and Sandwell, 2003). Positive Coulomb stress indicates a failure loading (or stress accumulation) condition whereas negative Coulomb stress implies stress values that have moved away from failure (or a stress drop). Stress calculations are performed on a fault-segment by fault-segment basis, and therefore the local fault geometry contributes to the overall stress value. Furthermore, stress varies as a function of depth within the seismogenic zone as deep slip on discrete faults causes an amplifying of stress directly above the slipping segment. Stresses at mid-locking depths can be up to 40% higher than the stresses at the surface of the crust (i.e., Sandwell et al., 2004; Smith-Konter and Sandwell, 2009; Burkhard et al., 2018). Alternatively, the depth-averaged stress over a locked fault is about equal to the stress at 0.7 times the fault depth (Sandwell et al., 2004). In this study, we compute representative stresses at 1/2 of the local locking depth (cf. King et al., 1994) for each fault segment (3.2-10.8 km observational depths), consistent with previous work (i.e., Smith-Konter and Sandwell, 2009). Additionally, stresses will vary as a function of along-strike position along a fault segment due to stress changes in the surrounding material of neighboring segments. To accommodate along-strike variations, we compute mean stress values (per fault segment) by extracting stress observations at every 2 km distance along-strike of each segment (see Appendix, Figure 2.A1).

Time-series simulations of earthquake cycle stress accumulation are constructed by adopting a paleoseismic slip chronology (i.e., MRM from Scharer and Yule, 2020) and assuming that the amount of co-seismic slip for each event is equal to the accumulated slip deficit on each segment (i.e., the slip rate multiplied by the time since the last major earthquake). The model requires a full stress drop (to zero) after each event, but includes viscoelastic stress relaxation and residual stress from nearby fault segments. In general, Coulomb stress accumulation rates are largely dependent on slip rate, locking depth, and fault strike (Smith and Sandwell, 2003). Coulomb stress accumulates fastest in regions with high slip rates and shallow locking depths due to the concentration in a small area. Time-series stress evolution models are generated over a 1000-year timespan for every 10 years. To allow careful inspection of near-event stress thresholds, we

also generate models for years encapsulating slip events of Cajon Pass segments to observe stress values before and after ruptures (see Figure 2.4).

Table 2.1. Modeled fault segments, locking depths and slip rates. Primary fault segments of this study adjacent to Cajon Pass are highlighted in green.

Segment Name	Abbreviation	Locking Depth (km)	Slip Rate (mm/year)
Carrizo	CAZ	18.7	34.0
Big Bend	BB	15.0	34.0
Mojave North	MON	16.8	32.5
Mojave South	MOS	16.8	32.5
North San Bernardino	NSB1	17.8	17.3
North San Bernardino	NSB2	17.8	13.0
San Gorgonio Pass	SGP	16.4	10.0
Mission Creek North	MCN	17.8	1.8
Mission Creek South	MCS	16.4	1.8
Coachella	COA	11.5	20.0
Brawley	BSZ	12.0	23.0
San Jacinto Bernardino	SJB	21.0	13.0
Clark	CLR	21.5	14.0
Clark	CRK	13.7	14.0
Coyote Creek North	NCOY	13.7	6.3
Coyote Creek	COY	6.3	6.7
Borrego Mountain	BOR	6.4	6.0

Note. Fault segments with abbreviated names, locking depths derived from previous modeling work using geodetic surface deformation measurements (GPS and InSAR velocity analyses; Tong et al., 2014), and geologic slip rates from the Uniform California Earthquake Rupture Forecast (UCERF3; Field et al., 2017).

2.4 Results

We investigate Coulomb stress accumulation thresholds, stress drop, and induced stress values for multiple paleoseismic earthquake cycles, spanning the three segments around the Cajon Pass (MOS, NSB1, and SJB) over the past 1000 years (see companion animation; Figures 2.6-2.9). Regional stress maps are provided to exemplify map-view snapshots of stress accumulation for specific times (Figures 2.6, 2.7), while 1000-year time-series (Figures 2.8, 2.9) of site-specific stress variations are provided to illustrate stress changes through time. Here, we provide a few case examples (i.e., 1812 and 1857 earthquake stress changes, Figure 2.7) but a comprehensive simulation is provided in our companion animation. The stress grids evaluated reflect Coulomb stress contributions from faults at observation depths of 1/2 the fault locking depth of each segment. Stresses have a lobe and shadow-effect causing values to drop or rise with an

event on another segment conditional on their proximity and geometry (King et al., 1994; Harris and Simpson, 1998).

Stresses in our model year 2022 are high (Figure 2.6) as there has not been a large earthquake in the southern SAF since 1857, and the last rupture on the SJF, in 1968, was moderate magnitude (M_w 6.4) and occurred at the southernmost end of the model domain (BOR). Coulomb stresses on the three segments adjacent to the Cajon Pass have a present mean value of 1.8-3.6 MPa. On segment Mojave South (MOS), current mean stresses are the highest they have been in the past 1000 years, with a present value of 2.8 MPa. The current mean stress value of 1.8 MPa on the North San Bernardino segment (NSB1) is lower than in the past as stresses could reach up to 2.6 MPa in the examined period. For segment San Jacinto Bernardino (SJB), the present mean stress value is 3.6 MPa, exceeding the highest value in the past 1000 years before the 1249 rupture of 2.9 MPa.

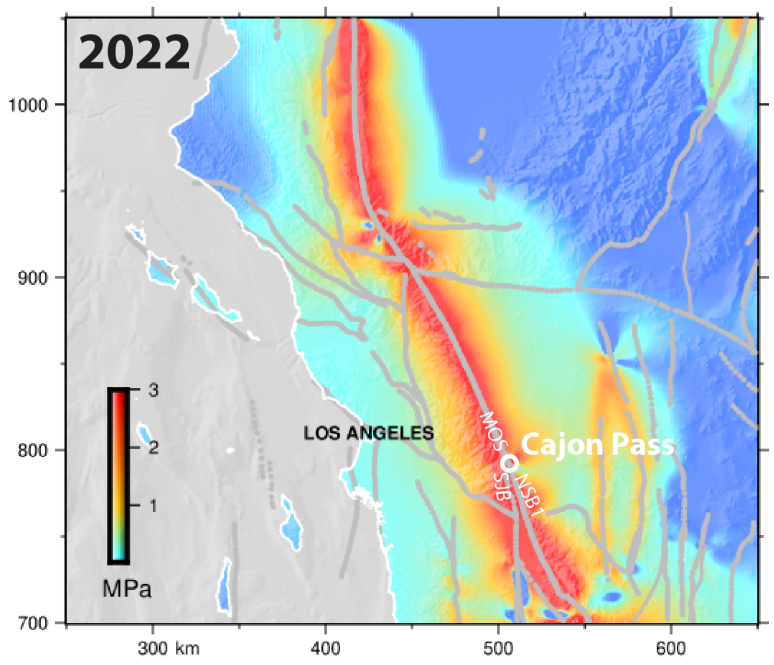

Figure 2.6. Stress accumulation of the southern SAFS at present (2022), observed from 1/2 the locking depth of each segment. Location of the Cajon Pass in white circle with abbreviations of the three adjacent segments indicated: Mojave South (MOS), North San Bernardino (NSB1), and San Jacinto Bernardino (SJB). Stresses have a present overall mean value of 2.8 MPa on MOS, 1.8 MPa on NSB1, and 3.6 MPa on SJB.

We model 1812 as a tripartite event, reflecting paleoseismic observations in Scharer and Yule (2020) and Padilla et al. (2022), and compare it with the 'Gate-Closed' rupture of 1857 (Figure 2.7). These map views show how each location along the fault is influenced by stress lobes of neighboring and adjacent segments, and how stresses change in the surrounding material through nearby earthquake events. Remaining stress lobes after a rupture and

accumulations from non-participating segments affect stress values especially on directly adjacent segments. In the example of the 1857 earthquake (Figure 2.7), segment San Jacinto Bernardino on the SJF experienced a stress drop, although the segment was not participating in this event. Modeled slip at the Cajon Pass segments for these ruptures in 1812 and 1857 is roughly consistent with slip reconstructions of these events (i.e., Sieh, 1978; Padilla et al., 2021), ranging from 1-5 m.

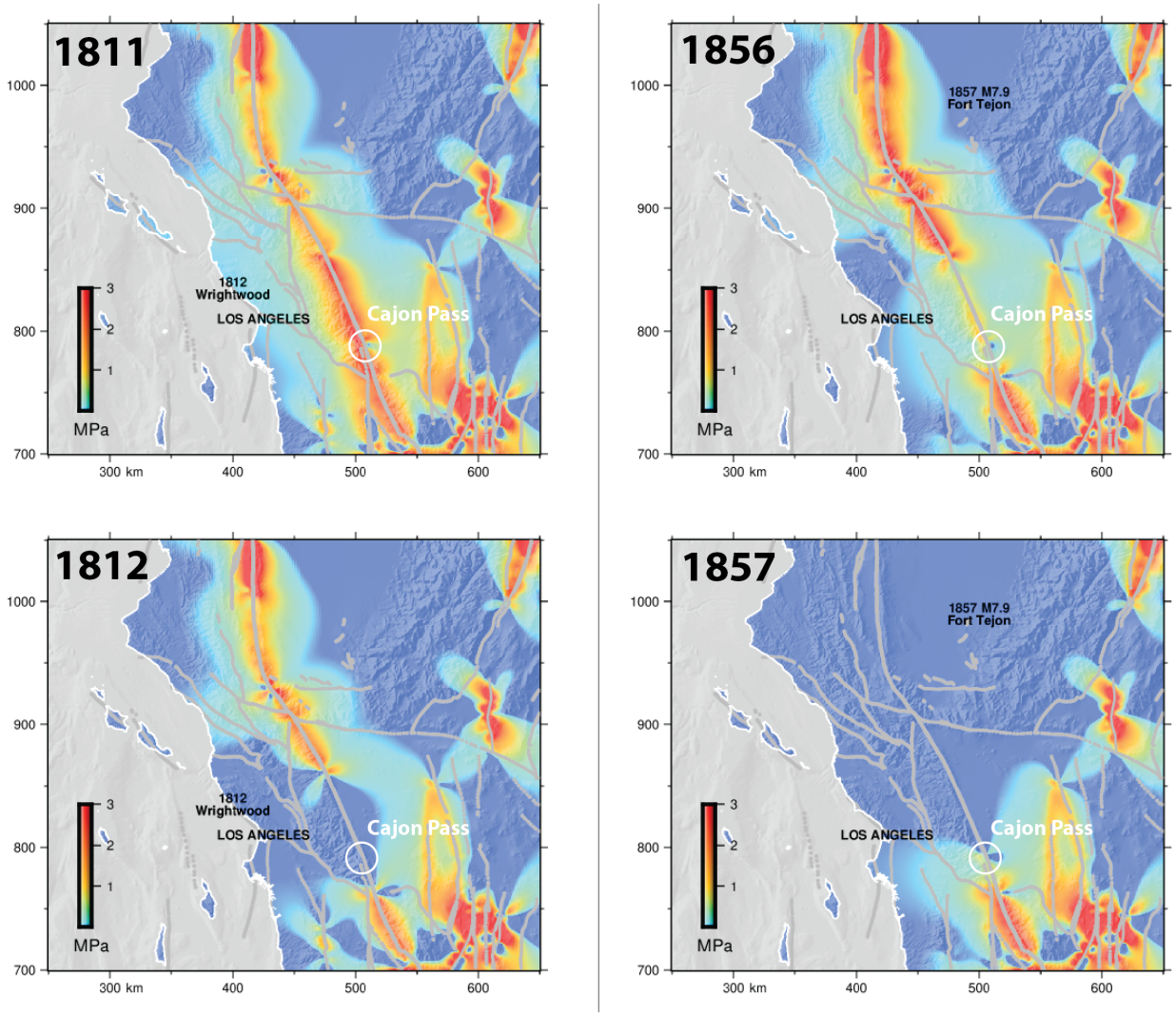

Figure 2.7. Stress accumulation of the SAFS assuming the Maximum Rupture Model (MRM), with view of the Cajon Pass before and after the complete junction rupture of 1812 Wrightwood (left) and the 1857 Fort Tejon earthquake that did not propagate past the Cajon Pass (right), showing remaining stress lobes and accumulations from non-participating segments to the south. Stress grids reflect an ensemble of stress contributions from faults at observation depths of 1/2 the local fault locking depth of each segment.

Stress accumulation rates are highest on the Mojave segment (~1.8 MPa/100yrs) due to a relatively higher slip rate (32.5 mm/yr; Table 2.1). In comparison, stress accumulation rates are ~1.0 MPa/100yrs for the North San Bernardino segment and ~1.4 MP/100yrs for the San Jacinto Bernardino segment. These different rates of stress accumulation give rise to higher stress thresholds on the Mojave segment for any given time between events, and likewise, lower overall stress thresholds on the North San Bernardino segment. An additional factor that will modulate stress accumulation rates is viscoelastic relaxation during the postseismic period of each event; viscoelastic stress changes are fairly small, ~1.3-1.0 kPa/yr for a period of ~10 years after an earthquake. After this time, stress accumulation rates typically recover as the relaxing layer rebounds and returns to its pre-earthquake configuration.

Stress variations throughout the entire 1000-year MRM sequence are also provided as a time-series (Figure 2.8), which show the cycle of stress accumulation due to fault locking, stress drop at each paleoseismic event of the MRM, and a resumption of stress accumulation due to re-locking of each fault segment. Segment Mojave South (MOS; Figure 2.8 a) borders the Cajon Pass to the north and lies together with adjoining segment North San Bernardino (NSB1; Figure 2.8 b) to the south on the main SAF trace. Segment San Jacinto Bernardino (SJB; Figure 2.8 c) intersects at the Cajon Pass to the other two segments, which is the commencing segment of the SJF. Mean stress per fault segment is reported as stresses extracted at every 2 km distance along-strike and averaged per segment. On-segment events, when the segment participated in a rupture, are indicated in colored bars, where green denotes passing ('Gate-Open') and red stopping ('Gate-Closed') earthquakes at the Cajon Pass. A first order result of these stress evolution time-series shows the variation in stress rates that inherently "drive" (or load) stress accumulation of the Mojave, North San Bernardino, and San Jacinto segments, respectively.

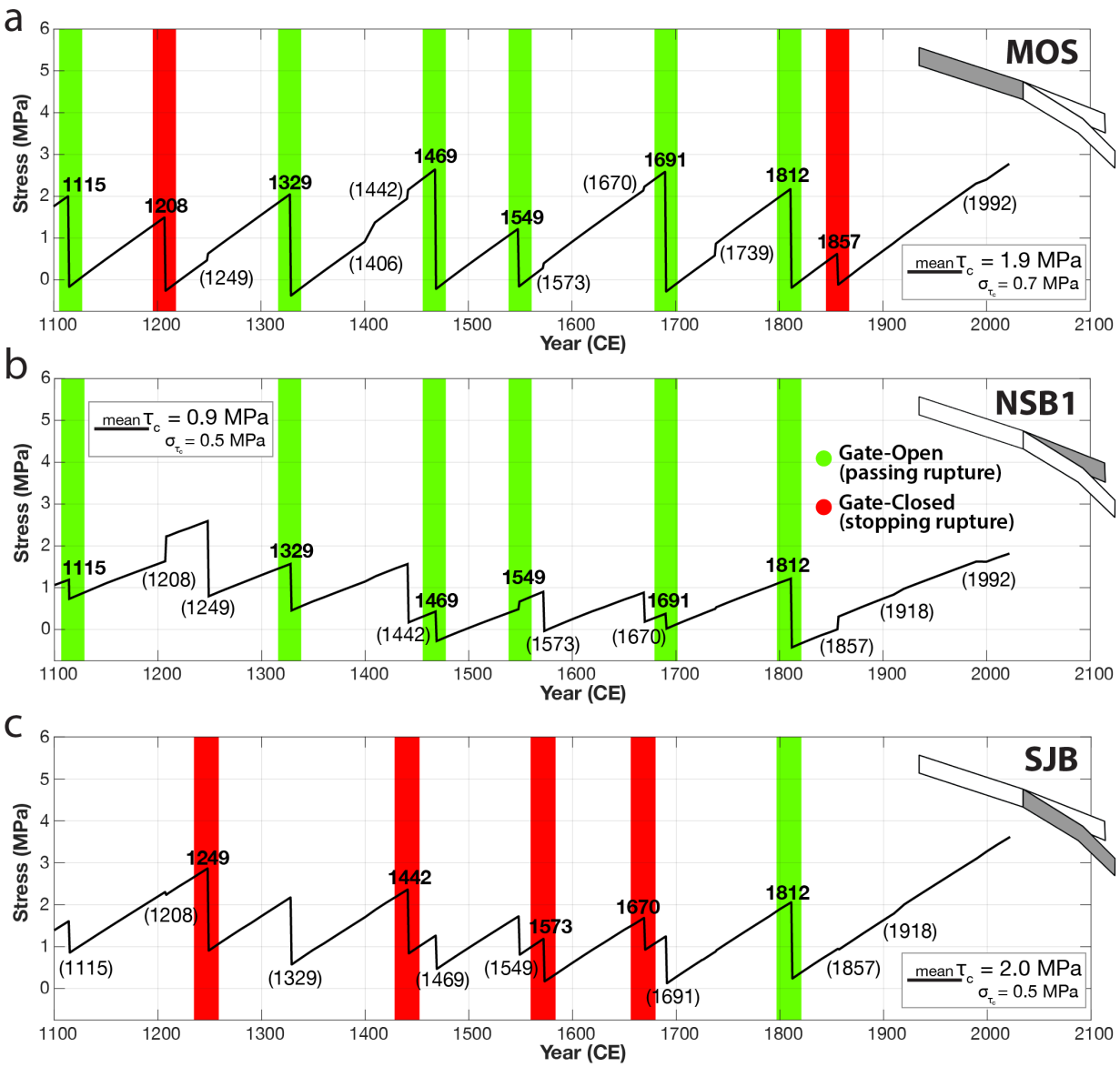

Figure 2.8. Stress evolution time-series for the Maximum Rupture Model (MRM) chronology. Mean stress values (MPa) for segments **a)** Mojave South (MOS), **b)** North San Bernardino (NSB1) and **c)** San Jacinto Bernardino (SBJ), with on-segment events indicated in colored bars. Green denotes passing ('Gate-Open'), red stopping ('Gate-Closed') ruptures at the Cajon Pass (see Figure 2.4). Dates in parentheses are ruptures on other segments inducing stress changes. Values extracted at every 2 km distance along the segments.

For the Mojave South (MOS) segment time-series (Figure 2.8 a), eight participating events are represented in the MRM (Table 2.2). Note that a drop or increase not highlighted in green/red denotes an induced stress change from another event on a separate segment. Mean stress thresholds are 1.9 MPa (with a standard deviation of $\sigma_{max\ \tau c}$ 0.7 MPa; Table 2.3) and reach a

maximum of 2.7 MPa in 1469 and 1691. The average model time between ruptures on this segment is 111 years, with the last rupture in 1857, which did not pass through the Cajon Pass onto the segments to the south. When assessing mean stress values including induced stress events, then the mean maximum stress value on segment Mojave South is 1.6 MPa (with a standard deviation of $\sigma_{max\ \tau c}$ 0.8 MPa). This segment experienced two 'Gate-Closed' ruptures (1208 and 1857), where stresses before these events were <1.5 MPa. For the six 'Gate-Open' events, mean stress values were >2.0 MPa (with the exception of 1549; 1.5 MPa).

Table 2.2. Mean Coulomb stress (τ_c) values of each segment before and after major earthquakes (MRM).

Year	MOS τ_c (MPa)			NSB1 τ_c (MPa)			SJB τ_c (MPa)		
	pre-event	post-event	stress change	pre-event	post-event	stress change	pre-event	post-event	stress change
1115	2.0	-0.2	-2.2	1.2	0.8	-0.4	1.6	0.9	-0.7
1208[x]	1.5	-0.3	-1.8	1.6	2.2	+0.6	2.3	2.2	-0.1
1249[x]	0.5	0.6	+0.1	2.6	0.8	-1.8	2.9	0.9	-2.0
1329	2.0	-0.4	-2.4	1.6	0.5	-1.1	2.2	0.6	-1.6
1442[x]	2.0	2.2	+0.2	1.6	0.2	-1.4	2.4	0.8	-1.6
1469	2.7	-0.2	-2.9	0.4	-0.3	-0.7	1.3	0.5	-0.8
1549	1.2	-0.2	-1.4	0.5	0.7	+0.2	1.7	0.8	-0.9
1573[x]	0.3	0.4	+0.1	0.9	-0.0	-0.9	1.2	0.2	-1.0
1670[x]	2.2	2.2	0.0	0.9	0.2	-0.7	1.7	0.9	-0.8
1691	2.6	-0.3	-2.9	0.4	0.0	-0.4	1.2	0.1	-1.1
1812	2.2	-0.2	-2.4	1.2	-0.4	-1.6	2.1	0.2	-1.9
1857[x]	0.6	-0.1	-0.7	0.0	0.3	+0.3	1.0	0.9	-0.1
2022	**MOS mean τ_c: 2.8 MPa**			**NSB1 mean τ_c: 1.8 MPa**			**SJB mean τ_c: 3.6 MPa**		

Note: Colors indicating segments participating in an earthquake, corresponding to Figure 2.4. Dates with [x] are 'Gate-Closed' events, when the rupture did not propagate beyond the Cajon Pass. Red highlighted values are 'Gate Closed' events, while green denote 'Gate-Open' events. Values in grey indicate stress rise after an event.

Over the past 1000 years, segment North San Bernardino (NSB1; Figure 2.7 b) participated in 6 ruptures, which are all 'Gate-Open' events, and joint ruptures with segment Mojave South, at mean stress thresholds of 0.9 MPa ($\sigma_{max\ \tau c}$ 0.5 MPa; Table 2.3). The segment does not rupture throughout the evaluated seismic record without the participation of segment Mojave South, although stress levels can reach higher values on the segment (i.e., up to 2.6 MPa in 1249) than the mean stress threshold before ruptures during this time. Mean stress values including induced stress events reach a mean maximum stress of 1.1 MPa ($\sigma_{max\ \tau c}$ 0.7 MPa). Since the tripartite

event with the SJF in 1812, there has not been a large earthquake on this segment in 210 years. However, the average modeled time between ruptures is usually 139 years on segment North San Bernardino.

On the first segment of the San Jacinto fault adjacent to the main San Andreas fault south of the Cajon Pass, segment San Jacinto Bernardino (SJB) has a mean maximum stress value or stress threshold of 2.0 MPa with a standard deviation of σ_{max} 0.5 MPa for events on the segment (Table 2.3). On average, an earthquake ruptures this segment every 171 years, with the tripartite event of 1812 being the last one. When a rupture occurred on the segment and also on either of the neighboring segments (induced stress), the mean maximum stress value on segment SJB is 1.8 MPa, with a standard deviation of σ_{max} 0.6 MPa (Table 2.3). There are five events on this segment, but only one (1812) is a joint Cajon Pass rupture. During the evaluated 1000 years, stresses on this segment have been within threshold range when neighboring segments experienced events, but no participating rupture occurred.

Table 2.3. Mean Coulomb stress (τ_c) values for events on event-participating segments only and values including induced stress events (all earthquake events in Cajon Pass region).

Mean values (participating)	**MOS**	**NSB1**	**SJB**
max. τ_c (MPa)	1.9	0.9	2.0
$\sigma_{max\ \tau c}$ (MPa)	0.7	0.5	0.5
τ_c drop (MPa)	2.1	0.9	1.4
$\sigma_{drop\ \tau c}$ (MPa)	0.7	0.5	0.5
Mean values (incl. induced)	**MOS**	**NSB1**	**SJB**
max. τ_c (MPa)	1.6	1.1	1.8
$\sigma_{max\ \tau c}$ (MPa)	0.8	0.7	0.6
τ_c drop (MPa)	2.1	1.0	1.0
$\sigma_{drop\ \tau c}$ (MPa)	0.7	1.0	1.0
Time between ruptures (yrs)	111.0	138.8	171.2
σ_{yrs} (yrs)	31.7	43.5	76.3
Stress rate τ_c/100yrs (MPa)	1.8	1.0	1.4

'Gate-Open' observations for joint Mojave South and North San Bernardino ruptures are inconclusive, as these segments do not seem to have a common stress threshold. The minimum mean stress value for rupturing segment North San Bernardino is 0.4 MPa (1469, 1691), which

is surpassed by +1.2 MPa in the 'Gate-Closed' event of 1208, where segment Mojave South participates but no rupture occurs on North San Bernardino. Before the tripartite event of 1812, stress values on both Mojave South and San Jacinto Bernardino surpassed 2 MPa, with a difference of only 0.1 MPa from each other, while segment North San Bernardino had a stress accumulation of 1.2 MPa.

When comparing spatial Coulomb stress drop variations along segments, we observe that stress values on segment Mojave South drop especially in the south closer to the Cajon Pass when there is an event exclusive to San Jacinto Bernardino and stopping at the Cajon Pass. Overall however, the Mojave South segment reacts with an average stress increase after 'Gate-Closed' events on this neighboring segment (with a plus of 0.1-0.2 MPa), as the northern parts of the Mojave South segment do not experience the effects of the stress lobes from the San Jacinto Bernardino segment. Stresses on the North San Bernardino segment drop throughout the segment during all events exclusive to the San Jacinto Bernardino segment and with a comparable magnitude due to close proximity. The event of 1249 for example caused a drop of 1.8 MPa on the North San Bernardino segment, which is almost as much as the drop of 2.0 MPa on the San Jacinto Bernardino segment itself. Overall, these drops on the North San Bernardino segment are 0.1-0.2 MPa smaller than the drops on the San Jacinto Bernardino segment during its on-segment events. However, at events exclusive to the Mojave South segment (participating-stopping events; 'Gate-Closed'), stresses tend to increase on average between 0.2 and 0.6 MPa on the North San Bernardino segment, such as after the earthquakes of 1208, 1549 and 1857. The San Jacinto Bernardino segment reacted with stress drops to all neighboring events, but with more varying magnitudes than the North San Bernardino segment. The San Jacinto Bernardino segment only ruptured once during the examined MRM chronology with the segments of the main SAF trace (1812), and reacts to all ruptures exclusive to the SAF trace with stress drops, regardless of whether rupture stopped at the Cajon pass (Mojave South segment only; participating-stopping events) or passed, rupturing both the Mojave South and the North San Bernardino segments (participating-passing or 'Gate-Open' events). However, the two events exclusive to the Mojave South segment that stopped at the Cajon Pass only induce very small stress drops of 0.02 MPa (1857) and 0.07 MPa (1208) on the San Jacinto Bernardino segment.

We further investigate stress drops and rupture scenarios for a hypothetical future event in 2023 (Figure 2.9; Table 2.4). Here, we explore several possible developments: Scenario 1) MOS only (Figure 2.9 b), Scenario 2) SJB only (Figure 2.9 c), Scenario 3) joint MOS & NSB1 (Figure 2.9 d), and Scenario 4) tripartite MOS, NSB1 & SJB (Figure 2.9 e). For the isolated event on the

Mojave South segment (Scenario 1; Figure 2.9 b), the resulting stress drop is 3.4 MPa on the MOS segment, while stresses are found to increase on the NSB1 and SJB segments (by 1.1 MPa and 0.2 MPa, respectively). For Scenario 2, an isolated event on the San Jacinto Bernardino segment (Figure 2.9 c), stresses drop on both the SJB and NSB1 segments (by 1.8 MPa and1.6 MPa, respectively); alternatively, stress on the MOS segment increases slightly by 0.2 MPa, consistent with previous behavior. For Scenario 3, a joint rupture on the Mojave South and North San Bernardino segments (Figure 2.9 d), stresses drop by 3.4 MPa on the Mojave South segment, the largest stress drop value simulated in our full 1000-year time-series. Resulting stress drops on the North San Bernardino and San Jacinto Bernardino segments are also significant from this event (1.4 MPa and 1.1 MPa, respectively). Finally, we explore Scenario 4, a tripartite (or complete junction rupture) of all Cajon Pass segments (Figure 2.9 e). This scenario results in the largest stress drops over the full 1000-year time-series for the North San Bernardino and San Jacinto Bernardino segments (3.0 MPa and 3.1 MPa), and the second largest modeled stress drop for the Mojave South segment (3.3 MPa).

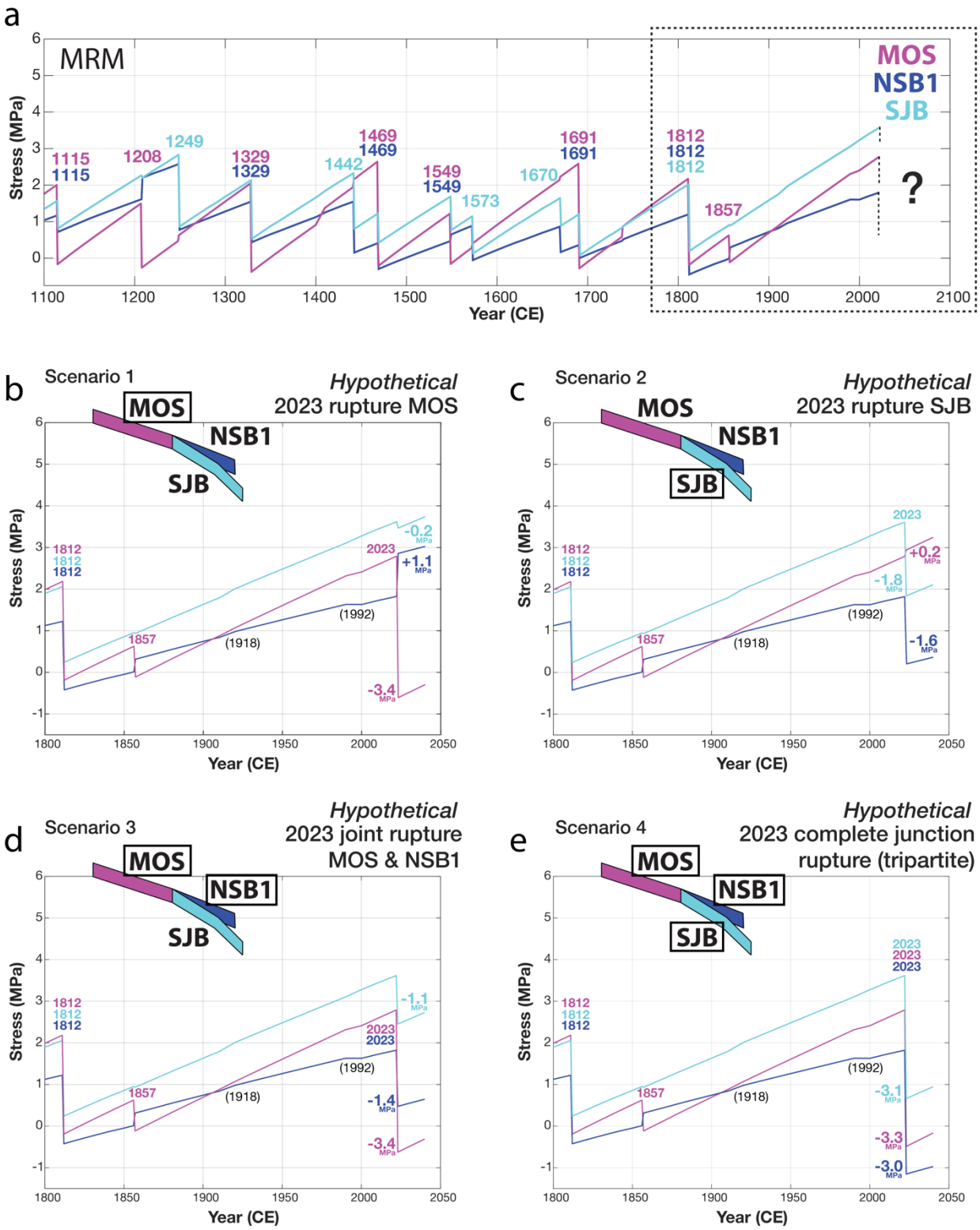

Figure 2.9. Combined view of Cajon Pass stress evolution using the MRM chronology and exploring multiple scenarios of a future hypothetical slip event in 2023. **a)** Full 1000-year time-series for all three segments, with the Mojave South segment (MOS) represented by the magenta line, the North San

Bernardino segment (NSB1) represented by the blue line, and the San Jacinto Bernardino segment (SJB) represented by the light blue line. **b)** Scenario 1: Hypothetical 2023 scenario with only the MOS segment slipping. **c)** Scenario 2: Hypothetical 2023 scenario with only the SJB segment slipping. **d)** Scenario 3: Hypothetical 2023 scenario with a joint MOS and NSB1 rupture, passing through the Cajon Pass. **e)** Scenario 4: Hypothetical 2023 scenario with a tripartite event (complete junction rupture involving all segments), passing through the Cajon Pass.

Table 2.4. Mean stress values (MPa) of Cajon Pass segments before and after a suite of slip scenarios for a hypothetical future earthquake in 2023 (Figure 2.9; see text for scenario descriptions). Ruptures stopping at the Cajon Pass indicated in red '(Gate-Closed'), passing in green ('Gate-Open'). Grey shaded values denote the largest stress drop of each segment.

Hypothetical **2023 rupture scenarios**	**MOS** τ_c **(MPa)**			**NSB1** τ_c **(MPa)**			**SJB** τ_c **(MPa)**		
	pre-event	post-event	stress change	pre-event	post-event	stress change	pre-event	post-event	stress change
1 MOS	2.8	-0.6	-3.4	1.8	2.9	+1.1	3.6	3.4	+0.2
2 SJB	2.8	3.0	+0.2	1.8	0.2	-1.6	3.6	1.8	-1.8
3 MOS/NSB1	2.8	-0.6	-3.4	1.8	0.5	-1.4	3.6	2.5	-1.1
4 MOS/NSB1/SJB	2.8	-0.5	-3.3	1.8	-1.2	-3.0	3.6	0.7	-3.1

2.5 Discussion

Various interpretations about stress behavior can be made from the MRM chronology stress evolution time-series (Figure 2.8), and we investigate how patterns of threshold stress for the Cajon Pass segments can possibly be assimilated, characterize stress drop effects on nearby segments, and explore temporal relationships throughout the 1000-year time-series. We further explore these relationships in the context of earthquake gate behaviors, rheology and present-day stress levels.

2.5.1 Stress thresholds

Key observations about stress thresholds include: (1) Mean stress thresholds for the Cajon Pass segments are largest for the MOS segment (1.9 MPa) and smallest for the NSB1 segment (0.9 MPa). This is fundamentally a result of larger slip rates on the Mojave segment and smaller slip rates as well as distributed stress accumulation on paralleling segments on the other. (2) There is no precise or common stress threshold preceding major ruptures of the Cajon Pass, but rather an elevated range of stress accumulation that appears to be characteristic to each

segment; stress accumulation greater than 1 MPa is observed on all MOS (except 1857) and SJB events, with stress threshold ranges of 1.2-2.7 MPa and 1.2-2.9 MPa for the MOS and SJB segments, respectively. In contrast, the NSB1 segment exhibits slip-failure tendencies for much lower stress thresholds of 0.4-1.6 MPa. (3) There is no significant correlation between stress thresholds of Cajon Pass segments as they participate in joint or tripartite (gate-open) ruptures. In fact, stress thresholds of all MOS-NSB1 joint events differ significantly, on average, by ~1.2 MPa. One exception to this observation is the common stress threshold of ~2 MPa for segments MOS and SJB observed for the tripartite 1812 event (discussed further below). (4) There is also no significant correlation between stress thresholds of Cajon Pass segments that function as 'Gate-Closed' ruptures; independent SJB events have stress thresholds that differ by more than 0.4 MPa when compared to MOS stress levels.

One obvious behavior of the Cajon Pass segments is the joint rupturing nature of the Mojave South and North San Bernardino segments on the main SAF trace. These segments participated in six ruptures together (participating-passing or 'Gate-Open' events) throughout the 1000-year MRM chronology (Figure 2.8). It is also important to note that the North San Bernardino segment does not rupture alone, or independent of the Mojave South segment. Alternatively, there are only two events (1208 and 1857) in the modeled chronology where the Mojave South segment ruptured without the North San Bernardino segment ('Gate-Closed' event). In these events, mean stresses increased by ~ +0.3-0.6 MPa on the North San Bernardino segment, but these induced stresses were seemingly not sufficient to promote failure. We further explore the effects of induced stress changes in the following sections.

2.5.2 Stress drop and induced stress changes

From our time-series analysis of the Cajon Pass, we compute stress drops from the MRM chronology (Table 2.3) that are confined to a range of 1–4 MPa, consistent with stress drops commonly reported in literature (~1-4 MPa; Cotton et al., 2013). Mean stress drop throughout the 1000-year model is 2.1 MPa for the Mojave South segment, while the North San Bernardino and San Jacinto Bernardino segments have a mean stress drop of 1.0 MPa. The observed larger stress drop magnitudes on the Mojave segment, which are twice as much as its southern companions across the Cajon Pass, can be attributed to higher stress accumulation due to the higher slip rate and the model requirement of a complete stress drop after an event.

One important question about multi-cycle stress simulations like those described above is how well modeled stress thresholds (or drops) can be reconciled with measured stress drops from

modern events. Measurements of an earthquake stress drop are made by determining the seismic moment and corner frequency from fitting a curve to the Fourier amplitude displacement spectrum, or equivalently, the acceleration amplitude spectrum, but a relative decrease in shear stress can also be estimated from fault dimensions and slip magnitude (Cotton et al., 2013). Since Aki (1967), the prevailing concept is that stress drop order-of-magnitude is roughly constant for all earthquakes. Although some studies show how stress drops increase with earthquake magnitude, overall, average earthquake stress drops are observed to be in the range of 1–4 MPa for the past ~35 years (Cotton et al., 2013). Although this mean value has generally been found over a wide range of earthquakes (Dong and Papageorgiou, 2003; Allmann and Shearer, 2009; Cotton et al., 2013), the widely cited compilations by Thatcher and Hanks (1973) and Hanks (1977) also show that the scatter around the mean in stress drop has at least a factor of 30. This is due to the disagreement between the uncertainty in the stress drop inferred from ground-motion prediction equations (GMPEs) and the uncertainty found by seismic moment-corner frequency. GMPEs use statistical regression analysis of many strong motion records and calculate the seismic ground motion intensity using the characteristics of the source, path, and site properties (Mori et al., 2020). The variability of the stress drop from measuring corner frequency and seismic moment is roughly 3–4 times larger than the variability predicted by GMPEs (Cotton et al., 2013). This implies that stress drop determined by source studies have greater uncertainty than calculations from ground-motion data. Nevertheless, mean stress drop results from our model (0.9-2.1 MPa) are within the range of these proposed stress drop values.

However, the SAFS is a mature fault, which implies that its segments are longer, more planar with less corrugations, smoother, and with less dense step-overs (Perrin et al., 2016; Manighetti et al., 2021). Longer segments on mature faults form longer asperities with lower fracture energy due to a more homogeneous strength. Therefore, mature faults are more likely to produce long earthquakes with fairly low stress drops while immature faults are likely to produce shorter and more energetic ruptures (Perrin et al., 2016; Manighetti et al., 2021). We consequently have to assume that there is incomplete stress drop on the SAFS in the modeled time frame. Our model requires the stress to drop to zero after each event, but results show that not all locations on each segment behave consistently with a complete stress drop due to stress lobes from stress accumulation on other nearby segments (see map view examples in Figure 2.7). As the overall computed stress drops are within the accepted range of ~1–4 MPa, we can conclude that the model requirement of complete stress drop is not an impediment for the results of this study.

Our modeling calculations show that spatial proximity of segments with earthquakes can cause stress values to decrease or increase on neighboring segments without a rupture, and we observe a stress drop connectivity manifested along the San Jacinto Bernardino and North San Bernardino segments. Because of the geographic proximity of these two segments (located only ~15 km apart at the southern end and converging in the north), there is an obvious pairing of stress drop between these two segments. For example, when the San Jacinto Bernardino segment slips in an MRM-prescribed earthquake, the North San Bernardino segment experiences an induced stress drop (0.7-1.8 MPa) that is comparable to the prescribed stress drop on the San Jacinto segment. An illuminating example of this behavior is the 1249 San Jacinto Bernardino event (Figure 2.8 b), which resulted in a 2.0 MPa stress drop on the SJB segment (host fault), but also caused a comparable induced stress drop (1.8 MPa) on the NSB1 segment. Typically, SJB events result in induced mean stress changes on the NSB1 segment that are only 0.1-0.2 MPa smaller.

The influence of stress lobes can also be seen in the Coulomb stress change for the M_w 7.3 1992 Landers earthquake, where principal stress lobes extended outwards of ~60 km in each direction (King et al., 1994), causing a mean stress drop of ~0.1 MPa on the North San Bernardino segment (Figure 2.8 b), some ~115 km away from the epicenter. In this fashion, participating-stopping events on segment San Jacinto Bernardino cause stresses on nearby segment North San Bernardino to drop significantly, but stresses increase slightly on segment Mojave South (Table 2.2). Conversely, participating-stopping events on segment Mojave South cause segment North San Bernardino to react generally with a slight stress increase, while the San Jacinto Bernardino segment reacts with small stress drops. Segment San Jacinto Bernardino acquires large induced stress drops from joint MOS-NSB1 events (0.7-1.6 MPa). This can be explained by the similar fault geometry and properties of the two segments on the main SAF trace (Schwartz et al., 2012; 2018). We also note a special case of slight stress increase in 1549 on the North San Bernardino segment, which can be attributed to a very high level of accumulated stress on the nearby San Jacinto segment, discussed in more detail in the Appendix. There are only two events in the modeled chronology rupturing Mojave South that stop at the Cajon Pass (1208 and 1857) and do not include the North San Bernardino segment, but instead include segments to the north of Mojave South. During both events, mean stresses increased by 0.3-0.6 MPa on the North San Bernardino segment due to its proximity to SJB. While the Mojave South and North San Bernardino segments on the main SAF trace participate in six ruptures together (participating-passing or 'Gate-Open' events) over the past 1000 years (Figure 2.8), it is important to note that

the North San Bernardino segment does not rupture throughout the evaluated seismic record without the participation of segment Mojave South.

2.5.3 Clustered chronology model

Stress accumulation is largely dependent on the accuracy of paleoseismic chronologies, which are simplified and constrained to reflect large ($M_w > 6$) to great (M_w ~7.8) earthquakes, as geologic evidence generated during smaller earthquakes is rarely preserved. Radiocarbon-derived uncertainties, for example, on the age of individual paleoseismic events are typically about ± 50 years (Scharer et al., 2019). In contrast, the extent and magnitude of the historic rupture of 1857 is reasonably well known. However, there is great uncertainty in the extent of the 1812 earthquake, which could have involved two separate events ranging northwest to Frazier Mountain (Scharer et al., 2017) and/or southeast onto the SJF to Mystic Lake (Lozos, 2016). Throughout this study, we adopted the rupture path for 1812 as described by Scharer and Yule et al. (2020), which included the Mojave South, North San Bernardino, San Jacinto Bernardino, and Clark segments. Moreover, only the most recent Cajon Pass slip event (1857) is relatively well-constrained in time and space.

To better understand the variability in stress accumulation related to our adopted chronology of the Maximum Rupture Model (MRM), we also constructed an alternative stress evolution time-series model that assumes an end-member clustered chronology model (Figure 2.10; K. Scharer personal communication), which we refer to as the Clustered Chronology Model (CCM). The rupture ages in the CCM are constrained by the age limits provided in Scharer and Yule (2020, their Table S2) but were selected to maximize time gaps between spatially clustered events. For example, four SJF earthquakes that occurred between 1231 and 1389 in the MRM (in MRM modeled as occurring in 1249, 1291, 1321, and 1346) were instead grouped towards the limits of their allowable age ranges to occur in just 36 years (1267, 1268, 1290, and 1303). We also modeled three tripartite events (1450, 1568 and 1812) instead of the single event observed in the historical record in 1812 reflected in the MRM, which adds to our modeling observation of stress threshold behavior of such ruptures. No other rupture lengths were changed. In this way, CCM minimizes the time between groups of similarly-aged ruptures, especially if spatially close, whether repeats on a single part of the fault or sequentially on neighboring segments. The CCM yields a few near-repeat events, but also provides several periods where 90-110 years pass with no ruptures on the system.

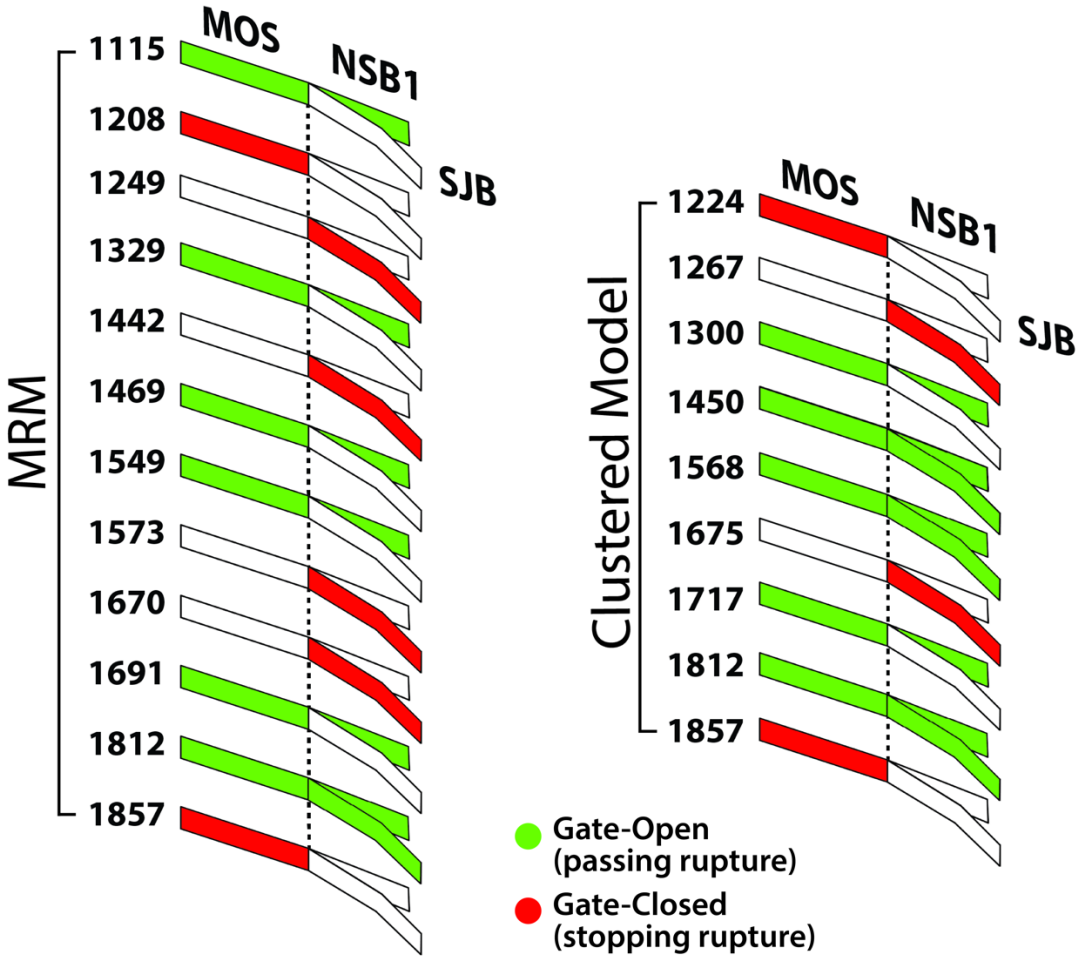

Figure 2.10. Comparison of Maximum Rupture Model (MRM) and end-member Clustered Chronology Model (CCM) slip events. Participating segments Mojave South (MOS), North San Bernardino (NSB1), and San Jacinto Bernardino (SJB) adjacent to the Cajon Pass are denoted in red for stopping events ('Gate-Closed'), and green for passing events ('Gate-Open'). The CCM methodology produces three tripartite events (1450, 1568 and 1812) compared to only the known historic event (1812) of the MRM.

From the CCM stress evolution time-series (Figure 2.11; Appendix, Table 2.A1), we find slightly higher stress thresholds (and similar standard deviations) compared to the MRM stress levels: 1.9 MPa ($\sigma_{max\ \tau c}$ 0.7 MPa) for the Mojave South segment, 1.1 MPa ($\sigma_{max\ \tau c}$ 0.5 MPa) for the North San Bernardino segment, and 2.4 MPa ($\sigma_{max\ \tau c}$ 0.6 MPa) for the San Jacinto Bernardino segment (Appendix, Table 2.A2). Differences between the CCM and MRM mean stress thresholds are between 0.03-0.6 MPa, with higher values for the CCM resulting from the grouping of slip events while maintaining somewhat similar periods for stress accumulation. Comparable stress drops also result from the CCM (Appendix, Table 2.A1). Moreover, the CCM supports the

results from the MRM model in that the stress accumulation and drop values from the MRM are fairly robust and not highly sensitive to the paleoseismic uncertainty. We also observe similar patterns of induced stress and joint rupturing behaviors. For example, for events limited to the Mojave South segment, stresses increase on the North San Bernardino segment. Because the historical ruptures of 1812 and 1857 remain unchanged in the CCM, present-day stress accumulation differences to the MRM are negligible.

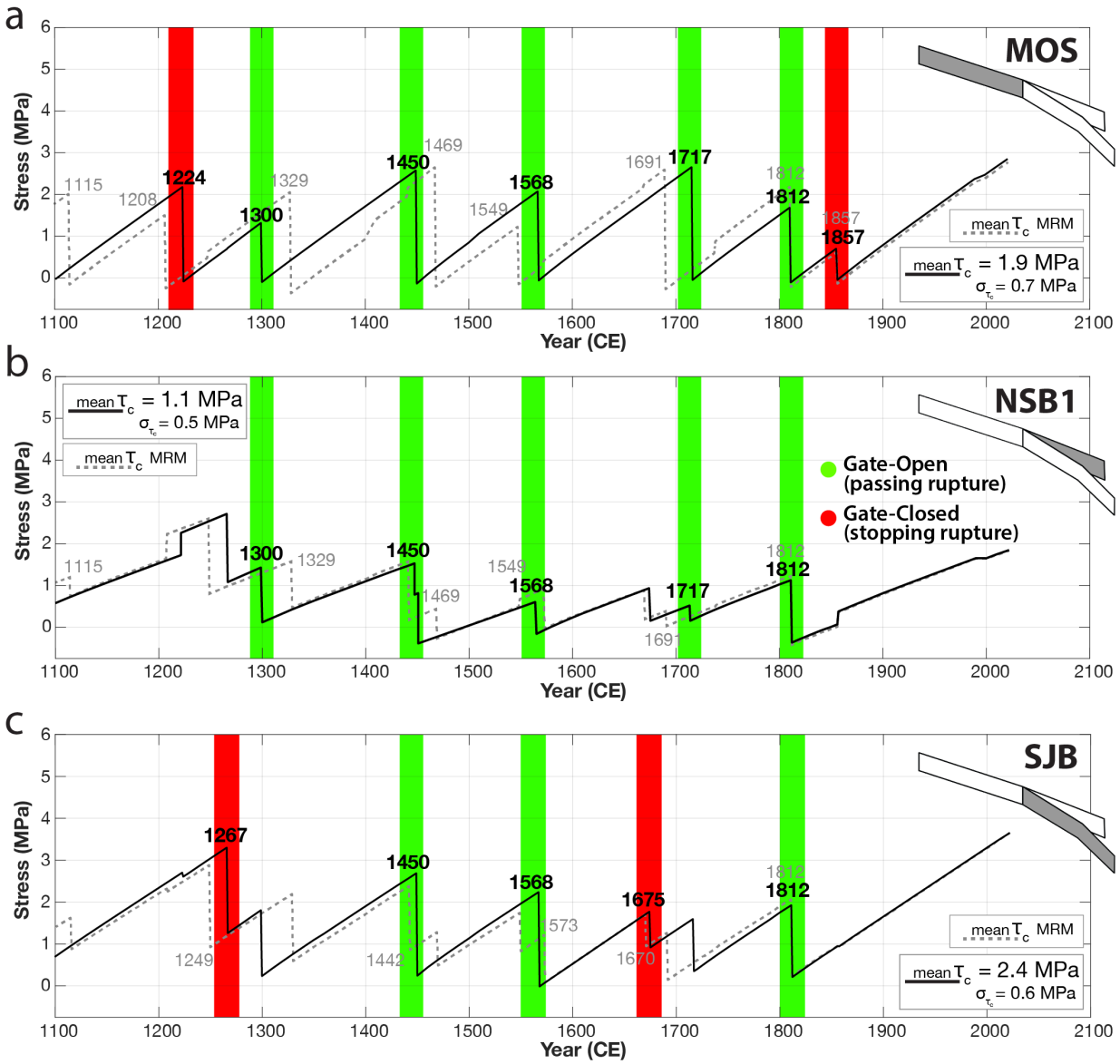

Figure 2.11. Stress evolution time-series for the Clustered Chronology Model (CCM). Mean stress values (MPa) for segments **a)** Mojave South (MOS), **b)** North San Bernardino (NSB1) and **c)** San Jacinto Bernardino (SBJ), with on-segment events indicated in colored bars: Green denotes passing ('Gate-Open'),

red stopping ('Gate-Closed') ruptures at the Cajon Pass. Dashed grey lines indicate MRM (Figure 2.8) mean stress values with dates for on-segment events.

2.5.4 Earthquake gate indicators from stress values

In our model of the MRM, all joint Mojave South and North San Bernardino ruptures cause stress levels to drop below 1 MPa on non-participating segment San Jacinto Bernardino. This could indicate that the non-induced accumulated stress value on the San Jacinto Bernardino segment needs to be >1 MPa in order for the segment to rupture for a tripartite event, with the gate opening to the south onto the SJF. In contrast, all 'Gate-Closed' events on segment San Jacinto Bernardino induce small stress rises (<0.2 MPa) on the Mojave South segment, and the highest value on that segment is 2.2 MPa (1670) for such an event. It can be speculated that the mean stress on MOS has to be >2.2 MPa for a gate-opening towards the north for a rupture from the SJF. When comparing to the CCM, stress values on Mojave South are between 1.7 and 2.6 MPa during tripartite ruptures with the SJF.

When further comparing the MRM and CCM stress time-series specific to segments Mojave South and San Jacinto Bernardino (Figure 2.12), we note consistent stress thresholds (i.e., small segment-to-segment differences, 0.1-0.3 MPa; Appendix, Table 2.A3) on the MOS and SJB segments for all three CCM tripartite ruptures in 1450, 1568 and 1812. A similar behavior emerged for the single MRM tripartite rupture of 1812, and may suggest that complete junction rupture events can be promoted when the MOS-SJB stress accumulation environment is at a consistent level at the same time. Furthermore, for all tripartite ruptures, both MOS and SJB segments have ~2 MPa or greater of accumulated stress. However, we note one outlier to this pattern in the CCM time-series as well as in the MRM. In the CCM, the independent-SJB event of 1675, where similar stress thresholds are represented (~2 MPa) on the SJB and MOS segments, there is no joint or tripartite slip evidence in the paleoseismic record. Similarly, in the MRM, one outlier event (1329) that included segments Mojave South and North San Bernardino on the SAF also shows a small difference of 0.1 MPa between the values of SJB and MOS with both accumulations at ~2 MPa, and the 'gate' towards the south onto the SJF remained closed. Nevertheless, these findings suggest that the Cajon Pass 'earthquake gate' could open when the stress differences between the San Jacinto Bernardino and Mojave South segments are within this threshold range.

However, the historical 1857 earthquake that stopped in Cajon Pass and the earthquake of 1812 that passed and may have ruptured all three adjacent segments of the Cajon Pass could be

outlier events themselves. Recent dynamic multicycle modeling concluded that the rupture extent of the 1857 earthquake can be reproduced but that ruptures with the extent comparable to the 1812 tripartite event are not common, and replicating the dynamics of these two earthquakes in terms of rupture extent, direction and especially timing is very challenging (Liu et al., 2022).

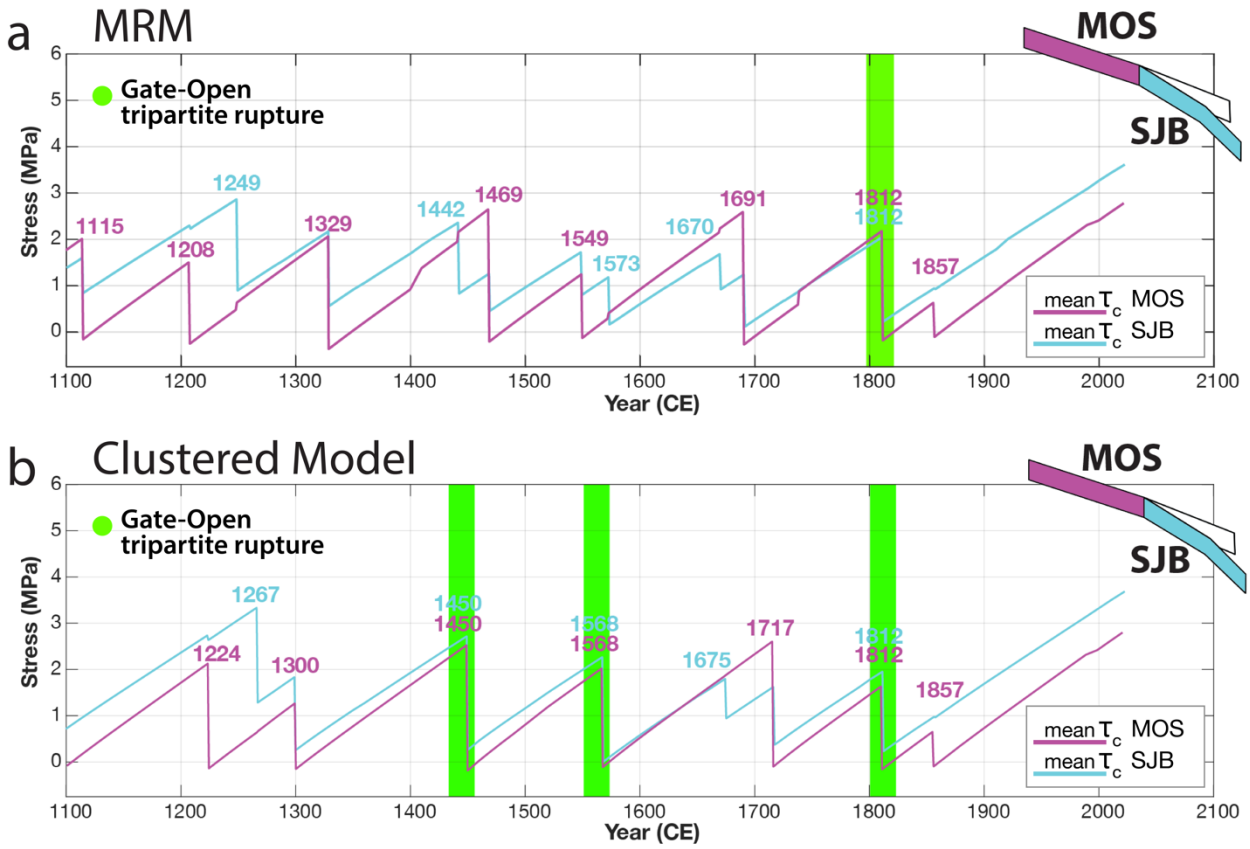

Figure 2.12. Comparison of stress evolution time-series for the **a)** MRM and **b)** Clustered (CCM) chronologies, showing mean stress amplitudes (MPa) for the Mojave South (MOS, magenta) and San Jacinto Bernardino (SJB, blue) segments.

2.5.5 Rheological variations of the southern SAFS

While there is no obvious indication of a rheological barrier that might promote or inhibit propagation of ruptures at the Cajon Pass (Machette et al, 2004; Onderdonk et al, 2018; Forand et al., 2018), several crustal attributes may contribute to local variations in slip and stress drop, including the style of faulting and dips, changes in average tectonic slip rates, mineralogical composition of the host rocks, and hypocentral depths of seismic events. Rheologic analyses

from heat flow data suggest a variation in crustal rigidity around the Cajon Pass area of ~2 GPa (Ward et al., 2021). The difference in lithology and transition temperatures across the SAFS not only controls the thickness of the seismogenic zone but also likely influences the stress drop of slip events in regions near the Cajon Pass. Several studies of the nearby San Gorgonio Pass region (spanning traces of the San Gorgonio and Mission Creek segments of the SAF) suggest feldspar-dominated Peninsular Range rocks have been moved next to quartz-rich Transverse Range rocks (Magistrale and Sanders, 1996) with very different brittle-ductile transition temperatures (Scholz, 1988; Thatcher et al., 2017). Goebel et al. (2015) observed anomalously high stress drops (>20 MPa) in a small region between the traces of the San Gorgonio and Mission Creek segments. Estimated stress drops were found to be higher below depths of ~10 km and along the San Gorgonio fault segment, but lower to the north and south away from San Gorgonio Pass, showing an approximate negative correlation with geologic slip rates (i.e., areas of highest stress drops are approximately co-located with the lowest slip rates; Boyd et al., 2017). At the Mission Creek segment, stress drop changes abruptly across the fault such that feldspar-dominated rocks to the south accommodate substantially larger stress drops compared to the quartz-rich material to the north (Thatcher et al., 2017). Similar observations have been made for mining-induced seismicity, for which stress drops are higher in feldspar-dominated diorite dikes compared to the surrounding quartzite host rocks (Kwiatek et al., 2011). Analysis of the host rocks directly at the Cajon Pass indicate schist to the north (segment MOS), gneiss to the adjacent south along the SAF (segment NSB1), and muscovite schist and granodiorite by the SJF (segment SJB) adjacent to the Cajon Pass (Forand et al., 2018). These observed differences in lithology may provide some guiding geological/rheological variations that promote the configuration and existence of an ‘earthquake gate’.

2.5.6 Present day stress levels and possible stress field alterations since 1857

At present, modeled stresses of the Cajon Pass, and indeed along most of the southern SAFS, are unusually high and at almost the highest levels they have been during the examined 1000-year paleoseismic record. In the past, segment Mojave South attained stress values of up to 2.7 MPa, which was surpassed in 2015, and with the mean stress threshold of 1.9 MPa reached in 1970. For segment San Jacinto Bernardino, the present mean stress value is 3.6 MPa, exceeding the past highest value of 2.9 MPa in 1980. Here, the mean stress accumulation of 2.0 MPa was reached in 1920. The current mean stress value of 1.8 MPa on segment North San Bernardino is below the highest value in the past (2.6 MPa); however, it also reached its mean

threshold value of 0.9 MPa in 1920. As noted in the MRM-CCM time-series comparison, segments Mojave South and San Jacinto Bernardino show consistent stress thresholds of ~2 MPa with small segment-to-segment differences of ~0.1-0.3 MPa during tripartite events. However, stress values of the two segments have not been able to reach such a configuration so far because of the 'Gate-Closed' event of 1857, where segment San Jacinto Bernardino did not rupture and continued to accumulate stress essentially uninterrupted. Nevertheless, a possible 'Gate-Open' rupture with a joint MOS-NSB1 earthquake could have occurred after 1930, when the lowest stress threshold value on the Mojave South segment for such a rupture (1.2 MPa) was reached.

Inspection of the recent record and our stress evolution time-series results could suggest that the stress-release mechanisms of the fault system have changed since the last major earthquake in 1857. Moreover, several physical modifications have occurred that could have influenced the stress field in the region, where human activity in drilling, injection and pumping since the 1890s may have altered the state of the host rock around the SAFS. Most notably, the discovery of gold and oil increased the population of Los Angeles County from 1,610 people in 1850 to ~10 million in 2022 (US Census Bureau). California has one of the largest reserves for heavy oil in the world, and by 1925 accounted for more than 22% of the world's oil production (Tennyson, 1998; Croft and Patzek, 2009; Hein, 2013); in 1985, oil production in California peaked at 1.1 million bbl/day (California Department of Conservation, 2022). Almost all of California's oil and gas fields were discovered between 1890 and 1930, and declines in conventional production during the last thirty years have prompted increasing interest in tight oil, shale oil and oil sands (also called tar sands), which require more sophisticated pumping and waste water management systems that are known to be able to trigger earthquakes regardless of vertical separation (Keranen et al., 2013; Goebel and Shirzaei, 2020). During the early instrumental period between 1932 to 1952, seven M_w >4 earthquakes occurred in the Los Angeles basin with evidence suggesting that they were induced by oil production (Hough and Bilham, 2018). Furthermore, predicted stress changes associated with the production from eight oil fields in the southwestern Los Angeles basin show that frictional failure was stimulated at a depth of 5 km with stress changes of >0.1 MPa. For example, studies at the Wilmington oil field in Long Beach, which experienced a subsidence of 8.8 m in 1967, showed that the maximum Coulomb stress at 2.5 km depth exceeded 1 MPa directly below the field during the first period of peak oil extraction of 17 million bbl in 1936 (Hough and Bilham, 2018). Four M_w 4.2-5.1 earthquakes occurred in the area of the Wilmington and Torrance oil fields in Long Beach from 1938 to 1941, coinciding with the first peak oil extraction at both locations. More recently, induced seismicity has also been studied

and observed near the SAFS in the San Ardo oil field further north, suggesting that a combination of mechanisms is required to explain the large vertical separation between injection and earthquakes (Goebel and Shirzaei, 2020). Pressure diffusion can be facilitated by fault damage zones acting as flow conduits (Zhang et al., 2013; Goebel et al., 2016) and as a result of the increase in pore pressure, elastic stresses can lead to fault activation without a direct hydraulic connection (Wang, 2000). A sharp increase in oil production seems to influence stress in the short term, however, pore pressure changes in the surrounding rock are controlled by flow and therefore have a delayed effect. The extraction of oil and injection of wastewater could have a far field effect on the stress of the SAFS, as the oil fields of Long Beach for example are only ~80 km away from the Cajon Pass junction. However, the findings of Hough and Bilham (2018) imply that the spatial extent of Coulomb stress lobes associated with oil production sets the perimeter for the size of induced earthquake events, which in their study are contained in an area of ~20 km in diameter and depth of ~8 km.

Elevated pore pressures within the SAFS have also been cited as explanations for the fundamental weakness of the fault system; however, no evidence of high pore pressure was found during drilling studies into the SAF in central California (SAFOD: San Andreas Fault Observatory at Depth; Zoback et al, 2010) nor from core samples of the Cajon Pass (Forand et al., 2018). Likewise, groundwater pumping can induce fault slip at depth because of the coupling of fluid flow and mechanical deformation (Jha and Juanes, 2014). In a mature fault, core permeability can be low due to comminution of grains, while permeability of damaged host rock can be high because of fracturing (Caine and Forester, 1999). Moreover, stress changes due to groundwater withdrawal have been assessed to be on the order of 0.1-0.3 kPa/yr (Borsa et al., 2014; Lundgren et al., 2022).

The increased earthquake activity in the Eastern California Shear Zone (ECSZ) since 1872 is associated with a zone of elevated strain rates, but its significance and cause are unknown (Chen et al., 2020). Because of proximity, large earthquakes close to the southern SAF in the ECSZ can result in stress changes around the Cajon Pass, such as the M_w 7.3 1992 Landers earthquake. With its epicenter ~115 km away from the Cajon Pass, this event caused a mean stress drop of ~0.1 MPa on the North San Bernardino segment (Figure 2.8 b). Stress lobes from the M_w 7.3 1992 Landers earthquake extended outwards ~100 km in each direction (Xu et al., 2018; King et al., 1994) and passing seismic waves could have affected pore-fluid pressures (Elkhoury et al., 2006). A change in Coulomb stress can also modulate long-term creep rates,

where such a step increase or decrease of ~20 kPa can result in multiyear modulations (Xu et al., 2018).

A combination of these factors altering the stress field around the southern SAFS could initiate or postpone a large earthquake on the fault system. In our study, modeled stresses are based on tectonic stress accumulation only, and the resulting present-day stress levels are not sensitive to paleoseismic chronology models as the most recent large rupture of 1857 is well constrained in extent and magnitude. However, several other factors could modulate the stress field around the Cajon Pass, possibly reducing the modeled present mean stress values.

2.6 Conclusions

The Cajon Pass is an important intersection for previous and future through-going ruptures and could serve as an earthquake 'gate', or a physical stress barrier that supports or encourages significant ruptures along the SAFS, allowing ruptures to pass or stop (Lozos, 2016). Several crustal and faulting characteristics, such as faulting style, tectonic slip rates, host rock mineralogical composition, and hypocentral depths of seismic events, may all play a role in local variations in stress drop and accumulation. This study explores earthquake cycle stress accumulation of the southern SAFS with a 4D Coulomb stress model constrained by the present-day archive of geodetic, geologic, and paleoseismic measurements. We focus our model on the Cajon Pass tripartite configuration of fault segments, Mojave South (MOS), North San Bernardino (NSB1), and San Jacinto Bernardino (SBJ), and attempted to assimilate patterns of threshold stress for these segments, characterize stress drop effects on nearby segments, and explore temporal relationships throughout the 1000-year time-series. First, we find that mean stress thresholds for the Cajon Pass segments are largest for the MOS segment (1.9 MPa) and smallest for the NSB1 segment (0.9 MPa), due to the higher slip rate on the Mojave segment. Second, while we cannot identify a precise or common stress threshold preceding major ruptures of the Cajon Pass, our results do suggest an elevated range of stress accumulation that appears to be characteristic to each segment, with stress threshold ranges of 1.2-2.7 MPa, 0.4-1.6 MPa, and 1.2-2.9 MPa, for the MOS, NSB1 and SJB segments, respectively.

We also explore these relationships in the context of earthquake gate open/closed behaviors. While there is no significant correlation between stress thresholds of Cajon Pass segments as they participate in joint or tripartite (‘Gate-Open’) ruptures, our results do suggest that past joint earthquake events on the SJB and MOS segments have shared a common stress threshold of

~2 MPa with less than 0.2 MPa differences in stress accumulation. This suggests that when the stress disparity between the San Jacinto Bernardino and Mojave South segments is within this threshold range, the Cajon Pass could act like an 'earthquake (open) gate', allowing the rupture to propagate between the SJF and SAF.

Fault interactions and rheological conditions in the region of the Cajon Pass may control whether a rupture could propagate towards the Los Angeles area. The structure and geomorphology of the SAFS through the Cajon Pass have been characterized to be relatively constant and do not show an obvious indication of a rheological barrier to the propagation of ruptures (Machette et al, 2004; Onderdonk et al, 2018; Forand et al., 2018). Since the last major earthquake in 1857, the SAFS has experienced a period of relative quiescence with major activity (>M_w 7) only in the Eastern California Shear Zone (ECSZ). There have been a number of physical changes that could have affected the stress field in the area, such as drilling, injection and pumping, that may have altered the stress state of the host rock around the SAFS; however, it is challenging to estimate and study the far-field impacts of these activities. Since the SAFS is a mature system, it can be inferred that permeability could be generally low and changes to the state of stress due to changing pore pressures are small. The population of Los Angeles County increased from 1,610 people in 1850 to ~10 million in 2022, and consequently the SAFS presents a great earthquake hazard that could cause unprecedented human loss as well as great infrastructure and economic damage. The San Andreas and San Jacinto faults have likely ruptured together multiple times in history, but because of the branching and structural geometry of the SAFS in the region of the Cajon Pass, a joint rupture of the San Jacinto fault with the Mojave section of the San Andreas fault is more likely to be the source of a major earthquake in Southern California than a rupture originating from the Mojave segment southwards to Coachella Valley (Onderdonk, et al., 2018). Given the elapsed time since these faults have ruptured, the probability of an earthquake in the near future is high (Liu et al., 2022). Modeled present-day stress accumulations at the Cajon Pass are 2.8 MPa on the Mojave South (MOS) segment, 1.8 MPa on the North San Bernardino (NSB1) segment and 3.6 MPa on segment San Jacinto Bernardino (SJB) segment. These values denote some of the highest magnitudes of stress accumulation during the past 1000 years. Results from the study presented here can further be used to advance our understanding of how fault loading and 1000-year rupture histories can influence earthquake cycle stress accumulation and assimilation between active fault segments.

Appendix

When assessing stresses of each segment, values were extracted every 2 km along the strike. As each location on the fault is influenced by stress changes on adjacent segments and neighboring events on other faults, stress values vary locally. This is illustrated in Figure 2.A1 for the Maximum Rupture Model (MRM) of Scharer and Yule (2020), where magenta lines denote extraction locations in the northern part of a segment and locations in the south of the segment in blue. Present values for example can range within and differ by as much as ~2 MPa for segment Mojave South, ~1.5 MPa for North San Bernardino, and ~3.5 MPa for San Jacinto Bernardino depending on location. Stress values on the San Jacinto Bernardino segment have greater variation with location on the segment than the other two segments, with present mean values raging from ~5.5 MPa in the north, to ~3.2 MPa in the middle, and ~2.2 MPa towards the southern end. This is mainly due to the large variations in strike and proximity to the parallel segment North San Bernardino, where stress lobes overlap. Events on other segments cause localized stress changes in areas directly adjacent to non-participating segments, as indicated in grey bars. For example, the ruptures of 1406 and 1739 to the north of the Mojave South segment induce a drop of up to 1.4 MPa in locations directly at the northern end of the MOS segment.

From mean stress value results for the participating-passing ('Gate-Open) rupture of 1549 on North San Bernardino, we observe that stresses increased by 0.2 MPa instead of dropping as prescribed in the model. When examining the values per location, only the northern parts of the segments within ~10 km distance from the Cajon Pass drop in values, while the locations towards the southern end of the segment do not experience a drop, with rising values at the end of the segment in the south. This can be attributed to the high stress accumulation on the parallel segment San Jacinto Bernardino, which has not experienced a participating rupture since 1442 at that time. As the southern end of the North San Bernardino segment is only ~15 km away from segment San Jacinto Bernardino and the northern ends converge, there is an obvious pairing of stress behavior between the segments with overlapping stress lobes.

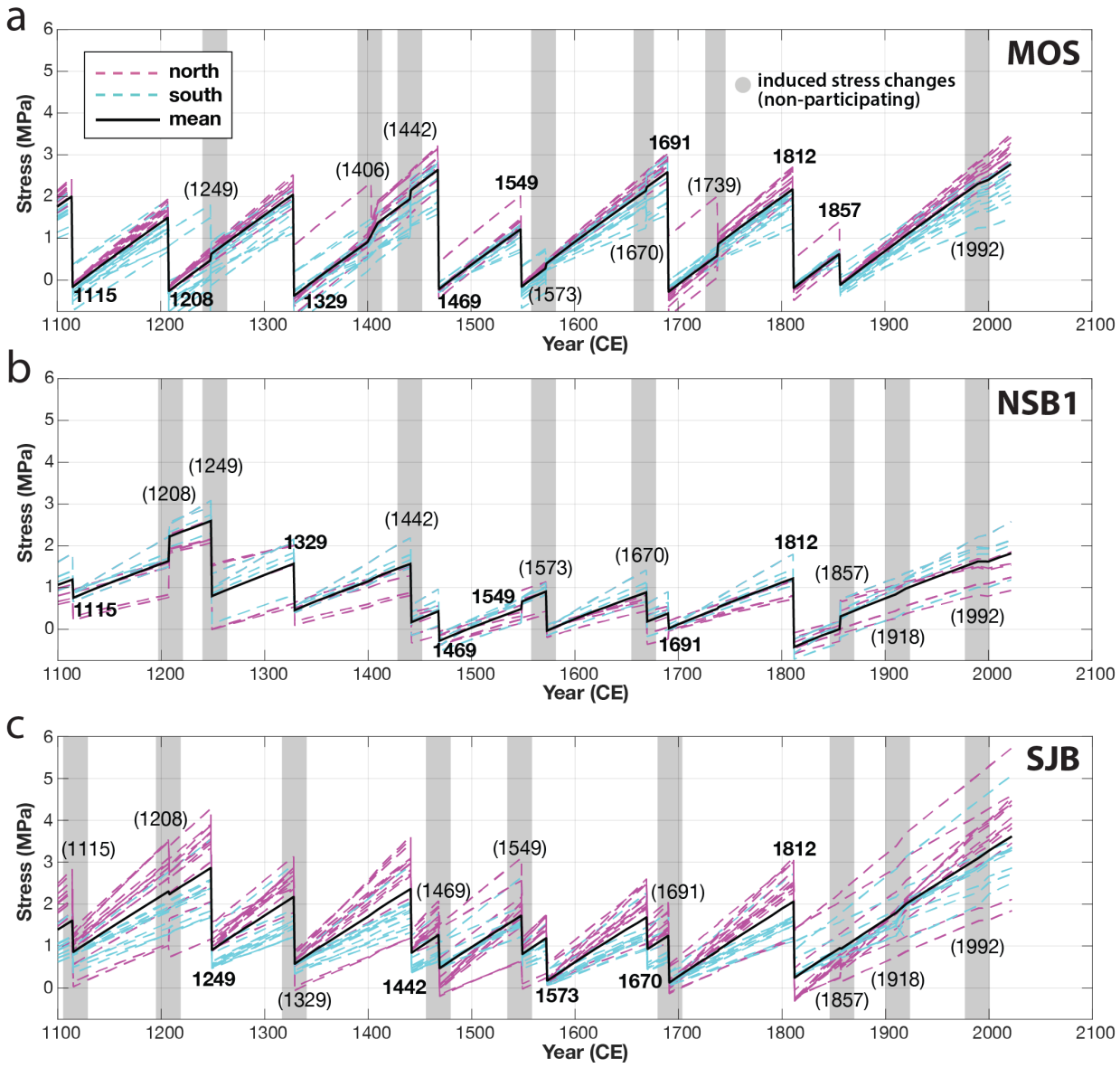

Figure 2.A1. MRM chronology stress values (MPa) extracted at every 2 km distance for segments **a)** Mojave South (MOS), **b)** North San Bernardino (NSB1), and **c)** San Jacinto Bernardino (SBJ). Mean stress values indicated as black lines, locations in northern part of segments in magenta, southern locations in blue dashed lines. Dates in parentheses highlighted with grey bars are ruptures on other segments inducing stress changes on non-participating segments.

When relating mean stress values from the MRM to the Clustered Chronology Model (CCM; K. Scharer personal communication), we find slightly higher stress thresholds (and practically unaffected standard deviations) in the CCM (Table 2.A1). The Mojave South segment mean value is unchanged in the CCM (Table 2.A2) compared to the MRM with 1.9 MPa, while the North San

Bernardino segment has an increase of +0.2 MPa (1.1 MPa in CCM), and San Jacinto Bernardino +0.4 MPa (2.4 MPa in CCM). These higher values are a result of grouping slip events together while retaining similar periods for stress accumulation. Stress drops in the CCM are likewise comparable to those in the MRM.

Table 2.A1. Mean stress (MPa) from values extracted at every 2 km distance for clustered chronology model (CCM) of each segment before and after major earthquakes.

Year	MOS τ_c (MPa)			NSB1 τ_c (MPa)			SJB τ_c (MPa)		
	pre-event	post-event	stress change	pre-event	post-event	stress change	pre-event	post-event	stress change
1224ˣ	2.2	-0.1	-2.3	1.7	2.5	+0.8	2.8	2.7	-0.1
1267ˣ	0.7	0.7	0.0	2.9	1.1	-1.8	3.4	1.3	-2.1
1300	1.3	-0.1	-1.4	1.4	0.1	-1.3	1.8	0.2	-1.6
1450	2.6	-0.3	-2.9	1.5	0.6	-0.9	2.7	0.2	-2.5
1568	2.1	-0.1	-2.2	0.6	-0.1	-0.7	2.3	-0.1	-2.4
1675ˣ	1.9	1.9	0.0	0.9	0.2	-0.7	1.8	0.9	-0.9
1717	2.7	-0.1	-2.8	0.5	0.2	-0.3	1.6	0.3	-1.3
1812	1.7	-0.1	-1.8	1.1	-0.3	-1.4	2.0	0.2	-1.8
1857ˣ	0.7	-0.1	-0.8	0.1	0.4	+0.3	0.9	0.9	-0.0

Note: Values in grey indicate stress rise after an event. Colors indicating segments participating in an earthquake, with green denoting passing Cajon Pass events. Dates with ˣ (red) are 'Gate-Closed' events, when the rupture did not propagate beyond the Cajon Pass.

Table 2.A2. Clustered chronology model (CCM) mean maximum stress values for ruptures on event-participating segments (extracted every 2 km distance).

Mean values (participating)	MOS	NSB1	SJB
max. τ_c (MPa)	1.9	1.1	2.4
$\sigma_{max\ \tau c}$ (MPa)	0.7	0.5	0.6
τ_c drop (MPa)	2.0	1.0	1.9
$\sigma_{drop\ \tau c}$ (MPa)	0.8	0.4	0.6
Time between ruptures (yrs)	105.5	128.0	136.3
σ_{yrs} (yrs)	41.6	26.6	35.5

The CCM produces three tripartite ruptures (1450, 1568 and 1812), where we note consistent stress thresholds of segments Mojave South and San Jacinto Bernardino at >2.0 MPa and small segment-to-segment differences of ~0.1-0.2 MPa (Table 2.A3). A similar behavior can be observed in the MRM for the single tripartite rupture of 1812. This suggests that complete junction rupture events could be promoted when the MOS-SJB stress accumulation environment is at a consistent level at the same time with a small segment-to-segment difference.

Table 2.A3. Differences mean stress values (MPa) between segments before events for MRM (Table 2.2) and clustered chronology (CCM) models (Table 2.A1).

Maximum Rupture Model (MRM)

Year	Difference τ_c MOS-NSB1	Difference τ_c MOS-SJB	Difference τ_c NSB1-SJB
1115	0.8	0.4	0.4
1208^x	0.1	0.8	0.7
1249^x	2.1	2.3	0.3
1329	0.5	0.1	0.6
1442^x	0.4	0.4	0.8
1469	2.2	1.4	0.8
1549	0.7	0.5	1.2
1573^x	0.6	0.9	0.3
1670^x	1.3	0.5	0.8
1691	2.2	1.4	0.9
1812	1.0	0.1	0.8
1857^x	0.6	0.3	0.9

Clustered Chronology Model (CCM)

Year	Difference τ_c MOS-NSB1	Difference τ_c MOS-SJB	Difference τ_c NSB1-SJB
1224^x	0.5	0.5	1.0
1267^x	2.2	2.7	0.4
1300	0.1	0.5	0.4
1450	1.1	0.1	1.2
1568	1.5	0.2	1.6
1675^x	1.0	0.1	0.9
1717	2.2	1.1	1.1
1812	0.6	0.2	0.8
1857^x	0.6	0.3	0.9

Note: Values highlighted in green denote passing Cajon Pass ruptures, values in grey indicate stopping events on segment San Jacinto Bernardino (SJB) at the Cajon Pass, not propagating further north. Dates with ^{x} are 'Gate-Closed' events, when the rupture did not propagate beyond the Cajon Pass. Values with close differences for 'Gate-Open' tripartite events (~0.1-0.3 MPa) indicated in red font, occurring between segments Mojave South (MOS) and San Jacinto Bernardino (SJB). Outlier events with small differences but no tripartite ruptures in purple font.

Supplemental files

Stress accumulation time-series movie from 1100-2022, produced with Generic Mapping Tools (Wessel et al., 2013):

https://figshare.com/articles/media/Coulombstress_1000yrs_mp4/21210464

CHAPTER 3. STRIKE-SLIP FAULTING ON TITAN: MODELING TIDAL STRESSES AND SHEAR FAILURE CONDITIONS DUE TO PORE FLUID INTERACTIONS

Note: This chapter was published in 2021 in the journal *Icarus* (Vol. 371) as 'Strike-slip faulting on Titan: Modeling tidal stresses and shear failure conditions due to pore fluid interactions', with co-authors B.R. Smith-Konter, S.A. Fagents, M.E. Cameron, G.C. Collins and R.T. Pappalardo (doi: 10.1016/j.icarus. 2021.114700).

Abstract

Expressions of strike-slip faulting are well documented on multiple ocean worlds (e.g., Europa, Enceladus, and Ganymede) and the motion along these faults is thought to be driven by variations in diurnal tidal stresses. Titan exhibits a complex and dynamic geology with a varied surface morphology developed from fluvial, aeolian, and possible cryovolcanic and tectonic activity. However, observational data are currently limited and no clear strike-slip indicators have been identified so far. Nevertheless, the inferred presence of a porous ice layer saturated with liquid hydrocarbons in Titan's shallow subsurface provides a unique environment for studying zones of frictional weakness, shear heating, and the promotion of cryovolcanism. This study examines Titan's ability to host shear deformation mechanisms, including considerations for how the presence of near-surface liquid hydrocarbons and the crustal porosity of ice significantly reduce the resistance to shear failure of strike-slip faults in flexed areas under maximum diurnal tidal stresses. We conduct a sensitivity analysis of Titan's shear failure tendencies, given optimal failure conditions that may exist due to pore fluid interactions, and we examine the possibility for strike-slip tectonics guided by Coulomb failure laws and tidal stress mechanisms. Using the SatStress tidal stress model for a Titan-appropriate rheology, we compute the diurnal tidal stress tensor and resolve shear and normal stresses onto a suite of fault orientations. We adopt plausible coefficients of friction and include the effect of a hydrostatic pore fluid pressure gradient for Titan. At shallow fault depths (< 1 km) and for optimally oriented faults, this exploratory model suggests shear failure is achievable under diurnal tidal stress conditions subject to such pore fluid pressures, especially in the polar regions. Our results suggest that under these conditions, shear failure is not only possible, but may be an active deformation mechanism on the surface and in the subsurface of Titan, and could potentially serve as a pathway for the exchange of surface and

subsurface materials through shear heating mechanisms. Moreover, the inference of conditions supporting strike-slip tectonism on Titan could have important implications for future Dragonfly observations and for future studies directed at better understanding the structural development of the surfaces of icy moons.

3.1 Introduction

Titan is a moon of complex and dynamic geology, with a varied surface morphology developed from fluvial, aeolian, and possible cryovolcanic and tectonic activity (e.g. Lopes et al., 2020). Surface observations, however, have yet to reveal large-scale, morphologically distinct characteristics of strike-slip faulting (i.e., *en echelon* structures, fault duplexes, and offset features) that have been well documented on multiple ocean worlds like Europa, Enceladus, and Ganymede (i.e., Kattenhorn, 2004; Yin and Pappalardo, 2015; Martin, 2016; Cameron et al., 2018). In short, strike-slip tectonism appears to be common among ocean worlds, serving as a critical driver of the structural development of these surfaces and potentially a pathway for the exchange of surface and subsurface materials through shear heating mechanisms (Nimmo and Gaidos, 2002; Nimmo et al., 2007). However, only rare inferences of strike-slip tectonism on Titan have been reported thus far (Paganelli et al., 2010; Liu et al., 2016 a; Matteoni et al., 2020), due in large part to limited quality and coverage of observational data. Nevertheless, optimal shear failure conditions may exist within Titan's shallow subsurface where the inferred presence of a porous ice layer saturated with liquid hydrocarbons provides a unique environment for zones of frictional weakness (Liu et al., 2016 b), shear heating (Nimmo et al., 2007), and potentially the promotion of cryovolcanism (Sohl et al., 2014; Malaska et al., 2016).

A major indicator of Titan's ability to host shear deformation, like other ocean worlds, can be examined through analysis of its diurnal gravitational tidal stress field (Helfenstein and Parmentier, 1985; Hoppa et al., 1999; Kattenhorn, 2002; Rhoden et al., 2012). Because of the eccentricity of its orbit ($e \approx 0.03$), Titan is subject to diurnal tidal stresses (Figure 3.1) which act to deform the moon (cf. Greenberg et al., 1998). Previous mapping of Titan's mountain terrains reveals a global pattern of faulting, suggesting the presence of a global stress field (Mitri et al., 2010). Although Titan's tectonic evolution is not well understood, global contraction is thought to have formed a pattern of E-W striking faults in the equatorial region (Cook-Hallett et al., 2015; Liu et al., 2016 b; Lopes et al., 2020), and de-spinning of the body could have produced strike-slip faults (Beuthe, 2010). Other stress mechanisms such as true polar wander (TPW) of the spin axis

due to a large-scale redistribution of mass or non-synchronous rotation (NSR) of a decoupled ice shell moving across the satellite's tidal bulge can also cause a buildup of long-term stresses and form a global pattern of geologic features on the surface of a satellite (Ojakangas and Stevenson, 1989). However, there is no tangible evidence for TPW on Titan and NSR seems only marginally possible (Karatekin et al., 2008; Nimmo and Bills, 2010; Baland et al., 2014; Cook-Hallett et al., 2015; Meriggiola et al., 2016). Inferences of fault orientations and strike-slip indicators on other ocean worlds, however, have suggested that the occurrence of strike-slip faulting may also be explained by a simple combination of diurnal stress and Coulomb failure, or frictional sliding dominated by the presence of increased shear stress and/or decreased compressive stress (Smith-Konter and Pappalardo, 2008; Cameron et al., 2020). Several other factors in the evolution of an icy crust, such as thermally produced stresses (i.e. convection of the warm ice layer below or contraction/expansion through cooling), topography-induced and impact stresses, can contribute to shear failure. Fractures of varied orientations may be strongly influenced by the interplay of tectonic force and topography, especially in the shallow crust (Moon et al., 2017).

In the study presented here, we focus on examining Coulomb failure conditions within Titan's shallow subsurface, including considerations for how the presence of near-surface liquid hydrocarbons, clathrates and the crustal porosity significantly reduce the resistance to shear failure, initiating hypothetical strike-slip faults subjected to diurnal tidal stresses. We first describe numerical model SatStress (Wahr et al., 2009) used to calculate diurnal tidal stresses (Section 3) and our method for computing shear failure based on the Coulomb failure criterion (Section 4). We then present candidate features and regions to evaluate shear failure as a function of ice friction, pore fluid pressure, fault geometry, and geographic location (Section 5). Finally, we present these results in a global context and analyze the role of tidal stress as a driver for global strike-slip tectonism (Section 6). Moreover, the objective of this exploratory study is to advance our knowledge of structural and hydrological crustal properties that promote or limit shear failure on Titan, and likewise, to better inform the future exploration of Titan (i.e., the Dragonfly mission).

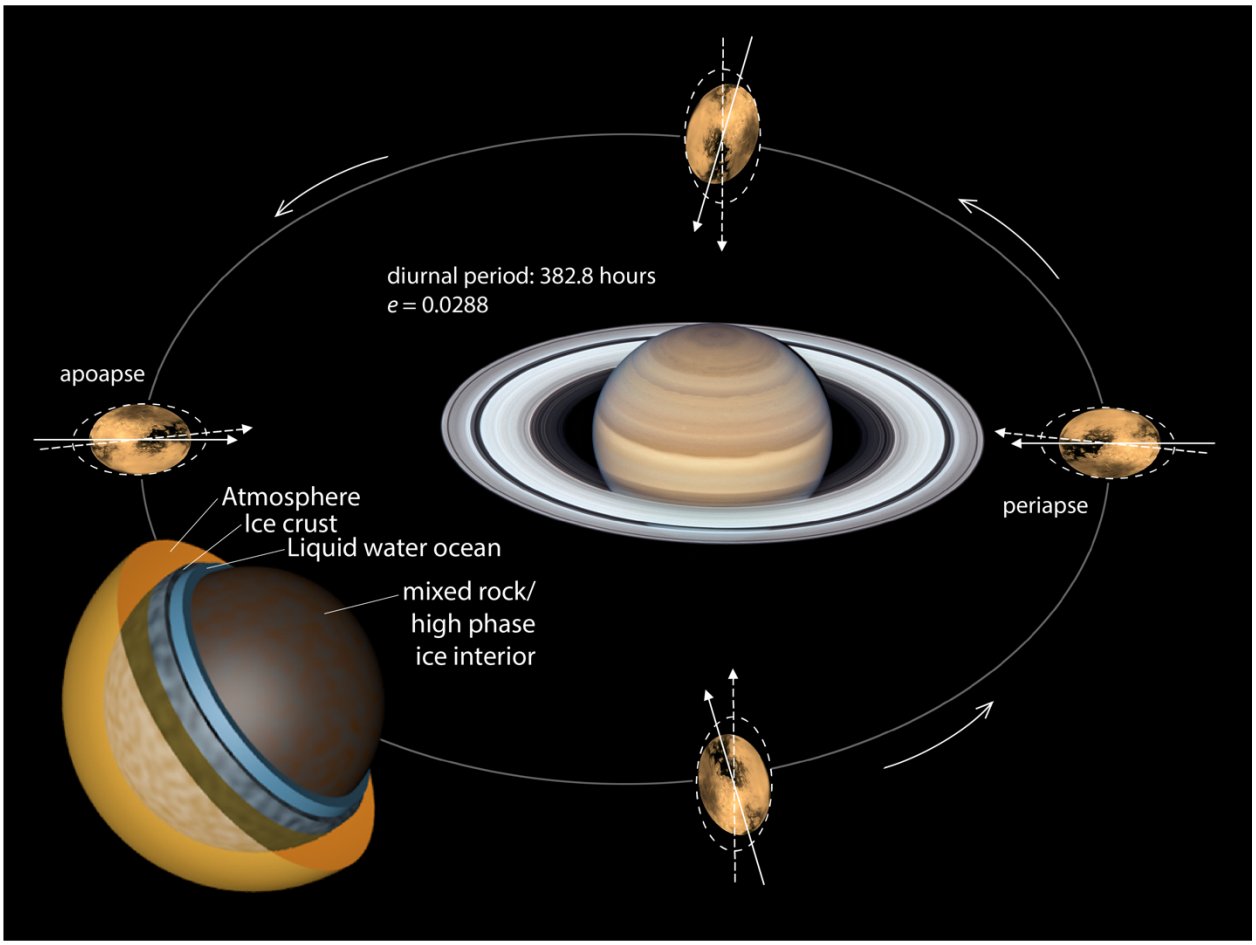

Figure 3.1. Titan structure and tidal stress schematic. Because of Titan's eccentric orbit (e=0.0288), variations in gravitational tidal forces directed toward Saturn (dashed arrows) act to deform the surface (graphic exaggerated). The permanent tidal bulge of the satellite (solid arrows) is facing towards the empty focus of the elliptical orbit. Diurnal tidal stresses are on the order of kPa. Inset: Titan's internal structure drawn to scale, consisting of an outer ice layer ~100 km thick, underlain by a liquid water ocean ~200 km deep, and a deep interior comprised of high-phase ices and a rock core.

3.2 Background

In many ways, Titan is similar to Earth and unlike any other body in the Solar System: it has an extensive and dense atmosphere (composed of mainly nitrogen with clouds of ethane and methane) and is the only known satellite to have stable liquids on the surface. Data from the Cassini-Huygens mission instruments - the Cassini Titan Radar Mapper (RADAR, operating in four modes: SAR, altimetry, scatterometry and radiometry), Visible and Infrared Mass Spectrometer (VIMS), Imaging Science Subsystem (ISS), and the Descent Imager and Spectral

Radiometer (DISR) on the Huygens probe - revealed networks of lineations interpreted as fluvial channels (Porco et al., 2005; Barnes et al., 2006, Burr et al., 2009). During the descent of the Huygens probe, the DISR imaged valley networks with inset stream channels that seemed to have formed by flowing liquids (Tomasko et al., 2005). However, these valleys are not apparent in the RADAR SAR data, because the DISR resolution is roughly an order of magnitude higher (~15-30 m/pixel) than RADAR SAR HiSAR data (average 351 m/pixel; Figure 3.2). ISS data show evidence that seasonal precipitation of methane has facilitated erosion on the surface of Titan (Turtle et al., 2011; Barnes et al., 2013) and liquid methane/ethane lakes have been observed at high latitudes near the north pole (Stofan et al. 2006, Hayes et al. 2008; Sotin et al. 2012). As such, Titan has an "alkanological" cycle that is analogous to the hydrological cycle on Earth, although at much lower temperatures (about 94 K) and replacing water with methane and other hydrocarbons (see Hayes et al., 2018 for post-Cassini review). Like Earth, Saturn's axis of rotation is tilted (~27º) and because Titan orbits almost along the same equatorial plane and has an equal tilt relative to the Sun, Titan's seasons are on the same time-scale as Saturn's, lasting over 7 Earth years (Dougherty et al., 2009). Finally, the scarcity of impact craters on Titan dates its surface to be rather young, around a few hundred million years old (Wood et al., 2010; Neish and Lorenz, 2012; Hedgepeth et al., 2020).

Although observational data are limited, several prominent structures are visible on Titan's surface. Cassini's RADAR mapper has imaged mountain ridges with a linear-to-arcuate morphology near the equator, with mountain chains and hills in E-W orientation within 30º of the equator (Figure 3.2). Mapping efforts have also revealed a global pattern of N-S oriented structures between 60º latitude and the poles, generally attributed to contractional tectonism (Mitri et al., 2010; Cook-Hallett et al., 2015; Liu et al., 2016 b; Lopes et al., 2020). For the study presented here, we explore selected features that could plausibly host strike-slip components and use modeling techniques to investigate the possibility for theoretical strike-slip faulting. The most prominent observable mountainous features are the subparallel ridges of Mithrim Montes (2º S, 127º W), which are also the location of Titan's known highest elevation (Figure 3.3). The ridges are spaced ~25-30 km apart in an E-SE direction and located in the Xanadu region, a terrain classified as 'hummocky' or hilly/mountainous (Lopes et al., 2020; Figure 3.2). While these parallel ridges at Xanadu likely formed from a dominant compressional stress field (Mitri et al., 2010; Cook-Hallett et al., 2015; Liu et al., 2016 b), transpressional Earth analogues suggest strike-slip may also be accommodated in such regions. On Earth, *in situ* tectonic stress indicators show horizontal compression nearly perpendicular to the strike of the San Andreas fault in the Big Bend

region, arising from the slightly convergent relative motion between the North American and Pacific plates (Zoback et al., 1987); here numerous active reverse faults and folds trend nearly parallel to this strike-slip tectonic boundary (Zoback et al., 1987). Conversely, the continental collision between India and Asia formed the Tibetan plateau, which has numerous strike-slip faults (i.e. Altyn Tagh, Kunlun, Haiyuan) in the north that trend along the same general direction as the general compressional tectonic zone and its mountain ridges (Tapponnier et al., 2001; Taylor et al., 2003). Terrestrial fault zone analogues such as these provide ample motivation for considering a range of stress regimes that may promote strike-slip faulting. On Titan, where observational data is insufficient, prominent ridges such as Mithrim Montes may provide some of the strongest evidence for similar tectonic processes, and thus their orientations have to be taken into consideration for modeling purposes, even if they have not been previously identified to be strike-slip in nature.

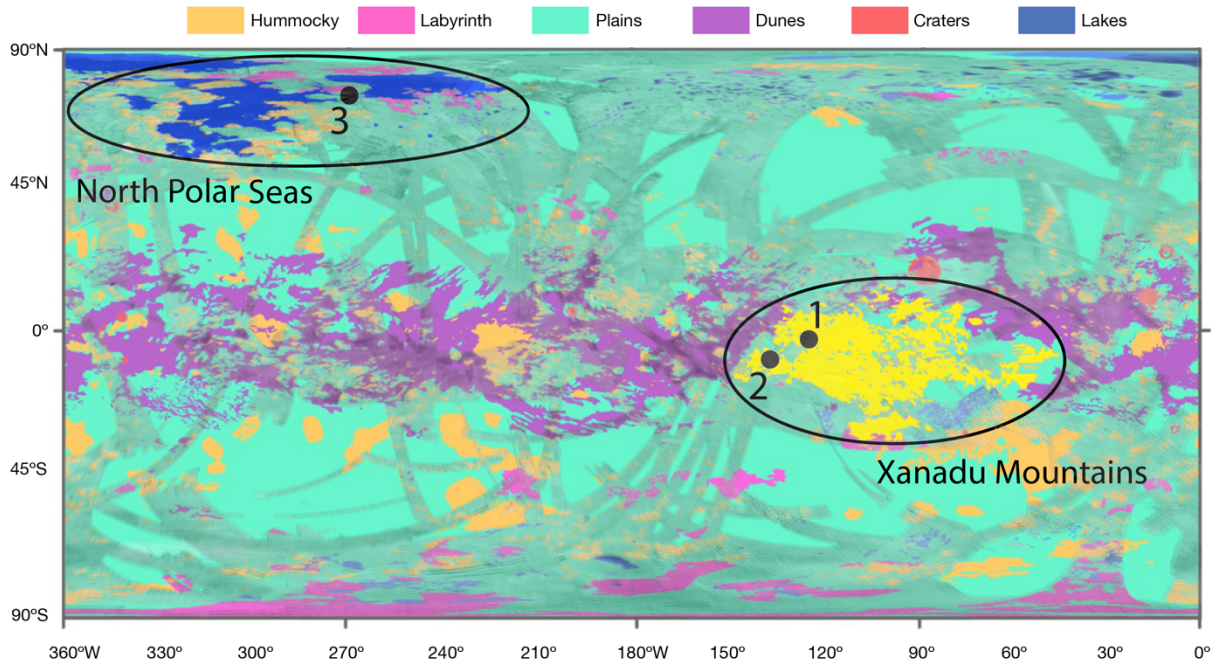

Figure 3.2. Global geomorphological map of Titan from Lopes et al. (2020) combined with shaded RADAR SAR HiSAR 351m coverage swaths from the entire Cassini mission in Mercator projection. In total, SAR data cover about 46% of Titan's surface at a resolution below 1 km/pixel, with an additional 24% at less than 5 km/pixel. Detailed locations examined in this study are indicated by numbers: (1) Mithrim Montes, (2) Western Xanadu fluvial features, and (3) Labyrinth terrain near Ligeia Mare. Colors correspond to the mapping of terrains and the major units of Lopes et al. (2020). The hummocky Xanadu region is enhanced in yellow, north polar seas enhanced in blue.

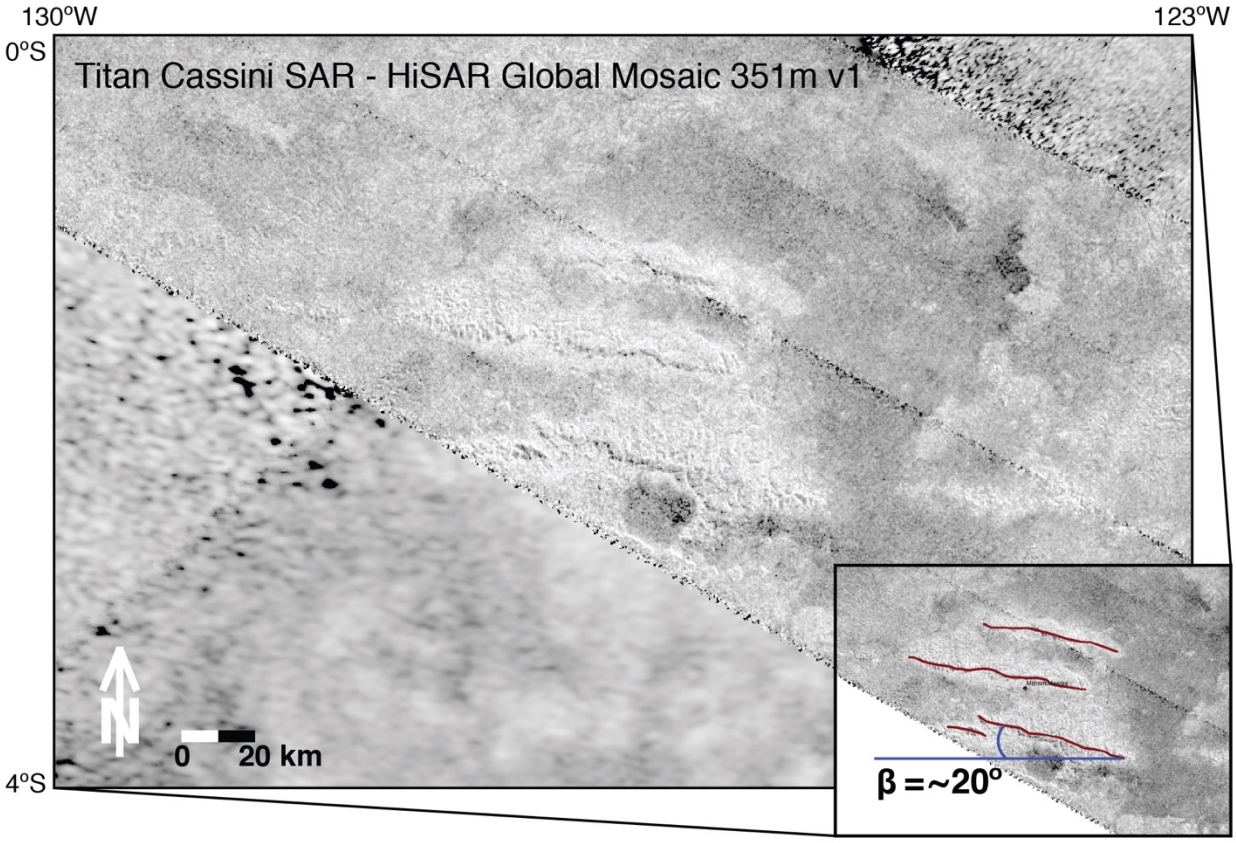

Figure 3.3. Mithrim Montes (2° S, 127° W; Region 1 in Figure 3.2) from Cassini SAR-HiSAR Global Mosaic 351m v1 (Cassini SAR Team, USGS Astrogeology Science Center) with inset of mapped lineaments in ArcGIS and average orientation angle β. The parallel ridges classified as 'hummocky' terrain (Lopes et al., 2020) are spaced ~25-30 km apart, oriented E-SE and located in the Xanadu region. The southernmost ridge is also the location of Titan's highest known elevation (3337 m).

Other salient features on Titan are fluvial networks. Several fluvial systems can be classified as rectilinear networks (Burr et al., 2013), which are characterized by bends and junction angles close to perpendicular (Figure 3.4). This behavior of a fluvial system is suggestive of subsurface tectonic features controlling the path of surface fluids (Burr et al., 2009). A prominent example of a rectilinear network on Earth is Wallace Creek, which exhibits ~130 m of displacement caused by several repeating earthquake cycles along the trace of the San Andreas Fault (Wallace, 1968; Sieh, 1978). The offset reach of Wallace Creek is subparallel to the fault and the up- and downstream reaches are close to parallel (Figure 3.4b). While a variety of factors can control fluvial drainage on Titan, the linked orientations of fluvial features west of the Xanadu region

suggest that there is a subsurface tectonic fabric trending roughly east-west guiding the flow of the rectilinear fluvial system. This region has also been described as a potential pull-apart basin containing small-scale strike-slip faulting (Matteoni et al., 2020). It is possible that this area could host shear displacements and a potential fault structure; the offsets on the eastern fluvial feature are about 10 km and a similar amount of displacement can be measured for the northernmost mapped structure on the next large radar-bright fluvial feature comparable in dimension, 98 km to the west. Furthermore, we note that the inferred trend of this possible structure is also very similar to the orientation of the Mithrim Montes ridges (Figure 3.3).

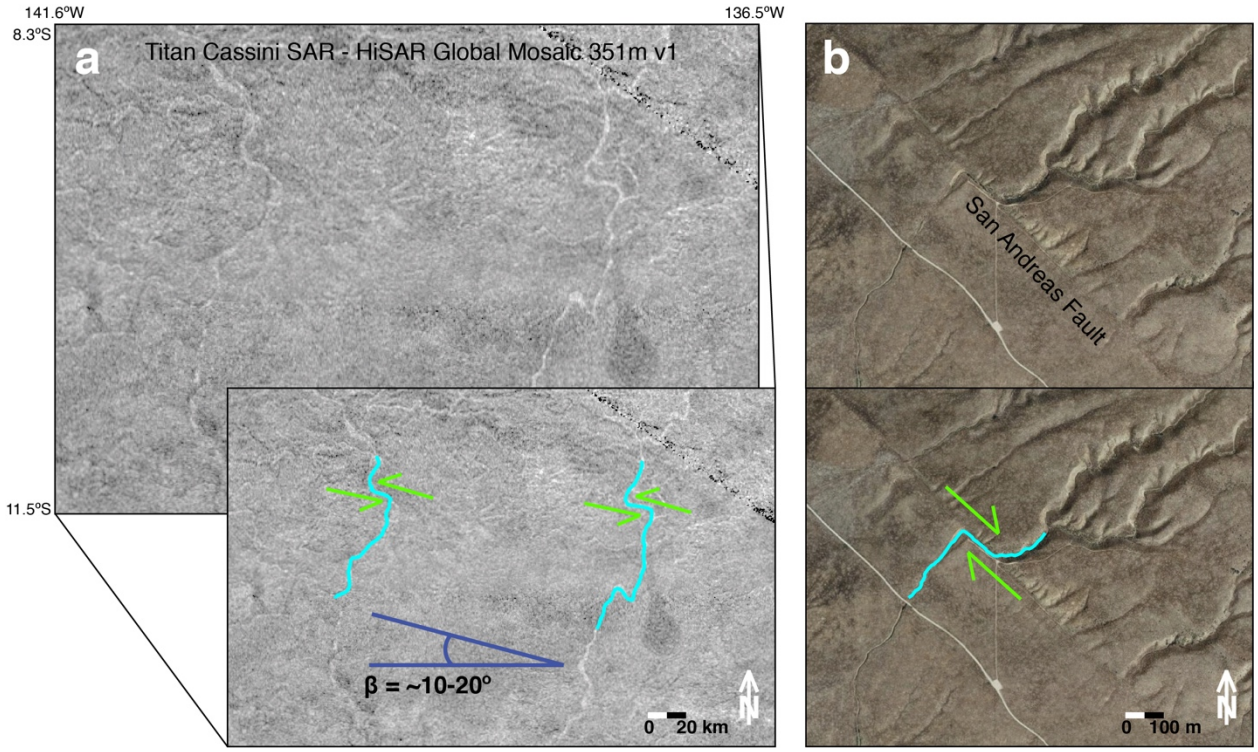

Figure 3.4. a) Western Xanadu radar-bright features ~10° S, 137° W (Region 2 in Figure 3.2) from Cassini SAR-HiSAR Global Mosaic 351m v1. The bright appearance of these fluvial features is thought to be internal reflections from debris with diameters larger than the RADAR wavelength of 2.17 cm (Le Gall et al., 2010). The visible fluvial network is an example of a rectilinear drainage pattern, with bends that are close to 90º (Burr et al., 2013). Arrows indicate the possible slip direction of displacement of fluvial features and a potential fault feature with average orientation angle β indicated. The offset for the northernmost mapped portion is about 10 km for both structures. A similar amount of displacement can be measured for the western fluvial feature. **b)** Earth analogue example of a rectilinear network on the San Andreas Fault (Wallace Creek; Google Maps satellite image), which exhibits ~130 m of strike-slip offset at the trace of the

fault (Wallace, 1968; Sieh, 1978). The offset reach is subparallel to the fault and the up- and downstream reaches are parallel.

As the Xanadu region hosts the only known example of a documented evenly spaced ridge system on Titan, we use the location of Mithrim Montes and the location of the rectilinear fluvial network for investigating the sensitivity of shear failure to crustal conditions applicable to Titan. Furthermore, because we know that there are liquid hydrocarbon seas and lakes present in Titan's north polar region, we also include a sensitivity analysis of stresses near Ligeia Mare (75º N, 270º W; location 3 in Figure 3.2), which is in a region classified as 'labyrinth' terrain (Lopes et al., 2020), more specifically 'valley labyrinth' terrain (Malaska et al. 2020). Labyrinth terrains are broadly characterized as highly eroded, elevated plateaus and remnant ridges. It is also hypothesized that Titan's radial labyrinth terrains specifically formed as cryomagmatic intrusions that rose within the ice shell, where they spread horizontally, uplifting the ice cover (Schurmeier et al., 2018; Malaska et al., 2020). The presence of stable liquids on the surface implies that fluids are present in the subsurface as well (Hayes et al., 2008; Mousis et al., 2014; Horvath et al., 2016; Hayes et al., 2018; Turtle et al., 2018; Faulk et al., 2020), as is the case on Earth. Strike-slip faulting can enable the exchange of surface and subsurface materials and possibly form pathways for subsurface liquids to rise to the surface. Using these three example regions (Mithrim Montes, a rectilinear fluvial network, and a labyrinth terrain near Ligeia Mare), we explore diurnal tidal stress variations on Titan as a function of orbital position and fault structure orientation and employ a Coulomb failure stress model to investigate the feasibility of tidally-induced shear failure.

3.3 Tidal stress mechanics and modeling

Stresses occurring from time-variable tidal deformation have been investigated by many previous studies as an explanation for the pattern of observed ridges and lineaments on the surfaces of icy satellites (e.g., Helfenstein and Parmentier, 1985; Greenberg et al., 1998; Hoppa et al., 1999; Kattenhorn, 2002; Schenk et al., 2008; Smith-Konter and Pappalardo, 2008, Cameron et al., 2019; 2020). As a moon orbits its parent planet, variations in gravitational tidal forces act to deform the satellite's surface (e.g., Ojakangas and Stevenson, 1989; Greenberg et al., 1998). Titan takes 15 Earth days, 22 hours to complete an orbit around Saturn and is tidally locked in synchronous rotation with the planet (Seidelmann et al., 2007). This behavior is common for moons as the large torques exerted by the parent planet eventually force the satellite to

progress into a synchronous configuration (Melosh, 1977; Helfenstein and Parmentier, 1980; Murray and Dermott, 1999). During the satellite's orbit, radial and librational tides combine to create a pattern of diurnal stresses that sweep across the surface. Satellites experience a tidal bulge due to the difference in gravitational attraction between the hemispheres facing toward and away from the planet, and if the orbit is elliptical rather than circular, this bulge will vary in magnitude and position (Murray and Dermott, 1999; Wahr et al., 2009). On Europa, Enceladus, and Ganymede, for example, inferred strike-slip structures have been attributed to tidal stresses (i.e., Greenberg et al., 1998; Nimmo et al., 2007; Martin, 2016). Diurnal tidal stress initiation of strike-slip faults on Ganymede however, is likely limited to a past period of higher eccentricity (e ~ 0.05; Cameron et al., 2020). Titan's comparable size and present-day eccentricity (e = 0.0288) suggest that the effect of tides on Titan could be a major source of stress and potentially shear failure.

To investigate diurnal tidal stresses on Titan, we use numerical code SatStress (http://code.google.com/p/satstress), which computes stresses based on tidal potential theory (Wahr et al., 2009; Patthoff et al., 2016), allowing for both elastic and layered Maxwell viscoelastic treatments of the lithosphere. SatStress computes both raw ($\sigma_{\phi\phi}$, $\sigma_{\theta\theta}$, $\sigma_{\theta\phi}$ or longitudinal, latitudinal and shear tractions, respectively) and diagonalized (principal) stress tensor components as a function of geographic location and orbital position (mean anomaly, m, with m = 0 defined as periapse) of the satellite. The methodology adopted here for computing tidal stresses has been demonstrated for a range of icy satellites (i.e. Smith-Konter and Pappalardo, 2008; Olgin et al., 2010; Cameron et al., 2019; 2020). Table 3.1 describes the model parameters adopted in this study. SatStress assumes a 4-layer satellite body (upper ice layer, lower ice layer, liquid ocean layer, and core). Because of the absence of robust data constraints other than mean density, polar moment-of-inertia factor, obliquity, and tidal potential Love number k_2 as derived from Cassini observations, the internal structure of Titan is not fully understood. Several candidate internal composition models have been proposed for Titan, depicting a wide range of structures with a relatively dense rock core (Nimmo and Bills, 2010; Néri et al., 2020), a low-density hydrated core (Fortes et al., 2012), or a partially differentiated interior comprised of a mixed rock/ice layer (Sohl et al., 2014; Néri et al., 2020). A comparison of published internal structure models and a demonstration of the sensitivity of resulting stress fields from internal structure assumptions is provided in the Appendix. In summary, we find that the surface stress field is not very sensitive to internal structure variations represented by these end-member models and varies by only a few kPa. Therefore, we adopt parameters consistent with those of Sohl et al. (2014) and calculate

degree-two Love numbers using the companion code available for SatStress, comparable to those of Sohl et al. (2003; 2014) and in agreement with or at the upper limit of error of other candidate models. In our model, the upper rigid ice layer is 110 km thick with a viscosity of 10^{20} Pa s, underlain by a transitional layer of ductile ice extending 1 km with a viscosity of 10^{14} Pa s, as the viscosity near melting point can be assumed to be between 10^{13} and 10^{14} Pa s (Goldsby and Kohlstedt, 2001). However, the brittle upper layer might be considerably thinner if convection is occurring below. Beneath the ice layer, we assume a global liquid ocean of 178 km depth. The deep interior is assumed to be comprised of a mantle of high-pressure ice and a rocky core, with a combined radius of 2286 km and density of 2450 kg/m^3. As SatStress assumes a 4-layer (upper ice layer, lower ice layer, liquid ocean layer, and core) satellite body, the deep interior's high-pressure ice and silicate core layers are represented as a single constituent.

Titan's global diurnal tidal stress field as a function of mean anomaly (m), represented by maximum compressive principal stress (σ_1), is shown in Figure 3.5 (see also companion animation). For our models, we assume normal tidal tractions as positive when in compression and negative when in tension. Maximum global stress amplitudes (± ~25 kPa) are centered around the equatorial area, where tensile stresses peak at m = 90°-100° and m = 260°-270°, and compressive stresses peak around apoapse at m = 160°-200°. In the polar regions, maximum tensile stress values occur near apoapse (~ -19 kPa), while minimum tensile stresses occur near periapse (~ -2 kPa). In comparison, diurnal stresses on Titan are ~5 times larger than present-day stresses for similarly sized Ganymede (Cameron et al., 2019) because of Titan's higher eccentricity. Titan's diurnal stresses in the polar regions are roughly 3x smaller than those of Enceladus (Smith-Konter and Pappalardo, 2008; Martin, 2016) because of Enceladus' much smaller size and distance from Saturn.

Table 3.1 Titan physical, orbital and rheological parameters used for SatStress modeling.

Physical and Orbital Characteristics	
Radius (km)	2575
Orbit eccentricity	0.0288
Orbit semi-major axis (km)	1221870
Gravity (m/s^2)	1.352
Saturn mass (kg)	5.683×10^{26}

Viscoelastic Parameters		
Ice (Upper and Lower)		
	Upper ice	Lower ice
Density (kg/m^3)	951	1000
Poisson's ratio	0.33	0.30
Young's modulus (GPa)	9.31	9.31
Thickness (km)	110	1
Viscosity (Pa s)	10^{22}	10^{14}
Ocean		
Density (kg/m^3)	1070	
Poisson's ratio	0.50	
Young's modulus (GPa)	0	
Thickness (km)	178	
Viscosity (Pa s)	0	
Deep Interior (high-phase ice + silicates)		
Density (kg/m^3)	2450	
Poisson's ratio	0.30	
Young's modulus (GPa)	100	
Thickness (km)	2286	
Viscosity (Pa s)	$\sim 10^{25}$	

SatStress Parameters	
NSR Period (yrs)	Infinity
Elastic Love number h_2	1.31031
Elastic Love number k_2	0.41550
Elastic Love number l_2	0.31063

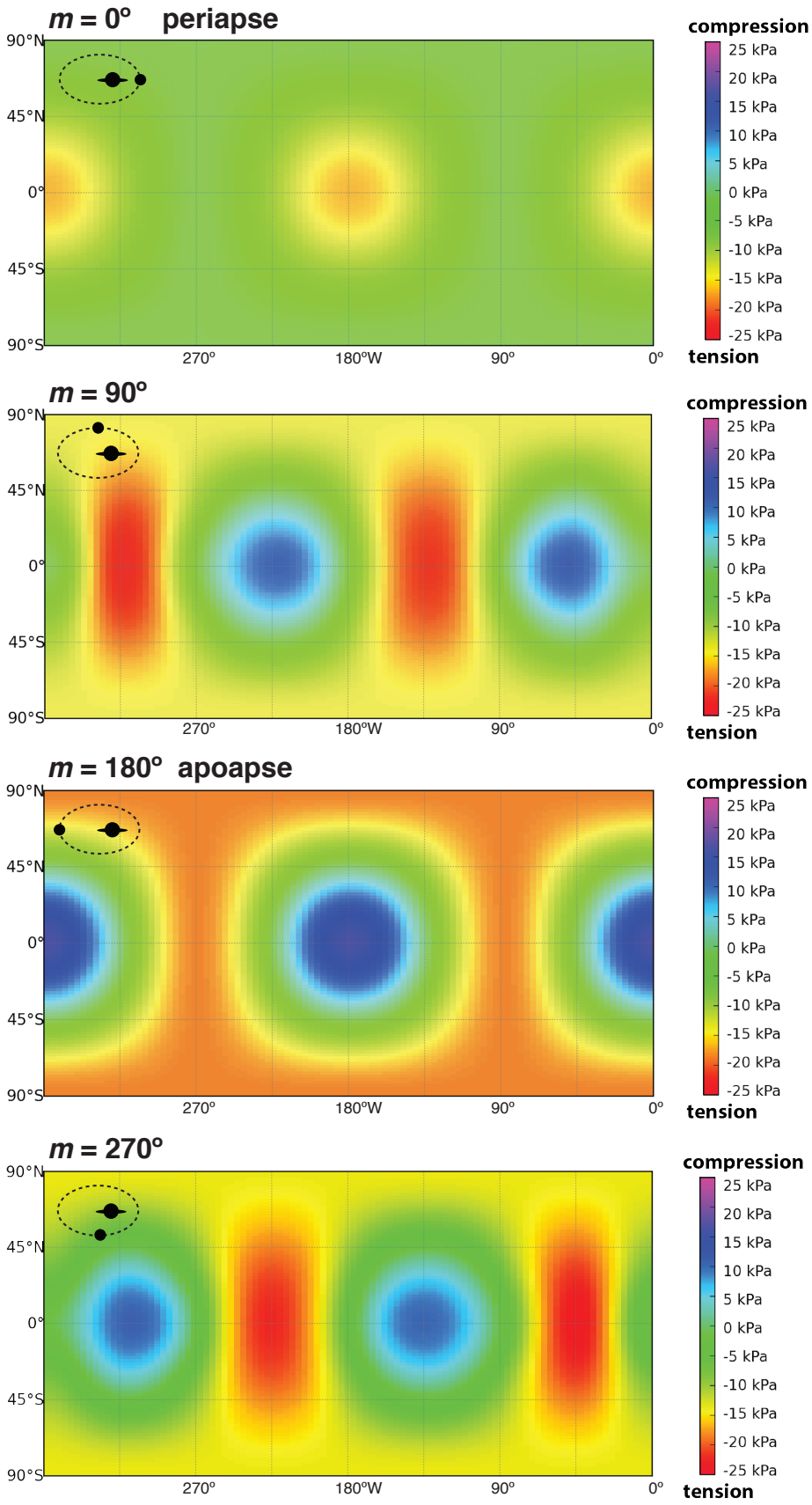
m = 0° periapse
m = 90°
m = 180° apoapse
m = 270°
90°N
45°N
0°
45°S
90°S
270°
180°W
90°
0°
compression
25 kPa
20 kPa
15 kPa
10 kPa
5 kPa
0 kPa
-5 kPa
-10 kPa
-15 kPa
-20 kPa
-25 kPa
tension

Figure 3.5. Maximum principal stress (σ_1) field of Titan in cylindrical equidistant projection assuming parameters provided in Table 3.1, at mean anomaly, *m* (orbital) positions 0º (periapse), 90º, 180º (apoapse), and 270º. A sketch of Titan's orbital position with respect to Saturn is also provided in the upper left corner of each panel. Negative (red) values indicate tensile stress, and positive (blue) values indicate compressive stress.

3.4 Tidally-induced Coulomb failure

3.4.1 Modeling Coulomb failure stress

To investigate the potential of shear failure due to variable diurnal tidal stresses, we conduct a sensitivity analysis of Titan's shear failure tendencies guided by Coulomb failure (Byerlee, 1978; Jaeger and Cook, 1979), which governs the formation of new fractures. The Coulomb failure criterion considers stresses that facilitate (tensile) and resist (compressive) shearing motions (i.e., the resolved normal and shear tidal tractions), simultaneously accounting for the coefficient of friction of ice, overburden, and pore fluid pressures. Following the methodology of previous studies (Hurford et al., 2007; Nimmo et al., 2007; Smith-Konter and Pappalardo, 2008; Cameron et al., 2019), we first resolve tidal stress tensor components derived from SatStress onto hypothetical fault plane segments of varying length and orientation, into normal (σ_n) and shear (τ_s) tractions:

$$\tau_S = \frac{1}{2}(\sigma_{\varphi\varphi} - \sigma_{\theta\theta})sin2\beta + \sigma_{\theta\varphi}cos2\beta$$
$$\sigma_n = \sigma_{\theta\theta}cos^2\beta + \sigma_{\varphi\varphi}sin^2\beta + \sigma_{\theta\varphi}sin2\beta \quad \text{(Eq. 1)}$$

where β is the segment's orientation, defined with respect to the latitudinal direction (β = 0° for a fault oriented due W, 90º for a fault due N) in Mercator projection. For each candidate fault segment (with presumed vertical dip), the resolved normal traction component acts perpendicular to each segment, while the resolved shear traction component acts parallel to each segment. Figure 3.6 illustrates the variation in both stress tensor components and resolved shear and normal tractions for an example lineament orientation (β = 20°) of Mithrim Montes. At this location, peak resolved normal and shear tractions approach 22 kPa and 6 kPa, respectively. Maximum tensile stress is predicted at *m* = 100º, while maximum compressive stress occurs at *m* = 280º. We note that in addition to this example case at Mithrim Montes, mapped feature traces with

measured orientations (in ArcGIS) were adopted, where possible, throughout this study; however, some feature orientations are estimations due to absence of clear, high-resolution imagery.

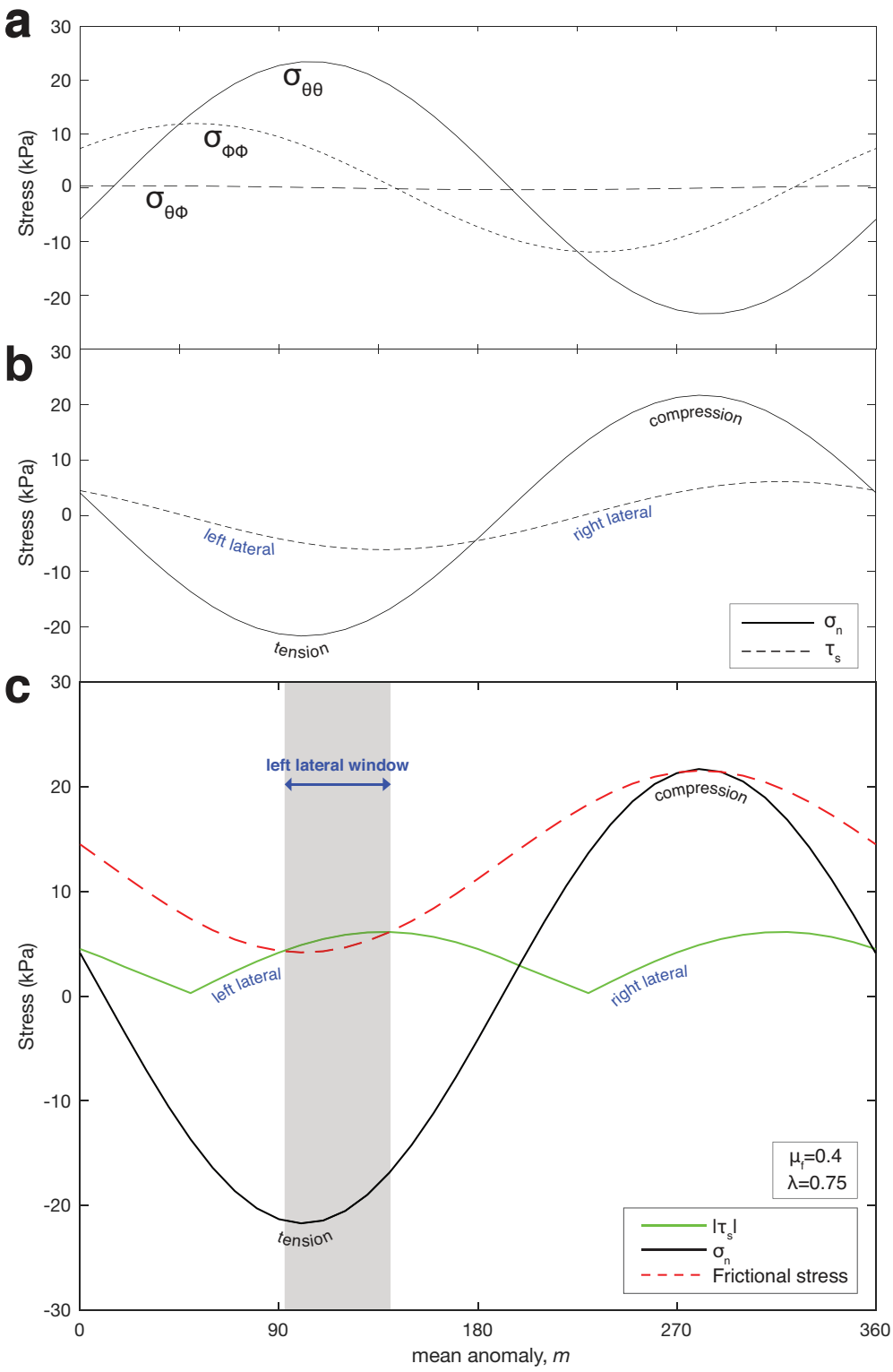

Figure 3.6. Tidal stresses at Mithrim Montes (2° S, 127° W). **a)** SatStress-derived diurnal stress tensor components as a function of mean anomaly, *m* (orbital position) at a location in the Mithrim Montes region, where $\sigma_{\theta\theta}$ is the latitudinal stress component, $\sigma_{\phi\phi}$ is the longitudinal stress component, and $\sigma_{\theta\phi}$ is the cross term. **b)** Resolved normal (σ_n, solid line) and shear (τ_s, dashed line) tractions for an assumed orientation of $\beta = 20°$, consistent with the average orientation of ridges at Mithrim Montes. **c)** Coulomb failure criterion for Mithrim Montes lineament average orientation ($\beta = 20°$), with resolved normal traction (σ_n) represented by the black line, resolved absolute tidal shear tractions ($|\tau_s|$) represented by the solid green line with the sense of shear stress labeled, and frictional stress (right side of Eq. 2) represented by the red dashed line. Shear failure will occur when the shear stress is greater than the frictional stress (gray shaded region). A coefficient of friction $\mu_f = 0.4$, pore fluid pressure ratio $\lambda = 0.75$, and an observational depth $z = 100$ m are assumed for this example case.

To evaluate shear failure feasibility, we calculate the Coulomb stress, τ_c, as

$$\tau_c = |\tau_s| - \mu_f (\sigma_n + \rho g z) \quad \text{(Eq. 2)}$$

where τ_s is the resolved shear stress acting on the initiated fault, σ_n is resolved normal stress, μ_f is the coefficient of friction, and $\rho g z$ is overburden pressure (where ρ is the material density, g is satellite gravity, and z is the observation depth along the fault plane). According to the Coulomb criterion, shear slip will occur when the resolved shear stress (τ_s) exceeds the frictional resistance [$\mu_f (\sigma_n + \rho g z)$] acting on the fault plane. The overburden stress is to be taken positive, while normal tidal tractions are assumed positive when in compression and negative when in tension. We also consider a conservative range of friction coefficients (μ_f = 0.3-0.5) consistent with laboratory studies (Schulson and Fortt, 2012; Schulson, 2016), as described in Section 4.2. Moreover, when failure conditions are met, the sign of the shear traction determines slip direction: positive for right-lateral and negative for left-lateral. Compressive tractions will lock a fault together and inhibit failure unless higher shear tractions act to overcome the failure criterion. Tensile tractions pull on a fault, reducing the contact between fault surfaces, and can promote failure if the acting shear traction is sufficiently large. Therefore, the Coulomb failure criterion is most easily met when tensile tractions are dominant. For tensile regimes, the overburden stress must be larger than the tensile traction, as the initiated fault would otherwise dilate. In the examples presented here, we

evaluate the depth sensitivity of Coulomb failure for fault zones at 0.1 km discretized depth observation planes.

Figure 3.6 c provides a demonstrative tidal stress scenario as a function of mean anomaly, *m* (orbital position) for the average lineament orientation (β = 20°) of Mithrim Montes with a coefficient of friction μ_f = 0.4. As Titan has liquids present on the surface, we incorporate the effects of a pore fluid pressure ratio (see Section 4.2), given that this can significantly reduce the shear strength of the crust. The frictional stress (right side of Eq. 2) mimics the pattern of the normal tidal stress curve as expected; in this particular example, frictional stress decreases as the shear stress increases, eventually exceeding the frictional resistance just past *m* = 90º. Here, the initiated fault is free to slip in a left-lateral sense, until the frictional stress is dominant again past *m* = 140º, after which stress conditions return it to a locked state.

It is important to recognize how Coulomb failure can vary as a function of fault segment orientation β, where β is defined relative to the latitudinal direction (β = 0° for a fault oriented due W, 90º for a fault due N); this angle can vary for each mapped segment from the overall fault zone orientation. To illustrate the dependency on fault orientation β, we construct diagrams of Coulomb failure as a function of fault trend and provide an example diagram for Mithrim Montes at *m* = 120º (Figure 3.7). For these diagrams, we use Eq. 1 to calculate the shear and normal tractions for a range of fault orientations (β = 0-360°) at 10º intervals. To illustrate the Coulomb criteria, we use Eq. 2 and adopt a binary color scheme to identify positive (free slip) and negative (locked fault) Coulomb stress regimes on circular diagrams, where the span of the wedge indicates the range of orientations of possible fault trends. The resulting Coulomb failure orientation diagram at *m* = 120º for Mithrim Montes shows the largest range of achievable fault orientations during any position in orbit that could produce strike-slip displacement (Figure 3.7a): left-lateral shear slip for fault orientations of β = 12-54º, and right-lateral shear slip for orientations of β = 124-164º). As depicted in this Coulomb failure diagram, the trend of the actual mapped lineaments of Mithrim Montes (Figure 3.7b) is within the range of possible fault orientations (β = 12º-54º) for a left-lateral slip in the corresponding quadrant of the failure diagram. In this range, Coulomb stress is positive and a fault would be free to slip. As there are no candidate strike-slip structures visible from the current data, these diagrams provide a visual guide to expected orientations of possible fault structures and plausible failure mechanisms.

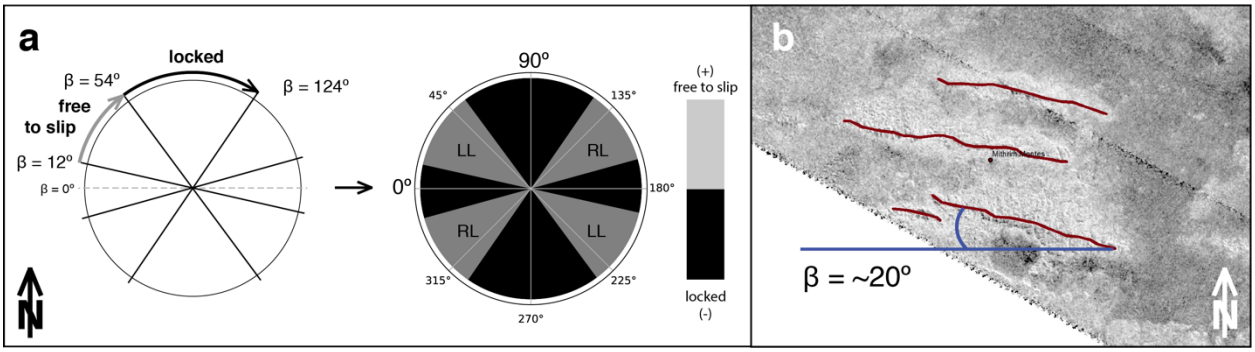

Figure 3.7. a) Coulomb failure orientation diagram for Mithrim Montes (2° S, 127° W) at m = 120° (orbital position), calculated with a coefficient of friction μ_f = 0.4 and pore fluid pressure ratio λ = 0.75 and evaluated at z = 100 m. Fault plane orientations with positive Coulomb stress are shaded in gray, indicating orientations that are free to slip. Fault plane orientations with negative Coulomb stress are shaded black, representing fault orientations that would be locked. This position of Titan in orbit around Saturn shows the largest range of possible fault orientations that could slip at this geographical location (β = 12-54° for left-lateral and β = 124-164° for right-lateral). **b)** Mithrim Montes (2° S, 127° W) lineaments mapped in ArcGIS. The trends of the mapped lineaments (β = ~20°) are in the range of possible fault orientations depicted in the Coulomb failure diagram for left-lateral slip.

3.4.2 Effects of pore fluid pressure and coefficient of friction

Because Titan has liquids present on the surface, the existence of a porous ice layer saturated with liquid hydrocarbons in the shallow subsurface has been inferred (Choukroun et al., 2010). This can provide a unique environment for zones of frictional weakness and shear heating that could potentially promote cryovolcanism. Models of Titan's shallow subsurface suggest that hydrocarbon-saturated porous ice is underlain by a clathrate-ice mix to depths of ~3-5 km (Lunine and Lorenz, 2009; Choukroun et al., 2010). It has also been suggested that the presence of clathrates within the crust can reduce the permeability by closing pore networks, increasing pore fluid pressures (Mousis and Schmitt, 2008), further reducing the shear strength of the crust. Given sufficiently high fluid pressures, fault blocks can slide over nearly horizontal surfaces, past one another or down significantly gentler slopes than otherwise possible (Hubbert and Rubey, 1959). In addition, ice crystals can form relatively quickly in this cold near-surface environment, trapping other constituents. Because the freezing process is slower at depth, the residual materials concentrated from freezing water ice crystals have time to drain downward, which is a process that has been observed on Earth on a small scale with salts in the formation of sea ice (Eicken,

1992). Moreover, the presence of near-surface liquid hydrocarbons and the crustal porosity of the ice can significantly reduce the resistance to shear failure of strike-slip faults in flexed areas under maximum diurnal tidal stresses.

To include hydrostatic pore pressure effects, the overburden stress can be scaled by 1- λ, where λ is the pore fluid pressure ratio (Hubbert and Rubey, 1959)

$$\lambda = \frac{\rho_f}{\rho_c} \quad \text{(Eq. 3)}$$

where ρ_f is the density of the fluid and ρ_c the density of the icy crust. Assuming ρ_f to be a bulk density of a mixed hydrocarbon fluid of 0.6 g/cm^3 (Lorenz, 2002) and a ρ_c of 0.9 g/cm^3 for the icy crust (Nimmo and Bills, 2010; Fortes, 2012; Sohl et al., 2014), the hydrostatic pore fluid pressure ratio for Titan could be λ = 0.67 (Liu et al., 2016 b). However, this ratio could be lower depending on the nature of the liquid present and its density. Conversely, ratios could also exceed this value (λ > 0.67) in fold belts where pore space is compressed and wherever permeability is restricted as a result of clathrates of methane and water within the crust (Mousis and Schmitt, 2008; Liu et al., 2016 b). For terrestrial fold-and-thrust belts, pore pressures may well exceed the hydrostatic pressure and the trapped fluid becomes overpressured (Hubbert and Rubey, 1959; Davis et al., 1983). Compaction or a possible permeability barrier such as a density disparity in the icy crust would also allow for higher pore fluid pressures. Incorporating the effect of the hydrostatic pore pressure is an important factor in studying current tectonics as well as the tectonic evolution of Titan. Here, we consider a range of hydrostatic pore fluid pressure ratios (λ = 0.67-0.9) to demonstrate the sensitivity to Coulomb failure.

Laboratory studies of the coefficient of friction μ_f as a function of ice temperature and sliding velocity is an area of active research. Previous studies of Coulomb failure and shear heating models on icy moons have adopted a coefficient of friction of μ_f = 0.1-0.2 (Nimmo et al., 2007; Smith-Konter and Pappalardo, 2008; Cameron et al., 2019; 2020; Hammond, 2020) as laboratory experiments suggest that μ_f for ice can range from ~ 0.15-0.75, depending on the pressure, temperature and sliding velocity (Beeman et al., 1988; Fortt and Schulson, 2007; Schulson and Fortt, 2012). For our analysis, we consider a conservative range of friction coefficients consistent with laboratory experiments at temperatures and pressures applicable to icy moons (Schulson and Fortt, 2012; Schulson, 2016). As the shear failure window expands when ice friction decreases, we investigate end-member cases (μ_f = 0.3) as well as high friction cases (μ_f = 0.5).

3.5 Results

3.5.1 Xanadu: Mithrim Montes

We evaluate Coulomb failure resulting from diurnal tidal stresses at Mithrim Montes in the Xanadu region, exploring whether the trend of the parallel ridges (β = ~20°) coincides with possible shear failure direction. To do so, we evaluate the potential for failure at 100 m depth and use intermediate values for coefficient of friction μ_f = 0.3-0.5 and pore fluid pressure ratios λ = 0.67-0.9 (Figure 3.8). For this example, left-lateral shear stress exceeds the frictional stress at orbital positions near m = 90°, suggesting that left-lateral slip is promoted here. This configuration of stresses provides a range of slip windows with durations that depend on both the frictional coefficient and the pore fluid pressure ratio. The largest range of possible fault orientations that could produce strike-slip displacement can be found at m ~120°. As depicted in the Coulomb failure diagram, the average trend of the mapped lineaments of Mithrim Montes is in the range of orientations (12°-53°) in the corresponding quadrant of the failure diagram.

These results also demonstrate the sensitivity of shear failure as a function of ice friction and pore fluid pressure ratio (Figure 3.8a). Coulomb failure is most easily achieved for a low coefficient of friction (μ_f = 0.3), spanning m = 82°-164°, accompanied by the largest range of fault orientations that could experience slip (wedges shaded in grey). From the sign of the dominant shear traction during the position in orbit, we can determine that the geographical location and orientation of Mithrim Montes could experience a left-lateral slip direction. For a coefficient of friction μ_f = 0.4, the Coulomb criterion is met at mean anomaly m ~90°-140° for the orientation of the lineaments with pore fluid pressure ratio λ = 0.75. As we test the width of the failure window with variable pore fluid pressure ratios of λ = 0.67-0.90 while retaining μ_f = 0.4 (Figure 3.8b), we predict no slip for λ = 0.67. For this more conservative value of pore fluid pressure ratio, a coefficient of friction of μ_f < 0.26 is needed for any slip to occur at a depth of 100 m.

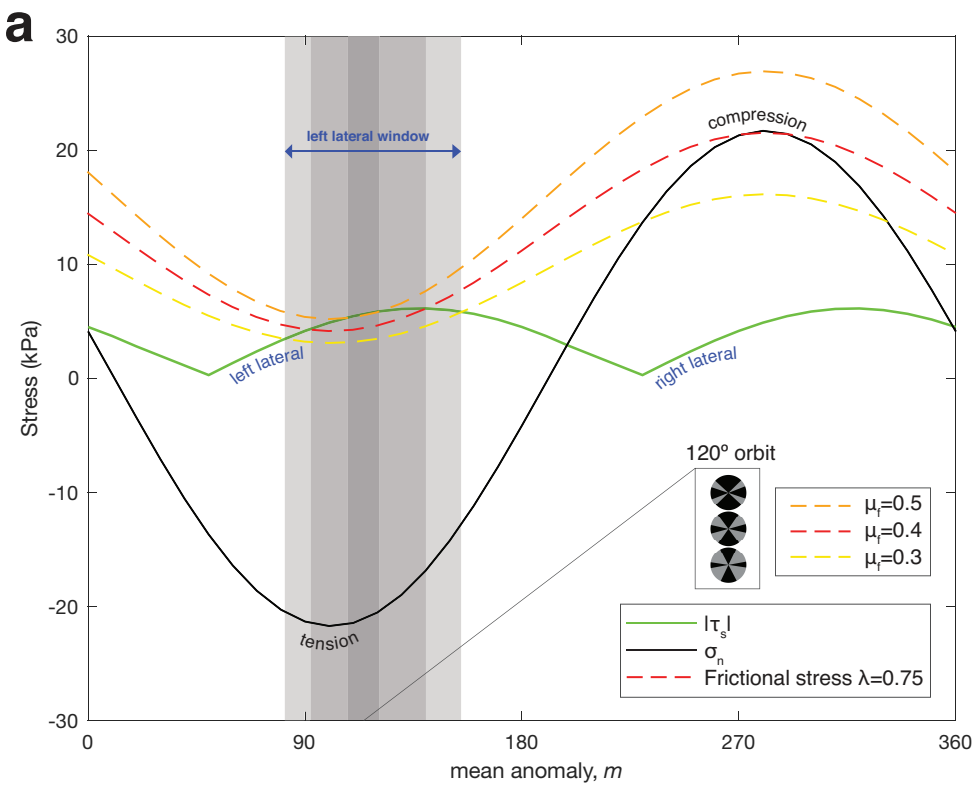
a
left lateral window
compression
left lateral
right lateral
tension
120° orbit
μf=0.5
μf=0.4
μf=0.3
|τs|
σn
Frictional stress λ=0.75
Stress (kPa)
mean anomaly, m
30
20
10
0
-10
-20
-30
0
90
180
270
360

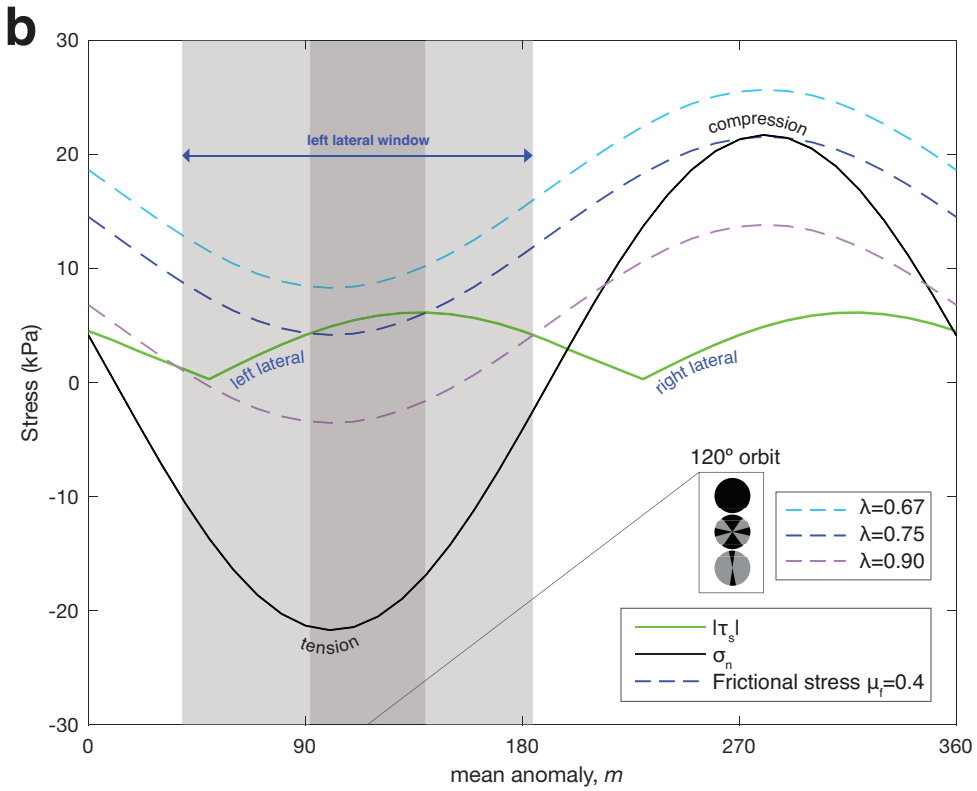
b
left lateral window
compression
left lateral
right lateral
tension
120° orbit
λ=0.67
λ=0.75
λ=0.90
|τs|
σn
Frictional stress μf=0.4
Stress (kPa)
mean anomaly, m
30
20
10
0
-10
-20
-30
0
90
180
270
360

Figure 3.8. Tidal stress and the Coulomb failure criterion as a function of orbital position past periapse (mean anomaly, *m*) for Mithrim Montes (orientation β = 20°). Gray shaded regions depict the sensitivity of possible failure windows to varying input parameters. Observational depth *z* = 100 m. **a)** Investigating the possible slip window with coefficients of frictions μ_f = 0.3-0.5 and fixed pore fluid pressure ratio λ = 0.75. Inset: Coulomb failure orientation diagrams for *m* = 120° and μ_f = 0.3-0.5 with positive Coulomb stress shaded in gray, indicating those vertical fault orientations that are free to slip. **b)** Modeling width of failure window with varying pore fluid pressure ratio λ = 0.67-0.90 while retaining μ_f = 0.4. Inset: Coulomb failure orientation diagrams for *m* = 120° and λ = 0.67-0.90, where gray areas are free to slip.

To better understand the spatial variations in shear, normal, and Coulomb stress at Mithrim Montes, we also constructed map view illustrations of the orbital dependency of these results with an example coefficient of friction μ_f = 0.4 and pore fluid pressure ratio λ = 0.75 (Figure 3.9). At *m* = 0°, little variation in the normal stress is predicted across the lineaments, while shear stresses are predominantly right-lateral with varying magnitude as function of β orientation. This configuration of stresses, however, is not sufficient to promote Coulomb failure at this orbital position; thus, slipping wedges are absent in the Coulomb failure orientation diagram. Alternatively, when approaching *m* = 90°, stresses increase in tension close to ~ -25 kPa, promoting left-lateral slip for several fault orientations. The largest range of possible initiated fault orientations that could produce strike-slip displacement can be found at *m* ~120° (see Figure 3.7). As depicted in this Coulomb failure diagram, the trends of the mapped lineaments of Mithrim Montes are in the range of possible fault orientations (β = 12°-53°) in the corresponding quadrant of the failure diagram. At *m* = 180°, stresses decrease to near 0 kPa, while remaining in a left-lateral sense, but with no failure possible. When approaching *m* = 270°, stresses increase to ~ 25 kPa in compression, clamping the terrain together, inhibiting any slip. According to the shear tractions, the governing slip-sense would be right-lateral in this orbital position.

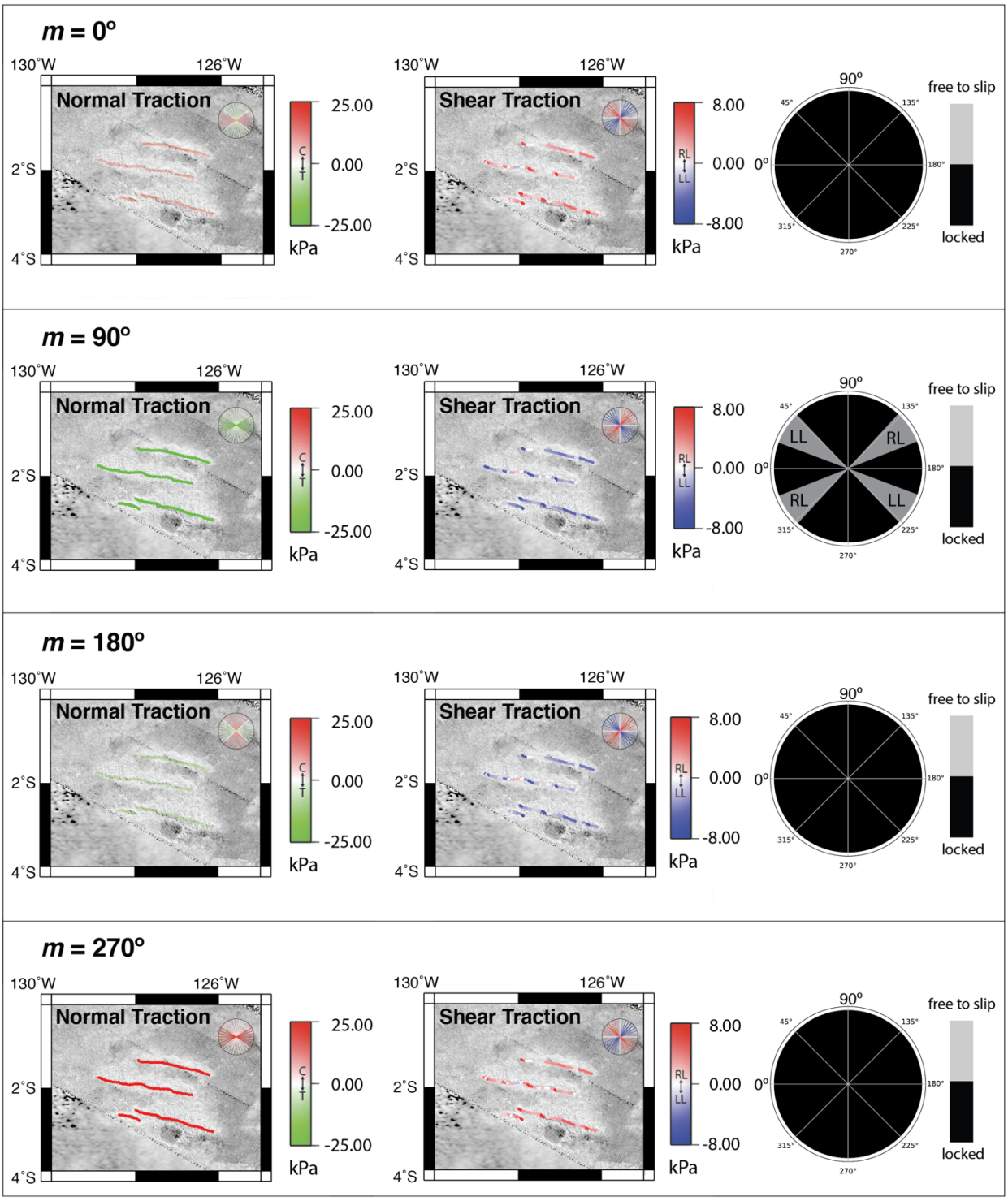

Figure 3.9. Resolved normal and shear tractions for mapped Mithrim Montes lineaments with map view representation of normal stress (C = compression, T = tension) and shear stress (RL = right-lateral, LL = left-lateral), as calculated at mean anomaly m = 0º, 90º 180º, and 270º. Corresponding Coulomb failure fault orientation diagrams for values of coefficient of friction μ_f = 0.4 and pore fluid pressure ratio λ = 0.75.

Possible fault orientations β that could experience slip are found within the gray wedges and correspond to the higher tensile stresses as found at m = 90º. There is no fault initiation at m = 0º, 180º and 270º (black diagrams) under the evaluated conditions.

3.5.2 West Xanadu: Rectilinear fluvial patterns

For the case of the rectilinear fluvial patterns farther west in the Xanadu region (10° S, 137° W), Coulomb stress along mapped orientations could also promote fault slip, assuming a coefficient of friction μ_f = 0.4 and pore fluid pressure ratio λ = 0.75 at an observational depth z = 100 m (Figure 3.10). The mapped lineaments with bends at close to 90º have an offset of roughly 10 km in a left-lateral slip direction with orientations (β = ~10-20°) that are in the range of possible orientations in the Coulomb failure diagrams. Because this location is not far from the previously evaluated Mithrim Montes lineaments, and given that the structures have a comparable average orientation, the results are very similar, as expected. The Coulomb failure model predicts a left-lateral slip sense, in agreement with the inferred left-lateral displacement mapped along the rectilinear fluvial features. At this location, shear displacement along a fault is encouraged when normal stress changes from compression to tension, which occurs during the window between m = 80º and 130º of the satellite's in orbit. For the average orientation of β = 15° specifically, failure is possible for m = 97º-113º. The position at m = 100º shows the largest range of possible fault orientations that could experience slip at this geographical location.

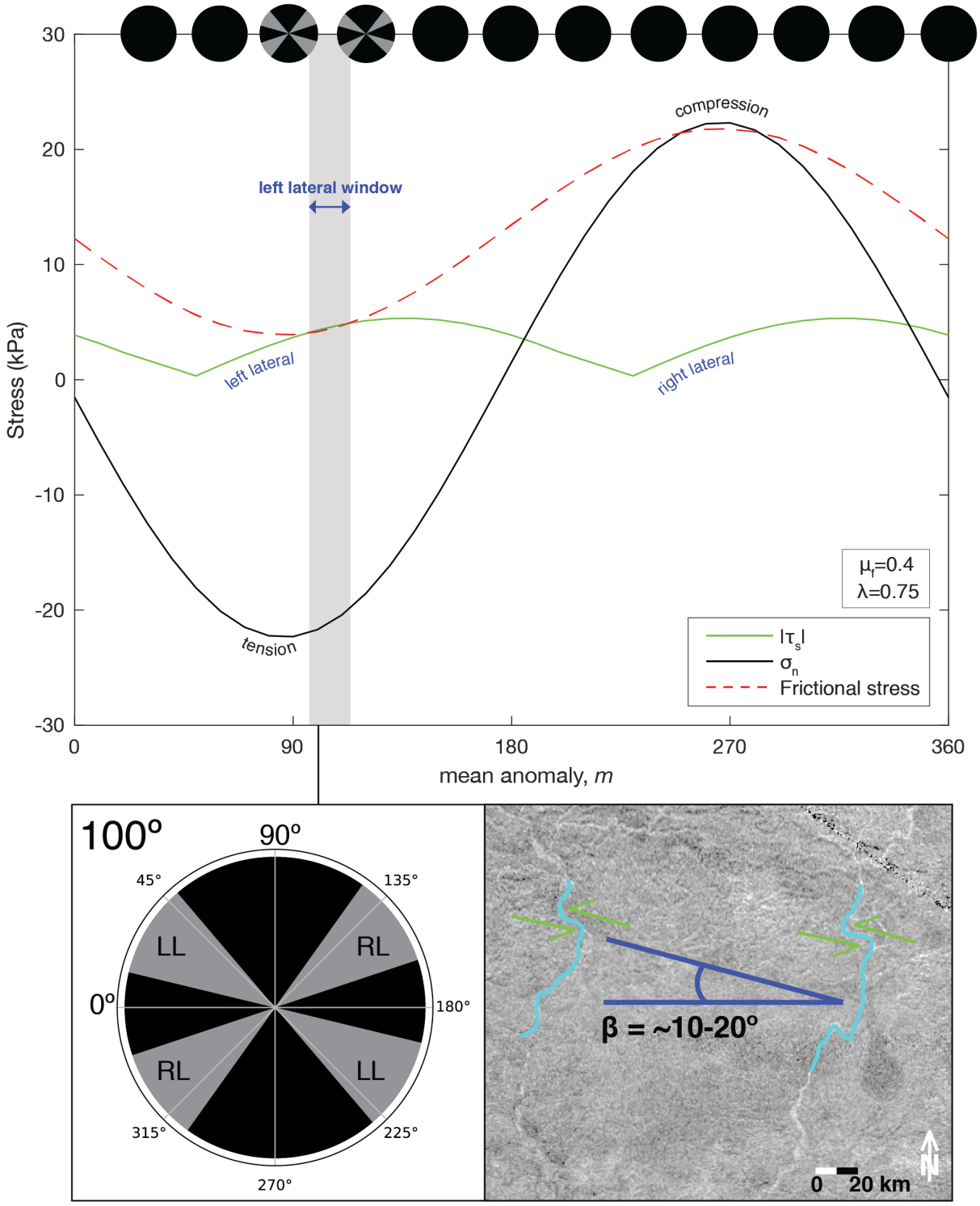

Figure 3.10. Coulomb failure criterion as a function of mean anomaly, *m* calculated for an average orientation β = 15° for the western Xanadu fluvial features (10° S, 137° W). We assume a coefficient of friction μ_f = 0.4 and pore fluid pressure ratio λ = 0.75, calculated at depth *z* = 100 m. Coulomb failure orientation diagrams for this location are shown along the top margin, evaluated every *m* = 30°. Possible

fault orientations β that could experience slip are estimated within the gray wedges, while black wedges depict locked orientations. Failure is possible between m = 80º and 130º for various fault orientations, and for β = 15° specifically between m = 97º-113º. (Bottom) The position at m = 100º shows the largest range of possible fault orientations that could experience slip at this geographical location. Insert of western Xanadu radar-bright fluvial features from Cassini SAR-HiSAR Global Mosaic 351m v1 with portions mapped. Arrows indicate the possible displacement and a potential fault feature. The offset is roughly 10 km for both structures in a left-lateral slip direction. The trends of the mapped rectilinear drainage pattern lineaments bend by nearly 90º (β = ~10-20°), and are in the range of possible fault orientations illustrated in the Coulomb failure diagrams, where calculated failure is also in a left-lateral sense.

3.5.3 North polar region

The polar regions experience the lowest compressional stresses throughout Titan's orbit and are therefore more favorable to Coulomb failure. Although we do not have any indication of apparent structure orientations from mapping, we can explore plausible scenarios from candidate structural orientations by inspecting Coulomb failure orientation diagrams. As an example, we consider candidate slip scenarios for a location near Ligeia Mare (75º N, 270º W, Figure 3.2), classified as 'labyrinth' terrain, which are highly eroded, elevated plateaus and remnant ridges (Lopes et al., 2020). We find that Coulomb failure in this north polar location (Figure 3.11) for hypothetical fault structures is possible during mean anomaly m = 70º-290º, assuming a coefficient of friction μ_f = 0.4 and a pore fluid pressure ratio λ = 0.75. For a given E-W oriented structure (β = 0°; Figure 3.11a), shear failure is promoted during mean anomaly m = 86º-151º and m = 119º-273º, where resolved shear and tensile stresses peak at 13.4 kPa and -18.75 kPa, respectively. Alternatively, for a NW-SE oriented structure (β = 45°; Figure 3.11b), shear failure is promoted during mean anomaly m = 173º-231º, where near-peak tensile and left-lateral shear stresses combine. Finally, for a N-S oriented structure (β = 90°; Figure 3.11c), failure is promoted during mean anomaly m = 71º-102º and m = 258º-289º. Depending on the magnitudes of stress and fault orientation, failure is promoted in both right- and left-lateral senses of slip for this example set of north polar structures. Given that sufficient data for Titan do not yet exist to constrain candidate slip models, we do not speculate on slip mechanisms in this study; however, such complications have been noted for other icy worlds (i.e., Smith-Konter and Pappalardo, 2008; Rhoden et al., 2012). Moreover, we recognize that identifying or diligently mapping features at Titan's high latitudes is currently not possible due to data and limitations in topographical

contrast. Increased coverage from a future mission may allow us to better understand the deformation mechanisms and the role fluids play in the north polar region where large liquid methane/ethane lakes are located.

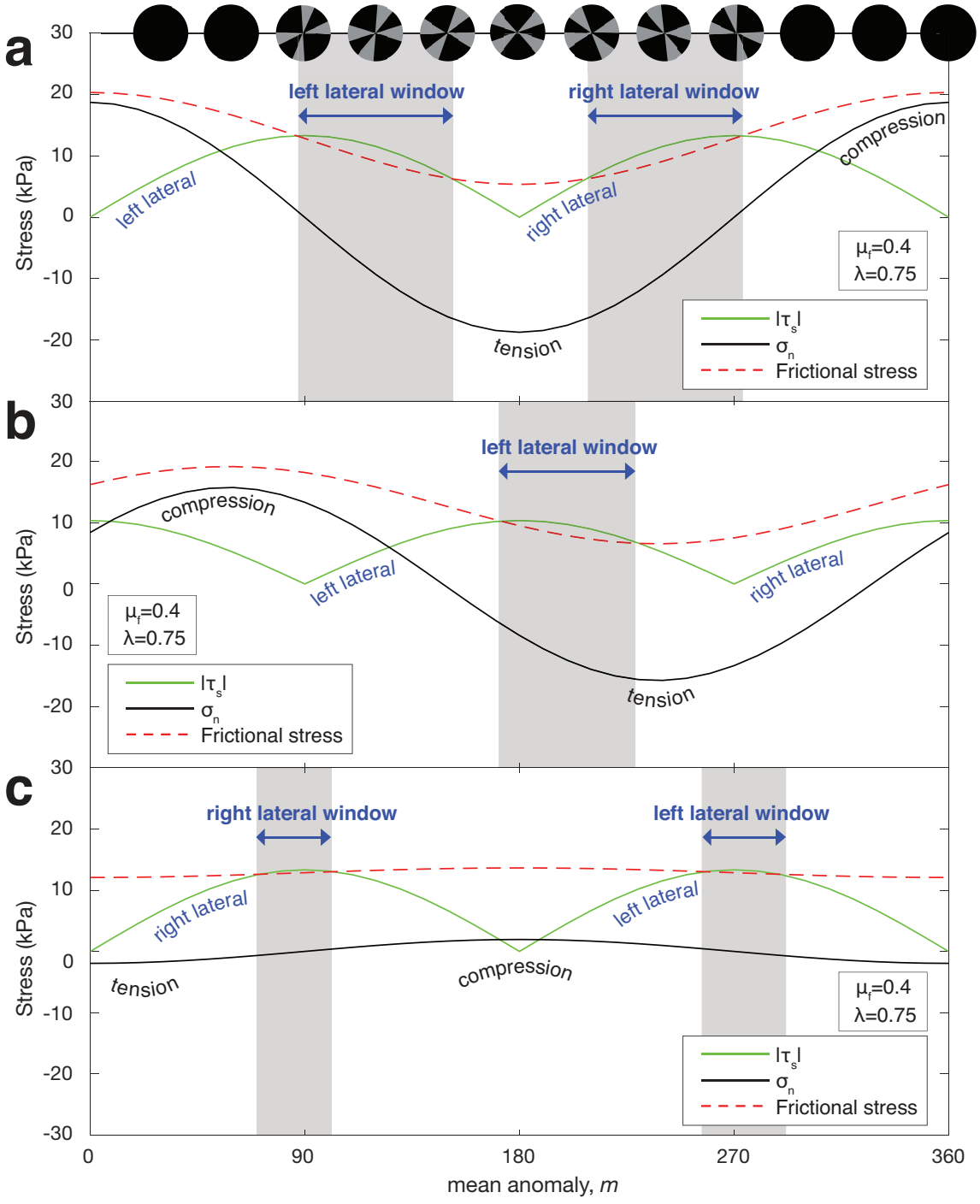

Figure 3.11. Coulomb failure criterion as a function of mean anomaly, estimated for a north polar region near Ligeia Mare (75° N, 270° W) for a range of hypothetical structures of orientation **a)** β = 0°, **b)** 45°, and **c)** 90° Coulomb failure orientation diagrams are provided at every *m* = 30° position, where gray shaded

wedges depict possible failure windows for a coefficient of friction $\mu_f = 0.4$ and pore fluid pressure ratio $\lambda = 0.75$ at an observational depth $z = 100$ m. Possible fault orientations β that could experience slip are within the gray areas and black areas depict locked orientations.

3.5.4 Global Coulomb failure

Combining both a spatial (geographic location) and temporal (orbital position) representation of Coulomb failure resulting from diurnal tidal stresses, we next explore shear failure conditions as a function of structure orientation spanning Titan's global stress field. Maintaining consistency with results described above, Coulomb failure orientation diagrams are calculated with a coefficient of friction $\mu_f = 0.4$ and a pore fluid pressure ratio $\lambda = 0.75$ at an observation depth of $z = 100$ m. Here, we demonstrate that Coulomb failure under these assumed conditions could be possible at shallow depths initiating a wide range of fault orientations and geographic locations on Titan (Figure 3.12). At periapse ($m = 0^o$), little variation and low values of normal stresses are observed, so slipping wedges are absent globally. However, when approaching $m = 90^o$, tensional stresses increase, allowing for slip conditions along several candidate fault orientations, especially near the polar regions. At apoapse ($m = 180^o$), favorable tensional stress regimes emerge near the equator, allowing more regions to experience failure. At $m = 270^o$, tensional and compressive stresses are similar to those at $m = 90^o$, although shifted eastward in geographic position, as is apparent in the shifted pattern of the failure diagrams.

A quantitative summation of the failure activity as a function of latitude is provided along the right margin of each panel in Figure 3.12, where each summary diagram demonstrates all possible structure orientations that could experience slip (per 15º latitude spatial window) at the given mean anomaly positions. These results show that Coulomb failure is more favorable in the polar regions at each sampled orbital position, because compressional stresses there are lowest throughout orbit. Alternatively, the mid-latitudes experience limited failure during the orbit as changing compressive and tensional stresses sweep across the surface of Titan. Coulomb failure is highly sensitive to compressive stresses in combination with low shear stress magnitudes, as is evident by the limited failure in the equatorial region, where the largest compressive stresses occur.

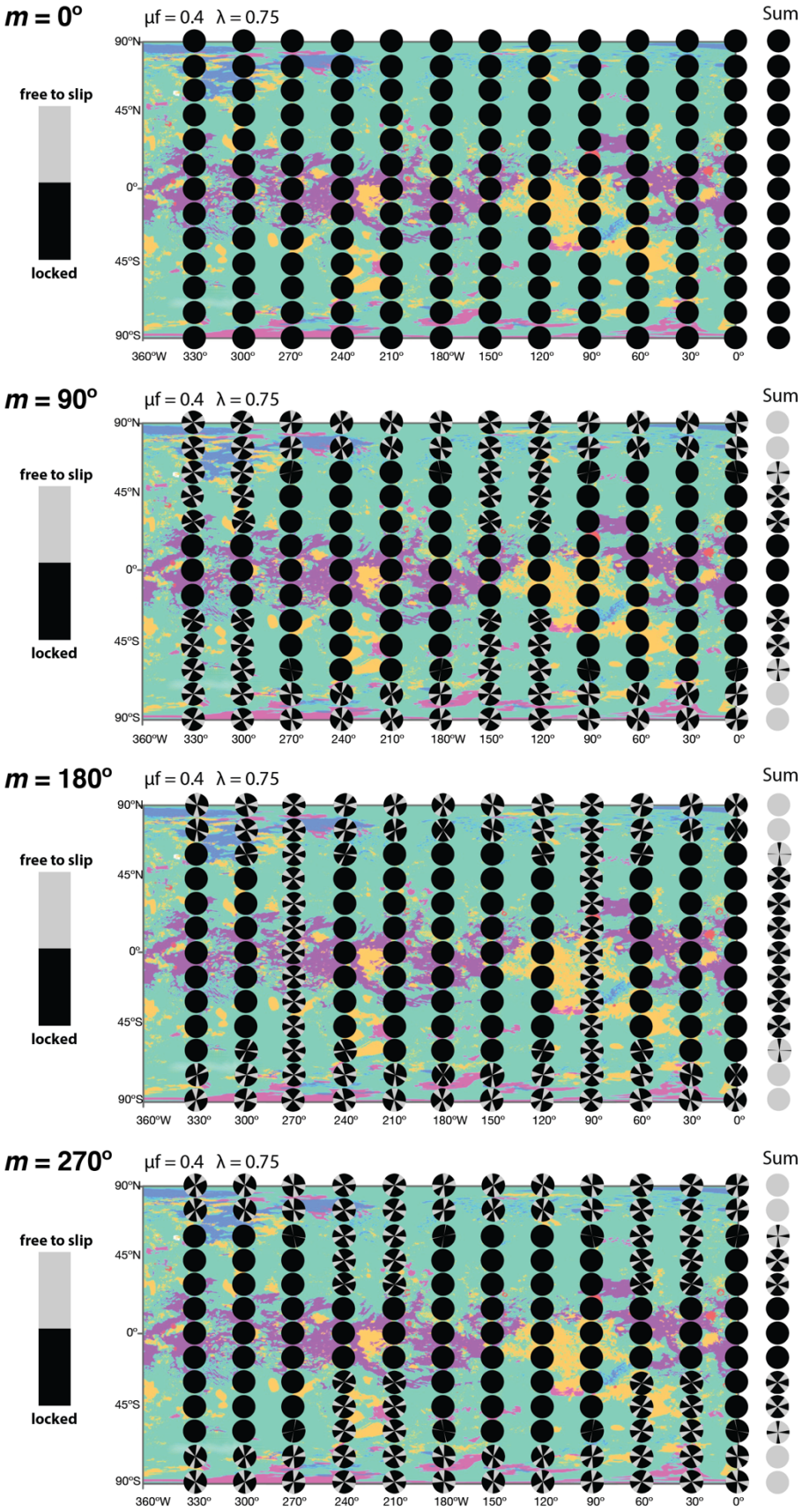
m = 0°
μf = 0.4 λ = 0.75
Sum
free to slip
locked
90°N
45°N
0°
45°S
90°S
360°W 330° 300° 270° 240° 210° 180°W 150° 120° 90° 60° 30° 0°
m = 90°
μf = 0.4 λ = 0.75
Sum
free to slip
locked
90°N
45°N
0°
45°S
90°S
360°W 330° 300° 270° 240° 210° 180°W 150° 120° 90° 60° 30° 0°
m = 180°
μf = 0.4 λ = 0.75
Sum
free to slip
locked
90°N
45°N
0°
45°S
90°S
360°W 330° 300° 270° 240° 210° 180°W 150° 120° 90° 60° 30° 0°
m = 270°
μf = 0.4 λ = 0.75
Sum
free to slip
locked
90°N
45°N
0°
45°S
90°S
360°W 330° 300° 270° 240° 210° 180°W 150° 120° 90° 60° 30° 0°

Figure 3.12. Coulomb failure orientation diagrams for m = 0º, 90º, 180º and 270º positions assuming a coefficient of friction μ_f = 0.4 and pore fluid pressure ratio λ = 0.75. These results overlie a global geomorphologic map of Titan (Lopes et al., 2020) for geologic context. Note regions of limited slip corresponding to high compressive stresses (see Figure 3.5). Diagrams are for every 15º latitude and every 30º longitude. Summary diagrams at right indicate all possible structural orientations that could experience slip, provided for every 15º latitude.

3.6 Discussion

Our Coulomb stress analysis of candidate strike-slip structures on Titan suggests that shear failure is possible under moderate diurnal tidal stresses subject to pore fluid pressures of a hydrologically active system. The results indicate that the crustal porosity of the ice and the presence of near-surface liquids can significantly reduce the resistance of faults subjected to diurnal tidal stresses. Optimal combinations of normal and shear tractions allow for slip on structures where the Coulomb criterion is met. However, many questions remain regarding whether and how the identified morphological regions are linked to Titan's global stress field and if present-day diurnal stresses play a major role in shaping the morphology observed today. Titan's surface terrain has clearly been subject to modification via aeolian and hydrological processes, but major topographic variations and pervasive common structural orientations that span large regions give rise to the hypothesis that there may be global stress contributions. Modeling global tidal stresses also improves our understanding of the formation of faults on Titan and the dependence of their orientation on resolved shear and normal tidal stresses.

3.6.1 Terrain assessments

Because of limitations in observational data, we restricted our localized analysis to obvious structures on Titan such as the ridges of Mithrim Montes ('hummocky' terrain), a rectilinear fluvial network in the Xanadu region, and a location in 'labyrinth' terrain near the north polar lakes. Around 14% of Titan's surface is classified as 'hummocky' (hilly or mountainous), while 1.5% is 'labyrinth' terrain, with valleys inferred to have been carved by rain and erosion (Lopes et al., 2020). Labyrinth terrains, in particular, are described by Lopes et al. (2020) and Malaska et al. (2020) as highly eroded, elevated plateaus and remnant ridges with an accumulation of organic-rich sediments. Hummocky and labyrinth terrains are also the oldest on Titan; therefore, they are of particular interest in communicating the most about the tectonic development of this moon.

In the areas examined within the Xanadu region near the equator, limited opportunities for Coulomb failure may exist (Figures 3.8 - 3.10). The ridges of Mithrim Montes have been interpreted as an exposure of crustal materials with a higher abundance of water-ice materials than other areas (Lopes et al., 2020). In general, ridges are inferred to be concentrated near the equator rather than the poles, which implies that this location was favored during ridge formation and/or preservation (Liu et al., 2016 a) and may have developed as a result of a common process or concentrated stress field. Previous studies propose that the ridges of Mithrim Montes are tectonic in origin, possibly fold-and-thrust belts formed by horizontal shortening (Mitri et al., 2010; Liu et al., 2016 a). On Earth, thrust zones can trend nearly parallel to strike-slip faults, as for example in California (Zoback et al., 1987), in the Tibetan plateau (Tapponnier et al., 2001; Taylor et al., 2003) or in the even more complex rotated region of the Bakharden-Quchan fault system in Iran (Hollingsworth et al., 2006). Unfortunately, we lack high-resolution observational data for Titan that could provide clear indications of offset or other strike-slip fault indicators to confirm the significance of shear failure in this region. However, given the agreement of structure orientation inferred at Mithrim Montes with the optimal Coulomb failure orientations estimated by our Titan stress model, future opportunities for finding indicators of shear failure on Titan may be greatest here.

The distribution of rectilinear and rectangular fluvial networks farther west of Mithrim Montes implies that faulting and fracturing may be an important tectonic mechanism and responsible for resurfacing of the lightly cratered surface on Titan (Black et al., 2012; Burr et al., 2013). Previous modeling work suggests that long-term cooling would lead to contractional tectonism on Titan, which may have formed the mountains of the 'hummocky' terrain with related general orientation (Mitri et al., 2010; Beuthe, 2010; Cook-Hallett et al., 2015). Nevertheless, extensional tectonism seems to be widespread on many other icy satellites (e.g., Pappalardo et al., 2004; Patterson et al., 2010), and fluvial network analyses show that distributed extensional tectonism is the most likely explanation for the observed fluvial network patterns (Burr et al., 2013; Matteoni et al., 2020). These fluvial features are located in regions of the highest tensile stress during orbit (Figure 3.5), which can explain the inferred extensional tectonism in this region (Matteoni et al., 2020). Offset drainage across a strike-slip fault forms well-defined right-angle bends at the intersection of the fault, consistent with the fluvial channel as observed at the rectilinear fluvial location analyzed in this study (Figure 3.4). However, other sources inducing similar directional favoritism are also possible: the geologic fabric, tilted bedding, or a frozen linear dune field might be capable of

comparably influencing the drainage of these fluvial networks. The inferred fault structures and offsets lack topographic expression, impeding a clear interpretation of these structures.

In the north polar region, we find that there is a high likelihood for strike-slip faulting, but no clearly defined fault-like structures have been identified in this area in previous mapping studies (Lopes et al., 2020). Labyrinth terrains are stratigraphically old and have been reworked by aeolian transport, phase changes and fluvial erosion (Malaska et al., 2020). Strike-slip faulting could have assisted these processes and shape the appearance of these terrains. If some labyrinth terrains formed as cryomagmatic intrusions rising from depth within the ice shell, spreading horizontally and uplifting the overlying ice (Schurmeier et al., 2018; Malaska et al., 2020), then strike-slip faulting in the shallow crust could have supported the exchange of subsurface and surface materials, and subsequently the migration of organic-rich sediments.

We also note the likelihood that Titan's seasonal cycle, which is on the same time-scale as Saturn's (Dougherty et al., 2009) and produces precipitation of methane that facilitates erosion, complicates studies of the tectonic evolution of Titan. Analogous to Earth (Chen et al., 2019), many regions on Titan likely record spatial variability in climate rather than tectonics. The observed pebbles (10-15 cm in size) at the Huygens landing site close to the equator (10.6ºS, 192.3ºW) are a testament that locally mapped structures may not be representative of large-scale tectonic processes; the rounded shape of the pebbles is indicative of fluid action. This indicates that seasonal changes in precipitation have influenced the appearance of regions well beyond the latitudes where liquids have been observed on the surface (Burr et al., 2009; Moore and Howard, 2010; MacKenzie et al., 2014; Hofgartner et al., 2020). In addition, given the properties of ice, precipitation can erase the cratering record (Neish et al., 2013; Neish and Lorenz, 2014; Neish et al., 2016; Werynski et al., 2019) and cause landscapes to appear very different from their most recent geologic alteration.

3.6.2 Global Coulomb failure assessment

From our global Coulomb failure analysis, predominant resolved normal and shear stress regimes are expected in the polar regions, where Coulomb failure opportunities for strike-slip faulting are abundant. Near the equator, large compressive and low shear stress regimes limit the possibility for failure. However, longitudinal zones of high tensile stresses along the equator can allow for Coulomb failure, given an optimal structure orientation. Near the equator, the predominantly favored fault orientations for Coulomb failure are close to E-W rather than N-S, which is in agreement with the pattern of previously mapped ridge terrain orientations (Cook-

Hallett et al., 2015; Liu et al., 2016 b; Lopes et al., 2020). These favored fault trends in areas closer to the equator also display only one direction of possible slip, whereas likely fault orientations in the polar regions have the possibility for displacement in both a left- and right-lateral sense during orbit, which may limit the extent of observable strike-slip indicators and likely prevent the occurrence of large offsets. From our global modeling, we conclude that strike-slip displacement on Titan: 1) is most likely to occur around the equatorial regions and low latitudes, where optimally oriented faults are more likely to exhibit a preferred sense of slip; and 2) may have limited expressions of shear in the polar regions, confined to optimally oriented faults with a preferred sense of slip. In general, ideal conditions for tidally driven fault failure exist mostly near apoapse (m = 140º-220º), during which favorably oriented faults near the equatorial region could experience slip, as well as in the polar areas.

3.6.3 Role of pore fluid pressure

Our results also demonstrate that opportunities for slip are much greater with increasing pore fluid pressure ratio values. For a conservative pore fluid pressure ratio $\lambda = 0.67$, the coefficient of friction would have to be $\mu_f \leq 0.25$ to achieve failure at Mithrim Montes and $\mu_f \leq 0.35$ for the north polar region. When extending our calculations beyond the observational depth of z = 100 m, as applied in the models presented here, we have determined that failure could not extend farther than ~120 m for a coefficient of friction $\mu_f = 0.4$ and pore fluid pressure ratio $\lambda = 0.75$ in any of the examined locations. However, if the highest modeled pore fluid pressure ratio $\lambda = 0.9$ and the lowest coefficient of friction $\mu_f = 0.3$ are combined, failure can occur up to a depth of ~375 m. Previous studies of Coulomb failure and shear heating models on icy moons have adopted a coefficient of friction of μ_f = 0.1-0.2 (Nimmo et al., 2007; Smith-Konter and Pappalardo, 2008; Cameron et al., 2019; 2020) as laboratory experiments suggest that μ_f for ice can range from ~ 0.15-0.75, depending on the pressure, temperature and sliding velocity (Beeman et al., 1988; Schulson and Fortt, 2012). These prior studies suggest that in order for shear failure to occur, low frictional coefficients are necessary. Here, our study shows that failure can be achieved on Titan with values of $\mu_f = 0.3$-0.5, consistent with more recent laboratory analysis for faults on icy moons (Schulson, 2016), if sufficient pore fluid pressures are considered.

Furthermore, potential pore fluid pressure ratios below Titan's fold belts may exceed the hydrostatic pressure and reach even higher values of λ (Liu, 2016). Given that hydrocarbon liquids are likely present in the shallow subsurface of Titan's icy crust (2-3 km; Lunine and Lorenz, 2009;

Choukroun et al., 2010), any crustal deformation need not include deformation of the entire thickness of the icy crust. In addition, the possible presence of clathrates of hydrocarbons and water within the crust is expected to reduce the permeability by closing pore space networks connecting to the surface. This decrease in permeability would result in an increased pore fluid pressure, reducing the shear strength of Titan's crust. Our modeling shows that with higher pore fluid pressure ratios, the window for the possibility of strike-slip faulting increases significantly (Figure 3.8b).

Several issues related to the properties of ice and clathrate hydrates also need to be considered for future work. First, the role of grain boundary processes in methane hydrates needs to be investigated further: deformation by grain-size sensitive (GSS) processes can be activated in laboratory ice more readily than in other oxides (Goldsby and Kohlstedt, 2001). Should this behavior extend to hydrates, the presence of small amounts of water has the ability to facilitate deformation. Second, if a polycrystalline methane hydrate is solid, it is possibly >20x stronger than water ice under the same conditions (Durham, 2003). Third, the density contrast of the ice crust and liquid will influence the pore fluid pressure ratio. A pure methane liquid, for example, would reduce the density parameter ρ_f used in this study from the bulk value of 0.6 g/cm^3 of a mixed hydrocarbon fluid (Lorenz, 2002) to 0.45 g/cm^3, resulting in a lower hydrostatic pore fluid pressure ratio. In addition, the crust may have pore spaces filled with gas bubbles, which could result in a lower density of the ice shell than studied here (Yin et al., 2016). More thorough compositional analysis of the icy crust and liquids present is needed to better constrain these parameters.

3.7 Conclusions

In this study, we investigate the conditions for tidally driven Coulomb failure on Titan. We explore the sensitivity of the coefficient of friction of ice (μ_f = 0.3-0.5; Schulson, 2016) and hydrostatic pore fluid pressure ratios (λ = 0.67-0.9; Liu et al., 2016 b). Our Coulomb failure modeling results for initiating shallow fault slip using a coefficient of friction μ_f = 0.4 suggest that shear failure is possible under tidal stresses subject to intermediate (λ = 0.75) pore fluid pressures in a hydrologically active system at several locations on Titan. This indicates that the presence of near-surface liquids can significantly reduce the resistance to Coulomb failure in tidally flexed areas under maximum diurnal stresses. Increased tensile and shear tractions permit slip windows

where the Coulomb criterion is met. Low friction, as well as increased pore fluid pressures, can permit failure during significant portions of Titan's orbit, especially in the polar regions.

Although clear interpretations of modes of tectonism on Titan are hampered by a paucity of suitable remote sensing data, these exploratory models of Coulomb failure allow us to explore the conditions for possible shear failure on Titan, in preparation for future remote sensing missions. These results will also be important for understanding the evolution of Titan's surface and how these faulting behaviors relate to processes on other icy satellites. Data from a future mission would help refine these calculations and advance our understanding of how pore fluids can influence tectonics and fault behavior on icy moons.

Acknowledgements

We thank Emily Costello for the python integration as well as An Yin and an anonymous reviewer for their helpful comments to improve this manuscript. A portion of the work by M. E. Cameron and R.T. Pappalardo was carried out at the Jet Propulsion Laboratory, California Institute of Technology, under a contract with the National Aeronautics and Space Administration (NASA). This is SOEST contribution #11394.

Appendix

Various internal composition models have been proposed for Titan. Given the limits from Cassini observations, it is difficult to distinguish among these internal structure models until further data are acquired. We analyzed the sensitivity of our calculations for a range of published structures with a relatively dense rock core (Nimmo and Bills, 2010; Néri et al., 2020), a low-density hydrated core (Fortes et al., 2012), or a partially differentiated interior comprised of a mixed rock/ice layer (Sohl et al., 2014; Néri et al., 2020), varying ice layer thicknesses (76 - 111 km) and ocean depths (178 - 394 km).

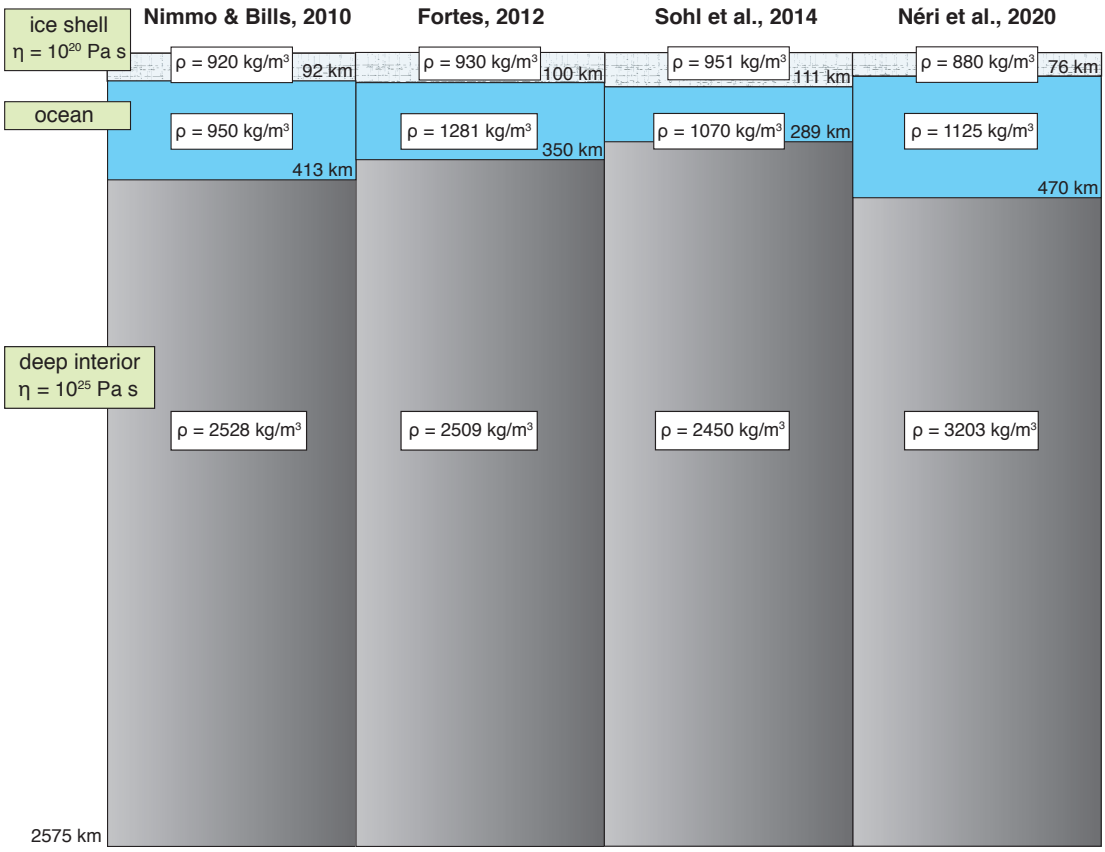

Figure 3.A1. Comparison of example internal model parameters for Titan from published works. For this study, the modeling parameters of Sohl et al. (2014) and Néri et al. (2020) have been selected for comparison in end-calculation values for Mithrim Montes.

To better understand the sensitivity of tidal stresses as a function of Titan's internal structural representation, we demonstrate the behavior of two end-member models (Figure 3.A2; Sohl et al., 2014; Néri et al., 2020). Using Mithrim Montes as an example location, we compare tidal stress amplitudes and resultant shear failure scenarios for these two cases. Parameters adopted by Sohl et al. (2014) assume an internal global ocean of a thickness of 178 km with an icy crust of 111 km. Néri et al. (2020) list a crustal thickness of 76 km and an ocean depth of 394 km as possible values. The densities for the deep interior and ocean are higher in the possibilities of values listed in Néri et al. (2020), however the ice shell density of Sohl et al. (2014) is greater by 71 kg/m^3.

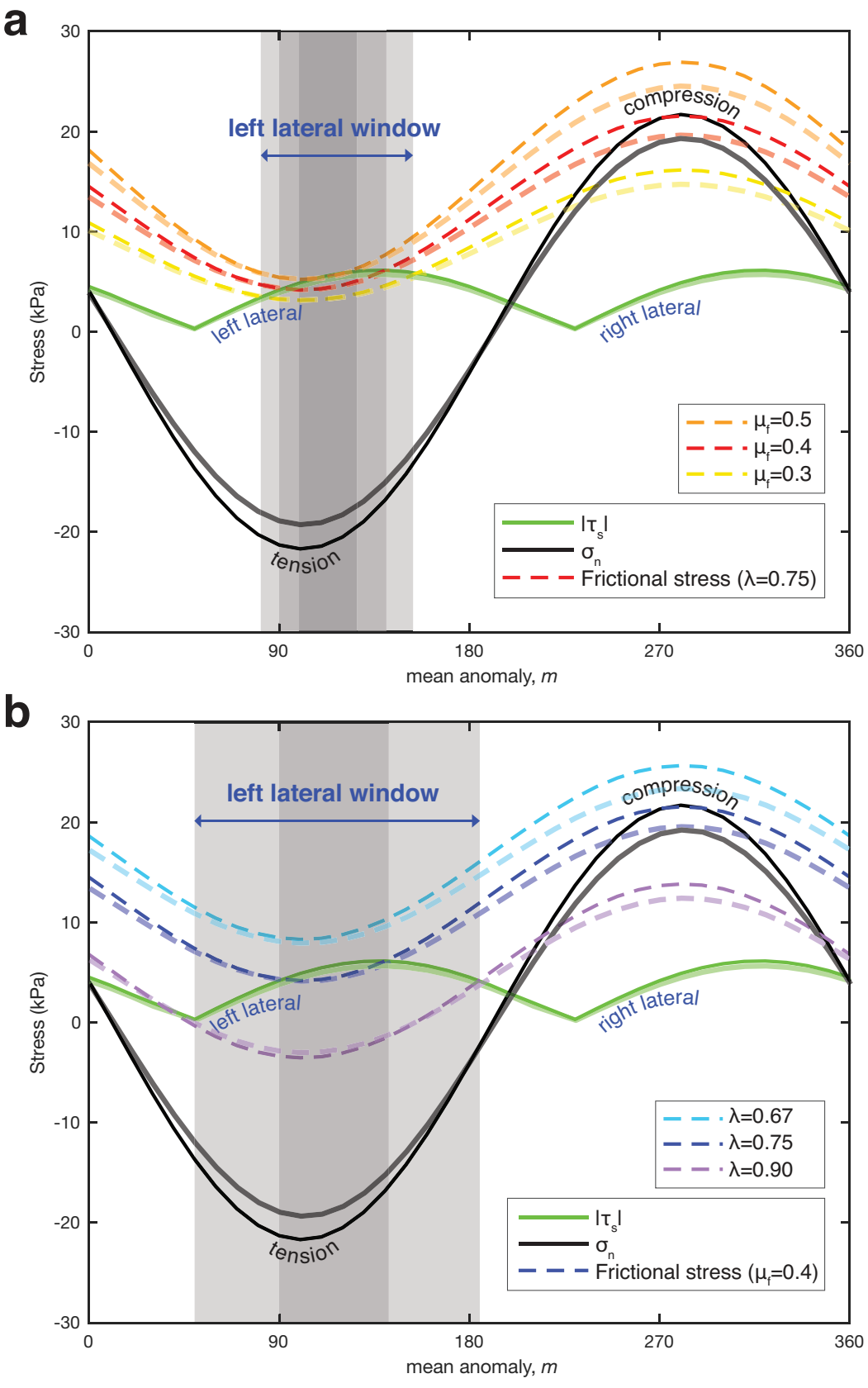
a
left lateral window
compression
left lateral
right lateral
tension
μf=0.5
μf=0.4
μf=0.3
|τs|
σn
Frictional stress (λ=0.75)
Stress (kPa)
mean anomaly, m
b
left lateral window
compression
left lateral
right lateral
tension
λ=0.67
λ=0.75
λ=0.90
|τs|
σn
Frictional stress (μf=0.4)
Stress (kPa)
mean anomaly, m

Figure 3.A2. Tidal stress and the Coulomb failure criterion as a function of mean anomaly, *m* (orbital position) for Mithrim Montes lineament average orientation (β = 20°). Resolved tidal normal stress (σ_n) is represented by the black line, resolved absolute tidal shear stress ($|\tau_s|$) is represented by the solid green line with the sense of shear stress labeled, and frictional stress (right side of Eq. 2) is represented by the dashed lines. The internal parameters for Titan used in this model are from Table 3.1 (Sohl et al., 2014), whereas the subdued shaded lines are for the same calculations with the internal parameters from Néri et al. (2020) for comparison. Shear failure will occur when the shear stress is greater than the frictional stress (gray shaded regions); in this case left-lateral slip during portions of the orbit. Here, the observational depth is z = 100 m. **a)** Investigating the possible slip window with coefficients of friction μ_f = 0.3-0.5 and pore fluid pressure ratio λ = 0.75. **b)** Modeling width of failure window with pore fluid pressure ratio λ = 0.67-0.90 while retaining μ_f = 0.4.

When comparing the calculations for the same coefficients of friction (μ_f) and pore fluid pressure ratios (λ), the modeling results show that the resolved tidal normal stress (σ_n) between the two end-member internal structural representations varies by a maximum of 2.41 kPa and the resolved absolute tidal shear stress ($|\tau_s|$) by a maximum of 0.43 kPa. The frictional stress differs by a maximum of 1.93 kPa when in compression. However, the frictional stress varies only by < 0.27 kPa between the models when in high tension, during which a slip window could be achieved. This sensitivity analysis shows that the calculated possibility for slip in our model is only marginally affected by the differences in these published internal composition models of Titan.

Supplemental files (online at doi: 10.1016/j.icarus.2021.114700)

Titan SatStress diurnal orbit movie (Titan_diurnal.mov):

Maximum principal stress (σ_1) field of Titan during orbit from SatStress assuming parameters provided in Table 3.1 in cylindrical equidistant projection and corresponding sketch of Titan's orbital position with respect to Saturn.

Mithrim Montes diagram orbit movie (Titan_MithrimMontes_CoulombFailure.mov):

Coulomb failure diagram during orbit for Mithrim Montes (2ºS, 127ºW) for a coefficient of friction $\mu_f = 0.4$, pore fluid pressure ratio $\lambda = 0.75$, and an observational depth $z = 100$ m. Fault orientations that are free to slip indicated in grey areas. Maximum principal stress (σ_1) field of Titan from SatStress assuming parameters provided in Table 3.1 in cylindrical equidistant projection with black circle indicating location of Mithrim Montes. Corresponding sketch of Titan's orbital position with respect to Saturn.

North pole location diagram orbit movie (Titan_LigeiaMare_CoulombFailure.mov):

Coulomb failure diagram during orbit for location near Ligeia Mare (75ºN, 270ºW) for a coefficient of friction $\mu_f = 0.4$, pore fluid pressure ratio $\lambda = 0.75$, and an observational depth $z = 100$ m. Fault orientations that are free to slip indicated in grey areas. Maximum principal stress (σ_1) field of Titan from SatStress assuming parameters provided in Table 3.1 in cylindrical equidistant projection with black circle indicating location. Corresponding sketch of Titan's orbital position with respect to Saturn.

CHAPTER 4. UNCOVERING GANYMEDE'S PAST: TECTONICS AT NIPPUR/PHILUS SULCI

Note: This chapter will be submitted pending co-author notes to the journal *Icarus* with co-authors E.S. Costello, B.R. Smith-Konter, M.E. Cameron, G.C. Collins and R.T. Pappalardo.

Abstract

Observations of Jupiter's largest moon Ganymede by *Voyager* and *Galileo* revealed fractures and evidence of strike-slip faulting. Previous studies for the mechanisms of these structures focused on gravitational tidal stresses and extensional tectonism. In this analysis, we investigate the geologic history of Ganymede in the area of Nippur/Philus Sulci (175ºE, 36.9ºN) by examining existing mapped evaluations of the *Galileo* high-resolution data available for this region (~100m/pixel), producing new crater counts and crater size frequency distributions to define the relative ages of terrains, and conducting a tidal stress investigation of Ganymede's past. Within our study region, various geologic units align on a single line of longitude, eliminating the need to correct for possible leading/trailing hemisphere disparities in crater counts. Several crosscutting bands of light terrain in the Nippur/Philus Sulci site show varying degrees of tectonic deformation, ranging from smooth and less distorted bands to highly grooved and deformed terrain. The chronology of tectonic activity implied by mapped crosscutting relationships is consistent with our findings from analyses of crater densities for each unit, revealing three eras of distinct geologic activity: 1. Ancient, 2. Intermediate and 3. Youngest. Our crater size frequency distribution analysis further suggests that the youngest light terrains may be correlated in age with the formation of the Gilgamesh impact basin. Indicators of shear deformation are found throughout all ages of terrain, but mapped early-stage indicators of strike-slip features are exclusively located in intermediate and youngest terrain. An investigated offset feature in intermediate-aged terrain corresponds in slip direction to the predictions from modeling stresses of a higher past eccentricity. However, the *en echelon* structures found in a younger geologic unit do not align in slip direction with typical first-order R shears. This suggests that these features could have formed through another process (e.g., impact-related extension) or as passive *en echelon* structures created through relatively rapid large displacement on a fault. Through modeling of Ganymede's past tidal stresses, we can conclude that a past higher eccentricity ($e > 0.02$) could have distorted the Nippur/Philus Sulci region in its second, intermediate phase of main deformation, yielding a stress field conducive to shear failure of the icy upper crust. New data from NASA's Juno mission,

as well as future observations by ESA's Jupiter Icy Moons Explorer (JUICE) mission and NASA's Europa Clipper mission, will further aid our understanding of the tectonic history of Ganymede and improve the resolution of crater density studies and tectonic feature analysis.

4.1 Introduction

In 1979, the *Voyager 1* and *2* spacecraft revealed Jupiter's satellite Ganymede to be an icy world banded with light and dark terrains. It was not until 1995 when the *Galileo* space probe entered the Jupiter system and returned high-resolution imagery of Ganymede's heavily deformed surface that the tectonic history represented by these bands of light and dark came into better focus (i.e., Pappalardo et al., 1998; 2004; Schenk et al., 2010; Collins et al., 2013; Cameron et al., 2018a; Rossi et al., 2018; 2020). Ganymede is the largest of Jupiter's moons, with a substantial water ice crust and subsurface ocean, as well as a magnetic field that is likely due to an internal dynamo (Kivelson et al., 1997). The precise depths of Ganymede's differentiated layers are not well constrained as there could be numerous alternating water and high-pressure ice layers (Vance et al., 2014). However, the outer ice shell is believed to be ~ 100-150 km thick (Schubert et al., 2004; Collins et al., 2013) and images show that the surface is considerably fractured. Ganymede is striped with terrains of light grooved subparallel ridge and trough systems that are interpreted to be the result of episodes of extensional tectonism (Murchie et al., 1986; Pappalardo et al., 1998; 2004; Collins et al., 1998; Pizzi et al., 2017; Cameron et al. 2018a). These terrains have age estimates between 400 Ma and 4 Ga, with an order of magnitude of uncertainty driven by limited resolution crater densities and uncertainty in the population and evolution of ancient impactors (Neukum et al., 1998; Zahnle et al., 1998, 2003). Ganymede's dark terrains are estimated to be about 4 Ga old based on the density of larger (>20 km diameter) craters (Shoemaker et al., 1982; Murchie et al., 1986; Murchie and Head, 1989; Neukum, 1997; Neukum et al., 1998; Prockter et al., 1998; Zahnle et al., 2003; Schenk et al., 2004).

High-resolution Galileo imagery provide many indicators of strike-slip faulting such as off-sets, strained craters, drag features and *en echelon* structures, which are theorized to have formed in a past elevated tidal stress field during a period of anomalously high eccentricity (e.g., Showman and Malhotra, 1997; Cameron et al., 2020) or through a combination of present-day tidal stresses and non-synchronous rotation (NSR) of a decoupled outer ice shell (Cameron et al., 2019). Ganymede may have previously been in Laplace-like resonances (Showman and Malhotra, 1997), and its mantle may have been warmer because of this higher state of

eccentricity, consistent with a decoupling of the ice shell and subsequently, of its rotation. Previous studies hypothesize that Ganymede orbited non-synchronously (NSR) in the geologically recent past (Zahnle et al., 2003), which implies that its interior must have been warmer. However, no independent evidence has been identified so far on the surface of Ganymede to support the hypothesis of present-day NSR.

Crater counts and size frequency distributions can be used to define the relative ages of geologic units and help us to understand geologic chronology. Age estimates for Ganymede's terrains are between 400 Ma and 4 Ga years (Neukum et al., 1998; Zahnle et al., 2003). Using the base maps (Collins et al., 2013) produced by Cameron et al. (2018a) and stitching high-resolution *Galileo* Solid State Imaging (SSI) camera images (Patterson et al., 2010; Cameron et al., 2018b) onto the base map, we digitized more than 850 craters within the area of Nippur/Philus Sulci (175ºE, 36.9ºN; Figure 4.1). In this region, several geologic units align on a single line of longitude, eliminating the need to correct for possible leading/trailing hemisphere disparities and asymmetry in the impact rate when exploring crater size-frequency distributions. The primary cratering of a synchronously rotating satellite like Ganymede is expected to be strongly asymmetric (Zahnle et al., 2001), with the leading hemisphere more heavily cratered than the trailing. Consequently, the distribution of > 10 km craters on Ganymede shows strong leading/trailing asymmetry (Zanhle et al. 2003; Schenk et al. 2004). The projected effect is that cratering rates are generally 20-60 times higher at the apex of motion than at the antapex of motion, with the exact ratio varying by planet and satellite (Zahnle et al., 2001).

Several crosscutting bands of light terrain in the Nippur/Philus Sulci site's four-frame mosaic (average resolution of 100 m/pixel; Figure 4.7) show varying degrees of tectonic modification, ranging from smooth and less deformed bands to highly grooved and deformed terrain. We investigate this distortion and its chronological context to classify eras and modes of tectonic activity, first by examining the crater counts (Section 3), and then in the context of tectonic activity caused by possible higher tidal stresses in the past (Section 4) using Coulomb failure conditions within the shallow icy subsurface that could possibly initiate strike-slip and thrust faults through diurnal tidal stresses. The goal of this investigative study is to advance our knowledge of Ganymede's geologic history and evolution through time, as well as to better inform future explorations of Ganymede (i.e., the ESA's JUICE and NASA's Europa Clipper missions).

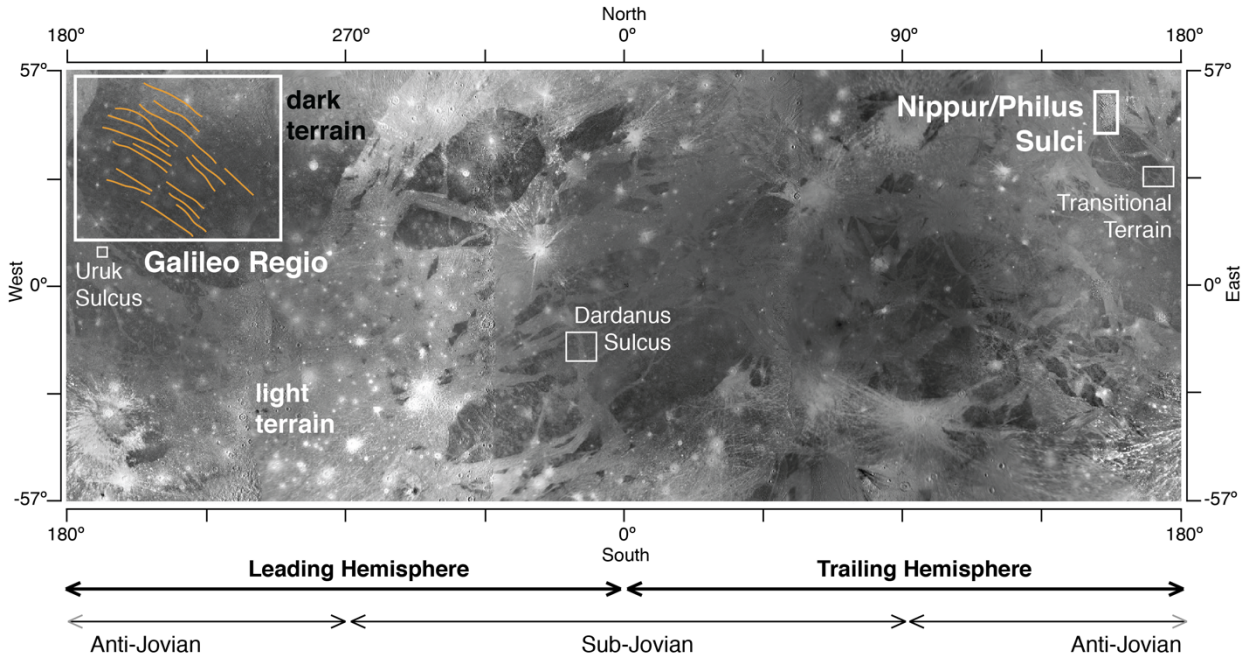

Figure 4.1. Ganymede global mosaic (0º-360ºE, 57ºN-57ºS) in Mercator projection. Examples of dark and light terrain labeled. Boxes denote region of Nippur/Philus Sulci mapped for this study, Dardanus Sulcus as a region with an example for a prominent strike-slip offset, and Galileo Regio with concentric furrows sketched in orange (detailed in Figure 4.5), implying an ancient impactor (Hirata et al., 2020). Leading and trailing, as well as anti-jovian/sub-jovian, hemispheres are labeled.

4.2 Background

On Ganymede's surface, tectonic scars of a turbulent geologic past are evident. Two-thirds of Ganymede's surface is cross-cut by bright terrain that has been altered by tectonic and/or possibly cryovolcanic events (e.g., Smith et al., 1979; Shoemaker et al., 1982; Pappalardo et al., 1998; Collins et al., 2013). Most of the tectonically deformed terrain, commonly referred to as "grooved terrain", appears to be extensional in nature, with regularly spaced ridges and troughs (Pappalardo et al., 1998; Collins et al., 2013; Rossi et al., 2020). The period of groove creation was likely accompanied by intense activity in the interior, possibly resulting in high surface heat fluxes, high surface tension, and potentially satellite expansion (Bland et al., 2009). Warming and global expansion associated with mobile-lid convection may have resulted in non-uniform heat flux and localized strain to create regions of grooved light terrain (Hammond and Barr; 2013: Bland and McKinnon, 2017). It is difficult to determine what exactly caused Ganymede's tectonic resurfacing periods, and while the satellite is in Laplace resonance with Io and Europa (Showman

and Malhotra, 1997), there is no forcing of its eccentricity, and therefore very little tidal energy currently dissipates in the interior (Bland et al., 2009). Based on cratering rates, it is estimated that the grooved terrain has an age of <2 Ga (Zahnle et al., 2003), which would mean that it could not have been produced through differentiation (separation of rock and ice) during early formation, as suggested by previous work (Mueller and McKinnon, 1988), unless differentiation occurred in stages. It consequently appears that the creation of grooved terrain during Ganymede's midlife required either extended or renewed geologic activity.

Among Ganymede's youngest teconic features, determined by cross-cutting relationships with other tectonic domains in their respective areas (Pappalardo et al., 2004; Cameron et al. 2018a), are strike-slip offsets most prominently visible on Dardanus Sulcus (Figure 4.2 a) near the equator, where a right-lateral strike-slip offset caused ~45 km displacement of preexisting features. Other large-scale strike-slip indicators, such as duplexes (Figure 4.2 b) and *en echelon* structures (Figure 4.2 c) are also found throughout Ganymede's surface.

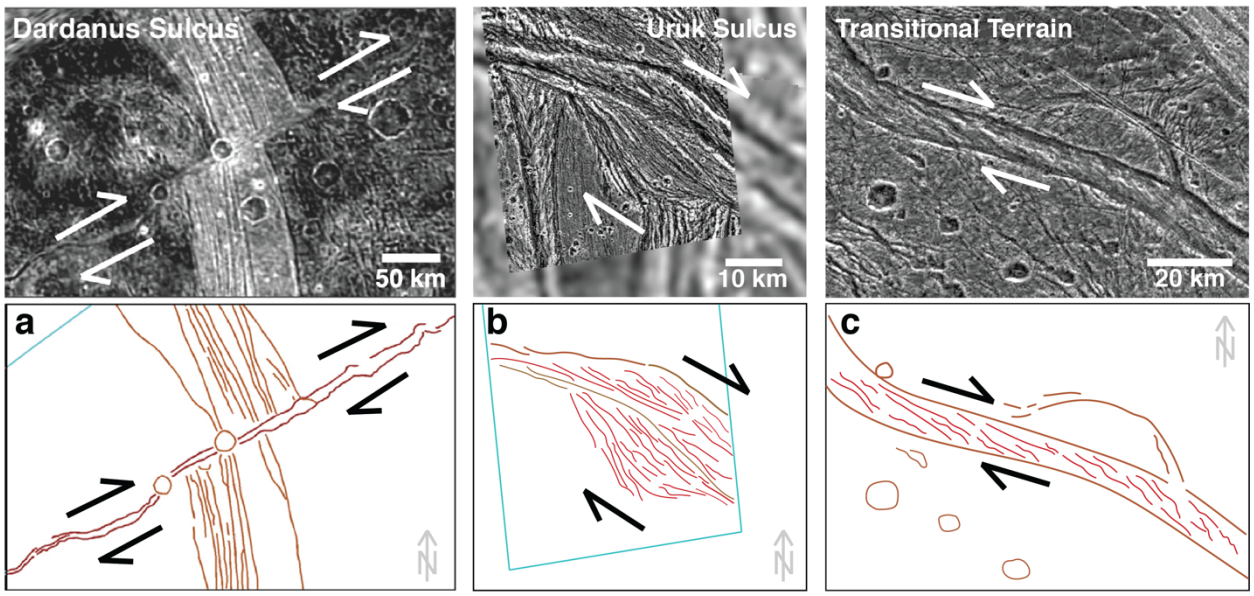

Figure 4.2. Examples of **a**) right-lateral offset feature at Dardanus Sulcus (346ºE, 18ºS; DeRemer and Pappalardo, 2003), **b)** a transtensional duplex lensoid (192ºE, 10ºN) in light grooved terrain with a subparallel internal structure in the Uruk Sulcus region and **c)** *en echelon* structures (173ºE, 30ºN) in the light subdued material found within Transitional Terrain, with corresponding sketch maps. Arrows indicate inferred sense of shear with transtensional origin, red lines outline main sheared features, brown lines indicate feature boundaries and blue lines specify image boundaries of high-resolution *Galileo* Solid State Imaging (SSI) camera frames.

Mechanically, a strike-slip fault is a pure anti-plane shear deformation governed by a hierarchical sequence of bifurcations (Goldstein and Osipenko, 2012; Donzé et al., 2021). Initial cracks join to form well-defined fractures and structures that can propagate individually from one another (Lin et al, 2010). Some can grow into *en echelon* fracture sets with regular intervals that can be observed at the surface (Goldstein and Osipenko, 2012; Donzé et al., 2021). Riedel shears form these subsidiary shear fractures that propagate a short distance away from the main fault and are used to determine large-scale strike-slip fault patterns (Pappalardo et al., 1998; Collins et al., 2013; Cameron et al., 2018) that can indicate as many as five directional families of associated fractures (Figure 4.3) during the early stages of an offset feature. Individual fractures can remain active after other types have developed, and synchronous movement of all fractures subsequently accommodate the strain in the fault zone. The geometric organization of Riedel shears can indicate the sense of movement in the strike-slip fault zone and its evolution. R Riedel shears are generally the most prominent factures and the first secondary cracks to occur, typically about 10-20º clockwise from a main right-lateral fault (anticlockwise for a left-lateral strike slip). These often form in an *en echelon* arrangement synthetic to the main fault as a series of sub-parallel lineaments separated by step-overs, where the acute angle with the fault points in the direction of relative movement (Pollard and Martel, 2020). R' shears develop with or after R shears and are antithetic faults that have a sense of movement opposed to the bulk movement. R' shears are oriented at a high angle, approximately 75-90º to the fault plane and often connect two parallel R shears (Tchalenko, 1970; Naylor et al., 1986). P shears are minor faults that are symmetrically oriented to R shears and can form also an *en echelon* arrangement. These shears are accommodating the fault-parallel shortening and are contractional in nature (Woodcock and Fisher, 1986). P shears are less common than R and R' shears and can require more fault displacement to form. As shearing continues, initial R shear structures can become inactive and localize along the P shear zone (Naylor et al., 1986). Y shears are microfaults that occur sub-parallel to the main fault and usually form last (Pollard et al., 1982; Thomas and Pollard, 1993; Pollard and Martel, 2020). Strike-slip duplexes are shaped through the bending of a strike-slip fault, creating lensoid or spindle-shaped features, stemming from tension gashes that form between R and R' shears (Figure 4.3 a; e.g., Woodcock and Fischer, 1988; DeRemer and Pappalardo, 2003). Sets of faults resembling duplex structures are numerous in Ganymede's light terrain, and linked to extensional regimes and transtension (DeRemer and Pappalardo, 2003; Cameron et al., 2018a). More unorganized duplex structures can also be found in Ganymede's oldest dark terrain and intermediate terrain (DeRemer and Pappalardo, 2003; Cameron et al.,

2018a). The interpretation of a fault system can be further complicated when Riedel-within-Riedel shears start to form.

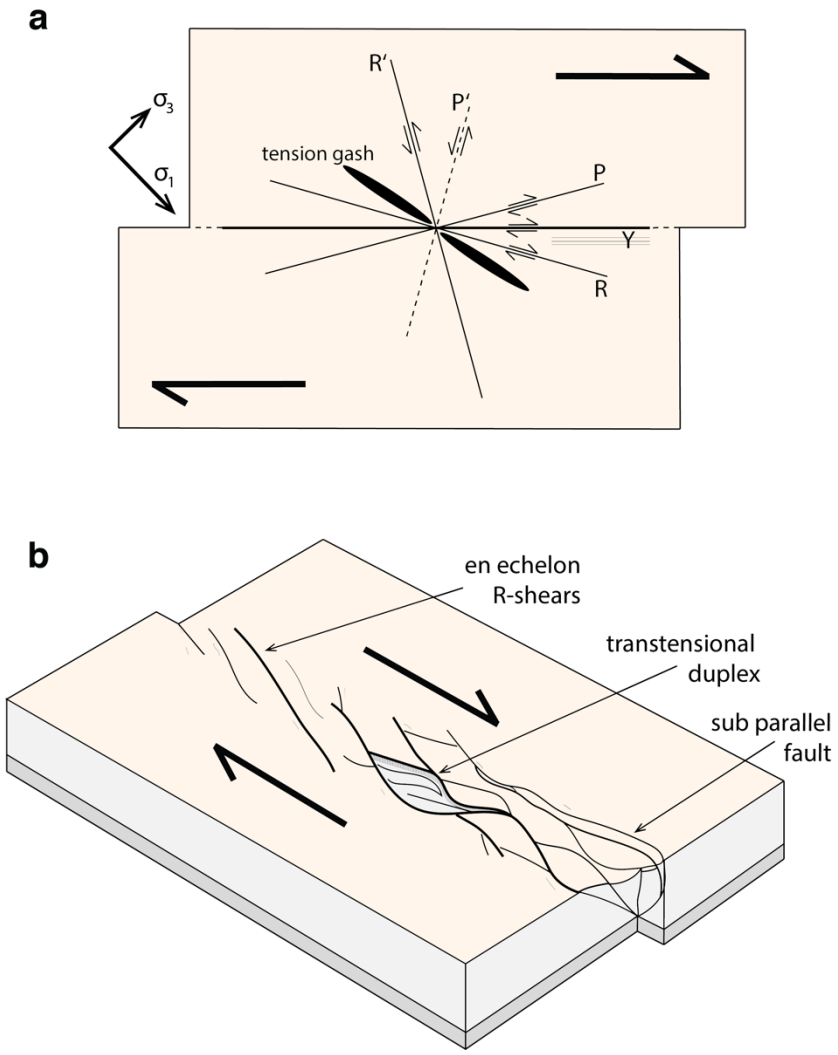

Figure 4.3. Illustrations of Riedel shears in a right-lateral strike-slip fault zone. Arrows specify associated sense of shear. **a)** Riedel shears indicated: R Riedel shears, R' Riedel shears, P shears and Y shears, maximum compressive stress σ_1 and minimum compressive stress σ_3. **b)** Characteristics of morphological predictions of Riedel shear features with labeled *en echelon* structures forming from R shears, sub-parallel faults created by Y shears and transtensional duplex from deformed tensional gashes indicative of large-scale strike-slip faulting characteristics (figure modified from Pappalardo and Greeley, 1995).

Previous studies propose that tidal stresses can create a high stress field that drives fault initiation, producing active tectonism (e.g., Showman and Malhotra, 1997; Cameron et al., 2019; 2020). At present, Ganymede's diurnal tidal stresses are not large enough to initiate strike-slip faulting. However, non-synchronous rotation (NSR) of the outer ice shell could cause shear and normal tractions of ~1 MPa, which would be sufficient to induce fault failure (Cameron et al., 2019). On Europa, this mechanism has been linked to the formation of extensional as well as strike-slip tectonics through the identification of migrated structures (Showman and Malhotra, 1997; Collins, 2009). But so far, no direct evidence for NSR has been established for Ganymede, only an indirect indication through the count of crater and crater chain distributions (Zahnle et al., 2001). When comparing stress values on other icy moons to Ganymede, diurnal tidal stresses for similarly sized Titan in the Saturn system are ~5 times larger than present-day stresses on Ganymede, mainly because of Titan's higher orbital eccentricity of e = 0.0288 compared to Ganymede's e = 0.0013 (Burkhard et al., 2021). Related to Enceladus in the same system, Titan's diurnal stresses are predicted to be roughly 3x smaller than those of Enceladus (Smith-Konter and Pappalardo, 2008; Martin, 2016) because of its small size and distance to Saturn. Active faulting mechanisms are currently apparent on Enceladus and hypothesized for Titan (Burkhard et al., 2021). For Ganymede however, a high value of eccentricity (e) in the satellite's past (Cameron et al., 2020) could promote strike-slip displacement, such as e = 0.05, compared to the known present-day e = 0.0013 (Showman and Malhotra, 1997; Baland and Van Hoolst, 2010). As Ganymede is a synchronously rotating satellite, its orbit creates a tidal bulge that varies in magnitude due to the eccentricity of the orbit (Bills, 2005; Wahr et al., 2009). The orbital history and its possible effects on the eccentricity of Ganymede has been explored in numerous previous studies (e.g., Yoder and Peale, 1981; Greenberg, 1987). Moreover, Showman and Malhotra (1997) demonstrated that the Galilean satellites could have been captured for a period of 10 Ma to 1 Ga in two Laplace-like resonances previous to the current state and eccentricity. In this past phase, the eccentricity could have been as high as e = ~0.07 and possibly driven internal activity as well as subsequent resurfacing (Greenberg, 1987; Showman and Malhotra, 1997).

A satellite's eccentricity can also be affected by a large ancient impact. The free eccentricity component stems from a combination of velocity and distance of a satellite after its formation around the parent planet. The total eccentricity (e) of a satellite is the sum of the free and the forced components, where the forced component arises from the gravitational interaction of two satellites in resonance (Greenberg, 1987). As Ganymede's free eccentricity should have damped long before present time, Showman and Malhotra (1997) calculated the size of an asteroidal or

cometary impactor required to excite Ganymede's free eccentricity from a value of 0 to 0.0015. It was concluded that a theoretical impactor would have required a mass of ~10^{20} kg. The most recent large impact basin, Gilgamesh (Figure 4.4), with an excavation diameter of about 550 km (Shoemaker et al., 1982), was probably created by an impactor of ~10^{17}-10^{18} kg (Showman and Malhotra, 1997) and therefore a diameter between ~60 and 130 km if consisting of pure ice.

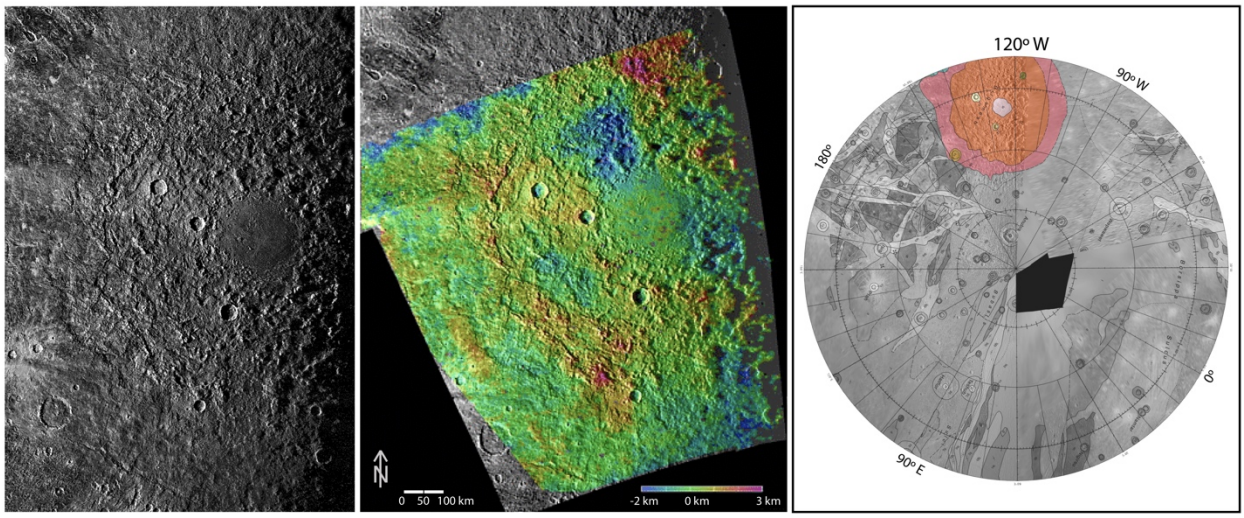

Figure 4.4. Mosaic of *Voyager 2* images processed by P. Schenk and color-coded topographic map of Gilgamesh (124°W, 62°S; Schenk, 1998). The central depression and massif zones are roughly the same elevation as the surrounding plains, indicating that Gilgamesh's relaxation is nearly complete. Right: Geologic map of the South Pole with Gilgamesh outer basin area in red, inner rugged basin in orange and dome smooth material in light pink (Collins et al., 2013).

However, we can also consider a more ancient and larger impactor that possibly created the concentric furrows in Ganymede's oldest dark terrains (Figure 4.5), which would correspond to an estimated diameter of about 300 km (Hirata et al., 2020) with a mass of at least 1.3x10^{19} kg if only consisting of ice. Large impactors from the outer solar system and afar do not necessarily have to be made up of pure ice, as is the case in the Asteroid Belt today (Carry, 2012), but can have a higher density with a mixture of silicate materials and nickel-iron. Showman and Malhotra (1997) argue that other large impact features besides the youngest basin, Gilgamesh, are so old that any eccentricity alterations produced by their impacts would be damped again by the present day, concluding that Ganymede's eccentricity change was not produced by an impact but rather a remnant of an ancient resonance passage. However, an impactor could have further excited Ganymede's possibly already existing eccentricity in the past if we do not assume the initial free

eccentricity to be 0. Nevertheless, the ancient impactor was likely not large enough to have caused a significant change in eccentricity and subsequently producing high diurnal tidal stresses. Nonetheless, such large impactors can break the icy crust, breach the internal ocean and induce melting in the interior, so it is therefore a valid argument to include the effects of sizable impactors in our tectonic analysis and explore their effect on shaping Ganymede's tectonic past.

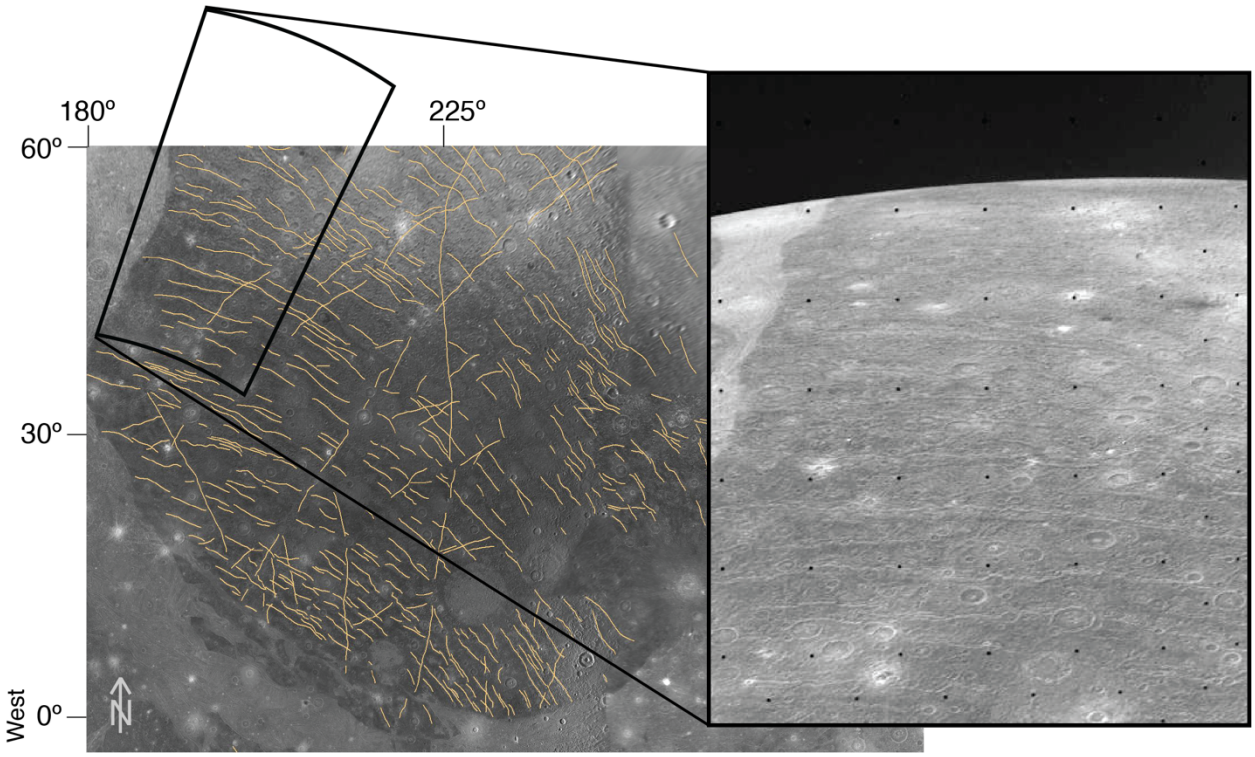

Figure 4.5. Mapped furrows in oldest dark terrain on Ganymede in Galileo Regio in Mercator projection with approximation of *Voyager* data acquisition. Right: *Voyager* image c2063641, 195°E, 50°N, with a resolution of 1.08 km/px at its center. The concentric furrows are indicative of an ancient impactor at location 180°W, 20°S, coinciding with the anti-Jovian longitude (Hirata et al., 2020). An impactor with a diameter of 300 km is estimated to be consistent with the properties of the furrow system.

Gilgamesh is the largest well-preserved impact feature preserved on Ganymede, consisting of at least four concentric structural rings (Schenk et al., 2004). The central zone is smooth and ~150 km across with an asymmetric domical surface rising up to ~500 m (Figure 4.4). The outer limits of the crater zone are bordered by a prominent concentric scarp that is on average 1 km

high and has a diameter of ~585 km, which may represent the basin rim (Schenk et al., 2004). It is assumed that large impact basins such as Gilgamesh are concurrent with the large lunar basins Orientale and Imbrium, dating to 3.8 billion years ago (Neukum, 1997). Newer Galileo-based crater counts on the floor and ejecta of Gilgamesh and revised observational estimates of the number of comets near Earth suggest that Gilgamesh is much younger, dating around 700 Ma (Zahnle et al., 2003). Because the Galilean satellites might have been previously captured for a period of 10 Myr to 1 Gyr in two Laplace-like resonances and the eccentricity could have caused deformation of the surface (Greenberg, 1987; Showman and Malhotra, 1997), the large young Gilgamesh impactor could have played a role in the most recent stage of geologic activity and extensional tectonism on Ganymede. However, impactors in general likely did not play a role in instigating a higher eccentricity.

We can consequently infer three hypothetical main stages of deformation on Ganymede: The ancient impactor stage as concluded by Hirata et al. (2020) producing the furrows in the oldest dark terrain, an intermediate stage of higher eccentricity that actively deformed the surface (Showman and Malhotra, 1997; Baland and Van Hoolst, 2010; Cameron et al., 2020), and a possible youngest stage affected by the large Gilgamesh impactor (Figure 4.6) that could have shaped the most recent light terrain smooth extensional features. To deduce the tectonic history and investigate the different stages of deformation, we examine the area of Nippur/Philus Sulci specifically (~100 m/pixel; 175ºE, 36.9ºN) as various geologic units align on one longitude, eliminating the need to correct for possible leading/trailing hemisphere disparities in crater counts. Here, several crosscutting bands of light terrain in the Nippur/Philus Sulci site show varying degrees of tectonic deformation, ranging from younger smooth and less distorted bands to highly grooved and deformed terrain. We investigate existing *Galileo* high-resolution imagery available for this region, and produce new crater counts and size frequency distributions to define the relative ages of terrains. We also model diurnal tidal stresses through Ganymede's past to explore a failure threshold for representative eccentricities.

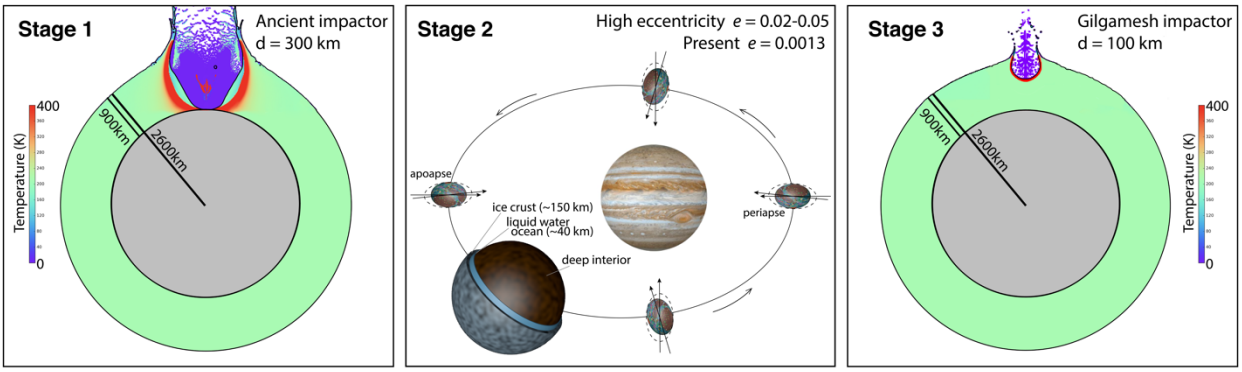

Figure 4.6. Hypothetical main stages of deformation. Stage 1: Ancient impactor with probable diameter d = 300 km (Hirata et al., 2020), breaching the surface down the icy mantle (900 km depth). Stage 2: Intermediate stage of higher orbital eccentricity depicted with generalized scaled internal model of Ganymede (see Table 4.1). Orbital eccentricity illustration not to scale. Variations in gravitational tidal forces directed toward Jupiter (dashed arrows) act to deform the surface (graphic exaggerated) during period of high eccentricity. Permanent tidal bulge of the satellite (solid arrows) is facing toward the empty focus of the elliptical orbit. Stage 3: Gilgamesh impactor with possible diameter d = 100 km, breaking the ice crust and penetrating the ocean layer (~300 km depth). Impactor figures adapted and modified from iSALE-2D model and movies from Appendix B of Hirata et al. (2020) with fixed icy mantle thickness of 900 km (ice crust, liquid water ocean and high-phase interior ice layers) and total radius of 2600 km.

4.3 Crater data collection and modeling

In order to analyze and determine relative ages of tectonic units beyond an investigation of superposition, we conduct a crater size frequency distribution analysis. Using ArcGIS (the community standard geographic information system (GIS) software), we expanded and refined the digitized crater population produced by the geologic analysis of Ganymede by Cameron et al. (2018a; b) to create a database of 848 craters at the Nippur/Philus Sulci site (Figure 4.7; supplementary material). These were used to derive cumulative crater size frequency distributions for geologic units of relatively small size. To capture the crater size frequency distributions of each unit, we divided the site into five regions with distinct morphologies (Figure 4.7).

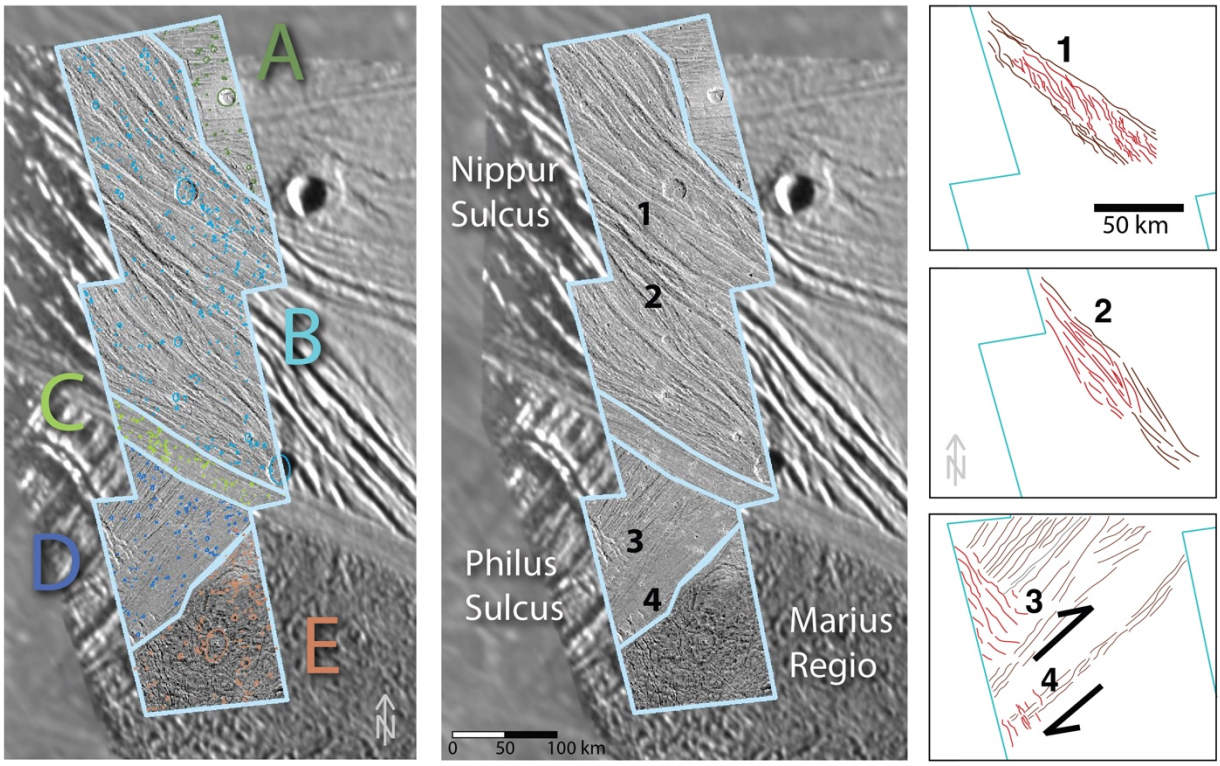

Figure 4.7. (Left) Nippur/Philus Sulci site (154.5º-158.2ºE, 44.5º-52.5ºN) divided into five regions of distinct morphology with mapped craters: Section A in the NE, Section B of Nippur Sulcus, Section C as the youngest cross-cutting feature, Section D of Philus Sulcus, and Section E of dark Marius Regio terrain. Relative ages can be interpreted from crosscutting relationships: E is oldest while B and C are younger than A and D. Crater counts of these sections were completed down to ~300 m diameter. (Center) Numbered shear indicators in respective units. (Right) (1) Location of *en echelon* structures as identified by Cameron et al. (2018), (2) newly-identified duplex-like structure, (3) drag features (fingers), and (4) inferred right-lateral (RL) offset. (Right) Corresponding sketch maps of each feature labeled at center. Red lines specify mapped primary lineaments, arrows denote inferred sense of shear, brown lines indicate contextual background features. Cyan polygons specify image boundaries of high-resolution *Galileo* Solid State Imaging (SSI) camera frames.

Following the guidelines of the Crater Analysis Working Group (1979), we produced an evaluation of cumulative crater size frequency for Nippur/Philus Sulci by setting the crater polygon area returned by ArcGIS equal to $\pi(D/2)^2$ to estimate crater diameter (D) for analysis of crater size frequency distributions. A steeply sloped cumulative size-frequency distribution implies a large proportion of small craters relative to large craters within the population. A relatively flat cumulative distribution implies craters are evenly distributed across all diameters. Cumulative

distributions reflect surface age by upper right/lower left diagonal offsets. A distribution that is further to the NE, the upper right of the plot, is older (has more craters of any given size) while a distribution that is offset to the SE of a plot is younger (has fewer craters of any given size). Thus, the produced crater size frequency distributions reveal the relative age of the units within Nippur/Philus Sulci (Figure 4.8).

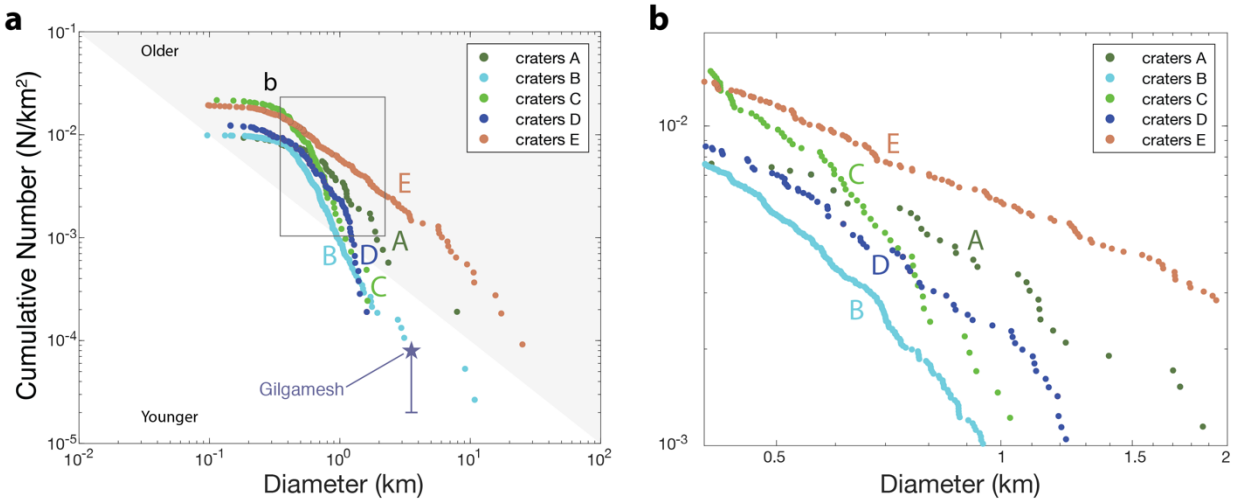

Figure 4.8. Crater size frequency distributions for Sections A, B, C, D and E of the Nippur/Philus Sulci site (Figure 4.7). **a)** Upper right/lower left diagonal offsets on the plot in crater distributions describe ages, where data positioned within the upper right corner of the plot (grey shaded region) indicates relatively older terrain while data positioned in the lower left corner (white region) suggest relatively younger terrains. It is apparent from its upper right offset that the dark Marius Regio terrain E is oldest. For comparison, the crater density of the Gilgamesh Basin ejecta (Schenk et al. 2004, Table 18.1) with error bar is plotted: 10^{-4} craters of at least 4 km in diameter have accumulated per km^2 on Gilgamesh since its formation. **b)** Detail of crater diameter range from 400 m - 2 km, showing that the chronology implied by crater counts on units A, B, C, and D agrees with the chronology interpreted from crosscutting relationships (see caption Figure 4.7), revealing three eras of distinct geologic activity: ancient, intermediate and youngest. Section E is oldest while B and C are younger than A and D due to their similar average slopes and offset to the lower left corner of the plot. The fairly steep slope of the crater size-frequency distribution for unit C is likely representative of numerous small secondary craters identifiable on this relatively smooth terrain, which can lead to misinterpretation of its age. However, in the tectonic crosscutting relationship analysis, it is apparent that C must be the youngest feature.

4.4 Tidal stress and Coulomb failure

While surfaces of icy satellites such as Europa can be dominated by extensional features (Nimmo, 2002), it has been proposed that a number of Ganymede's surface features have formed as a result of compressional and shear failure processes (Collins et al., 2013; Cameron et al., 2018a; 2020). On numerous ocean worlds, fault orientations and strike-slip indicators have revealed that their occurrence may be explained by a simple combination of diurnal stress and Coulomb failure, where frictional sliding is dominated by the presence of increased shear stress and/or decreased compressive stress (Smith-Konter and Pappalardo, 2008; Cameron et al., 2020; Burkhard et al., 2021). As Ganymede is a synchronously rotating satellite, it generates a tidal bulge that fluctuates in magnitude due to the eccentricity of the orbit (Wahr et al., 2009). A high value of eccentricity causes greater tension and compression on the ice shell, provoking possible fault failure. Ganymede's eccentricity could have been higher in the past, as modeled by Cameron et al. (2020) with a value of e = 0.05, compared to the present value of e = 0.0013 (Showman and Malhotra, 1997; Baland and Van Hoolst, 2010). Showman and Malhotra (1997) modeled that Ganymede could have been captured in two Laplace-like resonances previous to the current state and eccentricity, with a value as high as e = ~0.07, possibly driving internal activity as well as resurfacing.

To further investigate Ganymede's tectonic history and the deformed features visible in the younger terrains of Nippur/Philus Sulci, we use numerical code SatStress to compute the diurnal tidal stress tensor and resolve shear and normal stresses onto specified fault planes to assess the potential of fault failure at Nippur/Philus Sulci following Cameron et al. (2019; 2020). SatStress (http://code.google. com/p/satstress) computes stresses based on tidal potential theory (Wahr et al., 2009; Patthoff et al., 2016), allowing for both elastic and layered Maxwell viscoelastic treatments of the lithosphere. SatStress computes raw $\sigma_{\phi\phi}$, $\sigma_{\theta\theta}$, $\sigma_{\theta\phi}$ (longitudinal, latitudinal and shear tractions) and principal stress tensor components as a function of orbital position (mean anomaly, m; with m = 0 defined as periapse) and location on the satellite's surface. Currently, SatStress assumes a 4-layer satellite body (upper ice layer, lower ice layer, liquid ocean layer, and core) and we adopt appropriate physical and rheological parameters for Ganymede from Cameron et al. (2020). However, Ganymede's interior is likely more complex, with multiple layers of high-phase ice and liquid water (Vance et al., 2014) as well as an internal dynamo (Kivelson et al., 1997). Nevertheless, the current restrictions for modeling the interior with SatStress do not pose an impediment for the general validity of the results of this study.

Table 4.1 Ganymede physical, orbital and rheological parameters used for SatStress modeling.

Physical and Orbital Characteristics		
Radius (km)	2631	
Orbit eccentricity	Present: 0.0013	Past: 0.05
Orbit semi-major axis (km)	1.07×10^6	
Orbital period (h)	171.6	
Gravity (m/s^2)	1.428	
Jupiter mass (kg)	1.90×10^{27}	

Viscoelastic Parameters		
Ice (Upper and Lower)		
	Upper ice	Lower ice
Density (kg/m^3)	920	920
Poisson's ratio	0.30	0.30
Young's modulus (GPa)	9.30	9.30
Thickness (km)	10	140
Viscosity (Pa s)	10^{19}	10^{14}
Ocean		
Density (kg/m^3)	1000	
Poisson's ratio	0.50	
Young's modulus (GPa)	0	
Thickness (km)	40	
Viscosity (Pa s)	0	
Deep Interior (high-phase ice + silicates)		
Density (kg/m^3)	2450	
Poisson's ratio	0.25	
Young's modulus (GPa)	100	
Thickness (km)	2284	
Viscosity (Pa s)	$\sim 10^{20}$	

SatStress Parameters	
NSR Period (yrs)	Infinity
Elastic Love number h_2	1.40510
Elastic Love number k_2	0.44008
Elastic Love number l_2	0.35399

The shear failure potential due to variable diurnal tidal stresses caused by a higher past eccentricity could be quite significant as previous results have shown (Cameron et al., 2020). Because of this, we conduct a sensitivity analysis of shear failure tendencies at Nippur/Philus Sulci in accordance with Coulomb failure (Byerlee, 1978; Jaeger and Cook, 1979), with which new fractures can form. A Coulomb failure analysis considers tensile stresses that enable, and compressive stresses that resist, shearing motions (i.e., the resolved normal and shear tidal

tractions), and accounts for the coefficient of friction of ice and overburden pressures. Following the methodology of previous studies (Hurford et al., 2007; Nimmo et al., 2007; Smith-Konter and Pappalardo, 2008; Cameron et al., 2019; 2020; Burkhard et al., 2021), we first resolve local tidal stress tensor components onto the average orientation of mapped fault plane segments into normal (σ_n) and shear (τ_s) tractions:

$$\tau_S = \frac{1}{2}(\sigma_{\varphi\varphi} - \sigma_{\theta\theta})sin2\beta + \sigma_{\theta\varphi}cos2\beta$$
$$\sigma_n = \sigma_{\theta\theta}cos^2\beta + \sigma_{\varphi\varphi}sin^2\beta + \sigma_{\theta\varphi}sin2\beta$$

(Eq. 1)

where β is the segment's orientation, defined with respect to the latitudinal direction (β = 0° for a fault oriented due W, 90° for a fault due N) in Mercator projection. For each fault orientation (with presumed vertical dip), the resolved normal traction component acts perpendicular to each segment, and the resolved shear traction component acts parallel to each segment.

To evaluate the shear failure behavior, we calculate the Coulomb stress, τ_c, as

$$\tau_c = |\tau_s| - \mu_f(\sigma_n + \rho gz)$$

(Eq. 2)

where τ_s is the resolved shear stress acting on the initiated fault, μ_f is the coefficient of friction, σ_n is resolved normal stress, and ρgz is overburden pressure (where ρ is the density, g is satellite gravity, and z is the observation depth along the fault plane). Shear slip will occur when the resolved shear stress (τ_s) exceeds the frictional resistance [$\mu_f(\sigma_n + \rho gz)$] acting on the fault plane. The overburden stress is assumed to be positive, while normal tidal tractions are presumed positive when in compression and negative when in tension. For coefficient of friction, we assume a value of μ_f = 0.4, which is an average value consistent with laboratory studies for ice at a temperature and pressure resembling the state on Ganymede (Schulson and Fortt, 2012; Schulson, 2016). When failure conditions are met, the sign of the shear traction determines slip direction, where positive represents right-lateral slip and negative represents left-lateral slip direction. High tensile tractions can pull on a fault, reducing the contact between fault surfaces, and therefore stimulate failure. In the examples presented here, we evaluate the depth sensitivity of Coulomb failure for fault zones at 0.1 km depth observation planes for consistency.

At the Nippur/Philus Sulci site (Figure 4.7), we selected the locations of the possible right-lateral (RL) offset (location 4 in intermediate terrain unit D; 156°E, 46°N; Cameron et al., 2018a) and the duplex-like structure (location 2 in younger terrain unit B) newly identified in this work at

156ºE, 49ºN to demonstrate diurnal tidal stress sensitivity to eccentricity. The results of the right-lateral (RL) offset region indicate that there is no shear failure for the current eccentricity (e = 0.0013) configuration of Ganymede (Figure 4.9 a) as the resolved normal and shear stresses acting on the icy crust are very low (~5 kPa). In a past high-eccentricity case (e = 0.05), however (Figure 4.9 b), the resolved shear stress exceeds the frictional resistance just past m = 100º. The initiated fault is free to slip in a left-lateral sense, until the frictional stress dominates again past m = 165º, after which stress conditions return it to a locked form. It is important to recognize how Coulomb failure can vary as a function of fault segment orientation β, where β is defined relative to the latitudinal direction (β = 0° for a fault oriented due W, 90º for a fault due N); this angle can vary for each mapped segment from the overall fault zone orientation, and our calculations consider the average orientation of the mapped fault zone. In this case of the right-lateral (RL) offset region, another window of failure occurs where the resolved shear stress exceeds the frictional resistance past m = 205º, and the initiated fault is free to slip in a right-lateral sense. The frictional stress is dominant only past m = 340º, resulting in a larger period during orbit when the fault could slip in a right-lateral rather than a left-lateral sense, resulting in a feature that is displaced visibly in a right-lateral direction. At this location, peak resolved normal stress approaches 117 kPa when calculated as a higher eccentricity case (e = 0.05) compared to the value of ~5 kPa for the current eccentricity of e = 0.0013.

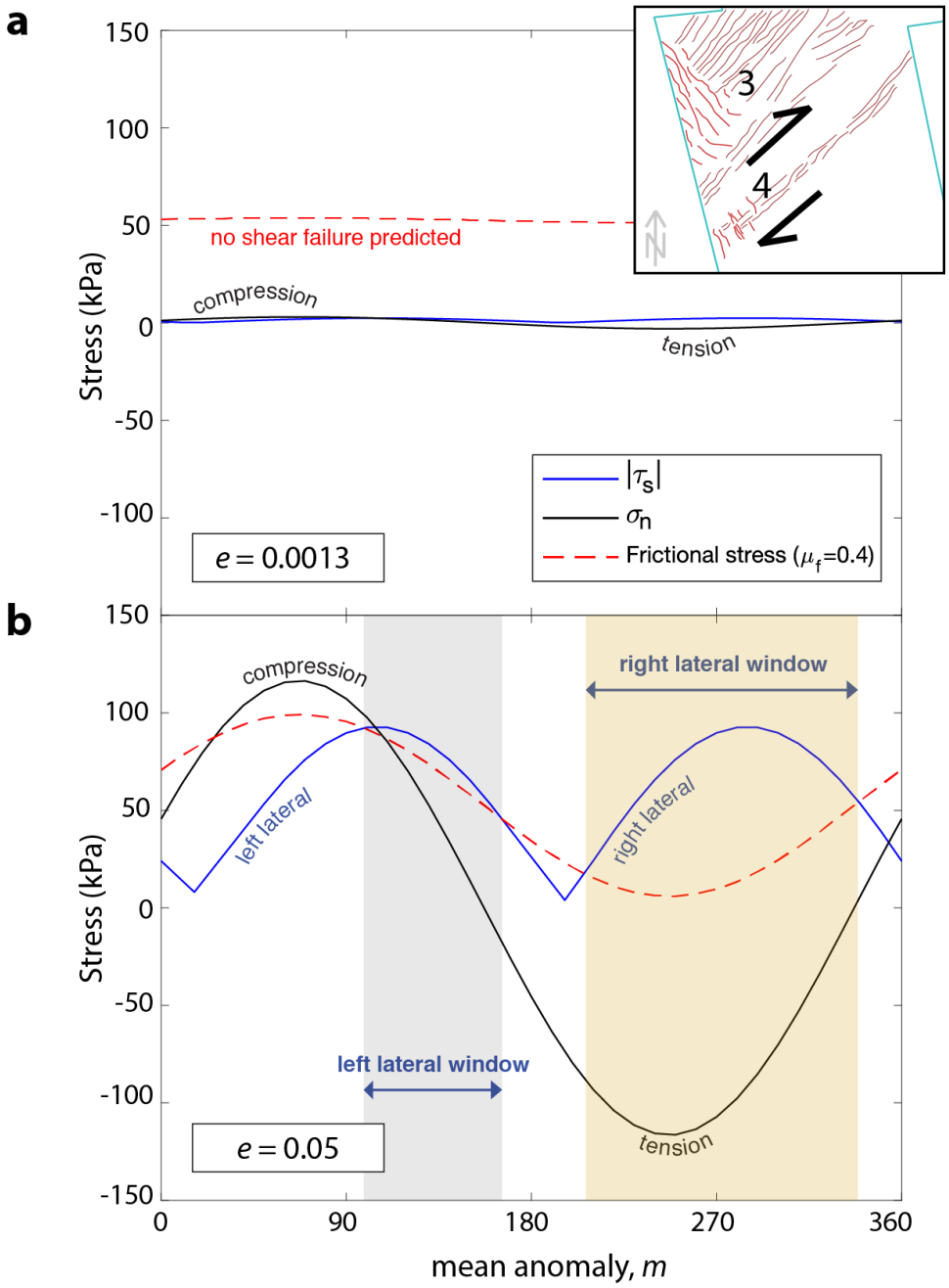

Figure 4.9. RL region, 156°E, 46°N (top right: mapping sketch and arrows indicating inferred direction of slip), calculated with a coefficient of friction $\mu_f = 0.4$ and observational depth $z = 100$. Resolved normal (σ_n, solid black line) and absolute shear ($|\tau_s|$, solid blue line) tractions for an assumed orientation of β = 130°, consistent with the average orientation of ridges observed, as a function of mean anomaly, m (orbital position). Frictional stress represented by the red dashed line. Shear failure will occur when the shear stress is greater than the frictional stress (shaded regions). **a)** Coulomb failure criterion for present-day eccentricity ($e = 0.0013$) with resolved normal traction (σ_n) in black, resolved absolute tidal shear tractions

($|\tau_s|$) in blue, and frictional stress as red dashed line. No shear failure is predicted for this case. **b)** Coulomb failure criterion for high eccentricity case (e = 0.05) with resolved normal traction (σ_n) represented by the black line, resolved absolute tidal shear tractions ($|\tau_s|$) represented by the solid blue line with the sense of shear stress labeled, and frictional stress (right side of Eq. 2) represented by the red dashed line. Shear failure during orbit indicated in shaded regions.

The duplex-like structure at location (2) in the younger terrain domain B is not as well defined as other identified transtensional duplex lensoids on Ganymede, such as in the example of Uruk Sulcus (Figure 4.2 b). Nevertheless, consistent with the average orientation observed, Figure 4.10 provides a demonstrative tidal stress deformation scenario as a function of mean anomaly, m (orbital position) for the average lineament orientation (β = 40°) of the duplex-like structure, also with a coefficient of friction μ_f = 0.4 as in the previous analysis of the right-lateral feature. The frictional stress (right side of Eq. 2) again mimics the pattern of the normal tidal stress curve as expected; in this high-eccentricity example (Figure 4.10 b), the frictional stress decreases as the shear stress increases, eventually exceeding the frictional resistance just past m = 34°. Here, the initiated fault is free to slip in a right-lateral sense, until the frictional stress is dominant again past m = 150°, after which stress conditions return it to a locked state. At m = 243°, the theoretical fault would be able to slip again in a left-lateral sense until m = 361° or 1° (periapse). As both windows of slip are almost equal in duration, it can be assumed that there would not be a displaced offset visible at this structure, as is the case for the right-lateral feature previously. The general trend suggests both right- and left-stepping fractures, and not conventional R shear transtensional duplex lensoid evidence of one slip direction.

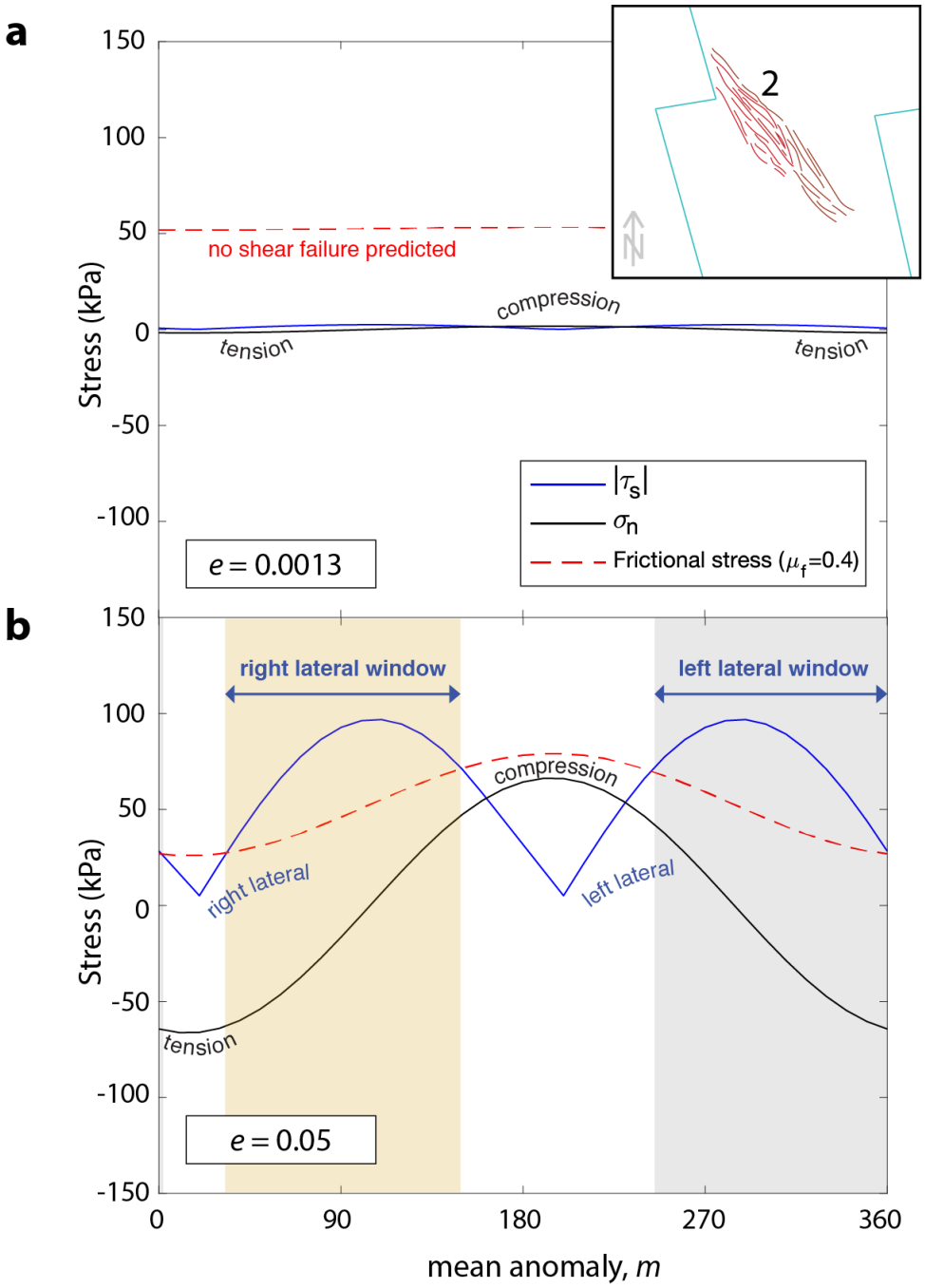

Figure 4.10. Region of the observed duplex-like structure, 156°E, 49°N (top right: mapping sketch), calculated with a coefficient of friction $\mu_f = 0.4$ and an observational depth $z = 100$ m. Resolved normal (σ_n, solid black line) and absolute shear ($|\tau_s|$, solid blue line) tractions for an assumed orientation of β = 40°, consistent with the average orientation observed, as a function of mean anomaly, m (orbital position). Frictional stress represented by the red dashed line. Shear failure will occur when the shear stress is greater than the frictional stress (shaded regions). **a)** Coulomb failure criterion for present-day eccentricity (e =

0.0013) with resolved normal traction (σ_n) in black, resolved absolute tidal shear tractions ($|\tau_s|$) in blue, and frictional stress as red dashed line. No shear failure is predicted for this case. **b)** Coulomb failure criterion for high eccentricity case ($e = 0.05$) with resolved normal traction (σ_n) represented by the black line, resolved absolute tidal shear tractions ($|\tau_s|$) represented by the solid blue line with the sense of shear stress labeled, and frictional stress (right side of Eq. 2) represented by the red dashed line. Shear failure will occur when the shear stress is greater than the frictional stress (shaded regions).

As we continue our analysis of eccentricity and failure thresholds, we evaluate the minimum required value of e for the location of Nippur/Philus Sulci by exploring values between $e = 0.05$ and 0.02 (Figure 4.11). The region of the of the possible right-lateral (RL) offset (4) requires a minimum eccentricity of $e = 0.02$ for failure, and is exclusively right-lateral at this value (Figure 4.11 b) as well as for a value of $e = 0.03$ (Figure 4.11 a). Failure for $e = 0.03$ occurs between mean anomaly position $m = 225^o$-321^o, and for $e = 0.02$ between $m = 265^o$-280^o, a much smaller window of potential failure. When evaluating the region of the duplex (2), we find that there is no failure for a value of $e = 0.02$ (Figure 4.11 d) or even for $e = 0.025$, and a possible failure for right and left-lateral sense for a value of $e = 0.03$ occurs between $m = 64^o$-120^o for right-lateral slip and $m = 272^o$-332^o for left-lateral slip (Figure 4.11 c).

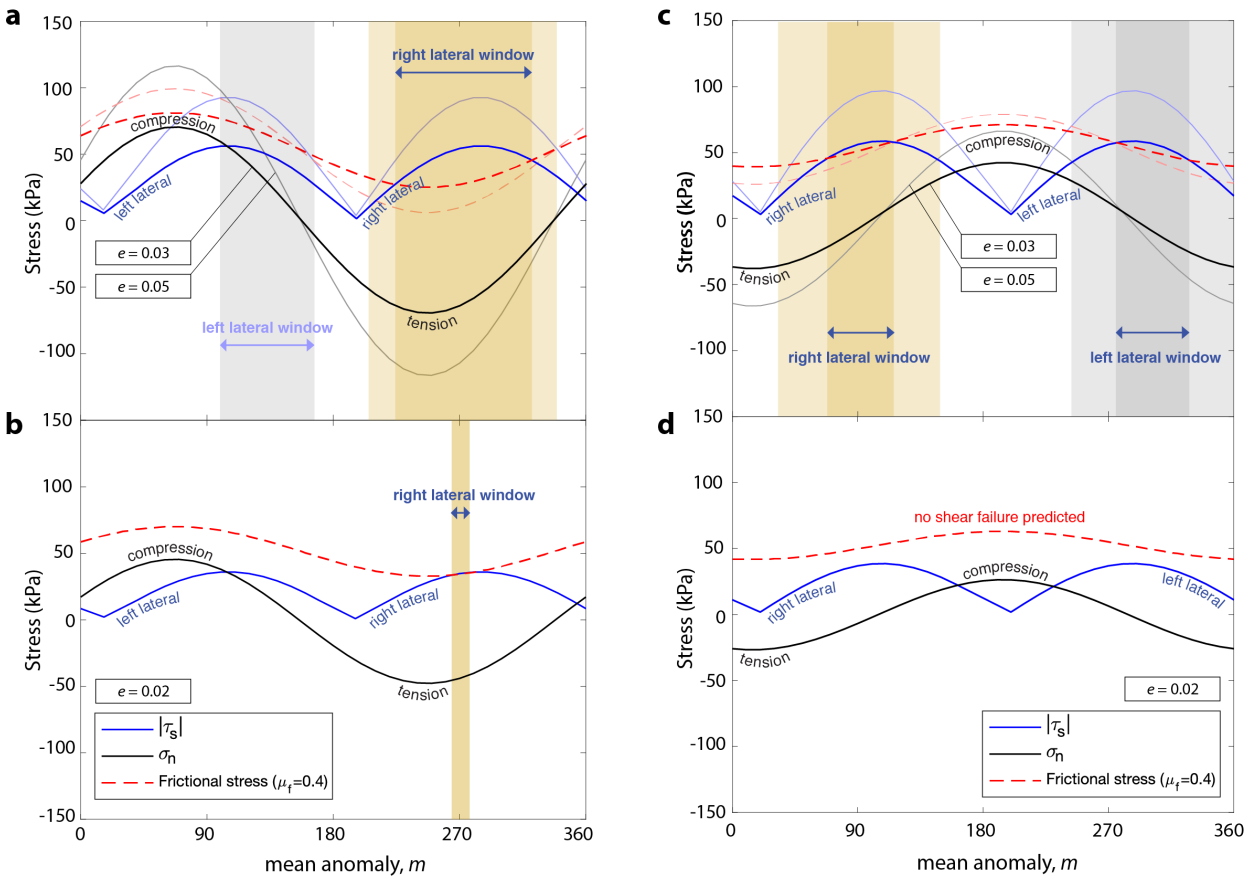

Figure 4.11. Comparison of tidal stress and failure thresholds for high eccentricity values at Nippur/Philus Sulci for the RL (4) and duplex (2) regions. Coefficient of friction of μ_f = 0.4 with observational depth z = 100 m. Resolved normal (σ_n, solid black line) and absolute shear (|τ_s|, solid blue line) tractions for the average orientation of β as a function of mean anomaly, m (orbital position). Frictional stress represented by the red dashed line. Shear failure arises when the shear stress is greater than the frictional stress (shaded regions). Tidal stress scenarios at RL region (4) for eccentricities of **a)** e = 0.05 and 0.03 and **b)** the failure limit for an eccentricity of 0.02. Tidal stress scenarios at duplex region (2) **c**) for e = 0.05 and 0.03, and **d)** 0.02 eccentricity.

Besides the duplex-like structures (2), the younger terrain domain B also contains inferred *en echelon* structures (1; Cameron et al., 2018a). When evaluating this region north of the duplex) with an average orientation of β = 36° (Figure 4.12 a), we find that failure could occur readily for an eccentricity value of e = 0.05 with windows for right- and left-lateral displacement between mean anomaly position m = 27°-146° for right-lateral slip and m = 234°-357° for left-lateral slip. These windows shrink to m = 55°-120° for right-lateral slip and m = 259°-332° for left-lateral slip

with an eccentricity value of e = 0.03 (Figure 4.12 b). When testing with a value of e = 0.025 (Figure 4.12 c), there is only failure possible for a left-lateral shear direction between m = 279º-311º for the observed average orientation of β = 36º. Using Eq. 1 to calculate the shear and normal tractions for a full range of fault orientations (β = 0º–360º) at 10º intervals, we can demonstrate the dependence on fault orientation β by creating diagrams for Coulomb failure as a function of fault trend (Figure 4.12 a, c). To illustrate the Coulomb criteria, we use Eq. 2 and adopt a binary color scheme to identify positive (free slip) and negative (locked fault) Coulomb stress regimes on circular diagrams, where the span of the wedge indicates the range of orientations of possible fault trends. Fault plane orientations with negative Coulomb stress are shaded black, indicating fault orientations that would be locked. Orientations with positive Coulomb stress are shaded in gray, representing fault planes that would be free to slip. These Coulomb failure orientation diagrams show that possible fault orientations that could experience slip are numerous between m = 220º and 310º in a right- and left-lateral sense.

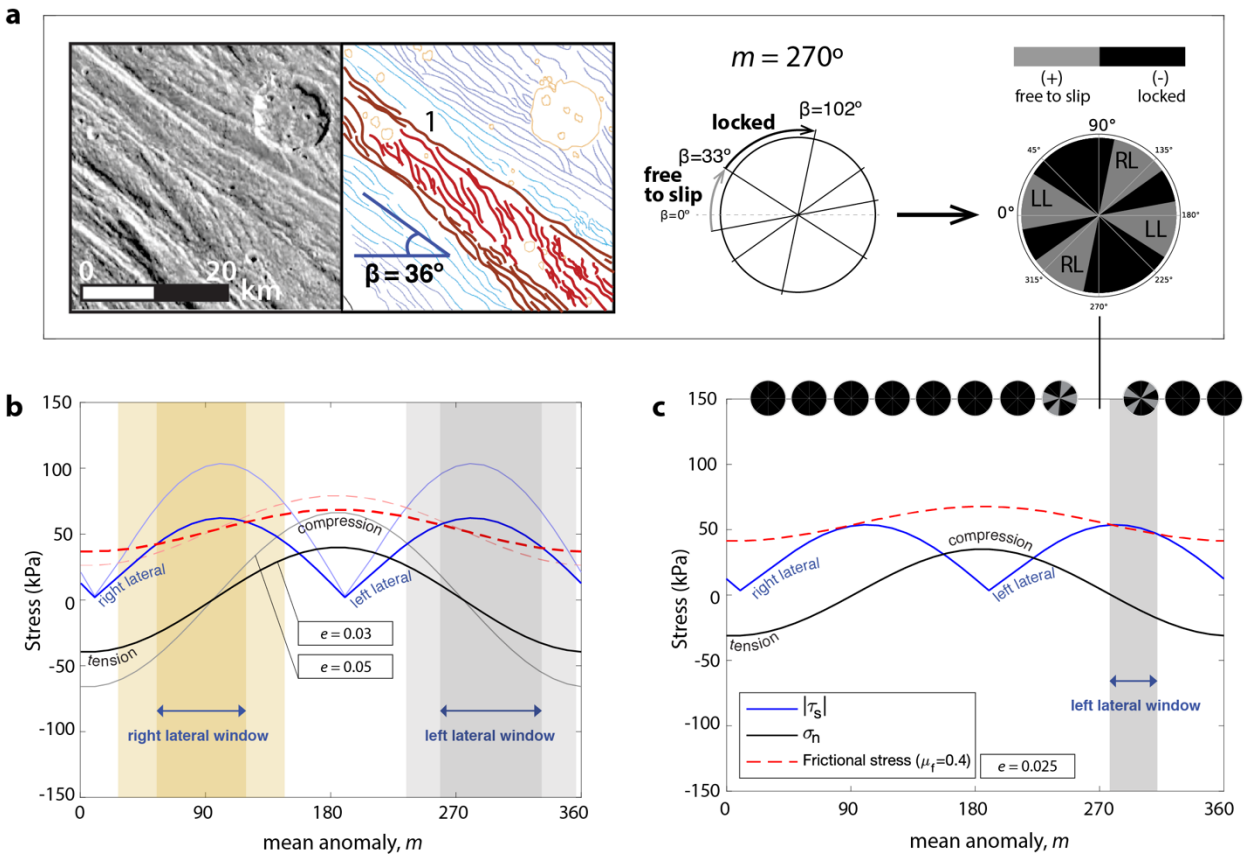

Figure 4.12. Coulomb failure for *en echelon* location (156ºE, 50.5ºN). **a)** mapping sketch with average feature orientation of β = 36°. Coulomb failure orientation diagram at m = 270º, calculated with a coefficient of friction μ_f = 0.4 and observational depth z = 100. Fault plane orientations with positive Coulomb stress

values are shaded in gray, indicating orientations that are free to slip. Black shaded regions represent fault orientations that are locked. Sense of slip for orientations indicated as LL (left-lateral) and RL (right-lateral). **b)** Resolved normal (σ_n, solid black line) and absolute shear ($|\tau_s|$, solid blue line) tractions for an average feature orientation of β = 36° with eccentricity e = 0.03 in thick lines and e = 0.05 in subdued lines, as a function of mean anomaly, m (orbital position). Frictional stress represented by red dashed line. Shear failure will occur when the shear stress is greater than the frictional stress (shaded regions). **c)** Coulomb failure for an eccentricity of e = 0.025. Coulomb failure orientation diagrams are shown along the top margin, evaluated every m = 30°. Possible fault orientations β that could experience slip are estimated within the gray wedges, while black wedges depict locked orientations. Failure is possible between m = 220° and 310° for various fault orientations, and for β = 36° specifically between m = 279°- 311°.

4.5 Discussion

The surface of Ganymede can be divided into dark and bright terrains conditional on differences in albedo, surface morphology and crater density (Oberst et al., 1999). The morphology is mainly driven by tectonization, which is characterized by the presence of grooves and furrows. These structures illustrate the brittle deformation of the icy shell. We focus our analysis on the terrain located in the region of Nippur/Philus Sulci, a terrain that is strongly deformed by sets of parallel/sub-parallel (often evenly-spaced) grooves at both a regional and local scales. The crater counts for Nippur/Philus Sulci demonstrate the effectiveness of this region to determine, at minimum, the relative age of individual geologic units. Stretching from North to South, this region offers the opportunity to study five distinctive geologic units aligning on one longitude. The Nippur/Philus Sulci crater size frequency distribution (Figure 4.8) shows that the southern Marius Regio dark terrain (E) is older than its light northern neighbors, which is consistent with stratigraphic findings. Because cumulative distribution reflects surface age by a upper right/lower left diagonal offset, as shown by the slope of terrain unit E, it can be concluded that terrain E is indeed the oldest by crater count analysis alone. The produced crater size frequency distributions also support the inferred three main stages of tectonic deformation identified by Cameron et al. (2018a), affirming that unit E was fractured during the initial deformation period (stage 1), and furthermore, we note that some structures may be impact related furrows in this oldest unit as the appearance of this domain is much more heavily fractured than the younger units.

The prominent unnamed strained crater (Pappalardo and Collins, 2005) in unit E suggests that during stage 2, possible right-lateral shearing could have affected the region and formed unit A through normal faulting. The tectonic deformation analysis by Cameron et al. (2018a) concludes that unit B was formed during deformation stage 3, which is also evident in the crater size frequency distribution analysis presented. Unit D contains furrows trending NE-SW (whereas the youngest domains trend more NW-SE), containing offsets of drag features (Figure 4.7; features 3 and 4) along a simple shear axis (Cameron et al., 2018a). This makes area D more difficult to date in a cross-cutting mapping analysis. Our crater counts ranging from 400-900 m in diameter (supplementary material) indicate that terrains D and A are of similar age. Terrains C and B are also closer in age to one another than they are to terrains A and D, as indicated by their distribution that is offset to the SE of the plot (Figure 4.8). We can resolve distinct phases of tectonic activity analyzing these crater densities, and the most recent phase, encompassing terrain units B and C, appears to be correlated in time with the formation of Gilgamesh impact basin, as indicated by the slopes. However, the steeply sloped cumulative size-frequency distribution, especially of terrain C, implies a large proportion of small craters relative to large craters within the population, and is indicative of secondary cratering. However, by examining the morphologies and cross-cutting relationships relating the terrains, it is obvious that unit C must be the youngest, as it has a very smooth appearance and few craters.

As shown in Figure 4.6, the second most recent era of activity, which led to the formation of terrains A and D, could be correlated with a time of higher eccentricity. Region D contains the modeled RL offset feature (Figures 4.7, 4.9), where we can reproduce a dominant right-lateral offset for eccentricities as low as $e = 0.02$ (Figure 4.11 b) for the observed feature orientation. For terrain unit B however, the results are not as clear, as seen in the almost equal right- and left-lateral failure windows for the orientation of the duplex structures of 116º for right- and 118º for left-lateral at $e = 0.05$ (Figure 4.10) and 56º and 60º for $e = 0.03$ (Figure 4.11 c, d). The *en echelon* structures in the same unit also have the potential for left- and right-lateral failure at higher eccentricities, but only fail in a left-lateral sense for a window of 32º at the threshold value of $e = 0.025$ (Figure 4.12). However, observational analysis focused on R shears (Cameron et al., 2018) concludes that the dominant shear direction is in a right-lateral sense (Figure 4.14). Our eccentricity modeling analysis agrees with the strain ellipse evaluation from mapped features of Cameron et al. (2018) for stages 1 and 2 (Figure 4.14 b), however, not for stage 3 (Figure 4.14 a, grey; revised version from eccentricity analysis in Figure 4.14 c). P shears are symmetrically oriented to R shears and can also form *en echelon* arrangements (Figure 4.14 d). These shears

are accommodating the shortening parallel to the fault and are contractional (Woodcock and Fisher, 1986). P shears are less common than R and R' shears because they need a larger fault displacement to form. Initial first-order R shear structures can become inactive and confine along the P shear zone (Naylor et al., 1986).

To further explain the difference in inferred slip direction from classic first-order Riedel shear features (Figure 4.3), we can refer to the possibility of normal slip along connecting faults that transfer fault slip (Figure 4.13 a), a transtensional regime with a combination of oblique strike- and normal slip along connecting faults (Figure 4.13 b), possible rotation where the vertical axis rotation of intervening fault blocks transfers fault slip along connecting faults (Figure 4.13 c), and especially passive *en echelon* folds which are stepped and allow determination of the potential slip direction of a related fault (Figure 4.13 d). These are common above strike-slip faults that have not broken the surface and are arranged spatially in a manner where depressions in successive folds lie along lines in an acute angle with the roughly parallel fold axes. *En echelon* structures and duplexes are prevalent in the youngest domain throughout Ganymede (DeRemer and Pappalardo, 2003; Cameron et al., 2018a). Strike-slip duplexes can form at confining bends and small *en echelon* faults can dissect the interior of the duplex (Woodcock and Fischer, 1986). Within the light terrains on Ganymede, duplexes form mostly due to extension (Pappalardo et al., 1998). The occurrence of such structures in light terrains is hypothesized to be also determined by processes of tilt-block normal faulting, which creates regularly spaced ridges and troughs (Mandl, 1987; Vendeville et al., 1987), crustal necking similar to mid-ocean ridges, or major dextral transpression (Papalardo et al., 1998; Rossi et al., 2018). It has been demonstrated that such structures show a fractal spatial clustering, and could represent a preferred pathway for fluid from the ~100-150 km-deep ocean (Lucchetti et al., 2021). Could this also be indicative of an impactor-related cracking of the surface?

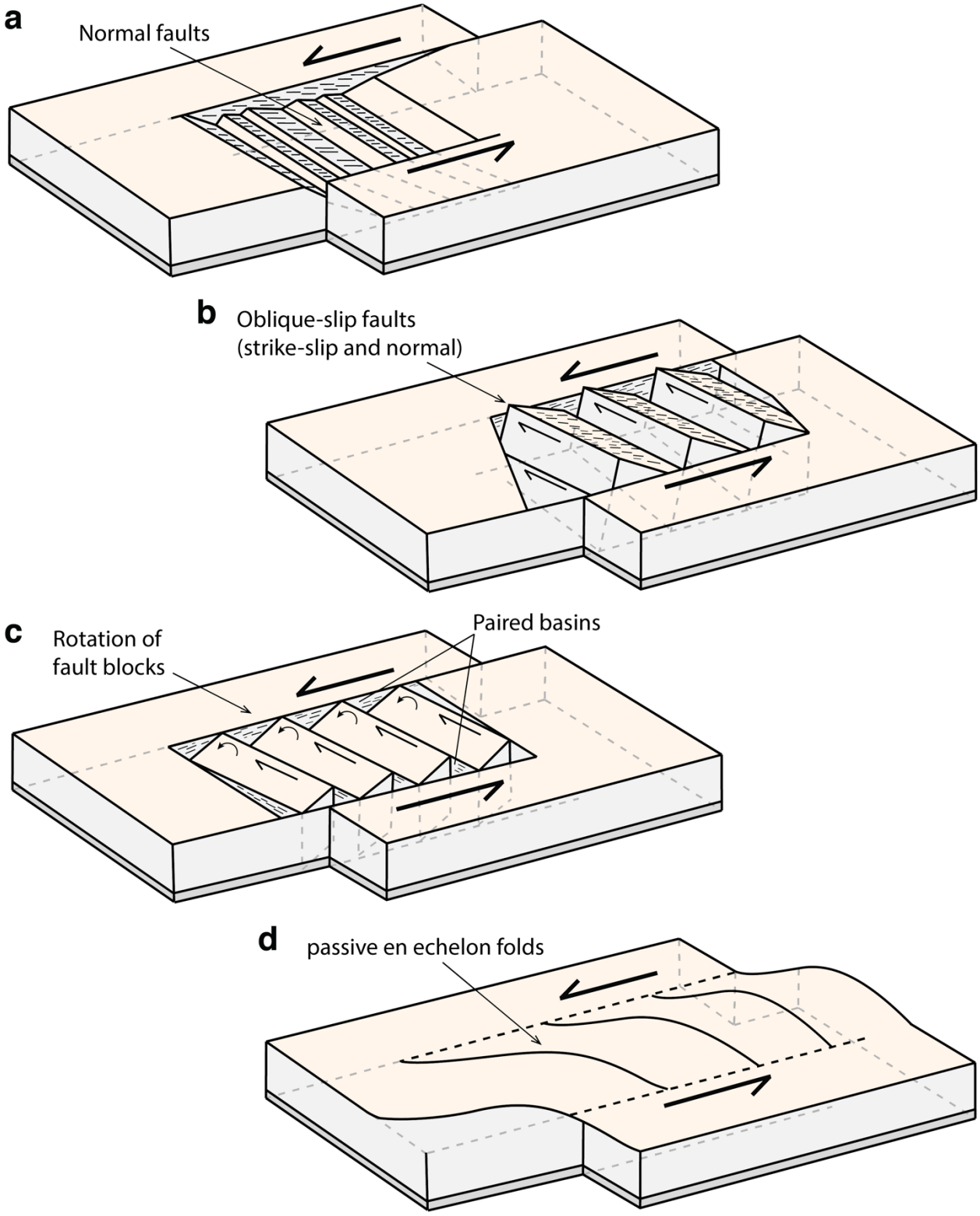

Figure 4.13. Block diagrams (modified and expanded from Nagorsen-Rinke et al., 2012) illustrating proposed modes of deformation to explain fault slip direction and appearance of observed structures. Fault

strike-slip direction is left-lateral. **a)** Displacement transfer model with normal slip along connecting faults that transfer fault slip. **b)** Diagram illustrating a transtensional model with a combination of oblique strike- and normal slip along connecting faults. **c)** Rotation model where vertical axis rotation of intervening fault blocks transfers fault slip along connecting faults (modified from McKenzie and Jackson, 1983; 1986). **d)** Passive *en echelon* folds.

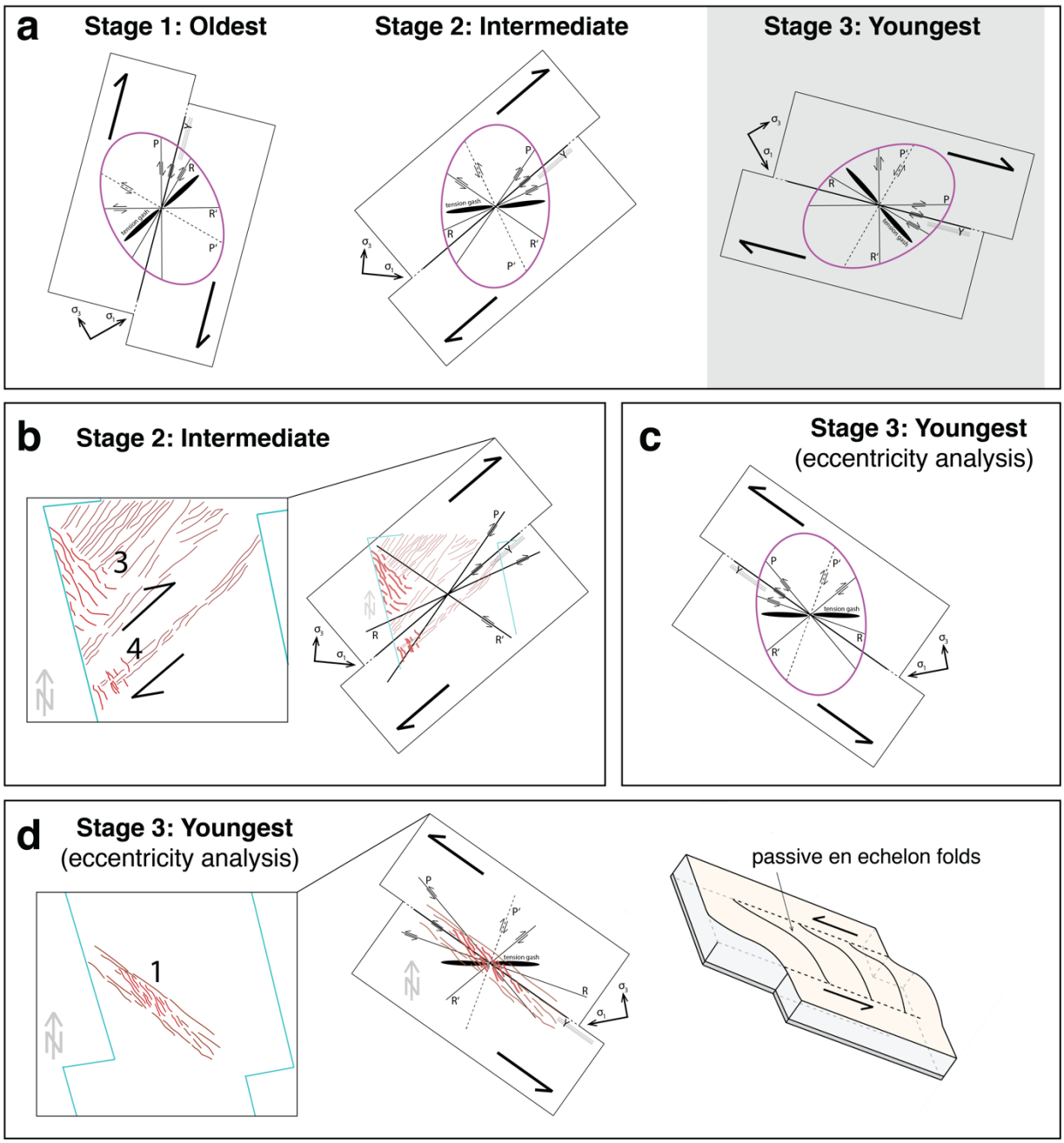

Figure 4.14. **a)** Strain ellipses from Cameron et al. (2018) adapted to block diagrams with sense of shear indicated by arrows. **b)** Stage 2 intermediate terrain site 4 (RL offset) superimposed on strain block diagram

with right-lateral movement. **c)** Stage 3 (youngest) strain ellipse on block diagram from result of eccentricity analysis with left-lateral shear for the modeled feature direction. **d)** Stage 3 youngest terrain location 1 *en echelon* structures superimposed on strain block diagram from eccentricity analysis. Structures do not line up to be R shear structures, but could stem from a passive *en echelon* folding regime or P shears, which require a larger fault displacement to form.

As we hypothesize that at least some of the youngest stage of deformation (extensional tectonism and deformation) might not be associated with a state of higher eccentricity but could be linked to the Gilgamesh impactor, we can infer from the iSALE (impact-SALE; 2-dimensional, multi-material, multi-rheology shock physics code; https://github.com/isale-code/isale-wiki/wiki/About-iSALE) modeling of Hirata et al. (2020) that an impactor with a diameter of 100 km (Figure 4.6) could breach Ganymede down to ~300 km depth, well beyond the assumed bottom of the expected liquid water ocean layer at 190 km depth assumed for this study. However, an impactor with a diameter of 100 km is closer to the upper limit of possible sizes for Gilgamesh, which is hypothesized to have been created by an impactor of ~10^{17}-10^{18} kg (Showman and Malhotra, 1997), corresponding to a pure ice impactor with a diameter between ~60 and 130 km. Such a large impactor could fracture the icy lithosphere and redistribute mass, induce melting and contribute to resurfacing and tectonic activity. Older faults could be reactivated and a disruption of the area antipodal to the impact focused seismic energy would be found (Murchie, 1990), However, there is only patchy and low-resolution observational data available for the area antipodal to Gilgamesh (62ºN, 56ºE) to date. On icy moons, concentric fractures and tectonic deformation to the extent of up to 10 radii from the site of the impact are to be expected (Murchie, 1990). The distance between Gilgamesh and the Nippur/Philus Sulci site is ~5,547 km, which is almost double the 10 radii of the outer limits of the Gilgamesh crater zone border with a diameter of ~585 km assumed to be the basin rim (Schenk et al., 2004). Could the youngest features found at Nippur/Philus Sulci have possibly formed through the cracking of the surface by the Gilgamesh impactor penetrating the ocean layer? Studies note that the relaxation of a crater and the distribution of smooth plains, as is the case with Gilgamesh, may at least partly result from cryovolcanic resurfacing, where craters are either covered or partially infilled by advancing flows (White et al., 2017). The areas around the Gilgamesh site are younger light terrain (Collins et al., 2013), linking a net of younger features throughout the surface and through the Nippur/Philus Sulcus site.

4.6 Conclusions

Building upon recent analyses of Ganymede's global morphology and tidal stress evolution (Cameron et al., 2018a; b; 2019; 2020), we further evaluated the evolution of terrain types, in combination with crater counting analyses, at Nippur/Philus Sulci to gain a deeper understanding of the tectonic history of Ganymede. While crosscutting and superposition relationships provide temporal context for the geologic sequences that produced the light terrains as we observe them today, the absolute age of the light terrains has not been well characterized. Previous estimates of light terrain absolute ages on Ganymede show a significant range, assuming ages between 400 Ma to 3.8 Ga (Neukum et al., 1998; Zahnle et al., 2003). The largest impact basin, Gilgamesh, is dated around 700 Ma (Zahnle et al., 2003). Cameron et al. (2019; 2020) showed that prominent first-order strike-slip features may have been produced by high values of temporally varying tidal stresses. Although Ganymede's diurnal stresses are small today, they may have been much larger during a previous time of high eccentricity, which is hard to constrain in scale through time (Malhotra, 1991; Showman and Malhotra, 1997; Cameron et al., 2020). Given the sizable body of work suggesting that diurnal and long-period tidal stresses play an important role in the development of surface features on ocean worlds throughout the Solar System (e.g., Nimmo, 2002; Hurford et al., 2007; Rhoden et al., 2012), Ganymede could have undergone an intermediate phase in its history where diurnal tidal stresses were a lot higher due to a higher eccentricity caused by two potential Laplace-like resonances previous to the current state (Showman and Malhotra, 1997) and the interior could have been substantially warmer.

The chronology of tectonic activity implied by crosscutting relationships (Cameron et al., 2018a) at Nippur/Philus Sulci is consistent with our findings from analyses of crater densities on each unit. However, there is no absolute consensus on how these individual geologic units formed. The Coulomb failure analysis of the right-lateral (RL) feature (4) indicates that tidal stresses could have induced the movement to form these structures. The right-lateral offset in region D was confirmed by the calculation in a higher eccentricity case (e = 0.05 to 0.02), which could coincide with the intermediate stage of Ganymede during another resonance stage (Showman and Malhotra; 1997) as this geologic unit is dated to be intermediate in age. The duplex is located in the youngest light terrain domain (Cameron et al., 2018a), and our high eccentricity analysis shows two possible slip windows of almost identical duration in right- and left-lateral direction. The *en echelon* structures in the same unit do not correspond in slip direction to Riedel shear structures, but rather to passive stepped *en echelon* folds. Such structures in light terrains are hypothesized to be caused by activities of tilt-block normal faulting, crustal necking, or major

dextral transpression (Papalardo et al., 1998), which could hypothetically be a product of impactor-related cracking of the surface, leading to upwelling and extensional features. Sets of faults resembling duplex and *en echelon* structures are plentiful in Ganymede's light terrain, and related to extensional regimes (DeRemer and Pappalardo, 2003; Cameron et al., 2018a). A recently published study investigating the concentric furrows in the oldest dark terrain units on Ganymede reveals that an ancient impactor must have struck the surface (Hirata et al., 2020). It can be hypothesized that the most recent formation of some light terrain features could be correlated with another large impactor such as Gilgamesh.

New images from NASA's Juno mission as well as future observations by the Jupiter Icy Moons Explorer (JUICE) mission of the European Space Agency that will investigate Ganymede in great detail will help to advance our understanding of the tectonic history of Ganymede. JUICE's RIME (Radar for Icy Moon Exploration) instrument for example will be able to characterize the subsurface ice shell structure, through which we can explore tectonic features and their geological evolution, and possibly find more direct evidence to link the Gilgamesh impact to the last large-scale tectonic activity. As our crater analysis agrees with previous studies of the sequence of tectonic events, we can use our method to expand upon the inferred history of Ganymede. The NASA Roadmap to Ocean Worlds (Hendrix et al., 2019) seeks to enhance our understanding of the geophysical processes that promote geologic activity and potentially habitability within the outer Solar System. New studies aim to build a structure for understanding first-order controls on the evolution of icy moons (Nathan et al., 2022), and the results presented here tie into this framework by offering candidate models of surface deformation mechanics that can also help inform future exploration of ocean worlds.

Supplementary material

Crater in areas A, B, C, D and E see *APPENDIX. Chapter 4 supplementary material* p. 125.

CHAPTER 5. CONCLUSIONS

5.1 Summary

This dissertation investigates the required stresses to initiate strike-slip fault movement on the most prominent strike-slip fault on Earth - the San Andreas Fault - and the large icy moons Titan and Ganymede. Beginning with a detailed stress accumulation study of the San Andreas Fault System (SAFS), we explore the hypothesis that the region of the Cajon Pass could act as an 'earthquake gate' as the San Andreas Fault (SAF) branches with the San Jacinto Fault (SJF), and produces multifault events through a stress threshold that unclamps the 'gate'. The rate of stress is a function of the applied slip rate and locking depth, and consequently, segments with high slip rates and/or shallow locking depths have higher stress rates. Multifault rupture paths can affect different receiver faults compared to a single fault rupture, as stress is transferred through this region of complex faulting. Chapter 2 also reviews characteristics of long ruptures and we can conclude that they commonly occur on continuous faults and segments with similar characteristics as well as limited branching, such as the segments on the main SAF trace. The SAF and the SJF have possibly ruptured together multiple times in the past and because of the structural geometry around the Cajon Pass and fault maturity, a joint rupture of the SJF with the Mojave section of the SAF is more likely to cause a major earthquake in Southern California than a rupture propagating towards Coachella Valley on the main SAF originating from the Mojave segment. The model presented can provide a conceptual framework for investigating the conditions that lead a fault to failure; however, there has been little evidence previously that faults rupture at a uniform threshold (Murray and Segall, 2002) or even just periodically (Scharer et al., 2010). If large ruptures are terminating, originating or passing through the Cajon Pass region as identified in the paleoseismic record, more work is needed to identify all responsible factors.

As strike-slip faulting has been observed on several icy moons in our Solar System, Chapter 3 explores the stress and conditions needed for strike-slip faults to exist on Saturn's largest moon Titan. It has been established that the source of possible tectonic activity on icy moons can be tidal stress experienced through the interaction with the parent planet. Because Titan has confirmed stable liquids on its surface, and therefore likely in the shallow subsurface, we can make the argument to integrate pore fluid pressures in the calculation, which reduce the resistance of the crust to shear stress. As Titan's surface is not well explored and only partially and coarsely mapped, inferences of strike-slip faults are very unclear and speculative to date. The study presented here computes systematically possible temporally varying stress

distributions with a realistic set of parameters for Titan and bridges the model results with observations from the surface. This work fills a knowledge gap for the study of Titan tectonics and concludes that strike-slip fault movement could be a currently active deformation process within the icy crust.

While Titan's present eccentricity (e = 0.0288) yields diurnal tidal stresses that are large enough to induce strike-slip faulting when combined with pore fluid pressures, Ganymede's eccentricity is currently too small (e = 0.0013), and no fluids are present on its surface to support any additional reduction in the strength of the icy crust. However, large offsets and other strike-slip indicators have been confirmed on its surface. In Chapter 4, we investigate the tectonic history of Ganymede through an analysis of the example region of Nippur/Philus Sulci using a combination of mapping, tidal stress models as well as crater counting methods. Stretching from North to South, this area from the currently available limited high-resolution data on Ganymede consists of five distinctive geologic units aligning on one longitude, eliminating the otherwise needed correction of leading/trailing hemisphere discrepancies in cratering rates, which has not been clearly defined for Ganymede to date. This study demonstrates the effectiveness of this region to determine the relative age of individual geologic units as well as determining real ages for future analysis. We demonstrate that during Ganymede's past, the failure potential due to variable diurnal tidal stresses caused by a higher past eccentricity could be quite significant. Modeled stresses are over 100 kPa greater than in the present orbital configuration. The opportunity for failure is however also limited to shallow depths (<250 m for e = 0.03) as they are for Titan (<900 m), and in general highly dependent on the distance to the parent planet during orbit. Ganymede could have also experienced tectonism through large impactors in the past, and future work will bring more insight into this hypothesis as more surface data is acquired.

Combined, these three studies in principle explore the stress values needed to produce movement for strike-slip faulting for a variety of crustal properties and provide new insights and contributions to the terrestrial as well as icy moon literature. A wide range of planetary issues, from surface measurements and morphological mapping to global tidal stress processes that drive and evolve large-scale tectonics, is covered. Given that ocean worlds are among the highest priority destinations to search for life beyond Earth, this dissertation attempts to uncover the potential of strike-slip tectonism on icy moons and interpret the tectonic past using the limited information available to date to provide a basic framework for future analyses with improved data resolution and additional methods.

5.2 Future work

5.2.1 Objectives and future directions for modeling

Stress accumulation plays an important role in terrestrial earthquake hazard assessments, and fault junctions such as the Cajon Pass can be a major element in the assessment of large strike-slip events. Because of this, detailed modeling of fault behavior and stress transfer on major fault junctions around the globe beyond the SAFS is needed. The model presented here considers only a vertical fault plane, and an improved analysis of the Cajon Pass should ideally include the individual average dips of the adjacent segment fault planes, as for example the SAF in the Cajon Pass area is interpreted to dip 40º-50º NE (Fuis et al, 2012; Barak et al., 2015). Our physics-based model makes use of historical and geological observations to calculate and interpret the stress accumulation at any given time. As stress accumulation and threshold modeling is dependent on the resolution of the paleoseismic record, regions with many active faults should consider all ruptures near the main fault as dating and computational methods improve. The methods outlined for the SAFS can also be translated to any of the icy moons in our Solar System when higher resolution data is returned in the future, evaluating the hazard of faults for surface explorations.

For icy moons, this dissertation primarily focuses on using the Coulomb failure criterion for assessing the possibility of slip along an inferred fault. However, this principle only applies if the overburden stress is larger than the tensile traction, as otherwise the fault would dilate and the Coulomb failure criterion does not apply. Tensile tractions facilitate fault slip because the pull on the fault reduces the frictional resistance between the surfaces. As noted in this work, the Coulomb failure criterion is most easily met when tensile tractions dominate. In near-surface regions (<50 m), where tensile tractions are larger than the overburden stress, frictionless shearing and slip are easily facilitated when shear stress is applied. Because the overburden stress must be larger than the tensile traction for the Coulomb criteria, this work evaluates the *z*-depth dependence of the overburden stress at 100 m discretized depth observation planes. For compressive regimes, no melting was assumed, as melts reduce the frictional resistance of the fault surfaces significantly and could potentially lead to orogeny. For the case of compressive tractions, this dissertation assumes that a fault interface will always be clamped together, unable to move.

Therefore, future modeling efforts should also explore other failure criterions such as Amonton's frictional failure and Byerlee's law, which consider the reactivation of preexisting fractures, whereas in this context the Coulomb failure criterion governs the creation of new

fractures. The formation of new fractures is related to a drop in strength upon failure. Byerlee's law describes the required shear stress for frictional sliding on existing faults. In essence, Byerlee's law is about the governing relationship between the critical frictional shear stress and normal stress on an existing shear plane, whereas the Coulomb failure criterion is about the shear and normal stress relationship when creating new fractures. When considering Byerlee's law, the preexisting weakness directions should be defined (Burr et al., 2009). Calculations for the failure tendency of a preexisting weakness in three dimensions are discussed in Tong and Yin (2011). Based on these criteria and methods described in these terrestrial-based publications, an analysis complementary to those presented here could improve the current understanding and behavior of preexisting observed fault zones on icy moons. Valuable insights could be gained especially for regions of high tensile stresses, as future instrumentation missions to these icy moons will focus on collecting data within the immediate subsurface (<50 m).

The SatStress model calculating the tidal stress tensor components assumes a 4-layer satellite body only, which is likely not completely realistic for many icy moons, especially Ganymede (Vance et al., 2014). Assuming an upper ice layer, lower ice layer, liquid ocean layer, and core only is a solid first conjecture in the effort to model tidal stress and subsequent shear failure; however, upgraded detailed layering as well as additional information on the interior of icy satellites is needed for more thorough future models.

5.2.2 Upcoming spacecraft missions

At present, we are lacking global high-resolution coverage of Ganymede and Titan. In addition, Titan has a thick atmosphere, and mapping complex features from the currently available RADAR data is very difficult. For Ganymede, expanding and interpolating from regional high-resolution images and mapping analyses to a global observation is problematic. The new additional images from NASA's *Juno* mission as well as future observations from the Jupiter Icy Moons Explorer (*JUICE*) mission of the European Space Agency investigating particularly Ganymede in great detail will significantly advance our understanding of Ganymede's tectonic history and evolution. *JUICE* will carry multiple spectral imaging instruments such as MAJIS (Moons And Jupiter Imaging Spectrometer), SWI (Submillimeter Wave Instrument), UVS (Ultraviolet Spectrograph), and the JANUS optical camera (Jovis, Amorum ac Natorum Undique Scrutator) mapping Ganymede globally at a resolution of 400 m/px (Della Corte et al., 2014). For Titan, NASA's *Dragonfly* mission is a novel rotorcraft that will take advantage of Titan's dense atmosphere and fly to several locations, investigating mainly chemical processes. It will be the

first vehicle ever to fly its entire payload to new target areas, travelling at a speed of about 36 km/h. *Dragonfly* will carry a mass and Gamma-Ray/Neutron spectrometer (DraMS, Dragonfly Mass Spectrometer; and DraGNS, Dragonfly Gamma-Ray and Neutron Spectrometer) to identify chemical elements, as well as a suite of meteorological sensors and a seismometer (DraGMet, Dragonfly Geophysics and Meteorology Package) on board. The DragonCam (Dragonfly Camera Suite) will image Titan's terrain with a set of eight cameras for imaging areas for sampling and build 360° panoramas (Lorenz et al., 2018). The mission is scheduled to land on Titan in 2037. Data from the seismometer in particular will be very useful to constrain the interior layers of Titan and significantly improve any of our current tidal stress models. For Ganymede, the GALA (Ganymede Laser Altimeter) instrument will give information about the tidal deformation, and RIME (Radar for Icy Moons Exploration) is able to penetrate the icy surface to characterize the subsurface (Bruzzone et al., 2013; Lingenauber et al., 2014). Together with the magnetometer investigating the unique internal magnetic field of Ganymede, we will develop a better overall understanding of the interior. Combining any of these new observations with the modeling techniques presented in this dissertation will strengthen our understanding of the tectonics on icy moons and identify the best locations for future lander missions and even possible access to the interior ocean.

APPENDIX. Chapter 4 supplementary material

Craters A

lon	lat	diameter (km)	lon	lat	diameter (km)
157.1207	51.6892	7.9106	157.0853	52.2216	0.7725
156.7705	52.0930	2.3522	156.6780	52.2002	0.7725
156.8995	52.2033	2.3522	156.9659	52.4459	0.7571
156.8765	52.5100	2.1362	156.6339	51.8257	0.7318
157.5584	50.6634	1.9255	156.3214	52.1317	0.6228
157.5077	50.9290	1.8653	156.0437	52.3690	0.5964
156.5171	52.4145	1.7387	157.4506	51.4205	0.5964
157.5906	50.7742	1.7387	156.8281	51.5541	0.5964
156.6238	52.1726	1.7013	156.6040	51.8419	0.5564
156.9404	52.3266	1.3953	156.7737	51.7176	0.5564
156.5588	51.8215	1.2214	156.0599	52.3942	0.5564
157.0658	51.8974	1.1747	157.0465	51.3214	0.5564
157.3520	51.3310	1.1297	157.0986	51.1268	0.5215
156.7788	51.9275	1.1261	156.6202	52.4596	0.4926
156.9187	51.2863	1.1228	157.5444	51.0741	0.4091
157.1405	51.0838	1.0925	157.5531	51.0976	0.3771
156.6138	51.8771	1.0822	156.8079	52.2441	0.3561
156.1032	52.4273	1.0543	156.0237	52.3233	0.3298
156.8729	52.2379	0.9302	157.1089	51.2925	0.3298
157.1220	52.0988	0.9181	157.3160	51.6215	0.3298
156.5828	52.0373	0.8703	156.3319	52.3896	0.2892
156.8737	52.3399	0.8680	157.1388	51.2353	0.2667
156.7737	51.3906	0.8284	157.1276	51.1431	0.2332
157.0545	52.0775	0.7963	156.3544	52.3904	0.1829
157.1025	51.8881	0.7821			

Craters B

lon	lat	diameter (km)	lon	lat	diameter (km)
158.0430	47.5004	10.8014	155.7140	51.3347	0.5214
156.4010	50.6653	9.1175	156.8700	50.4360	0.5197
156.2740	48.9810	3.5407	155.4360	52.3462	0.5153
157.4900	47.8763	3.1135	157.0230	50.7640	0.5109
156.2390	48.3429	2.9568	156.8780	47.8536	0.5109
154.8420	51.6085	2.7819	157.1750	47.7892	0.5090
155.2980	50.6149	1.9389	155.7110	49.0630	0.5075

157.4650	50.5584	1.7628	155.7900	48.9160	0.5070
155.2600	49.1650	1.7349	157.2750	48.7605	0.5047
157.7230	49.7210	1.7186	155.9170	52.0868	0.5035
157.6370	47.7989	1.5289	156.9000	50.1188	0.5016
155.2250	50.6610	1.5054	156.7490	47.7733	0.4998
156.6710	49.3163	1.4846	157.2040	50.2682	0.4991
156.2550	48.2217	1.4108	156.4040	48.3492	0.4955
155.7460	51.9991	1.3830	157.5500	47.7645	0.4948
157.7760	47.7832	1.3344	156.4770	50.8375	0.4920
156.9550	49.3790	1.2999	156.8930	50.1740	0.4918
154.7440	49.2607	1.2816	155.2720	51.1677	0.4912
155.5450	50.9067	1.2426	156.3100	50.8164	0.4892
156.1890	50.1528	1.2338	156.8170	48.8552	0.4890
155.7510	52.1425	1.2075	154.7880	49.4240	0.4883
155.4440	51.2694	1.1867	157.2780	49.0341	0.4871
155.6460	52.1318	1.1842	155.5660	51.3339	0.4867
154.6950	49.5191	1.1376	157.2760	50.2468	0.4861
157.4650	48.1179	1.1126	157.5210	50.3996	0.4841
157.0360	49.5899	1.0838	155.2900	51.5383	0.4839
154.6560	52.1097	1.0751	157.2750	49.7923	0.4827
157.3140	48.8478	1.0709	155.8620	51.8877	0.4821
154.5760	51.9876	1.0564	157.4130	50.2341	0.4814
157.4370	49.9824	1.0532	156.6160	47.8660	0.4810
156.0120	48.9810	1.0462	156.9120	50.1470	0.4808
155.9810	51.6259	1.0462	154.5450	52.1453	0.4807
156.8010	47.7450	1.0080	157.4920	49.6340	0.4804
156.2520	51.6822	1.0040	156.9750	50.4493	0.4800
158.0970	47.3729	1.0023	157.2400	49.7751	0.4786
156.5600	49.4160	0.9820	154.9920	51.1854	0.4778
157.1130	49.3098	0.9669	155.2680	51.1831	0.4774
157.7330	50.2297	0.9460	156.5230	50.2662	0.4751
155.7250	51.4373	0.9409	156.1280	51.4782	0.4748
157.3050	50.3249	0.9401	156.2090	51.8023	0.4745
155.2530	50.8245	0.9365	156.5040	51.5484	0.4745
155.4010	51.3973	0.9253	154.7740	49.4435	0.4741
155.1900	49.5561	0.9211	156.3780	48.3520	0.4733
156.8850	50.9319	0.9165	155.7940	51.2798	0.4685
155.2760	48.1164	0.9041	157.2560	49.1312	0.4674
155.1990	48.9409	0.8805	155.8420	48.1493	0.4673
155.4900	50.9497	0.8783	157.4950	47.5924	0.4651

156.3090	51.9668	0.8775	154.8960	51.1624	0.4638
156.8430	49.2975	0.8774	156.8730	50.2906	0.4630
156.4960	48.5770	0.8770	155.7410	52.1960	0.4599
155.4010	51.2827	0.8740	154.7710	51.9508	0.4598
156.0740	50.4136	0.8672	157.0460	47.6928	0.4589
156.5470	50.6713	0.8565	155.0460	50.9562	0.4546
157.5320	47.8134	0.8561	155.6730	52.1824	0.4539
157.3060	47.6954	0.8505	154.8060	51.9197	0.4537
156.5690	48.5963	0.8483	155.8920	52.0597	0.4536
156.2880	50.7329	0.8385	155.6280	47.8814	0.4534
155.4190	48.4196	0.8379	157.6000	49.7389	0.4488
154.7590	49.4614	0.8358	156.8350	50.3304	0.4478
157.2010	50.8247	0.8354	156.8510	47.7870	0.4448
156.7980	50.3096	0.8277	155.7860	48.9341	0.4447
154.8840	51.2418	0.8252	157.7490	49.7882	0.4436
155.0480	50.9214	0.8120	157.0250	47.6925	0.4396
157.0990	50.7343	0.8084	156.8820	50.6935	0.4395
157.8330	49.8334	0.8058	157.7550	49.7638	0.4372
157.4400	49.1738	0.8053	155.2720	48.6884	0.4369
157.1080	50.0640	0.8039	156.9040	47.3058	0.4366
157.0710	50.1620	0.7981	156.8910	50.1397	0.4364
156.9230	50.8895	0.7937	155.8900	51.2570	0.4359
155.3360	51.9402	0.7771	156.4130	48.3152	0.4348
154.7970	52.0358	0.7760	156.8940	47.7699	0.4347
157.3370	49.3991	0.7760	155.4460	48.9030	0.4338
155.1170	51.1712	0.7746	155.7130	49.4772	0.4337
157.5810	50.2628	0.7740	154.9770	50.9379	0.4331
156.7040	49.2662	0.7595	155.5150	48.2799	0.4327
154.8070	51.2219	0.7453	157.2740	48.9583	0.4324
157.7840	49.6553	0.7390	156.8280	48.9683	0.4324
156.3800	50.6024	0.7347	156.1020	47.6929	0.4323
156.4130	50.7007	0.7339	155.6020	48.9365	0.4307
156.8540	50.3065	0.7338	156.5690	49.4625	0.4304
156.8510	50.9147	0.7314	157.7730	49.7751	0.4277
155.6940	52.2037	0.7261	154.8230	49.1857	0.4260
156.7180	50.4823	0.7245	154.8110	51.9311	0.4234
155.7250	48.3143	0.7212	154.7000	49.3857	0.4192
154.7470	51.9600	0.7210	154.9170	51.8659	0.4191
156.5480	51.0845	0.7161	156.6120	47.8037	0.4185
155.5140	50.9881	0.7148	154.5820	52.2135	0.4175

157.7270	50.3391	0.7080	157.5370	50.2162	0.4170
157.7650	49.9504	0.7069	156.9640	50.3587	0.4149
155.7460	52.0640	0.7064	157.5960	49.7218	0.4126
156.5020	51.2433	0.7064	155.3710	49.7608	0.4122
154.8230	51.9097	0.7013	155.4450	51.0458	0.4103
157.1140	50.1886	0.7012	157.1860	47.5658	0.4097
155.7950	48.5252	0.7001	155.4650	49.4909	0.4067
156.1250	50.4402	0.6999	154.8690	52.1540	0.4053
156.3250	47.6409	0.6991	156.8880	49.9276	0.4045
157.2510	47.7728	0.6975	157.1290	48.9165	0.4033
155.2030	49.0626	0.6969	156.9050	50.1343	0.4026
157.2070	50.4496	0.6956	157.2540	50.0071	0.4013
156.9450	50.4704	0.6942	157.1010	50.0266	0.4012
157.2530	50.5995	0.6927	156.6990	50.6249	0.3987
156.7780	49.7220	0.6922	156.6320	50.7426	0.3982
156.0020	49.7838	0.6914	156.9860	49.3320	0.3974
155.8020	51.5152	0.6889	156.3640	47.9977	0.3972
156.7170	50.4627	0.6886	155.6460	48.5720	0.3971
156.8800	50.2775	0.6833	157.6190	49.6027	0.3963
156.9790	50.8589	0.6822	155.6510	48.9306	0.3911
155.6810	49.8473	0.6821	157.6670	49.6773	0.3911
156.0930	50.1924	0.6813	155.9780	51.0558	0.3905
156.4360	51.6578	0.6768	156.8300	50.4106	0.3887
155.2700	48.9376	0.6753	157.4770	50.2167	0.3870
156.9740	48.9820	0.6710	155.5910	51.3342	0.3864
156.1980	51.1090	0.6682	156.5520	50.1746	0.3864
156.0060	51.2396	0.6673	156.2280	50.8875	0.3857
157.9820	47.7201	0.6623	156.1840	49.4804	0.3849
157.4900	49.1813	0.6607	156.9250	49.7481	0.3818
156.3570	51.3454	0.6585	157.3360	50.2410	0.3816
157.9000	47.4901	0.6560	157.0770	49.9923	0.3784
155.7630	51.2120	0.6476	155.6250	48.6306	0.3777
156.6480	48.5497	0.6443	156.1330	51.8529	0.3648
157.7590	47.5253	0.6384	156.8290	50.4651	0.3647
156.4870	50.6669	0.6380	155.4980	48.5964	0.3639
157.3140	49.8728	0.6368	156.1260	51.8691	0.3628
156.6910	50.4907	0.6326	154.9410	51.2164	0.3620
156.7950	50.4617	0.6255	155.6220	51.2939	0.3617
155.3860	49.7411	0.6196	155.2930	51.4758	0.3612
157.6680	49.8867	0.6167	155.3780	51.4724	0.3609

156.7850	50.4408	0.6157	154.7920	51.2455	0.3596
154.5640	51.4510	0.6132	154.7620	49.2194	0.3575
156.7090	50.5039	0.6115	155.2840	48.6773	0.3559
157.2750	48.6941	0.6105	157.3660	49.2562	0.3515
157.0310	47.7087	0.6092	155.6440	50.8170	0.3421
157.1560	49.4901	0.6043	155.6140	48.5873	0.3411
157.3880	49.4305	0.6006	155.4740	48.0894	0.3369
157.7230	47.5359	0.6005	157.2220	47.7960	0.3293
155.9510	50.2816	0.5961	155.3120	51.4722	0.3277
156.6660	50.5737	0.5947	157.1340	50.7132	0.3268
155.3260	52.0005	0.5945	157.6910	49.7971	0.3251
157.1760	47.8020	0.5920	156.9270	50.1646	0.3251
155.9880	48.9617	0.5904	156.0990	47.6193	0.3245
155.7740	51.1717	0.5901	156.8940	49.3820	0.3242
156.1610	51.4091	0.5893	154.8610	51.1256	0.3241
156.6000	48.5116	0.5892	157.3060	49.8356	0.3227
155.0200	50.9452	0.5859	156.9190	50.1167	0.3155
157.1870	50.2214	0.5842	157.3230	49.8505	0.3055
157.3280	47.5836	0.5812	156.8040	49.3786	0.3046
157.4670	48.5336	0.5807	156.7780	49.8038	0.3033
156.8450	50.3201	0.5785	154.9300	49.1126	0.3014
155.6380	52.0347	0.5784	155.9450	50.6361	0.3006
157.2240	49.4974	0.5784	156.9440	49.9423	0.2993
154.7510	52.0922	0.5781	157.9410	49.7445	0.2953
156.9750	50.2799	0.5758	156.7740	49.5985	0.2883
157.4350	48.0593	0.5755	156.4510	50.8940	0.2876
157.6160	47.4422	0.5752	155.1270	52.1965	0.2876
156.5570	50.0718	0.5739	155.3120	51.4552	0.2742
157.7290	47.5154	0.5734	157.1980	50.0635	0.2673
156.0010	51.0403	0.5665	156.2570	50.8047	0.2652
155.5220	49.9024	0.5659	154.7470	49.4167	0.2650
157.2120	49.4726	0.5648	156.9560	47.7588	0.2647
155.1860	51.6293	0.5629	155.8660	51.9025	0.2631
155.3620	47.8820	0.5600	155.2720	51.0103	0.2616
154.6660	49.5499	0.5598	154.8800	52.2200	0.2581
157.0430	49.7771	0.5594	155.6960	48.5405	0.2543
156.7510	50.1769	0.5589	156.9490	50.1147	0.2519
157.1480	50.8228	0.5585	155.6310	48.5465	0.2517
155.9210	48.2075	0.5573	157.1240	50.0071	0.2466
156.8260	49.3369	0.5553	155.5540	49.5742	0.2385

155.0960	52.1012	0.5538	157.6820	49.7885	0.2326
156.3040	50.8771	0.5485	156.9760	50.1202	0.2315
157.3010	49.8059	0.5474	155.1980	51.0092	0.2294
156.5150	51.5615	0.5445	157.0780	48.3196	0.2194
154.8890	49.1209	0.5435	157.3720	49.3285	0.2172
157.2700	47.5775	0.5433	157.3530	49.3585	0.2171
156.4410	49.7709	0.5394	157.4000	49.1757	0.2158
156.3720	50.9204	0.5364	157.2880	49.7404	0.2088
156.7140	50.4054	0.5355	157.2730	49.7517	0.2088
157.1190	50.1226	0.5344	154.9180	51.0891	0.2050
156.4780	50.5216	0.5322	154.7440	49.4363	0.1987
155.7940	51.9413	0.5314	156.7840	50.5125	0.1881
157.0620	49.5555	0.5305	156.2800	50.8220	0.1875
156.6850	50.5051	0.5304	157.4520	49.6553	0.1869
155.5070	49.9194	0.5293	154.7900	49.1990	0.1505
156.9890	50.3591	0.5281	156.0340	50.9930	0.1457
157.3030	47.7167	0.5265	156.1460	51.4270	0.1317
157.3000	47.5786	0.5252	156.7510	49.3290	0.0963
157.1520	50.2675	0.5218			

Craters C

lon	lat	diameter (km)	lon	lat	diameter (km)
156.3250	47.6409	0.6991	156.9250	47.3249	0.2211
156.5720	47.6287	0.4081	157.2120	47.4956	0.3034
156.6070	47.6214	0.4155	158.1090	47.2124	0.7598
156.6710	47.6146	0.4206	157.8450	47.1954	0.4630
156.0590	47.7742	0.6783	157.4550	47.4335	0.4209
156.0560	47.7883	0.4309	157.6580	47.3313	0.4365
155.8830	47.8078	0.6191	157.5610	47.3792	0.5977
155.8080	47.9333	0.5257	157.6130	47.3816	0.3611
155.8350	47.9095	0.6300	157.6070	47.1956	0.1844
155.8430	47.8923	0.4392	157.3770	47.1525	0.2895
155.7910	47.8852	0.4130	157.4200	47.1052	0.3238
155.4530	48.2307	0.3400	157.4530	47.2038	0.3724
155.4630	48.2216	0.2677	157.1010	47.3313	0.3612
155.4440	48.2192	0.3701	157.1190	47.3151	0.3428
155.5770	48.0638	0.3693	157.0360	47.3930	0.2553
155.5560	48.0828	0.3980	156.9260	47.3849	0.2042
155.5130	48.0731	0.4347	156.7140	47.4335	0.3680

155.5590	48.0616	0.4168	156.9450	47.4890	0.1839
155.8410	47.7462	0.6411	156.8040	47.5876	0.4699
155.8370	47.7065	0.5913	156.4640	47.6062	0.5121
155.8800	47.7230	0.4767	156.6580	47.7207	0.5804
155.3820	47.8815	0.4334	156.6070	47.6853	0.4105
155.4530	47.9340	0.5023	156.8900	47.5652	0.4204
155.6140	47.8893	0.5210	156.8480	47.6314	0.1139
155.7630	47.9334	0.4372	156.8850	47.6047	0.2279
156.0810	47.6710	0.3749	156.1010	47.5902	0.2598
156.4380	47.7853	0.3650	156.2340	47.5134	0.9903
156.4400	47.7727	0.5084	156.0450	47.6419	0.1528
156.9940	47.6007	1.2190	155.9990	47.6459	0.4805
156.7250	47.5373	1.0286	156.0460	47.6144	0.4202
156.7720	47.5719	0.6554	155.9300	47.8303	0.6688
156.0670	47.7301	0.9075	155.9730	47.7885	0.6104
155.6560	48.0964	0.5719	155.9070	47.8967	0.7622
155.7930	47.8334	0.6538	155.9610	47.9657	1.6281
155.7890	47.7617	1.1037	155.2510	47.9881	0.7882
156.2260	47.7595	0.5401	155.2450	48.2395	0.7109
156.0690	47.8295	0.7859	155.1910	48.2889	0.6158
156.1370	47.6724	0.3057	155.3210	48.1338	0.3016
157.0780	47.2717	0.3432	155.4740	48.0894	0.2800
157.2100	47.3269	0.7276	155.6280	47.8814	0.5071
157.1060	47.3562	0.8942	155.2760	48.1164	2.0169
157.5500	47.3252	0.9268	156.1020	47.6929	0.4611
157.4080	47.2493	0.4475	156.0990	47.6193	0.2597
157.4920	47.1111	0.4861	156.9040	47.3058	0.4703
157.2880	47.3600	0.2948			

Craters D

lon	lat	diameter (km)	lon	lat	diameter (km)
155.9023	47.5150	1.6077	156.3262	47.1002	0.5351
156.7891	46.6879	1.6077	155.4791	46.3186	0.5342
155.5834	45.5319	1.4225	156.8824	46.5252	0.5183
157.2760	46.7813	1.3924	157.1564	46.8416	0.5157
156.7798	46.5471	1.3866	157.1543	46.8573	0.5128
155.8326	47.2776	1.3119	156.2294	46.0601	0.5128
156.2497	45.9034	1.3023	156.8130	46.9062	0.5128
156.4210	47.0438	1.2861	156.5772	46.4665	0.5085

155.1190	46.9305	1.2861	157.3232	46.7454	0.5012
155.5874	46.9582	1.2327	155.3688	45.8146	0.4934
156.3415	47.1773	1.2225	155.8344	47.4129	0.4672
155.6806	47.4247	1.2052	155.3140	45.8540	0.4672
156.8117	46.9884	1.1947	157.1617	46.7734	0.4644
156.4811	47.0968	1.1912	155.2298	46.4948	0.4581
155.5993	47.4368	1.1912	156.8859	46.5057	0.4581
155.8308	46.1219	1.1590	157.1599	46.9570	0.4581
157.1228	46.9401	1.1481	155.8114	47.0465	0.4581
156.2975	46.7679	1.1147	156.3049	46.9928	0.4568
156.0974	46.2182	1.1089	155.5312	45.6945	0.4235
155.4478	47.1269	1.1034	155.5621	45.7766	0.4235
155.6682	45.7457	1.0686	156.5058	46.7505	0.4235
156.9407	46.5750	1.0447	155.7091	46.7189	0.4228
157.4512	46.9174	1.0367	155.8734	47.3921	0.4221
155.1234	46.3608	1.0325	155.1823	46.2843	0.4109
155.3483	46.1903	0.9740	155.5309	46.6691	0.4097
155.8667	47.1605	0.9163	155.5506	46.2001	0.4019
157.2606	46.8664	0.9024	155.4832	47.7519	0.3805
156.5996	47.1485	0.8692	156.5069	46.6846	0.3777
156.2816	46.4546	0.8644	156.7280	46.8911	0.3697
155.9068	46.2087	0.8448	156.7794	46.9535	0.3697
155.4702	47.3722	0.8448	155.7120	46.2748	0.3632
156.3819	46.2386	0.8122	156.9949	46.4800	0.3632
156.8329	46.5154	0.7829	156.5772	46.5995	0.3632
155.9056	46.8761	0.7775	157.1952	46.9562	0.3306
155.8185	47.3075	0.7556	157.3077	47.0082	0.3248
155.7460	47.5765	0.7556	157.0890	47.0292	0.3082
155.8538	47.3087	0.7556	156.0289	47.4194	0.3077
157.3412	46.9797	0.7500	155.3796	47.6637	0.3077
155.7036	46.5215	0.7387	155.4976	47.7267	0.3077
155.9890	47.4751	0.7387	157.0694	47.1227	0.2995
155.6099	47.6765	0.7387	157.0215	46.4636	0.2905
156.5688	47.0540	0.7264	156.2670	46.5709	0.2900
156.9460	46.4887	0.7156	156.6350	46.5752	0.2900
156.2637	46.9823	0.6607	155.4738	46.1144	0.2897
156.5829	46.6544	0.6538	155.4402	46.3345	0.2748
156.3422	46.1232	0.6486	156.8322	46.8469	0.2748
156.9053	46.4887	0.6479	157.2875	46.7403	0.2718
155.0524	46.5022	0.6332	156.0456	46.2076	0.2619

155.8538	46.1622	0.6146	157.1942	47.0903	0.2619
155.5498	46.3235	0.6146	156.9966	47.1265	0.2619
155.0305	47.0968	0.6146	155.8361	46.4631	0.2591
155.6505	47.3996	0.6146	157.1609	47.0543	0.2522
156.2285	46.7485	0.5867	155.4387	46.1662	0.2297
155.3486	46.9148	0.5867	156.5558	46.7204	0.2293
155.8025	47.0838	0.5867	157.0397	47.1040	0.2256
155.4191	45.7933	0.5857	156.0865	46.8600	0.2238
155.4205	45.7698	0.5857	157.1927	47.0569	0.2179
156.5772	46.4935	0.5857	157.1297	47.0569	0.2179
156.4260	47.0065	0.5851	157.2263	46.9670	0.2170
155.9517	46.3308	0.5673	157.0329	47.1208	0.2080
156.4077	46.8292	0.5673	156.6678	46.7912	0.1832
155.8167	46.4290	0.5573	157.2572	47.0402	0.1819
155.7089	47.3637	0.5573	155.5214	46.2060	0.1452
156.1898	45.9928	0.5523	157.2726	46.9872	0.1452
156.2801	47.0041	0.5434	155.8990	46.0134	0.1450

Craters E

lon	lat	diameter (km)	lon	lat	diameter (km)
157.1332	46.0839	25.1008	156.8350	46.2241	0.5763
157.5649	44.9872	17.2772	157.3971	46.5922	0.5734
156.7866	45.4156	15.5952	157.1008	46.4751	0.5699
157.8874	45.1623	10.7088	157.4102	44.7378	0.5539
156.5935	45.0041	10.6021	156.7546	45.5015	0.5434
156.2590	45.1790	9.4446	157.4273	46.5076	0.5434
156.9121	45.2956	7.7803	157.2411	46.1862	0.5408
158.0703	44.9170	7.0980	157.4524	46.2455	0.5399
157.7815	45.2178	6.7730	156.0140	45.5040	0.5304
156.9399	45.4388	6.6819	157.4773	44.7123	0.5296
157.0093	44.9784	6.0540	157.7867	45.9273	0.5273
157.8240	44.7615	5.7852	157.4682	44.8463	0.5273
156.7386	45.6239	5.7054	157.7563	44.7579	0.5273
157.1395	44.9172	5.6901	157.4043	46.2319	0.5272
156.9010	45.7031	4.3156	157.4170	46.7256	0.5241
157.6449	45.7160	3.5134	157.1123	46.0721	0.5241
157.0645	45.6917	3.4466	157.3162	44.9514	0.5111
157.6250	44.9948	3.4222	157.2286	46.4573	0.5105
157.0024	45.7785	3.3458	156.6941	45.4608	0.5039

156.7355	45.7101	3.1440	157.2767	46.1039	0.5018
157.4423	45.7206	2.9876	157.7423	46.0395	0.4896
157.0414	44.7443	2.8107	157.6781	45.6493	0.4896
157.4286	45.1076	2.8059	157.7178	45.5370	0.4896
157.4493	45.1909	2.6361	157.4567	46.5483	0.4843
155.5324	45.2243	2.5710	156.6097	45.3728	0.4760
157.6147	45.3440	2.5456	157.3021	46.5387	0.4760
156.0034	44.8292	2.3391	157.5374	46.3787	0.4659
157.2619	45.7382	2.2191	157.1616	45.9339	0.4659
156.2316	44.8566	2.1161	157.6800	46.0093	0.4619
156.9078	44.7901	2.0301	157.7820	45.9824	0.4514
156.7212	44.7067	1.9439	157.4448	44.8276	0.4514
156.8227	45.8264	1.9223	156.7783	45.8946	0.4507
157.5700	45.7361	1.8703	157.1975	46.4346	0.4478
157.4884	45.6659	1.7952	156.0041	44.6620	0.4420
156.7975	45.7539	1.7892	157.5281	46.0765	0.4350
156.4040	45.4359	1.7134	157.7348	45.9049	0.4183
157.5572	46.0226	1.7109	155.8409	45.2250	0.4173
155.6331	45.2931	1.7093	156.7186	45.4410	0.4167
156.6866	46.0327	1.6503	157.5442	46.5509	0.4167
157.5754	45.9478	1.6465	157.6441	45.9174	0.4154
156.3966	45.5026	1.6275	157.6630	45.8826	0.4154
155.7497	44.6131	1.5814	156.9222	46.2770	0.4132
155.8560	45.3893	1.5466	157.2036	46.4727	0.4128
156.6287	45.6193	1.4601	156.1042	44.7665	0.4002
157.5470	45.8265	1.4082	157.7858	45.8990	0.3947
155.8606	44.6114	1.3710	157.6658	45.9003	0.3916
156.1419	45.6099	1.3246	157.4178	46.6255	0.3852
157.6812	45.9233	1.3180	157.5640	46.6077	0.3842
157.0085	45.9548	1.2753	157.0178	46.0438	0.3738
157.7384	45.9331	1.2676	157.7725	45.9075	0.3728
157.8783	45.0326	1.2581	157.9841	45.3634	0.3728
157.8538	45.6122	1.2538	157.4633	45.4984	0.3727
156.9207	46.0600	1.2434	155.8075	44.7845	0.3644
157.2916	45.0802	1.2357	156.6193	45.3576	0.3644
157.6506	44.9412	1.1789	157.5041	46.1484	0.3632
157.2792	46.0608	1.1658	157.4316	46.5369	0.3610
157.7792	45.8614	1.1003	157.5016	46.5239	0.3610
156.8686	46.0401	1.0908	157.6384	45.9338	0.3530
156.0162	44.6302	1.0627	157.5361	46.1790	0.3498

157.2803	45.8551	1.0544	157.2174	46.5078	0.3497
157.4673	46.2083	1.0420	157.0735	46.0417	0.3460
155.8668	44.9362	1.0081	157.5206	46.4846	0.3410
156.3263	45.2808	1.0001	157.1526	46.3493	0.3229
157.6800	45.3819	0.9853	157.1578	46.4465	0.3229
157.6233	45.0706	0.9656	156.9605	46.0436	0.3139
157.3594	45.4548	0.9595	157.7414	45.5416	0.3134
156.8241	45.5344	0.9562	156.9310	46.2410	0.3108
156.6611	45.2995	0.9504	157.4288	46.2495	0.3014
156.6485	45.5103	0.9226	155.7363	45.0701	0.2980
157.0825	46.3934	0.8792	157.5388	46.6633	0.2947
157.6111	46.5249	0.8592	157.1906	46.4971	0.2867
156.3109	45.2484	0.8592	157.5422	46.7221	0.2867
155.6966	45.2256	0.8502	157.4438	46.1529	0.2849
157.3019	46.1376	0.8336	157.0773	46.1673	0.2795
155.5413	45.1151	0.8150	157.3297	46.1340	0.2785
157.6596	46.1127	0.8017	157.9870	45.3435	0.2769
155.7973	45.3162	0.8010	156.9408	46.2652	0.2730
156.1114	44.7460	0.7604	157.3848	46.1559	0.2698
155.7690	44.8999	0.7604	157.6593	46.4568	0.2635
157.8018	45.9594	0.7601	157.4593	46.1546	0.2631
157.2675	46.5031	0.7344	157.5189	46.7108	0.2611
156.7677	45.2447	0.7316	156.7291	45.4134	0.2577
157.1401	46.0690	0.7097	157.0966	46.1707	0.2577
157.7782	44.8952	0.7010	157.1276	46.4733	0.2533
157.4696	46.7144	0.6820	157.4376	44.7378	0.2447
157.7149	45.8905	0.6819	157.1725	46.2879	0.2411
157.5194	46.4110	0.6784	156.9958	46.0429	0.2326
156.6305	45.3223	0.6784	157.3231	46.1644	0.2317
156.0789	44.7357	0.6761	157.5284	46.4953	0.2283
156.7186	45.3589	0.6720	157.3360	46.2021	0.2269
157.3631	45.3821	0.6645	157.2698	46.1448	0.2212
157.2220	45.9457	0.6645	157.4618	45.0453	0.2189
157.2558	45.9969	0.6645	157.4403	45.8031	0.2083
156.8625	45.5178	0.6590	157.2958	46.1075	0.2014
157.8443	45.8339	0.6568	157.4195	46.5489	0.1791
157.4235	44.7526	0.6383	157.7631	46.0493	0.1765
157.2263	46.3996	0.6251	157.2390	46.3356	0.1614
157.6129	44.9043	0.6251	157.2204	46.1350	0.1424
156.5910	45.3387	0.6251	157.2317	46.1366	0.1424

157.3020	44.9788	0.6231	157.3575	46.1395	0.1315
157.7263	45.5601	0.6193	157.0536	46.0408	0.1204
157.4637	44.8229	0.6134	157.6384	45.9450	0.1094
157.2461	46.1152	0.5967	157.3019	46.1601	0.1007
157.2659	45.4536	0.5967	157.4247	46.5566	0.1001
156.7927	45.8803	0.5930	157.7253	46.0329	0.0979
157.2765	44.9654	0.5916			

REFERENCES

Aki, K. (1967), Scaling law of seismic spectrum, Journal of Geophysical Ressearch 72, pp. 1217-1231.

Allmann, B.P. and P.M. Shearer (2009), Global variations of stress drop for moderate to large earthquakes, J. Geophys. Res. 114, B01310, doi. 10.1029/2008JB005821.

Baland, R.M. and T. Van Hoolst (2010), Librations of the Galilean satellites: The influence of global internal liquid layers, Icarus, 209 (2), pp. 651-664, doi. 10.1016/j.icarus.2010.04.004.

Barak, S., S.L. Klemperer and J.F. Lawrence (2015), San Andreas fault dip, Peninsular Ranges mafic lower crust and partial melt in the Salton Trough, southern California, from ambient-noise tomography, Geochemistry Geophysics Geosystems, Vol. 16, pp. 3946-3972.

Barnes, J.W., R.H. Brown, J. Radebaugh, B.J. Buratti, C. Sotin, S. Le Mouélic, S. Rodriguez, E.P. Turtle, J. Perry, R. Clark, K.H. Baines and P.D. Nicholson (2006), Cassini observations of flow-like features in western Tui Regio, Titan, Geophys. Res. Lett., Vol. 33, doi. 10.1029/2006 GL026843.

Barnes, J.W., B.J. Buratti, E.P. Turtle, J. Bow, P.A. Dalba, J. Perry, R.H. Brown, S. Rodriguez, S. Le Mouélic, K.H. Baines, C. Sotin, R.D. Lorenz, M.J. Malaska, T.B. McCord, R.N. Clark, R. Jaumann, P.O. Hayne. P.D. Nicholson, J.M. Soderblom and L.A. Soderblom (2013), Precipitation-induced surface brightenings seen on Titan by Cassini VIMS and ISS, Planetary Science 2:1, doi. 10.1186/2191-2521-2-1.

Becker, T.W., J. Hardebeck and G. Anderson (2004), Constraints on fault slip rates of the southern California plate boundary from GPS velocity and stress inversions, Geophys. J. Int., doi. 10.1111/j.1365-246.

Bennett, R.A., W. Rodi and R.E. Reilinger (1996), Global Positioning System constraints on fault slip rates in southern California and northern Baja, Mexico, J Geophys. Res. 101, 21, 943-21, 960.

Beuthe, M. (2010), East–west faults due to planetary contraction, Icarus, Vol. 209 (2), pp. 795-817, doi. 10.1016/j.icarus.2010.04.019.

Biasi, G.P. and R.J. Weldon (2009), San Andreas Fault rupture scenarios from multiple paleoseismic records: Stringing pearls, Bulletin of the Seismological Society of America, 99(2A), pp. 471-498, doi. 10.1785/0120080287.

Biasi, G.P. and S.G. Wesnousky (2016), Steps and gaps in ground ruptures: Empirical bounds on rupture propagation, Bulletin of the Seismological Society of America, 106(3), pp. 1110-1124, doi. 10.1785/0120150175.

Bierhaus, E.B., C.R. Chapman and W.J. Merline (2005), Secondary craters on Europa and implications for cratered surfaces, Nature, 437(7062), pp. 1125-1127.

Bills, B.G. (2005), Free and forced obliquities of the Galilean satellites of Jupiter, Icarus, 175(1), pp. 233–247, doi. 10.1016/j.icarus.2004.10.028.

Black, B.A., J.T. Perron, D.M. Burr and S.A. Drummond (2012), Estimating erosional exhumation on Titan from drainage network morphology, J. Geophys. Res., doi. 10.1029/2012JE004085.

Bland, M.T., A.P. Showman and G. Tobie (2009), The orbital-thermal evolution and global expansion of Ganymede, Icarus, 200, pp. 207-221, doi. 10.1016/j.icarus. 2008.11.016.

Bland, M.T. and W.B. McKinnon (2017), Viscous relaxation as a prerequisite for tectonic resurfacing on Ganymede: Insights from numerical models of lithospheric extension, Icarus, 306, pp. 285-305, doi. 10.1016/j.icarus.2017.10.1017.

Borsa, A.A., D.C. Agnew and R.C. Cayan (2014), Ongoing drought-induced uplift in the western United States, Science, Vol. 345, Issue 6204.

Boyd, O.S., D.E. McNamara, S. Hartzell and G. Choy (2017), Influence of lithostatic stress on earthquake stress drops in North America, Bulletin of Seism. Society of America, Vol. 107 (2), pp. 856-868, doi. 10.1785/0120160219.

Burkhard, L., B.R. Smith-Konter and D. Sandwell (2018), Stress accumulation rates of the San Andreas Fault System derived from spatial variations in crustal rigidity, Abstract #460627, American Geophysical Union Conference, Washington DC.

Burkhard, L., B.R. Smith-Konter, L. Ward, K. Scharer and D. Sandwell (2018), Earthquake cycle stress accumulation disparities of the Cajon Pass region, Abstract #262, Southern California Earthquake Center Annual Meeting, Palm Springs, CA.

Burkhard, L.M., B.R. Smith-Konter, M.E. Cameron, S.A. Fagents, G.C. Collins and R.T. Pappalardo (2021), Strike-slip faulting on Titan: Modeling tidal stresses and shear failure conditions due to pore fluid interactions, Icarus, doi. 10.1016/j.icarus.2021.114700.

Burkhard, L.M., E.S. Costello and M.E. Cameron (2021), Uncovering Ganymede's past: Crater Size Frequency Distributions on Nippur/Philus Sulci, #2033, 12th Planetary Crater Consortium Meeting.

Burr, D.M., R.E. Jacobsen, D.L. Roth, C.B. Phillips, K.L. Mitchell and D. Viola (2009), Fluvial network analysis on Titan: Evidence for subsurface structures and west-to-east wind flow, southwestern Xanadu, Geoph. Research Letters, Vol. 36, doi. 10.1029/2009 GL040909.

Burr, D.M., J.T. Perron, M. P. Lamb, R.P. Irwin III, G.C. Collins, A.D. Howard, L.S. Sklar, J.M. Moore, M. Ádámkovics, V.R. Baker, S.A. Drummond and B.A. Black (2013), Fluvial features on Titan: Insights from morphology and modeling, GSA Bulletin, Vol. 125; no. 3/4, pp. 299-32. doi. 10.1130/B30612.1.

Bruzzone, L., J.J. Plaut, G. Alberti, D.D. Blankenship, F. Bovolo, B.A. Campbell, A. Ferro, Y. Gim, W. Kofman, G. Komatsu and W. McKinnon (2013), RIME: Radar for icy moon exploration, Geoscience and Remote Sensing Symposium (IGARSS), 2013, IEEE International, pp. 3907-3910.

Byerlee, J. (1978), Friction of rocks: pure and applied geophysics, Vol. 116, pp. 615-626, doi. 10. 1007/BF00876528.

Caine, J.S., and C.B. Forster (1999), Faults and Subsurface Fluid Flow in the Shallow Crust, Geophys. Monogr. Ser., vol. 113, edited by W. C. Haneberg et al., AGU, Washington, D. C.

Cameron, M.E., B.R. Smith-Konter, L. Burkhard, G.C. Collins, F. Seifert, and R.T. Pappalardo (2018a), Morphological mapping of Ganymede: Investigating the role of strike-slip tectonics in the evolution of terrain types, Icarus, 315, pp. 92-114, doi. 10.1016/j.icarus. 2018.06.024.

Cameron, M.E., B.R. Smith-Konter, L. Burkhard, F. Seifert, G.C. Collins and R.T. Pappalardo (2018b), ArcGIS Map Package with Ganymede imagery and locations of morphological strike-slip indicators, Mendeley Data, v1.

Cameron, M.E., B.R. Smith-Konter, G.C. Collins, D.A. Patthoff and R.T. Pappalardo (2019), Tidal stress modeling of Ganymede: Strike-slip tectonism and Coulomb failure, Icarus, 319, pp. 99-120, doi. 10.1016/j.icarus.2018.09.002.

Cameron, M.E., B.R. Smith-Konter, G.C. Collins, D.A. Patthoff, and R.T. Pappalardo (2020), Ganymede, then and now: How past eccentricity may have altered tidally driven Coulomb failure, JGR-Planets, doi. 10.1029/2019JE005995.

Carr, M.H., Belton, M.J.S., Bender, K., Breneman, H., Greeley, R., Head, J.W., Pappalardo, R.T., (1995), The Galileo Imaging Team plan for observing the satellites of Jupiter, J. Geophys. Res. Planets 100 (E9), 18935-18955.

Carry, B. (2012), Density of asteroids, Planetary and Space Science 73, pp. 98-118, doi. 10.1016/j.pss.2012.03.009.

Casacchia, R. and R.G. Strom (1984), Geologic evolution of Galileo Regio, Ganymede, J. Geophys. Res. Solid Earth 89 (S02), B419–B428, doi. 10.1029/JB089iS02p0B419.

Chen, K., J.P. Avouac, S. Aati, C. Milliner, F. Zheng and C. Shi (2020), Cascading and pulse-like ruptures during the 2019 Ridgecrest earthquakes in the Eastern California Shear Zone, Nature Communications, doi. 10.1038/s41467-019-13750-w.

Chen, S.-A., K. Michaelides, S.W.D. Grieve and M. Bliss Singer (2019), Aridity is expressed in river topography globally, Nature, 573, doi. 10.1038/s41586-19-1558-8.

Choukroun, M., O. Grasset, G. Tobie and C. Sotin (2010), Stability of methane clathrate hydrates under pressure: Influence on outgassing processes of methane on Titan, Icarus, Vol. 205(2), pp. 581-593, doi. 10.1016/j.icarus.209.08.011.

Collins, G. C., J. W. Head III, R. T. Pappalardo, and N. A. Spaun (2000), Evaluation of models for the formation of chaotic terrain on Europa, J. Geophys. Research, Vol. 105, pp. 1709-1716.

Collins, G.C. (2009), The origin of grooved terrain on Ganymede. Eur. Planet. Sci. Cong. 4, 516.

Collins, G.C., R.T. Pappalardo, P.M. Schenk, F. Nimmo, L.M. Prockter, W.B. McKinnon and J.M Moore (2010), Tectonics of the outer planet satellites, Tectonics 11, pp. 264-350.

Collins, G.C., G.W. Patterson, J.W. Head, R.T. Pappalardo, L.M. Prockter, B.K. Lucchitta and J.P. Kay (2013), Global geologic map of Ganymede, U. S. Geol. Surv. Scientific Investigations Map, 3237, doi. 10.3133/sim3237.

Cook-Hallett, C., J.W. Barnes, S.A. Kattenhorn, T. Hurford, J. Radebaugh, B. Stiles and M. Beuthe (2015), Global contraction/expansion and polar lithospheric thinning on Titan from patterns of tectonism, JGR: Planets, doi. 1002/2014JE004645.

Costello, E.S., L. Burkhard and M.E. Cameron (2020), Crater size frequency distributions reveal the relative age of Sulci on Ganymede, 11th Planetary Crater Consortium Meeting.

Cotton, F., R. Archuleta and M. Causse (2013), What is the Sigma of stress drop?, Seismological Research Letters Vol. 84 (1), doi. 10.1785/0220120087.

Crater Analysis Techniques Working Group (1979), Standard techniques for presentation and analysis of crater size-frequency data, Icarus, 37(2), pp. 467-474.

Croft, G.D. and T.W. Patzek (2009), The future of California's oil supply: Society of Petroleum Engineers Western Regional Meeting, San Jose, California, SPE Paper 120174-PP.

d'Alessio, M.A., I.A. Johanson, R. Burgmann, D.A. Schmidt and M.H. Murray (2005), Slicing up the San Francisco Bay Area: Block kinematics and fault slip rates from GPS-derived surface velocities, J. Geophys. Res. 110, doi. 10.1029/2004JB003496.

Davis, D., J. Suppe and F.A. Dahlen (1983), Mechanics of fold-and-thrust belts and accretionary wedges, J. Geophys. Res.: Solid Earth 88 (B2), pp. 1153-1172.

Della Corte, V., N. Schmitz, M. Zusi, J.M. Castro, M. Leese, S. Debei, D. Magrin, H. Michalik, P. Palumbo, R. Jaumann and G. Cremonese (2014), The JANUS camera onboard JUICE mission for Jupiter system optical imaging, Space Telescopes and Instrumentation 2014: Optical, Infrared, and Millimeter Wave, Vol. 9143, p. 91433I.

DeRemer, L. and R.T. Pappalardo (2003), Manifestations of strike-slip faulting on Ganymede, In: Lunar Planet. Sci. Conf. XXXIV, pp. 2033.

Dong, G. and A.S. Papageorgiou (2003), On a new class of kinematic models: symmetrical and asymmetrical circular and elliptical cracks, Phys. Earth Planet. In. 137, pp. 129–151.

Donzé, F.-V., Y. Klinger, V. Bonilla-Sierra, J. Duriez, L. Jiao and L. Scholtès (2021), Assessing the brittle crust thickness from strike-slip fault segments on Earth, Mars and Icy Moons, Tectonophysics, doi. 10.1016/j.tecto.2021.228779.

Douilly, R., D.D. Oglesby, M.L. Cooke and J.L. Hatch (2020), Dynamic models of earthquake rupture along branch faults of the eastern San Gorgonio Pass region in California using complex fault structure, Geosphere, 16(2), pp. 474-489, doi. 10.1130/GES02192.1.

Dougherty, M., L.W. Esposito and S.M. Krimigis (2009), Saturn from Cassini-Huygens, Springer, doi. 10.1007/978-1-4020-9217-6.

Durham William B. (2003), The strength and rheology of methane clathrate hydrate, Journal of Geophysical Research, Vol. 108, doi. 10.1029/2002JB001872.

Eicken, H. (1992), Salinity profiles of Arctic sea ice: Field data and model results, J. Geophys. Res., Vol. 97, doi. 10.1029/92JC01588.

Elkhoury, J.E., E.E. Brodsky and D.C. Agnew (2006), Seismic waves increase permeability, Nature, 441(7097), pp. 1135-1138, doi. 10.1038/nature04798.

Faulk, S.P., J.M. Lora, J.L. Mitchell and P.C.D. Milly (2020), Titan's climate patterns and surface methane distribution due to the coupling of land hydrology and atmosphere, Nature Astronomy 4, pp. 390-398, doi. 10.1038/s41550-019-0963-0.

Fay, N.P. and E.D. Humphreys (2005), Fault slip rates, effects of elastic heterogeneity on geodetic data, and the strength of the lower crust in the Salton Trough region, southern California, J. Geophys. Res. Solid Earth, 110(B9), doi. 10.1029/2004JB003548.

Forand, D., J.P. Evans, S.U. Janecke and J. Jacobs (2018), Insight into fault processes and geometry of the San Andreas fault system: Analysis of core from deep drill hole at Cajon Pass, California, GSA Bulletin, v. 130, no ½, pp. 64-92, doi. 10.1130/B31681.1.

Fortt, A.L., and E.M. Schulson (2007), The resistance to sliding along Coulombic shear faults in ice: Acta materialia, Vol. 55, pp. 2253-2264.

Freed, A.M., and J. Lin (1998), Time-dependent changes in failure stress following thrust earthquakes, J. Geophys. Res., 103, 24, 393-24, 409.

Freed, A.M., and J. Lin (2001), Delayed triggering of the 1999 Hector Mine earthquake by viscoelastic stress transfer, Nature, 411, pp. 180-183.

Freymueller, J.T., M.H. Murray, P. Segall and D. Castillo (1999), Kinematics of the Pacific-North America plate boundary zone, northern California, J.Geophys. Res. 104, pp. 7419-7441.

Fuis, G.S., D.S. Scheirer, V.E. Langenheim M.D. and Kohler (2012), A new perspective on the geometry of the San Andreas fault in Southern California and its relationship to lithospheric structure, Bulletin of the Seismological Society of America, Vol. 102, pp. 236-251.

Goebel, T.H.W., E. Hauksson, P.M. Shearer and J.P. Ampuero (2015), Stress-drop heterogeneity within tectonically complex regions: a case study of San Gorgonio Pass, southern California, Geophys. J. Int. 202, pp. 514-528.

Goebel, T.H.W., S.M. Hosseini, F. Cappa, E. Hauksson, J.P. Ampuero, F. Aminzadeh and J.B. Saleeby (2016), Wastewater disposal and earthquake swarm activity at the southern end of the Central Valley, California, Geophys. Res. Lett. 43, pp. 1-8.

Goebel, T.H.W. and M. Shirzaei (2022), More Than 40 yr of Potentially Induced Seismicity Close to the San Andreas Fault in San Ardo, Central California, Seismol. Res. Lett. 92, pp. 187-198, doi. 10.1785/0220200276.

Goldsby, D. L., and D. L. Kohlstedt (2001), Superplastic deformation of ice: Experimental observations, J. Geophys. Res., Vol. 106, doi. 10.1029/2000JB900336.

Goldstein, R.V. and N.M. Osipenko (2012), Fracture structure near a longitudinal shear macro-rupture, Mechanics of Solids, 47(5), pp. 505-516.

Greenberg, R. (1987), Galilean satellites: Evolutionary paths in deep resonance, Icarus, 70(2), 334–347, doi. 10.1016/0019-1035(87)90139-4.

Greenberg, R., P. Geissler, G. Hoppa, B.R. Tufts, D.D. Durda, R.T. Pappalardo, J.W. Head, R. Greeley, R. Sullivan and M.H. Carr (1998), Tectonic processes on Europa: tidal stresses, mechanical response and visible features, Icarus, Vol. 135, pp. 64-78.

Groenleer, J. M., and S. A. Kattenhorn (2008), Cycloid crack sequences on Europa: Relationship to stress history and constraints on growth mechanics based on cusp angles, Icarus, Vol. 193, pp. 158-181, doi. 10.1016/j.icarus.2007.08.032.

Guns, K.A. and R.A. Bennett (2020), Assessing long-term postseismic transients from GPS time series in Southern California, Journal of Geophysical Research: Solid Earth,125, doi. 10.1029/ 2019JB018670.

Hammond, N.P. and A.C. Barr (2013). Formation of Ganymede's grooved terrain by convection-driven resurfacing, Icarus, 227, pp. 206-209, doi. 10.1016/j.icarus.2013.08.024.

Hammond, N.P. (2020), Estimating the magnitude of cyclic slip on strike-slip faults on Europa, JGR Planets, 125, doi. 10.1029/2019JE006170.

Hanks, T.C. (1977), Earthquake stress drops, ambient tectonic stresses, and the stresses that drive plate motions, Pure Appl. Geophys. 115, pp. 441-458.

Harris, R.A. and R.W. Simpson (1998), Suppression of large earthquakes by stress shadows: A comparison of Coulomb and rate-and-state failure, Journal of Geophysical Research, Vol. 103, No. B10, pp.24, 439-24, 451.

Hayes, A., O. Aharonson, P. Callahan, C. Elachi, Y. Gim, R. Kirk, K. Lewis, R. Lopes, R. Lorenz, J. Lunine, K. Mitchell, G. Mitri, E. Stofan and S. Wall (2008), Hydrocarbon lakes on Titan: Distrubution and interaction with a porous regolith, Geophys. Res. Lett., 35, L09204, doi. 10.1029/2008GL033409.

Hayes, A., R.D. Lorenz and J.I. Lunine (2018), A post-Cassini view of Titan's methane-based hydrologic cycle, Nature Geoscience, Vol. 11, Issue 5, pp. 306-313, doi. 10.1038/ s41561-018-0103-y.

Head, J., Pappalardo, R., Collins, G., Belton, M.J., Giese, B., Wagner, R., Moore, J. (2002), Evidence for Europa-like tectonic resurfacing styles on Ganymede. Geophysical Research Letters 29 (24).

Hearn, E.H. (2003), What can GPS data tell us about the post-seismic deformation?, Geophysical Journal International, Vol. 155, pp. 753-777.

Hedgepeth, J.E., C.D. Neish, E.P. Turtle, B.W. Styles, R. Kirk and R.D. Lorenz (2020), Titan's impact crater population after Cassini, Icarus, Vol. 344, doi. 10.1016/j.icarus. 2020.113664.

Hein, F.J. (2013), Overview of heavy oil, seeps, and oil (tar) sands, California, in F.J. Hein, D. Leckie, S. Larter, and J.R. Suter, eds., Heavy-oil and oil-sand petroleum systems in Alberta and beyond: AAPG Studies in Geology 64, pp. 407-435.

Helfenstein, P. and E.M. Parmentier (1985), Patterns of fracture and tidal stresses due to nonsynchronous rotation: Implications for fracturing on Europa, Icarus, Vol. 61, pp. 175-184.

Hendrix, A.R., T.A. Hurford, L.M. Barge, M.T. Bland, J.S. Bowman, W. Brinckerhoff, B.J. Buratti, M.L. Cable, J. Castillo-Rogez, G.C. Collins, S. Diniega, C.R. German, A.G. Hayes. T. Hoehler, S. Hosseini, C.J.A. Howett, A.S. McEwen, C.D. Neish, M. Neveu, T.A. Nordheim, G.W. Patterson, D.A. Patthoff, C. Phillips, A. Rhoden, B.E. Smidt, K.N. Singer, J.M. Soderblom and S.D. Vance (2019), The NASA Roadmap to Ocean Worlds, Astrobiology, Vol. 19, No. 1, doi. 10.1089/ast.2018.1955.

Hirata, N., R. Suetsugu and K. Ohtsuki (2020), A global system of furrows on Ganymede indicative of their creation in a single impact event, Icarus 352, doi. 10.1016/j.icarus.2020.113941.

Hofgartner, J.D., A.G Hayes, D.B. Campbell, J.I. Lunine, G.J. Black, S.M. MacKenzie, S.P.D. Birch, C. Elachi, R.D. Kirk, A. Le Gall, R.D. Lorenz and S.D. Wall (2020), The root of anomalously specular reflections from solid surfaces on Saturn's moon Titan, Nature Communications 11, doi. 10.1038/s41467-020-16663-1.

Hollingsworth, J., J. Jackson. R. Walker, M.R. Gheitanchi and M.J. Bolourchi (2006), Strike-slip faulting, rotations, and analog-strike elongation in the Kopeh Dagh mountains, NE Iran, Geophys. J. Int., 166, pp. 1161-1177, doi. 10.1111/j/1365-246X.2006.02983.x.

Hoppa, G., B.R. Tufts, R. Greenberg and P. Geissler (1999), Strike-slip faults on Europa: global shear patterns driven by tidal stress, Icarus, Vol. 141, pp. 287-298.

Horvath, D.G., J.C. Andrews-Hanna, C.E. Newman, K.L. Mitchell and B.W. Stiles (2016), The influence of subsurface flow on lake formation and north polar lake distribution on Titan, Icarus, Vol. 277, pp. 103-124, doi. 10.1016/j.icarus.2016.04.042.

Hough, S.E. and R. Bilham (2018), Revisiting earthquakes in the Los Angeles, California, basin during the early instrumental period: Evidence for an association with oil production. Journal of Geophysical Research: Solid Earth, 123, 10, 684-10, 705, doi. 10.1029/2017JB014616.

Hubbert, M.K. and W.W. Rubey (1959), Role of fluid pressure in mechanics of overthrust faulting, Bulletin of the Geologic Society of America, Vol. 70, pp. 115-166.

Hurford, T.A., P. Helfenstein, G.V. Hoppa R. Greenberg and B.G. Bills (2007), Eruptions arising from tidally controlled periodic openings of rifts on Enceladus. Nature 447 (7142), pp. 292.

Hurford, T.A., A.R. Sarid and R. Greenberg (2007), Cycloidal cracks on Europa: Improved modeling and non-synchronous rotation implications, Icarus, Vol. 186, pp. 218–233, doi. 10.1016/j.icarus.2006.08.026.

Jaeger, J.C. and N.G.W. Cook (1979), Fundamentals of rock mechanics, 3rd Ed., Chapman and Hall, London.

Jara-Orué, H.M., and B.L.A. Vermeersen (2016), Tides on Jupiter's moon Ganymede and their relation to its internal structure, Netherlands Journal of Geosciences, Vol. 95, pp. 191-201, doi. 10.1017/njg.2015.23.

Jha, B. and R. Juanes (2014), Coupled multiphase flow and poromechanics: A computational model of pore pressure effects on fault slip and earthquake triggering, Water Resources Research, doi. 10.1002/2013WR015 175.

Jiang, J. and N. Lapusta (2017), Connecting depth limits of interseismic locking, microseismicity, and large earthquakes in models of long-term fault slip, Journal of Geophysical Research: Solid Earth, doi. 122. 10.1002/2017JB014030.

Karatekin, Ö., T. Van Hoolst, and T. Tokano (2008), Effect of internal gravitational coupling on Titan's non-synchronous rotation, Geophys. Res. Lett., 35, L16202.

Kattenhorn, S.A. (2002), Nonsynchronous rotation evidence and fracture history in the bight plains region, Europa, Icarus, Vol. 157, pp. 490-506.

Kattenhorn, S.A. (2004), Strike-slip fault evolution on Europa: evidence from tailcrack geometries, Icarus, Vol. 172, pp. 582-602, doi. 10.1016/j.icarus.2004.07.005.

Keranen, K.M., H.M. Savage, G.A. Abers, E.S. Cochran (2013), Potentially induced earthquakes in Oklahoma, USA: Links between wastewater injection and the 2011 M_w 5.7 earthquake sequence, Geology, 41 (6), pp. 699–702, doi. 10.1130/G34045.1.

King, G.C.P., R.S. Stein and J. Lin (1994), Static stress changes and the triggering of earthquakes, Bulletin of the Seismological Society of America, Vol. 84, No. 3, pp. 935-953.

Kivelson, M.G., K.K. Khurana, F.V. Coroniti, S. Joy, C.T. Russell, R.J. Walker, J. Warnecke, L. Bennett and C. Polanskey (1997), The magnetic field and magnetosphere of Ganymede, Geophysical Research Letters, 24(17), pp. 2155-2158, doi. 10.1029/97GL02201.

Kivelson, M.G., K.K. Khurana and M. Volwerk (2002), The permanent and inductive magnetic moments of Ganymede, Icarus, Vol. 157 (2), pp. 507-522.

Kwiatek, G., K. Plenkers and G. Dresen (2011), Source parameters of picoseismicity recorded at Mponeng deep gold mine, South Africa: implications for scaling relations, Bull. seism. Soc. Am., 101(6), pp. 2592-2608.

Le Gall, A., M.A. Janssen, P. Paillou, R.D. Lorenz, S.D. Walls and the Cassini RADAR Team (2010), Radar-bright channels on Titan, Icarus, Vol. 207(2), pp. 948-958, doi. 1016/j.icarus.2009.12.027.

Lienkaemper, J.J., and C. Bronk Ramsey (2009), OxCal: Versatile tool for developing paleoearthquake chronologies-A primer, Seismological Research Letters, 80(3), pp. 431-434, doi. 10.1785/gssrl.80.3.431.

Lin, B., M.E. Mear and K. Ravi-Chandar (2010), Criterion for initiation of cracks under mixed-mode I+III loading, International journal of fracture, 165(2), pp. 175-188.

Lingenauber, K., H. Hussmann, H. Michaelis, J. Oberst, M. Kobayashi, N. Namiki, N. Thomas and K. Seiferlin (2014), The Ganymede Laser Altimeter (GALA) on ESA's JUICE mission: Overview of the instrument design, Instrument for Planetary Mission (IPM).

Liu, D., B. Duan, K. Scharer and D. Yule (2022), Observation-constrained multicycle dynamic models of the Southern San Andreas and the Northern San Jacinto Faults: Addressing complexity in paleoearthquake extent and recurrence with realistic 2D fault geometry, JGR Solid Earth, doi. 10.1029/2021JB023420.

Liu, Z., J. Radebaugh, R.A. Harris, E.H. Christiansen, C.D. Neish, R.L. Kirk, R.D. Lorenz, and the Cassini RADAR Team (2016 a), The tectonics of Titan: Global structural mapping from Cassini RADAR, Icarus, Vol. 270, pp. 14-29, doi. 10.1016/j.icarus. 2015.11.021.

Liu, Z., J. Radebaugh, R.A. Harris, E.H. Christiansen and S. Rupper (2016 b), Role of fluids in the tectonic evolution of Titan, Icarus, Vol. 270, pp. 2-13, doi. 10.1016/j.icarus. 2016. 02.016.

Lopes, R.M.C., E.R. Stofan, R. Peckyno, J. Radebaugh, K.L. Mitchell, G. Mitri, C.A. Wood, R.L. Kirk, S.D. Wall, J.I. Lunine, A. Hayes, R. Lorenz, T. Farr, L. Wye, J. Craig, R.J. Ollerenshaw, M. Janssen, A. LeGall, F. Paganelli, R. West, B. Stiles, P. Callahan, Y. Anderson, P. Valora, L. Soderblom and the Cassini RADAR Team (2009), Distribution and interplay of geologic processes on Titan from Cassini RADAR data, Icarus, Vol. 205(2), pp. 540-558, doi. 10.1016/ j.icarus.2009.08.010.

Lopes, R.M.C., M.J. Malaska, A.M. Schoenfeld, A. Solomonidou, S.P.D. Birch, M. Florence, A.G. Hayes, D.A. Williams, J. Radebaugh, T. Verlander, E. P. Turtle, A. Le Gall and S. D. Wall (2020), A global geomorphologic map of Saturn's moon Titan, Nature Astronomy Letters, doi. 10.1038/s41550-019-0917-6.

Lorenz, R.D. (2002), Thermodynamics of Geysers: Application to Titan, Icarus, Vol. 156, pp. 176-183, doi. 10.1006/icar.2001.6779.

Lorenz, R.D., R.M. Lopes, F. Paganelli, J.I. Lunine, R.L. Kirk, K.L. Mitchell, L.A. Soderblom, E.R. Stofan, G. Ori, M. Myers, H. Miyamoto, J. Radebaugh, B. Stiles, S.D. Wall and C.A. Wood (2008), Fluvial channels on Titan: Initial Cassini RADAR observations, Planet, Space Sci. 56 (8), pp. 1132-1144, doi. 10.1016/j. pss.2008.02.009.

Lorenz, R.D., E.P. Turtle, J.W. Barnes, M.G. Trainer, D.S. Adams, K.E. Hibbard, C.Z. Sheldon, K. Zacny, P.N. Peplowski, D.J. Lawrence, M.A. Ravine, T.G. McGee, K.S. Sotzen, S.M. MacKenzie, J.W. Langelaan, S. Schmitz, L.S. Wolfarth and P.D. Bedini (2018), Dragonfly: A Rotorcraft Lander Concept for Scientific Exploration at Titan, Johns Hopkins APL Technical Digest, 34(3), pp. 374-387.

Loveless, J.P. and B.J. Meade (2011), Stress modulations of the San Andreas Fault by interseismic fault interactions, Geology, 39 (11), pp. 1035-1038, doi. 10.1130/G32215.1.

Lozos, J.C. (2016), A case for historic joint rupture of the San Andreas and San Jacinto faults. Science Advances, 2(3), e1500621, doi. 10.1126/sciadv.1500621.

Lozos, J.C., D.D. Oglesby, B. Duan and S.G. Wesnousky (2011), The effects of double fault bends on rupture propagation: A geometrical parameter study, Bulletin of the Seismological Society of America, 101(1), pp. 385-398, doi. 10.1785/0120100029.

Lucchetti, A., C. Rossi, F. Mazzarini, M. Pajola, R. Pozzobon, M. Massironi and G. Cremonese, (2021), Equatorial grooves distribution on Ganymede: Length and self-similar clustering analysis. Planetary and Space Science 195, 105140, doi. 10.1016/j.pss.2020.105140.

Lucchita, B.K. (1980), Grooved terrain on Ganymede, Icarus, Vol. 44, pp. 481-501.

Lunine, J.I., C. Elachi, S.D. Wall, M.A. Janssen, M.D. Allison, Y. Anderson, R. Boehmer, P. Callahan, P. Encrenaz, E. Flamini, G. Franceschetti, Y. Gim, G. Hamilton, S. Hensley, E.T.K. Johnson, K. Kelleher, R.L. Kirk, R.M. Lopes, R. Lorenz, D.O. Muhleman, R. Orosei, S.J. Ostro, F. Paganelli, P. Paillou, G. Picardi, F. Posa, J. Radebaugh, L.E. Roth, R. Seu, S. Shaffer, L.A. Soderblom, B. Stiles, E.R. Stofan, S. Vetrella, R. West, C.A. Wood, L. Wye, H. Zebker, G. Alberti, E. Karkoschka, B. Rizk, E. McFarlane, C. See and B. Kazeminejad (2008), Titan's diverse landscapes as evidenced by Cassini RADAR's third and fourth looks at Titan, Icarus, Vol. 195(1), pp. 415-433, doi. 10.1016/j.icarus.2007.12.022.

Lunine, J.I. and R.D. Lorenz (2009), Rivers, lakes, dunes, and rain: Crustal processes in Titan's methane cycle, Annual Review of Earth and Planetary Sciences, Vol. 37, pp. 299-320.

Machette, M., K. Haller and L. Wald (2004), Quaternary Fault and Fold Database for the Nation, U.S. Geological Survey Fact Sheet, pp. 2004-3033.

MacKenzie, S.M., J.W. Barnes, C. Sotin, J.M. Soderblom, S. Le Mouélic, R. Sebastien, K.H. Baines, B.J. Buratti, R.N. Clark, P.D. Nicholson and T.B. McCord (2014), Evidence of Titan's climate history from evaporite distribution, Icarus, Vol. 243, pp. 199-207, doi. 10.1016/j.icarus.2014.08.022.

Magistrale, H. and C. Sanders (1996), Evidence from precise earthquake hypocenters for segmentation of the San Andreas fault in San Gorgonio Pass, J. Geophys. Res., 101(B2), pp. 3031-3044.

Malaska, M.J., R.M.C. Lopes, D.A. Williams, C.D. Neish, A. Solomonidou, J.M. Soderblom, A.M. Schoenfeld, S.P.D. Birch, A.G. Hayes, A.Le Gall, M.A. Janssen, T.G. Farr, R.D. Lorenz, J. Radebaugh, E.P. Turtle (2016), Geomorphological map of the Afekan Crater region, Titan: Terrain relationships in the equatorial and mid-latitude regions, Icarus, Vol. 270, pp. 130-161.

Malaska, M.J., J. Radebaugh, R.M.C. Lopes, K.L. Mitchell, T. Verlander, A.M. Schoenfeld, M.M. Florence, A. Le Gall, A. Solomonidou, A.G. Hayes, S.P.D. Birch, M.A. Janssen. L. Schurmeier, T. Cornet. C. Ahrens, T.G. Farr and the Cassini RADAR Team (2020), Labyrinth terrain on Titan, Icarus, Vol. 344, doi. 10.1016/j.icarus.2020.113764.

Malhotra, R. (1991), Tidal origin of the Laplace resonance and the resurfacing of Ganymede, Icarus, 94(2), pp. 399-412, doi. 10.1016/0019-1035(91)90237-N.

Mandl, G. (1987), Tectonic deformation by rotating parallel faults: the “bookshelf” mechanism, Tectonophysics, 141(4), pp. 277-316.

Manighetti, I., A. Mercer and L. De Barros (2021), Fault Trace Corrugation and Segmentation as a Measure of Fault Structural Maturity, Geophys. Res. Letters, doi. 10.1029/2021GL095372.

Martin, E. (2016), The distribution and characterization of strike-slip faults on Enceladus, Geophys. Res. Lett., Vol. 43, doi. 10.1002/2016GL067805.

Matteoni, P., G. Mitri, V. Poggiali and M. Mastrogiuseppe (2020), Geomorphological Analysis of the Southwestern Margin of Xanadu: Insights on Tectonics, JGR Planets, doi. 10.1029/2020JE006407.

McKenzie, D. and J. Jackson (1983), The relationship between strain rates, crustal thickening, paleomagmatism, finite strain and fault movements within a deforming zone, Earth and Planetary Science Letters, V. 65, pp. 182-202, doi. 10.1016/0012-821X (83)90198-X.

McKenzie, D. and J. Jackson (1986), A block model of distributed deformation by faulting, Geological Society of London Journal, V. 143, pp. 349-353, doi. 10.1144/gsjgs. 143.2.0349.

Meade, B.J. and B.H. Hager (2004), Viscoelastic deformation for a clustered earthquake cycle, Geophys. Res. Lett., 31, doi. 10.1029/2004GL019643.

Meade, B.J. and B.H. Hager (2005), Block models of crustal motion in southern California constrained by GPS measurements, J. Geophys. Res. 110, doi. 10.1029/2004JB003209.

Melosh, H.J. (1977), Global tectonics of a despun planet, Icarus, Vol. 31, pp. 221-243.

Melosh, H.J. (1989), Impact cratering: A geologic process: Research supported by NASA, New York, Oxford University Press (Oxford Monographs on Geology and Geophysics, No. 11), 253 p., Vol. 11.

Meriggiola, R, L. Iess, B.W. Stiles, J.I. Lunine and G. Mitri (2016), The rotational dynamics of Titan from Cassini RADAR images, Icarus, Vol. 275, pp. 183-192, doi. 10.1016/j.icarus. 2016.01.019.

Mitri,G., M.T. Bland, A.P. Showman, J. Radebaugh, B. Stiles, R.M.C. Lopes, J.I. Lunine and R.T. Pappalardo (2010), Mountains on Titan: Modeling and observations J. Geophys. Res., Vol. 115, doi. 10.1029/2010JE003592.

Moon, S., J.T. Perron, S.J. Martel, W.S. Holbrook and J. St. Clair (2017), A model of three-dimensional topographic stresses with implications for bedrock fractures, surface processes, and landscape evolution, J. of Geophys. Res.: Earth Surface, Vol. 122, Issue 4, pp. 823-846, doi. 10.1002/2016JF004155.

Moore, J.M. and A.D. Howard (2010), Are the basins of Titan's Hotei Regio and Tui Regio sites of former low latitude seas?, Geophys. Res. Letters, Vol. 37, Issue 22, doi. 10.1029/ 2010GL045234.

Mori, T. M. Shigefuji, S. Bijukchhen, T. Kanno and N. Takai (2020), Ground motion prediction equation for the Kathmandu Valley, Nepal based on strong motion records during the 2015 Gorkha Nepal earthquake sequence, Soil Dynamics and Earthquake Engineering, Vol. 135, doi. 10.1016/j.solidyn.2020.106208.

Mousis, O. and B. Schmitt (2008), Sequestration of ethane in the cryovolcanic subsurface of Titan, The Astrophysical Journal Letters, 677, L67-L70.

Mousis, O., M. Choukroun, J.I. Lunine and C. Sotin (2014), Equilibrium composition between liquid and clathrate reservoirs on Titan, Icarus, Vol. 239, pp. 39-45, doi. 10.1016/ j.icarus.2014.05.032.

Mueller, S. and W.B. McKinnon (1988), Three-layered models of Ganymede and Callisto: Compositions, structures, and aspects of evolution. Icarus 76, pp. 437-464.

Murchie, S.L., J.W. Head, P. Helfenstein and J.B. Plescia (1986), Terrain types and localscale stratigraphy of grooved terrain on Ganymede, In: Lunar Planet. Sci. Conf.Proceedings, pp. 17.

Murchie, S.L. and J.W. Head (1988), Possible breakup of dark terrain on Ganymede by large-scale shear faulting, J. Geophys. Res. 93 (B8), pp. 8795-8824.

Murchie, S.L., J.W. Head and J.B. Plescia (1989), Crater densities and crater ages of different terrain types on Ganymede, Icarus, Vol. 81, pp. 271-297.

Murchie, S.L. (1990), The tectonics of icy satellites, Adv. Space. Res., Vol. 10, No. 1 (1)173-(1)182.

Murray, C.D. and S.F. Dermott (1999), Solar system dynamics, Cambridge university press.

Murray, J. and P. Segall (2002), Testing time-predictable earthquake recurrence by direct measurement of strain accumulation and release, Nature, Vol. 419, pp. 287-291.

Nagorsen-Rinke, S., J. Lee and A. Calvert (2012), Pliocene sinistrial slip across Adobe Hills, eastern California-western Nevada: Kinematics of fault slip across the Mina deflection, Geosphere, pp. 37-53, doi. 10.1130/GES00825.1.

Nathan, E., C. Huber and J.W. Head (2022), A stress-based framework for understanding the evolution of icy worlds, 53rd Lunar and Planetary Science Conference, Abstract #1075.

Naylor, M.A., G.T. Mandl and C.H.K. Supesteijn (1986), Fault geometries in basement-induced wrench faulting under different initial stress states, Journal of Structural Geology, 8(7), pp. 737-752.

Neish, C.D. and R.D. Lorenz (2012), Titan's global crater population: A new assessment, Planet. Space Sci. 60 (1), pp. 26-33, doi. 10.1016/ j.pss.2011.02.016.

Neish, C.D., R.L. Kirk, R.D. Lorenz, V.J. Bray, P. Schenk, B.W. Stiles, E. Turtle, K. Mitchell, A. Hayes and the Cassini RADAR Team (2013), Crater topography on Titan: Implications for landscape evolution, Icarus, Vol. 233, pp. 82-90, doi. 10.1016/j.icarus. 2012. 11.030.

Neish, C.D. and R.D. Lorenz (2014), Elevation distribution of Titan's craters suggest extensive wetlands, Icarus, Vol. 228, pp. 27-34, doi. 10.1016/j.icarus.2013.09.024.

Neish, C.D., J.L. Molaro, J.M. Lora, A.D. Howard, R.L. Kirk, P. Schenk, V.J. Bray and R.D. Lorenz (2016), Fluvial erosion as a mechanism for crater modification on Titan, Icarus, Vol. 270, pp. 114-129, doi. 10.1016/j.icarus.2015.07.022.

Neukum, G. (1997), Bombardment history of the Jovian system, The Three Galileos: The Man, the Spacecraft. the Telescope, pp. 201-212.

Neukum, G., R. Wagner, U. Wolf, B.A. Ivanov, J.W. Head III, R.T. Pappalardo and the Galileo; SSI Team (1999), Cratering chronology in the Jovian system and derivation of absolute ages. In: Lunar Planet. Sci. Conf. XX IX, pp. 1742.

Neukum, G., B.A. Ivanov and W.K. Hartmann (2001), Cratering records in the inner solar system in relation to the lunar reference system, In: Chronology and evolution of Mars (pp. 55-86), Springer, Dordrecht.

Nimmo, F. and E. Gaidos (2002), Strike-slip motion and double ridge formation on Europa, J. Geophys. Res., Vol. 107, doi. 10.1029/2000JE001476,

Nimmo, F., J.R. Spencer, R.T. Pappalardo, M.E. Mullen (2007), Shear heating as the origin of the plumes and heat flux on Enceladus, Nature, 447, pp. 289-291.

Nimmo, F. and B.G. Bills (2010), Shell thickness variations and the long-wavelength topography of Titan, Icarus, Vol. 208, pp. 896-904, doi. 10.1016/j.icarus.2010.02.020.

Oberst, J., B. Schreiner, B. Giese, G. Neukum, J.W. Head, R.T. Pappalardo and P. Helfenstein (1999), The distribution of bright and dark material on Ganymede in relationship to surface elevation and slopes, Icarus, 140(2), pp. 283-293.

Ojakangas, G. and D. Stevenson (1989), Thermal state of an ice shell on Europa, Icarus, Vol. 81, pp. 220-241.

Olgin, J.G., B.R. Smith-Konter and R.T. Pappalardo (2011), Limits of Enceladus's ice shell thickness from tidally driven tiger stripe shear failure, Geophysical Research Letters, Vol. 38.

Onderdonk, N., S. McGill and T. Rockwell (2018), A 3700 yr paleoseismic record from the northern San Jacinto fault and implications for joint rupture of the San Jacinto and San Andreas faults, Geopshere, Vol. 14, Nr. 6, pp. 2447-2468.

Padilla, A.M.R., M.E. Oskin, T.K. Rockwell, I. Delusina and D.M. Singleton (2021), Joint earthquake ruptures of the San Andreas and San Jacinto faults, California, USA, Geology, doi. 10.1130/G49415.1.

Paganelli, F., R.T. Pappalardo, G. Schubert, B. Stiles, G.C. Collins, K. Mitchell and E. Stofan (2010), Preliminary analysis of structural elements of Titan and implication for stress, Lunar Planet. Sci. 41. Abstract 2664 (Houston, TX).

Pappalardo, R.T. and R. Greeley (1995), A review of the origins of subparallel ridges and troughs: generalized morphological predictions from terrestrial models, J. Geophys. Res. 100 (E9), pp. 18985-19007.

Pappalardo, R.T., W. Head, G.C. Collins, R.L. Kirk, G. Neukum, G., J. Oberst, J.M. Moore, A. McEwen, B.R. Tufts, D.A. Senske, H.H. Breneman and K. Klaasen (1998), Grooved Terrain on Ganymede: First Results from Galileo High-Resolution Imaging, Icarus, 135(1), pp. 276-302, doi. 10.1006/icar.1998.5966.

Pappalardo, R.T., G.C. Collins, J.W. Head, P. Helfenstein, T.B. McCord, J.M. Moore, L.M. Prockter, P.M. Schenk and J.R. Spencer (2004), Geology of Ganymede, In: Bagenal F., T.E. Dowling, W.B. McKinnon (Eds.), Jupiter. The Planet, Satellites and Magnetosphere, Cambridge University Press, Cambridge, pp. 363-396.

Pappalardo, R.T. and G.C. Collins (2005), Strained craters on Ganymede, J. Struct. Geol. 27, pp. 827-838.

Pappalardo, R.T., Davis, D.M. (2007), In: Workshop on Ices, Oceans, and Fire: Satellites of the Outer Solar System (LPI 1357, 2007), pp. 108-109.

Patterson, G.W., G.C. Collins, J.W. Head, R.T. Pappalardo, L.M. Prockter, B.K. Lucchitta and J.P. Kay (2010), Global geologic mapping of Ganymede, Icarus, Vol. 207, pp. 845-867, doi. 10.1016/j.icarus.2009.11.035.

Patthoff, D. A., R.T. Pappalardo, A. Ismailyan, P. Sinclair, J. Li, B. Ayton, L. Tang, J. Kay and S.A. Kattenhorn (2016), Simulating tidal stresses on satellites using SatStressGUI: Now with Polar Wander, American Geophysical Union, Fall General Assembly, Abstract P51B-2147.

Perrin, C., I. Manighetti, J.P. Ampuero, F. Cappa and Y. Gaudemer (2016), Location of largest earthquake slip and fast rupture controlled by along-strike change in fault structural maturity due to fault growth, Journal of Geophysical Research: Solid Earth, 121(5), pp. 3666-3685, doi. 10.1002/2015JB012671.

Pizzi, A., A. Di Domenica, G. Komatsu, A. Cofano, G. Mitri and L. Bruzzone (2017), Spreading vs. Rifting as modes of extensional tectonics on the globally expanded Ganymede, Icarus 288, pp. 148-159.

Pollard, D.D., P.A.U.L. Segall and P.T. Delaney (1982), Formation and interpretation of dilatant echelon cracks, Geol. Soc. Am. Bull. 93 (12), pp. 1291-1303.

Pollard, D.D. and S.J. Martel (2020), Structural Geology: A Quantitative Introduction, Cambridge University Press, doi. 10.1017/9781139547222.

Porco, C. C., E. Baker, J. Barbara, K. Beurle, A. Brahic, J.A. Burns, S. Charnoz, N. Cooper, D.D. Dawson, A.D. Del Genio, T. Denk, L. Dones, U. Dyudina, M.W. Evans, S. Fussner, B. Giese, K. Grazier, P. Helfenstein, A.P. Ingersoll, R.A. Jacobson, T.V. Johnson, A. Mcewen, C.D. Murray, G. Neukum, W.M. Owen, J. Perry, T. Roatsch, J. Spitale, S. Squyres, P. Thomas, M. Tiscareno, E.P. Turtle. A.R. Vasvada, J. Veverka, R. Wagner and R. West (2005), Imaging of Titan from the Cassini spacecraft, Nature, 434, pp. 159-168, doi. 10.1038/nature03436.

Prockter, L.M., J.W. Head, R.T. Pappalardo, D.A. Senske, G. Neukum, R. Wagner, U. Wolf, J.O. Oberst, B. Giese, J.M. Moore, C.R. Chapman, P. Helfenstein, R. Greeley, H.H. Breneman and M.J. Belton (1998), Dark Terrain on Ganymede: Geological Mapping and Interpretation of Galileo Regio at High Resolution, Icarus, 135(1), pp. 317-344, doi. 10.1006/icar.1998.5981.

Reid, H.F. (1910), The California Earthquake of 1906, Report of the State Earthquake Investigation Commission, Washington D.C.

Rhoden, A.R., B. Militzer, E.M. Huff, T.A. Hurford, M. Manga and M.A. Richards (2010), Constraints on Europa's rotational dynamics from modeling of tidally-driven fractures, Icarus, Vol. 210, pp. 770-784.

Rhoden, A.R., G. Wurman, E.M. Huff, M. Manga and T.A. Hurford (2012), Shell tectonics: A mechanical model for strike-slip displacement on Europa, Icarus, Vol. 218 (1), pp. 297-307, doi. 10.1016/j.icarus.2011.12.015.

Rossi, C., P. Cianfarra, F. Salvini, G. Mitri and M. Masse (2018), Evidence of transpressional tectonics on the Uruk Sulcus region, Ganymede, Tectonophysics, 749, pp. 72-87, doi. 10.1016/j.tecto.2018.10.026.

Rossi, C., P. Cianfarra and F. Salvini (2020), Structural geology of Ganymede regional groove systems (60°N–60°S), Journal of Maps, 16:2, 6-16, doi. 10.1080/17445647.2019.1685605.

Roten, D., K.B. Olsen, S.M. Day, Y. Cui and D. Fah (2014), Expected seismic shaking in Los Angeles reduced by San Andreas fault zone plasticity, Geophysical Research Letters, V. 41, pp. 2769-2777, doi. 10.1002/2014GL059411.

Sandwell, D.T., Y. Zeng, Z.-K. Shen, J. Crowell, B., Murray, R. McCaffrey and X. Xu (2016), The SCEC Community Geodetic Model V1: Horizontal Velocity Grid, https://topex.ucsd.edu/CGM/technical_report/CGM_V1.pdf.

Sandwell, D.T. and B.R. Smith-Konter (2018), Maxwell: A semi-analytic 4D code for earthquake cycle modeling of transform fault systems, Computers and Geosciences, Vol. 112, doi. 10.1016/j.cageo.2018.01.009.

Scharer, K. M., G.P. Biasi, R.J. Weldon and T.E. Fumal (2010), Quasi-periodic recurrence of large earthquakes on the southern San Andreas fault, Geology, Vol. 38, doi. 10.1130/G30746.

Scharer, K.M., R.J. Weldon, G.P. Biasi, A. Streig and T.E. Fumal (2017), Ground-rupturing earthquakes on the northern Big Bend of the San Andreas Fault, California, 800A.D. to Present, J. Geophys. Res. Solid Earth, Vol. 122, pp. 2193-2218, doi. 10.1002/ 2016JB013606.

Scharer, K.M. and A. Streig (2019), The San Andreas Fault System: Complexities along a major transform fault system and relation to earthquake hazards, In Transform Plate Boundaries and Fracture Zones, pp. 249-269, Elsevier.

Scharer, K.M. and D. Yule (2020), A maximum rupture model for the southern San Andreas and San Jacinto faults, California, derived from paleoseismic earthquake ages: Observations and limitations, Geophys. Res. Let., doi. 10.1029/2020GL088532.

Schenk, P. (1998), Geology of Gilgamesh, Ganymede: New insights from stereo and topographic mapping, 29th Lunar and Planetary Science Conference, Abstract #1949.

Schenk, P. M., Chapman, C. R., Zahnle, K., & Moore, J. M. (2004). Ages and interiors: The cratering record of the Galilean satellites. Jupiter: The planet, satellites and magnetosphere, 2, p. 427.

Schenk P. M., I. Matsuyama and F. Nimmo (2008), True polar wander on Europa from global-scale small-circle depressions, Nature, 453, pp. 368-371.

Schenk, P. (2010), Atlas of the Galilean satellites, Cambridge University Press.

Schenk, P.M. and S.W. Murphy, S.W. (2011), The Rayed Craters of Saturn's Icy Satellites (Including Iapetus): Current Impactor Populations and Origins, 42nd Lunar and Planetary Science Conference, Abstract #2098.

Schmidt, B.E., D.D. Blankenship, G.W. Patterson and P.M. Schenk (2011), Active formation of 'chaos terrain'over shallow subsurface water on Europa: Nature, Vol. 479, p. 502.

Scholz, C.H. (1988.), The brittle-plastic transition and the depth of seismic faulting, Geologische Rundschau, 77(1), pp. 319-328.

Schubert, G., J.D. Anderson, T. Spohn, T. and W.B. McKinnon (2004), Interior composition, structure and dynamics of the Galilean satellites, Jupiter: The Planet, Satellites and Magnetosphere, Vol. 1, pp. 281-306.

Schulson, E.M. and A.L. Fortt (2012), Friction of ice on ice, J. of Geophys. Res.: Solid Earth, Vol.117, doi. 10.1029/2012JB009219.

Schulson, E.M. (2016), Low-speed friction and brittle compressive failure of ice: fundamental processes in ice mechanics, International Material Reviews, doi. 10.1179/ 1743280415Y. 0000 000010.

Schurmeier, L.R., A.J. Dombard, J. Radebaugh and M. Malaska (2018), Intrusive and extrusive cyovolcanism and the composition of Titan's icy crust, 49th Lunar and Planetary Science Conference, LPI Contribution 2083.

Schwartz, D.P., P.J. Haeussler, G.G. Seitz and T.E. Dawson (2012), Why the 2002 Denali fault rupture propagated onto the Totschunda fault: Implications for fault branching and seismic hazards, Journal of Geophysical Research, 117, B11304, doi. 10.1029/2011JB008918.

Schwartz, D.P. (2018), Review: Past and future fault rupture lengths in seismic source characterization -The long and short of it, Bulletin of the Seismological Society of America, doi. 10.1785/0120160110.

Seidelmann, P.K., B.A. Archinal, M.F. A'hearn, A. Conrad, G.J. Consolmagno, D. Hestroffer, J.L. Hilton, G.A. Krasinsky, G. Neumann, J. Oberst, P. Stooke, E.F. Tedesco, D.J. Tholen, P.C. Thomas and I.P. Williams (2007), Report of the IAU/IAG Working Group on cartographic coordinates and rotational elements: 2006, Celestial Mech Dyn Astr 98, pp. 155-180, doi. 10.1007/s10569-007-9072-y.

Shoemaker, E.M., B.K. Lucchitta, D.E. Wilhelms, J.B. Plescia and S.W. Squyres (1982), The geology of Ganymede. In Satellites of Jupiter, pp. 435-520.

Showman, A.P. and R. Malhotra (1997), Tidal evolution into the Laplace resonance and the resurfacing of Ganymede. Icarus, 127(1), doi. 10.1006/icar.1996.5669.

Showman, A.P., D.J. Stevenson and R. Malhotra (1997), Coupled orbital and thermal evolution of Ganymede, Icarus, 129(2), pp. 367-383, doi. 10.1006/icar.1997.5778.

Sieh, K.E. (1978), Slip along the San Andreas Fault associated with the great 1857 earthquake, Bulletin of the Seismological Society of America, Vol. 68, pp. 1421-1448.

Sieh, K.E. and Jahns, R.H. (1984), Holocene activity of the San Andreas fault at Wallace Creek, California, Geological Society of America Bulletin 95, pp. 883-896.

Smith, B.A., et al. (1979 a), The Jupiter system through the eyes of Voyager 1, Science 204, pp. 951-972.

Smith, B.A., L.A. Soderblom, R. Beebe, J. Boyce, G. Briggs, M. Carr, S.A. Collins, A.F. Cook, A.F., G.E. Danielson, M.E. Davies, G.E. Hunt, A. Ingersoll, A., T.V. Johnson, H. Masursky, J. McCauley, D. Morrison, T. Owen, C. Sagen, E.M. Shoemaker, R. Strom, V.E. Suomi and J. Veverka (1979b), The Galilean satellites and Jupiter: Voyager 2 imaging science results. Science 206, pp. 927-950.

Smith, B.R. and D.T. Sandwell (2004), A three-dimensional semianalytic viscoelastic model for time-dependent analyses of the earthquake cycle, Journal of Geophysical Research, Vol. 109, doi. 10.1029/2004JB003185.

Smith, B.R. and D.T. Sandwell (2006), A model of the earthquake cycle along the San Andreas Fault System for the past 1000 years, Journal of Geophysical Research, Vol. 111, doi. 10.1029/2005JB003703.

Smith-Konter, B., R.T. Pappalardo (2008), Tidally driven stress accumulation and shear failure of Enceladus's tiger stripes, Icarus, Vol. 198, doi. 10.1016/j.icarus.2008.07.005.

Smith-Konter, B.R. and D.T. Sandwell (2009), Stress evolution of the San Andreas Fault System: Recurrence interval versus locking depth, Geophysical Research Letters, Vol. 36, L13304, doi. 10.1029/2009GL037235.

Smith-Konter, B.R, D.T. Sandwell and P. Shearer (2011), Locking depths estimated from geodesy and seismology along the San Andreas Fault System: Implications for seismic moment release, Journal of Geophysical Research, Vol. 116, doi. 10.1029/2010JB 008117.

Sohl, F., H. Hussmann, B. Schwentker, T. Spohn and R.D. Lorenz (2003), Interior structure models and tidal Love numbers of Titan, J. Geophys. Res., Vol. 108, doi. 1029/2003 JE002044.

Sohl, F., A. Solomonidou, F.W. Wagner, A. Coustenis, H. Hussmann, and D. Schulze-Makuch (2014), Structural and tidal models of Titan and inferences on cryovolcanism, J. of Geophys. Res.: Planets, doi. 10.1002/2013JE004512.

Sotin, C., K.J. Lawrence, B. Reinhardt, J.W. Barnes, R.H. Brown, A.G. Hayes, S. Le Mouélic, S. Rodriguez, J.M. Soderblom, L.A. Soderblom, K.H. Baines, B.J. Buratti, R.N. Clark, R. Jaumann, P.D. Nicholson and K. Stephan (2012), Observations of Titan's Northern lakes at 5 μm: Implications for the organic cycle and geology, Icarus, Vol. 221, pp. 768-786, doi. 10.1016/j.icarus.2012.08.017.

Stofan, E.R., C. Elachi, J.I. Lunine, R.D. Lorenz, B. Stiles, K.L. Mitchell, S. Ostro, L. Soderblom, C. Wood, H. Zebker, S. Wall, M. Janssen, R. Kirk, R. Lopes, F. Paganelli, J. Radebaugh, L. Wye, Y. Anderson, M. Allison, R. Boehmer, P. Callahan, P. Encrenaz, E. Flamini, G. Francescetti, Y. Gim, G. Hamilton, S. Hensley, W.T.K. Johnson, K. Kelleher, D. Muhleman, P. Paillou, G. Picardi, F. Posa, L. Roth, R. Seu, S. Shaffer, S. Vetrella and R. West (2007), The lakes of Titan, Nature 445, pp. 61-67, doi. 10.1038/nature 05438.

Tapponnier, P., Z. Xu, F. Roger, B. Meyer, N. Arnaud, G. Wittlinger and J. Yang (2001), Oblique Stepwise Rise and Growth of the Tibetan Plateau, Science, Vol. 294 (5547), pp. 1671-1677, doi. 10.1126/science.105978.

Taylor, M., A. Yin, F.J. Ryerson, P. Kapp and L. Ding (2003), Conjugate strike-slip faulting along the Bangong-Nujiang suture zone accommodates coeval east-west extension and north-south shortning in the interior of the Tibetan Plateau, Tectonics, Vol. 22 (4), doi. 10.1029/2002TC001383.

Tchalenko, J. S. (1970), Similarities between shear zones of different magnitudes, Geological Society of America Bulletin, 81(6), pp. 1625-1640.

Tennyson, M.E. (1998), Estimates of ultimate recovery of oil from California's giant fields (>100 million barrels), 1923–1995: U.S. Geological Survey Open-File Report 98-513-A.

Thatcher, W. and T.C. Hanks (1973), Source parameters of Southern California earthquakes, J. Geophys. Res. 78, pp. 8547-8576.

Thatcher, W.R., D.S. Chapman, A.A. Allam C.F. and C. Williams (2017), Refining Southern California geotherms using seismologic, geologic, and petrologic constraints, Poster Presentation at 2017 SCEC Annual Meeting, SCEC Contribution 7857.

Thomas, A.L. and D.D. Pollard (1993), The geometry of echelon fractures in rock: Implications from laboratory and numerical experiments, J. Struct. Geol 15 (3), pp. 323-334.

Tomasko, M. G., et al. (2005), Rain, winds, and haze during the Huygens probe's descent to Titan's surface, Nature, 438, pp. 765–778, doi. 10.1038/nature04126.

Tong, H. and A. Yin (2011), Reactivation tendency analysis: A theory for predicting the temporal evolution of preexisting weakness under uniform stress state, Tectonophysics, Vol. 503, pp. 195-200, doi. 10.1016/j.tecto.2011.02.012.

Tong, X., B.R. Smith-Konter and D.T. Sandwell (2014), Is there a discrepancy between geological and geodetic slip rates along the San Andreas Fault System?, J. Geophys. Res. Solid Earth, 119, pp. 2518-2538, doi. 10.1002/2013JB010765.

Toppozada, T.R., D.M. Branum, M.S. Reichle and C.L. Hallstrom (2002), San Andreas Fault Zone, California: M>5.5 earthquake history, Bulletin of the Seismological Society of America, Vol. 92, pp. 2574-2578, doi. 10.1785/0120000614.

Turcotte, D.L. and G. Schubert (2002), Geodynamics, 2nd ed., 456 pp., Cambridge University Press, ISBN 0521 66186 2.

Turtle, E.P., J.E. Perry, A.G. Hayes, R.D. Lorenz, J.W. Barnes, A.S. Mcewen, R.A. West, A.D. Del Genio, J.M. Barbara, J.I Lunine, E.L. Schaller, T.L. Ray, R.M.C. Lopes and E.R. Stofan (2011), Rapid and extensive surface changes near Titan's equator: Evidence of April showers, Science, Vol. 331 (6023), pp. 1414-1417, doi. 10.1126/ science.1201063.

Turtle, E.P., J.E. Perry, J.M. Barbara, A.D. Del Genio, S. Rodriguez, S. Le Mouélic, C. Sotin, J.M. Lora, S. Faulk, P. Corlies, J. Kelland, S.M. MacKenzie, R.A. West, A.S. McEwen, J.I. Lunine, J. Pitesky, T.L. Ray and M. Roy (2018), Titan's Meteorology Over the Cassini Mission: Evidence for Extensive Subsurface Methane Reservoirs, Geophys. Res. Lett., Vol. 45, doi. 10.1029/2018GL078170.

Vance, S., M. Bouffard, M. Choukroun and C. Sotin (2014), Ganymede's internal structure including thermodynamics of magnesium sulfate oceans in contact with ice, Planetary and Space Science, 96, pp. 62-70.

Vendeville, B., P.R. Cobbold, P. Davy, J.P. Brun and P. Choukroune (1987), Physical models of extensional tectonics at various scales, in Continental Extensional Tectonics (M.P. Coward et al., eds.), Geol. Soc. Amer. Spec. Publ. No. 28, pp. 95-107.

Wahr, J., Z.A. Selvans, M.E. Mullen, A.C. Barr, G.C. Collins, M.M. Selvans and R.T. Pappalardo (2009), Modeling stresses on satellites due to nonsynchronous rotation and orbital eccentricity using gravitational potential theory, Icarus, Vol. 200, doi. 10.1016/j.icarus. 2008. 11.002.

Wallace, R.E. (1968), Notes on stream channels offset by the San Andreas fault, Southern Coast Ranges, California. Stanford University Publications, Geological Sciences 11, pp. 6-20.

Wang, H. (2000), Theory of Linear Poroelasticity with Applications to Geomechanics and Hydrogeology, Princeton University Press, Princeton, New Jersey.

Ward, L.A., B.R. Smith-Konter, X. Xu and D.T. Sandwell (2021), Seismic Moment Accumulation Response to Lateral Crustal Variations of the San Andreas Fault System, JGR Solid Earth, doi. 10.1029/2020JB021208.

Wdowinski, S., B.R. Smith-Konter, Y. Bock and D.T. Sandwell (2007), Spatial characterization of the interseismic velocity field in southern California, Geology, doi. 10.1130/G22938A.1.

White, O.L., P.M. Schenk, A.W. Bellagamba, A.M. Grimm, A.J. Dombard and V.J. Bray (2017), Impact crater relaxation on Dione and Tethys and relation to heat flow, Icarus, Vol. 288, pp. 37-52, doi. 10.1016/j.icarus.2017.01.025.

Weldon, R.J. and K.E. Sieh (1985), Holocene rate of slip and tentative recurrence interval for large earthquakes on the San Andreas fault, Cajon Pass, southern California, Geol. Soc. Am. Bull. 96, pp. 793-812.

Weldon, R., T. Fumal and G. Biasi (2004), Wrightwood and the earthquake cycle: What a long recurrence record tells us about how faults work, GSA Today, Vol. 14, pp. 4-10, doi. 10.1130/1052–5173.

Werynski, A., C.D. Neish, A. Le Gall, M.A. Janssen and the Cassini RADAR Team (2019), Compositional variations of Titan's impact craters indicate active surface erosion, Icarus, Vol. 321, pp. 508-521, doi. 10.1016/j.icarus.2018.12.007.

Wessel, P., W.H.F. Smith, R. Scharroo, J. Luis and F. Wobbe (2013), Generic Mapping Tools: Improved Version Released, EOS, Vol. 94(45), pp. 409-410.

Williams, A.P., B.I. Cook and J.E. Smerdon (2022), Rapid intensification of the emerging southwestern North American megadrought in 2020–2021, Nature Climate Change, Vol. 12, doi. 10.1038/s41558-022-01290-z.

Wood, C.A., R. Lorenz, R. Kirk, R.M.C. Lopes, K. Mitchell, E. Stofan and The Cassini RADAR Team (2010), Impact craters on Titan, Icarus, Vol. 206(1), pp. 334-344, doi. 10.1016/j.icarus. 2009.08.021.

Woodcock, N.H. and M. Fischer (1986), Strike-slip duplexes, Journal of Structural Geology, Vol. 8 (7), pp. 725-735.

Working Group on California Earthquake Probabilities (1995), Seismic Hazards in Southern California: Probable Earthquakes, 1994 to 2024, Bull. Seismol. Soc. Amer. 85, pp. 379-439.

Working Group on California Earthquake Probabilities (2003), Earthquake probabilities in the San Francisco Bay Region: 2002-2031, U.S. Geol. Surv. Open File Rep., 03-214.

Xu, X., L. Ward, J. Jiang, B.R. Smith-Konter, E. Tymofyeyeva, E.O. Lindsey, A.G. Sylvester and D.T. Sandwell (2018), Surface creep rate of the southern San Andreas Fault modulated by stress perturbations from nearby large events, Geophys. Res. Letters, 45, doi. 10.1029/2018GL080137.

Yin, A. and R.T. Pappalardo (2015), Gravitational spreading, bookshelf faulting, and tectonic evolution of the South Polar Terrain of Saturn's moon Enceladus, Icarus, Vol. 260, pp. 409-439, doi. 10.1016/j.icarus.2015.07.017.

Yin, A., A.V. Zuza and R.T. Pappalardo (2016), Mechanics of evenly spaced strike-slip faults and its implications for the formation of tiger-stripe fractures on Saturn's moon Enceladus, Icarus, Vol. 266, pp. 204-216, doi. 10.1016/j.icarus.2015.10.027.

Yoder, C.F. and S.J. Peale (1981), The tides of Io, Icarus, 47(1), pp. 1-35, doi. 10.1016/0019-1035(81)90088-9.

Zhang, Y., M. Person, J. Rupp, K. Ellett, M.A. Celia, C.W. Gable, B. Bowen, J. Evans, K. Bandilla, P. Mozley, T. Dewers and T. Elliot (2013), Hydrogeologic controls on induced seismicity in crystalline basement rocks due to fluid injection into basal reservoirs, Groundwater 51, pp. 525–538, doi. 10.1111/gwat.12071.

Zahnle, K., Dones, L. and H.F. Levison, H.F. (1998), Cratering rates on the Galilean satellites, Icarus, Vol. 136 (2), pp. 202-222.

Zahnle, K., P. Schenk, S. Sobieszczyk, L. Dones and H. Levison (2001), Differential cratering of synchronously rotating satellites by ecliptic comets, Icarus 153, pp. 111-129.

Zahnle, K., P. Schenk, P., H. Levison, H. and L. Dones (2003), Cratering rates in the Outer Solar System, Icarus, 163(2), pp. 263-289.

Zielke, O., J.R. Arrowsmith, L.G. Ludwig and S.O. Akciz (2012), High-Resolution Topography-Derived Offsets along the 1857 Fort Tejon Earthquake Rupture Trace, San Andreas Fault, Bulletin of the Seismological Society of America, Vol. 102, No. 3, pp. 1135-1154, doi. 10.1785/01201 10230.

Zoback, M.D., M.L. Zoback, V.S. Mount, J. Suppe, J.P. Eaton, J.H. Healy, D. Oppenheimer, P. Reasenberg, L. Jones, C.B. Raleigh, I.G. Wong, O. Scotti and C. Wentworth (1987), New evidence on the state of stress of the San Andreas Fault System, Science, Vol. 238 (4830), pp. 1105-1111, doi. 10.1126/science.238.4830.1105.

Zoback, M.D., S.H. Hickman and W.E. Ellsworth (2010), Scientific drilling into the San Andreas fault zone: Eos (Transactions of the American Geophysical Union, Washington, D.C.), v. 91, no. 22, pp. 197-204.